MECHANISM AND KINETICS OF GOLD ELECTRODEPOSITION FROM ACIDIC SOLUTIONS

by

Yigen Li

Thesis presented to Département de chimie
for the doctoral degree in sciences (Ph. D.)

FACULTÉ DES SCIENCES
UNIVERSITÉ DE SHERBROOKE

Sherbrooke, Québec, Canada, May 1996

ISBN 0-612-15454-8

To my parents

To my wife and my daughter

To my friends

ABSTRACT

Gold deposition in a commercial acid gold plating bath (Ronovel N) was investigated by means of various electrochemical and microscopic techniques, mainly focused on the studies of the nucleation and crystal growth in the initial stages of deposition. The mechanism and kinetics of nucleation and crystal growth for both soft and hard gold deposition were determined, and were found to depend strongly on the applied potential, the solution composition and the substrate used.

It was found from voltammetric and chronopotentiometric measurements that a self-inhibition phenomenon occurs during gold deposition at more positive potentials. An equation describing the dependence of current on rotation rate of rotating disk electrode was derived based on the hypothesis that the reduction of adsorbed AuCN occurs at more positive potentials. This hypothesis was confirmed by the results obtained from voltammetric measurements.

Nucleation and crystal growth during gold deposition were studied by the analysis of chronoamperometric curves using nonlinear least-squares (NLS) method. The potential-dependent inhibition of crystal growth was found during both soft and hard gold deposition at more positive potentials. The growth rate constant of hard gold is much lower than that of soft gold. Nucleation rate constant of hard gold increases with overpotential, in agreement with the atomistic theory. However, nucleation for soft gold is inhibited.

A partial inhibition growth model was developed. It was based on the hypothesis that crystal growth is partially inhibited and the vertical crystal growth rate decreases exponentially to a constant at longer times. This model combines the right-circular cones growth model and the complete inhibition growth model. It was shown that the partial inhibition growth model may be applied to hard gold deposition. Chronoamperometric curves obtained on gold, glassy

carbon and nickel substrates at more negative potentials are well described by this model. The time-dependent inhibition of crystal growth was found for hard gold deposition at more negative potentials. For glassy carbon electrode, alternatively, another simple model of three-dimensional cylindrical growth presented in the work also gives a good description for the experimental data.

The surface morphology of gold deposits was characterized using SEM and AFM techniques. The inhibition of crystal growth observed electrochemically was further confirmed by *ex-situ* SEM and AFM observation. Three-dimensional progressive nucleation was found in gold deposition at more positive potentials. Furthermore, AFM confirmed that the growth features of gold deposits, obtained on Cu substrate at more positive potentials, are pyramids rather than rounded "hemispheroids", in a good agreement with the assumption of right-circular cones growth used in the nucleation and crystal growth model. The bimodal distribution of crystal size was observed from the SEM of hard gold obtained at more negative potentials, showing an evidence of the partial inhibition of crystal growth.

SOMMAIRE

La déposition de l'or dans un bain de placage acide commercial (Ronovel N) a été étudiée au moyen de différentes techniques électrochimiques et microscopiques, se concentrant principalement sur les études de nucléation et de croissance des cristaux aux stades initiaux de la déposition. Le mécanisme et la cinétique de nucléation et de croissance des cristaux ont été déterminés pour la déposition de l'or dur et doux. Ils dépendent fortement du potentiel appliqué, de la composition de la solution et du substrat utilisé.

Il fut déterminé à partir des mesures voltampérométriques et chronopotentiométriques qu'un phénomène d'auto-inhibition se produit durant la déposition de l'or à potentiels plus positifs. Une équation décrivant la dépendance du courant sur la vitesse de rotation de l'électrode tournante à disque a été dérivée en se basant sur l'hypothèse que la réduction du AuCN adsorbé se produit aux potentiels plus positifs. Cette hypothèse fut confirmée par les résultats obtenus à partir des mesures voltampérométriques.

La nucléation et la croissance des cristaux durant la déposition de l'or dur furent étudiées par l'analyse des courbes chronoampérométriques en utilisant la méthode des moindres carrés non linéaires. La dépendance de l'inhibition de la croissance des cristaux sur le potentiel fut trouvée pour la déposition des deux types d'or, dur et doux, aux potentiels plus positifs. La constante de vitesse de nucléation pour l'or dur augmente avec la surtension, en accord avec la théorie atomistique. Toutefois, la nucléation de l'or doux est inhibée.

Un modèle pour l'inhibition partielle de la croissance a été développé. Il fut basé sur l'hypothèse que la croissance des cristaux est partiellement inhibée et que la vitesse verticale de croissance des cristaux décroit exponentiellement jusqu'à une valeur constante aux temps longs. Le modèle développé combine le modèle de croissance en cônes circulaires et le modèle d'inhibition complète de la croissance. Il fut démontré que le modèle d'inhibition partielle de la

croissance peut être appliqué à la déposition de l'or dur. Les courbes chronoampérométriques obtenues sur les substrats d'or, de carbone vitreux et de nickel aux potentiels plus négatifs sont bien décrites par ce modèle. Il fut trouvé que l'inhibition de la croissance des cristaux pour la déposition de l'or dur depend du temps aux potentiels plus négatifs. Pour l'électrode tournante à disque de carbone vitreux, un autre modèle simple de croissance cylindrique en trois dimensions présenté dans le travail donne aussi une bonne description des donneés expérimentales.

La morphologie de la surface des dépôts de l'or fut caractérisée par les techniques de MEB et de microscope à force atomique (MFA). L'inhibition de la croissance des cristaux observée électrochimiquement fut confirmée par l'observation *ex-situ* en MEB et MFA. La nucléation progressive en trois dimensions a été observée pour la déposition de l'or aux potentiels plus positifs. Le MFA a confirmé que les caractéristiques des dépôts, obtenus sur le substrat de Cu aux potentiels plus positifs, est pyramidal plutôt qu'hémisphérique, en bon accord avec l'hypothèse de la croissance en cônes circulaires utilisée dans le modèle de nucléation et de croissance des cristaux. La distribution bimodale de la grosseur des cristaux est observée par MEB pour l'or dur aux potentiels plus négatifs, amenant l'évidence de l'inhibition partielle de la croissance des cristaux.

ACKNOWLEDGMENTS

I would like to express my deep and sincere appreciation to Prof. Andrzej Lasia, first for his never-ending advice, patient guidance and kind help, secondly for his financial support throughout this work.

Great thanks are due to Dr. Linlin Chen for his assistance and discussions in the initial stages of this work and for taking AFM images shown in the thesis. The helps of Mr. Pierre Magny in taking SEM pictures, and Prof. Daniel Guay in the use of AFM equipment, are very appreciated. Thanks are also due to my colleagues, especially Dr. W. Chrzanowski for his helps in the initial stages of this work, and Dr. D. Miousse for her helps in the work. I also would like to thank Prof. Hugues Menard and Prof. Jean Lessard for allowing to use the equipment in their laboratories.

My special thanks are due to my various friends for their helps, encouragement and friendship throughout this work.

Finally, I wish to thank my parents and my wife. Their endless love, encouragement, patience and sacrifice made this work possible.

TABLE OF CONTENTS

LIST OF TABLES

LIST OF FIGURES

MAJOR SYMBOLES

A'	rate of conversion of one site into a nucleus (s^{-1})
A	nucleation rate constant (nuclei cm^{-2} s^{-1})
A_{2D}	nucleation rate constant for two-dimensional nucleation and growth
A_{3D}	nucleation rate constant for three-dimensional nucleation and growth
C	concentration of depositing metal in solution (mol cm^{-3})
C_{dl}	double layer capacity (μF cm^{-2})
D	diffusion coefficient (cm^{-2} s^{-1})
E	potential (V) and the expection of coverage in Evans theory.
F	Faraday constant (C mol^{-1})
ΔG	free energy for hetergeneous critical nucleation (J mol^{-1})
h	height of atomic layer (cm)
i	current (mA)
j, j_{max}, j_{st}	current density (mA cm^{-2}), maximum and steady-state current density.
k, k'	growth rate constants (mol cm^{-2} s^{-1}) in lateral and vertical directions, respectively.
k_1, k_2	constants in the partial inhibition model
k_1, k_{-1}, k_f	reaction rate constants
K, K' K'' K_1	constants
M	atomic weight of depositing metal (g)
N	the number of nuclei formed at time t (cm^{-2})
N_0	the total number of active sites per unit surface area (cm^{-2})
P_0, P_1, P_2, P_3	constants in models
r	reaction rate, and radius of growing crystal
R	gas constant (J mol^{-1} K^{-1})
R_a, R_{max}	mean surface roughness and maximum grain height (nm)
S	actual fractional area of growth centres
S_{ext}	the extended fractional area in Avrami theory

t	time (s)
T	absolute temperature (K)
v	growth rate (cm s^{-1})
V	volume of deposited metal (cm^3) and growth rate
V'	growth rate
V_0	constant
z	number of electron transfered
α	transfer coefficient
β	constant
ε	eccentricity of ellipsoids
γ	surface energy (J mol^{-1})
η	overpotential (V or mV)
λ	inhibition parameter in partial inhibition model
ν	kinematic viscosity (cm^{-2} s^{-1})
θ	surface coverage of adsorbed AuCN
ρ	density of deposited metal (g cm^{-3})
ω	angular frequency
δ	diffusion layer thickness (cm) and the Dirac δ function

INTRODUCTION

Gold deposits are extensively used in the electrical and the electronic industries as well in decoration. The unique combination of good electrical conductivity coupled with excellent physical and chemical properties has led to its widespread adoption as standard materials for contacts, bonding, joining and high performance, high reliability conductors in electronic industry.

Gold deposits are usually classified into two categories, *i.e.*, soft gold and hard gold deposits. So-called soft gold deposit (Vickers hardness 60~90 KV N_{25} (1)) is usually pure gold, which has high electrical conductivity, high corrosion resistance, good ductility and solderability. It is used mainly in semiconductor devices, in which bond strength is of primary importance. However, soft gold has relatively poor wear resistance, its applications in contacts and connectors are limited. Hard gold (hardness 120~260 KV N_{25} (1)), which contains a small amount of transition elements as hardeners, meets the combined requirements of low electrical contact resistance, low porosity, high corrosion resistance and excellent wear resistance, hence, it is used as contact materials in electrical and printed circuit boards.

Although practiced for more than 150 years, the technology of gold electroplating has been developed to its present high level of efficiency only in the last decades, due to the fast development of electronic industry since 1940's. This industry becomes the major user of gold plating. For example, the world consumption of gold electrodeposits in electronic applications in 1990 was up to 110 000 kg (1). It is the continuous growth of electronic industry that has ensured and stimulated the necessary research and development work in the field of gold electroplating. In spite of its widespread use in electronic industry, the fundamentals of gold deposition process are not fully understood and still need to be explored.

The aim of the present work is to study the mechanism and kinetics of gold deposition in a proprietary acid solution (Renovel N bath) by means of various techniques, mainly focused on the mechanism and kinetics of nucleation and crystal growth in the initial stages of gold deposition. As a background to this work, chapter 1 reviews the study of gold electrodeposition, chapter 2 reviews the theory of nucleation and crystal growth. The experimental details are given in chapter 3. The results obtained by voltammetry and chronopotentiometry are presented in chapter 4 and 5, respectively. Chapter 6 and 7 present the results obtained from chronoamperometric measurements for soft gold and hard gold. The mechanism and kinetics of nucleation and crystal growth of gold deposits in the initial stages are discussed in details by analyzing chronoamperometric curves. Furthermore, a partial inhibition model is developed in the section 7.2. Chapter 8 deals with the influence of substrates on gold deposition, a three-dimensional nucleation and cylindrical growth model is derived in the section 8.4. In chapter 9, gold deposits obtained on Au and Cu substrates are characterized using scanning electron microscopy (SEM) and atomic force microscopy (AFM).

The present work has led to following publications:

1. W. Chrzanowski, Y. G. Li, A. Lasia, J. App. Electrochem. **26**, 385 (1996).
2. Y.G. Li, W. Chrzanowski, A. Lasia, "Nucleation and crystal growth in gold electro-deposition from acid solutions. Part I. Soft gold". J. App. Electrochem., in press (1996).
3. Y.G. Li and A. Lasia, "Nucleation and crystal growth in gold electrodeposition from acid solution. Part II. Hard gold". J. App. Electrochem., in press (1996).
4. Y.G. Li and A. Lasia, "The study of gold electrodeposition on Cu by electrochemical and microscopic techniques", J. App. Electrochem., submitted (1996).
5. Y.G. Li and A. Lasia, "The influenec of substrate on gold electrodeposition", under preparation.

CHAPTER 1
ELECTRODEPOSITION OF GOLD

The electrodeposition of gold may date back to the 18th century, the first record of gold electroplating being in 1802 by Brugnalelli (2). However, it was not until 1840 that the Elkington brothers patented the forerunner of modern gold electroplating formation based on the gold potassium cyanide (3). Since then, especially in the last a few decades, a large number of studies have been undertaken from various points of view, and these studies are still in progress. The main investigation interests in gold deposition lay in four aspects:

- chemistry of baths;
- new plating techniques;
- mechanism and kinetics of the deposition;
- structure and properties of deposits.

1.1 Evolution of gold plating baths

The main aims of studies on the chemistry of gold plating bath are: to develop new baths for specific applications, to modify old bath to improve the quality of deposits, to understand the performance of the electrolyte and the function of individual components in solution.

Wide application of gold deposits has led to the development of hundreds of greatly diversified, mostly proprietary bath formulations (4). In the past 155 years, the original plating bath patented by the Elkington brothers, which was initially developed for decorative use, has evolved into about 300 different modifications in the United States and about 100 in Europe due to the change of fads and fashions in the decorative fields. With the development of the electronic industry in the 1940's and 1950's, there appeared a new demand for different

deposits that had been required for decorative plating. The physical properties rather than the colors of the gold deposit should be modified. This has resulted in the evolution of over 200 more gold and gold-alloy baths. The development of hundreds of different gold baths was paralleled by only about 40 different baths for nickel or copper plating. Nevertheless, only a small number of bath types are really required at any given times. It seemed in the past that gold plating bath changed gradually from alkaline to acid solutions. The classification of gold plating bath is usually based on the pH of the solution which is one of determining factors for the properties of the deposit. Although hundreds of baths were developed in the past, they can be classified into four main groups according to the pH of the solution (5), *i.e.*, alkaline cyanide, neutral cyanide, weakly acidic and strongly acidic baths, as shown in Table 1.

Alkaline cyanide electrolytes have traditionally been used for deposition of decorative coating of various colors. High concentrations of free cyanide are usually contained in solution. Pure gold coating used in semiconductors in electronic industry is mainly deposited from neutral electrolytes, in which a gold coating of high purity, high ductility, good solderability and bondability are called for. The weakly acidic electrolytes are by far the most important in the electronic industry. They are less toxic and permit one to use much higher current densities as compared with traditionally used alkaline cyanide solutions. They are used, for example, in the plating of contacts and printed circuit boards. A further development in recent years is the use of weakly acidic gold electrolytes in a modified form, in selective plating under high speed conditions. This process is used increasingly in the electronic industry.

Generally, each kind of bath contains: 1) gold complex salt, usually gold cyanide, sometimes $Na_3Au(SO_3)_2$; 2) conducting salts; 3) buffer salts; 4) complex or chelate salts; 5) brightener or hardener; 6) additives, *etc.* Typical bath formulations for hard gold plating are given in Table 2.

Table 1. Classification of gold electrolytes based on the pH of solution (5).

Bath type	pH range	Au complex	Conducting and buffer salts	Year of introduction	Main application
Alkaline	8-13	$KAu(CN)_2$ or $(Na_3Au(SO_3)_2)$	Alkaline	Since 1840 (baths with $KAu(CN)_2$)	Decorative (electrical engineering)
Neutral	6-8	$KAu(CN)_2$	Phosphates Citrates	After 1945	Electronics
Weakly acidic	3-6	$KAu(CN)_2$	Phosphates Weak organic acids (e.g. citric acid)	After 1955	Electrical engineering, electronics
Strongly acidic	0.5-2.5	$KAu(CN)_4$	Acids Acid salts	After 1980	Decorative (electronics)

Table 2. Examples of bath composition (g l^{-1}) and operating conditions for hard gold plating (1).

	1	2
Gold as $KAu(CN)_2$	4	12
Citric acid	120	105
Tetraethylene Pentamine	20	
Phosphoric acid		12.5
Ni-citrate	2.5	
Co-EDTA		1
Temperature, °C	40	35
Current density (A cm^{-2})	20	5

In weakly acidic solutions, there are two basic types of buffer systems used, *i.e.*, citrate and phosphate, or their mixtures (6-8), although other organic compounds were also patented (10). Except for its buffering effect, citrate also acts as a conducting salt and a complexing agent.

Transition elements such as cobalt, nickel and/or iron are the preferred alloying metals in acid hard gold bath (4). The codeposition of only 0.5% of these metals is sufficient to create a bright, hard and abrasion resistant gold layer characterized by electrical conductivity, contact resistance and corrosion resistance comparable with pure gold. In addition to the alloying metal, the gold deposits usually contain 0.5 ~1.0 % of organic matter (5). In order to control and maintain a certain level of hardener in solution, the hardener should be complexed with an organic compound. Various nickel or cobalt complexes are used. For example, in nickel hardened gold deposition, Ni-EDTA, Ni-citrate, Ni-cyanide, Ni-sulphmate, Ni-sulphate, Ni-

oxalate, Ni-ATMP (ATMP is nitrilotri(methylene)phosphonic acid), *etc.*, were reported (7,8,10,11). If the complex is too weak, the free concentration of nickel is not easily controlled, the properites of deposits obtained may vary with the age of the bath. If the complex is too strong, then the total concentration of nickel in solution should be very high to maintain a suitable level of free nickel. In the earlier practice, very weak complexes were used. Now, mediate complexes are preferred in the application. Sometimes, mixtures of complexes are used.

In gold deposition, Au (I) may be partially oxidized at the anode to Au (III), leading to a decrease of current efficiency because only Au (I) is reduced to Au on the cathode (12). In order to prevent the oxidation of Au (I), a reducing agent is needed in the bath. Oxalic acid may be a suitable selection since it has a weak reducing ability for Au (III) (8). Oxalic acid may also act as a complex for metal impurities. However, it should be noticed that a too high concentration of oxalic acid may cause electroless reduction of gold on the walls of the tank, which results in the loss of gold. Instability of solution may also be caused by a relatively high concentration of oxalic acid in the solution.

A large improvement in the modern gold deposition bath resulted from the introduction of a current extender into the solution. Typically, such a current extender increases the bath's ability to plate at high current density without the deposit being "burnt" (a "burnt" deposit is spongy and black). This is specially important for modern selective high speed plating. Various compounds, for example, formic acid (10), a heterocylic azohydrocarbon sulfonic acid and or its salts (13), glycolic acid and its salts (14), and substituted pyridine compounds (8), *etc.* are commonly used as current extenders.

As mentioned above, many bath formulations for gold plating are proprietary. Table 3 gives the examples of proprietary hard gold baths. These baths contain a special combination of conductivity-buffer-complex salts complemented by a unique current extender.

Table 3. Examples of proprietary hard gold baths (9).

	Nickel-hardened gold bath ($g\ l^{-1}$)	Co-hardened gold bath ($g\ l^{-1}$)
Gold as $KAu(CN)_2$	4-30	4-30
Nickel as a proprietary complex	0.6 to 0.7	
Cobalt as a proprietary complex		0.3 to 0.7
Conductivity-buffer salts	150	140
Current density extender	60	60
Complexing agent	20	10
pH	3.8	4.1

1.2 Development of new plating techniques

The developments in gold plating are determined by its economic laws, *i.e.*, using the smallest amount of gold to provide the desired thickness and plating as fast as possible from a minimum amount of solution to lower the investment in gold plating facilities (4). In addition to the developments of bath chemistry described above, techniques and equipment for gold plating have been improved greatly during the last twenty years. This technical revolution has been stimulated by increases in production costs and in the price of gold. Especially in the electrical and electronic industry, selective high speed plating has replaced vat and barrel plating, which was formerly widely used. Strips and spots are plated on the functional areas of technical parts using different approaches such as reel to reel plating, selective dipping, jet plating with masks and tampon plating (15). With these new techniques available for plating faster, more efficiently and with less gold, attention has been focused on ways and means of increasing current densities and deposition rates. Weakly acidic gold baths are currently used in high speed plating of connectors, contacts and printed circuit boards (16-20).

Pulse plating (21-24) is another approach to overcome problems resulting from the bath chemistry. The current density during the pulse is very high to give an acceptable high deposition rate. The main advantages of pulse plating are an increase in throwing power of the electrolyte and a decrease in the porosity of deposit (23).

Finally, laser enhanced plating (LEP) (16, 25) has been provided as a hopeful way to increase the deposition rate in selective plating without masking. In LEP, gold deposition occurs preferentially from electrolyte which is locally heated to temperature of 100 °C or higher as the result of laser-irradiation of the substrate surface. However, further research still must be done before there is a wide application of this new technique.

1.3 Mechanistic and kinetic aspects of gold deposition

In its early practice, the processing of gold plating was somewhat unreliable, success mainly depended on the experience and skills of operators due to a serious lack of the basic knowledge on the process. Because gold film has gained a widespread application as a functional coating in various technical areas and the performance of this relatively thin film is critical to the correct functioning of many devices, a full understanding of the mechanism and kinetics of gold deposition is of great importance for practical applications.

1.3.1 Thermodynamics

Since the potential of free Au (I) is very positive (E^0 =1.68 V), it must be presented as a complex in the plating solution in order to obtain a good deposit. The electrochemical reduction of gold in cyanide-containing electrolytes is represented by:

$$Au(CN)_2^- + e \rightleftharpoons Au + 2CN^- \qquad [1.1]$$

The standard electrode potential, E^0, of this reaction was determined by Maja (26) to be -0.600 V (SHE) at 25^0. In practice, the equilibrium potential of the $Au(CN)_2^-$ /Au couple may be affected by following reactions:

$$Au(CN)_2^- \rightleftharpoons Au^+ + 2CN^- \qquad K_d = 5.0\times10^{-39} \qquad [1.2]$$

$$HCN \rightleftharpoons H^+ + CN^- \qquad K_a = 4.93\times10^{-10} \qquad [1.3]$$

$$HAu(CN)_2^- \rightleftharpoons H^+ + Au(CN)_2^- \qquad K_a = 10^{-1} \qquad [1.4]$$

$$H_2O \rightleftharpoons H^+ + OH^- \qquad K_w = 1.008\times10^{-14} \qquad [1.5]$$

where the equilibrium constants (27,28) are for 25 °C. Accordingly, the principle cyanide containing species in weak acid solution at pH 3.5 ~ 5 are $Au(CN)_2^-$ and HCN. The reversible electrode reaction [1.1] may be better rewritten as

$$Au(CN)_2^- + 2H^+ + e \rightleftharpoons Au + 2HCN \qquad [1.6]$$

The standard potential of reaction [1.6] at 25^0 is estimated to 0.501 V (SHE), or 0.257 V vs. SCE. The thermodynamic reversible potential of Au(I)/Au couple at 25^0 is

$$E = E^0 + 0.0591 \log [Au(CN)_2^-] - 0.1183\, pH - 0.1183 \log [HCN] \qquad [1.7]$$

here brackets indicate activities, or, approximately, concentrations. Thermodynamically, gold deposition in acid solution may occur at much more possitive potentials than that in alkaline solution since the value of E in eq. [1.7] is more positive at lower pH and lower [HCN].

The potential of gold electrode essentially depends on the state of the surface and it is a mixed potential by its nature (29). In gold-plating studies, the concentration of free HCN or CN^- in solution increases continuously with the amount of gold deposited. Furthermore, the rest potential of the gold electrode may be influenced by the adsorption of cyanide species (30) and gold cyanide (31). Besides, a number of chemical side reactions (32), for example, the hydrolysis of CN^-, can also affect the concentration of HCN or CN^- at the electrode surface, leading to a change in the equilibrium potential of reaction [1.6]. Thus, under actual operating conditions, the true reversible potential is usually not well determined in acid solutions, it is

different from the case of alkaline plating solution containing a large excess of free cyanide in which the concentration of cyanide on the surface is constant during deposition.

A very high stability of the gold (I) cyanide complex, $Au(CN)_2^-$, enables it to be used in plating solutions at a pH as low as 3.0 (2). The complex stability also raises the deposition potential sufficiently to allow less noble metals to be codeposited simultaneously with gold.

$$Ni^{2+} + 2e = Ni \qquad E^0 = -0.50 \text{ V (SCE)} \qquad [1.8]$$

$$Co^{2+} + 2e = Co \qquad E^0 = -0.52 \text{ V (SCE)} \qquad [1.9]$$

The reduction-oxidation potential of reactions [1.8] or [1.9] is determined by the concentration of free metal in the complex solution.

1.3.2 Reaction mechanism and kinetics

Although the individual bath formulations used in industry differ significantly, the cathodic process of gold deposition from potassium dicyanoaurate containing electrolyte, in princible, can be described by the following overall reaction [1.1]:

$$Au(CN)_2^- + e \rightleftharpoons Au + 2CN^- \qquad [1.1]$$

This reaction in an acidic solution is highly irreversible since the concentration of CN^- is very close to zero. Available experimental data indicate that this reaction is complicated in character.

Maja (26) studied both the thermodynamic and electrochemical kinetic behavior of gold in an alkaline cyanide bath with the excess of free cyanide. Adsorbed $Au(CN)_2^-$ was suggested as a reaction intermediate for cathodic deposition. He concluded that the reaction occurs as follows:

$$Au(CN)_2^- \rightleftharpoons | Au(CN)_2 |_{ads} \qquad [1.10]$$

$$| Au(CN)_2 |_{ads} + e \rightleftharpoons Au + 2CN^- \qquad [1.11]$$

Subsquently, the mechanism of gold deposition from alkaline, neutral and acid gold solutions was studied by other authors (33-37) by means of cyclic voltammetry, chronopotentiometry, chronoamperometry, impedance spectroscopy, *etc.* The suggestion of the adsorption of $Au(CN)_2^-$ as reactive species in gold deposition (26) was later criticized by Mac Arthur (33), based on his voltammetric and chronopotentiometric results. He found a prepeak with a constant capacity, independent of sweep rate, occurring on the voltammograms of gold deposition at less negative potentials from alkaline cyanide solutions, and suggested that the prepeak is caused by the reduction of AuCN adsorbed on the electrode surface. He postulated two reduction paths for gold deposition, in which the one, at lower overpotentials, involves the adsorbed intermediate AuCN as reactive species and the other, at higher overpotentials, is a direct charge transfer to the soluble $Au(CN)_2^-$. The so-called prepeak at the foot of the polarization curve was also observed by other authors (34,38,40-45). It was found (33, 34,40,42) that such a prepeak was usually not affected by the rotation rate of the electrode and the sweep rate, especially for gold deposition from alkaline cyanide solution containing an excess of free cyanide, although the influence of rotation rate on the prepeak (or plateau) current was observed by Eisenmann (38) for gold deposition from a neutral phosphate electrolyte. As an origin for the prepeak, nevertheless, various suggestions can be found in literature. The electroless deposition of gold caused by CN^- oxidation was suggested by Eisenmann (38) to explain the reaction at lower overpotentials. The following reactions were suggested, *i.e*,

$$CN^- \rightleftharpoons 1/2(CN)_2 + e \qquad [1.12]$$

$$Au(CN)_2^- + e \rightleftharpoons Au + 2CN^- \qquad [1.13]$$

and the total reaction

$$Au(CN)_2^- \rightleftharpoons Au + CN^- + 1/2(CN)_2 \qquad [1.14]$$

The plateau current at lower overpotentials was found to be proportional to $\omega^{1/4}$. Most authors, however, agreed that such prepeak is associated with film formation. Burrows *et al.* (34), and Harrison and Thompson (35) claimed that the film is an Au oxide containing CN^-,

while Kurnoskin *et al.* (37) believed that the prewave is relative to the electroless deposition of gold *via* the disproptionation of AuOH. Finally, as a generally accepted view, it is most likely that the prepeak arises from the reduction of adsorbed AuCN film (33,36,39,40,42), which was proved by various techniques used for the identification of AuCN in gold deposits (see subsection 1.4.2). Therefore, the two reduction paths first proposed by Mac Arthur (33) are accepted for gold deposition from potassium dicyanoaurate. At lower overpotentials, gold deposition occurs *via* the chemical adsorption of AuCN followed by the charge transfer step:

$$Au(CN)_2^- \rightleftharpoons AuCN_{ads} + CN^- \qquad [1.15]$$

$$AuCN_{ads} + e \rightleftharpoons Au + CN^- \qquad [1.16]$$

and at higher overpotentials, it proceeds *via* direct charge transfer reaction

$$Au(CN)_2^- + e \rightleftharpoons Au + 2\ CN^- \qquad [1.17]$$

where CN^- should exist as HCN in above reactions if an acidic or neutral electrolyte is considered.

The kinetics of gold deposition from different baths, mostly confined to alkaline cyanide solutions, was studied by various authors (33-47). Most of the measurements were carried out at potentials more negative than -0.8 V. The kinetic parameters given by different authors are often shown to be quite different, due to a difference in the composition of solutions and techniques used. Two Tafel slopes were usually obtained. The larger one (from 250~350 mV dec^{-1}, depending on the solution compositions) observed at potentials less negative than ~ -0.8 V, corresponds to the reduction of adsorbed AuCN (reactions [1.15] and [1.16]), while the smaller one (about 110 to 150 mV dec^{-1}), observed at more possitive potentials, corresponds to the direct reduction of $Au(CN)_2^-$. The cathodic charge-transfer coefficient α_c equals 0.4 according to Survila (39), 0.5 according to Harrison and Thompson (35), and 0.7 according to Cheh and Sard (47). The exchange current density j_0 equals 0.82 mA cm^{-2} and the standard rate constant, k_s, for $Au(CN)_2^-$ electroreduction is 3.9×10^{-3} cm sec^{-1} (47). The activation

energy of the whole process equals to 59.5 kJ mol^{-1} according to Beltowska-Brzezinska and Dutkiewicz (36).

In phosphate solution, a well-defined limiting current density is observed. However, no direct experimental information on the magnitude of j_o for this system can be obtained since it was not possible to measure the equilibrium potential, presumably due to a change in the concentration of free CN^- in the solution during deposition. It was found (47) that the Tafel slope is 0.101 V dec^{-1}, corresponding to a value of $\alpha_c = 0.65$, and $k_s = 6 \times 10^{-11}$ cm sec^{-1}. The activation energy of gold deposition from phosphate electrolyte was measured by Kublanovsky *et al.* (46), its value confirms that the process of gold deposition is limited by the electron transfer.

Polarization curves of citrate gold plating solutions containing $KAu(CN)_2$, citric and KOH were obtained by Taran *et al.* (48). No limiting current was observed in acid medium. This was attributed to the onset of hydrogen evolution before reaching mass transfer limitations for gold deposition. Similar behavior was observed by Cheh and Sard (47) by means of a rotating disk electrode. No kinetic parameters for this system are available in the literature.

The electrochemical reduction of $Au(CN)_2^-$ is a slow process, which requires high overpotentials. It was found that the process of gold deposition can be influenced by foreign metal ions added to the electrolyte (38,40,42,43). The depolarization effects of Pb, Tl, Bi and Hg on gold deposition were observed by McIntyre and Peck (42). A large catalytic effect of Sb was found by Davidovic and Adzic (43), this was explained by its influence on the adsorption of CN^- containing species. Adsorption of Sb results in a decrease of the self-inhibition of the deposition reaction caused by the adsorption of cyanide species. The effect of base metal ions on the electrochemical behavior of $Au(CN)_2^-$ was studied by Bindra *et al.* (40). They established the underpotential deposition (UPD) of Pb and Tl on gold substrate, which

leads to the depolarization effect. It was found that Ni and Co cannot undergo the UPD on gold substrate, however, they form a continous solid alloy in the hard gold deposition.

The mechanism of nucleation and crystal growth plays an important role on the surface morphology and structure of deposits. The final grain structure of the deposited film is governed by the interplay of nucleation, crystal growth, grain coarsening and film thickening. Few works were carried out to correlate the mechanism of gold deposition in the initial stages with the composition of solution, metal additives, the nature of substrate, *etc.* (38,43,48). The only work done by Davidovic and Adzic (43) was attempted to explain the electrochemical behavior of $Au(CN)_2^-$ in phosphate electrolyte by analyzing the current-time transients in view of the theory of nucleation and crystal growth. They found that the nucleation of Au changes from instantaneous in the absence of additive Sb into progressive in its presence. However, they were unable to explain the whole transient behavior, in which a minimum, maximum and steady-state observed on a current-time transients were potential-dependent. The mechanism of nucleation and crystal growth of gold deposition on semiconductors was also studied qualitatively by Jacobs and Rikken (49) with simple discussion in view of nucleation theory. The mechanism of gold deposition from chloride solution was studied by Harrison *et al.* (50) by analysing current-time curves using nucleation and crystal growth model. No work dealing quantitatively with the phenomenon of nucleation and crystal growth of gold deposition was done in the citrate-buffer acid gold solutions.

1.4 Microstructure of deposits and inclusions in the deposit

1.4.1 Microstructure of deposit

A microstructural observation may provide a better insight into the growth and mechanical properties of gold deposits. Various techniques such as scanning electron microscopy (SEM), transmission electron microscopy (TEM), X-ray diffraction (XRD), *etc.* were used

to characterize gold deposits from various solutions including many proprietary baths (16-21,38,40,43,47,51-62).

The morphology of gold deposits depends strongly on the solution composition, temperature, current density or potential applied, agitation, the nature of substrate, *etc.* Chech and Sard (47) studied the morphology of gold deposits from alkaline cyanide, citric acid, and phosphate electrolytes, respectively. The initial stage of gold deposition is rather complex and consists of a substrate-dominated stage which results in an epitaxial layer of several hundred angstroms thick, followed by another stage where three dimensional growth occurs. At the beginning of this stage, which is controlled by the deposition conditions, structural defects such as twin faults and grain boundaries in the epitaxial layer act as preferential sites for nucleation. The nucleation and initial growth of pulse-plated and direct current-plated gold on crystalline copper and amorphous electroless nickel substrates in citric acid solution was studied by Holmbom and Jacobson using SEM and XRD techniques (57). The growth of gold on crystalline Cu-substrate was found initially strongly substrate-dependent, and it gradually turned from substrate-controlled to transport-controlled growth resulting in a morphological change.

The metallic additives have a profound effect on the grain size and its distribution, as studied by Bindra *et al.* using SEM and TEM (40). The grain size was observed to increase in the order: Co, Ni, no additives, Tl and Pb. They found that the grain growth in the cases of Ni, Tl and no additives is partially inhibited because the grain size distribution was bimodal. By contrast, in the cases of Pb and Co, the grain structure is uniformly large and small, respectively, showing the absence of inhibition of recrystallization in the case of Pb and almost total inhibition in the case of Co. The grain growth occurring in the deposition is accompanied by a change in the orientation distribution of the grains. An extremely strong (100) texture was observed for Au-Tl and Au-Pb systems, while in Au-Ni or Au-Co systems, the number of (100) oriented grains is only slightly above that which would be expected in a random

distribution of grain orientations. It was also observed that increasing the concentration of the grain growth-inhibiting additive (Ni and Co) drives the orientation distribution toward a more random behavior. The voids/ bubbles in Co-Au and Ni-Au films, plus the grain size effect together result in hard gold, while the large grain size and absence of hardening from bubbles and voids in the Pb/ Tl cases give soft gold.

The influence of organic additives on the orientation and property of gold plating in citric acid solution was studied by Lin *et al.* (59). It was shown that the growth of the (111) facets in gold plating predominates at lower temperatures and higher current densities. The addition of sodium laurysulfate, decylamine, and dodecylamine to the bath were found to suppress the growth of the (111) facets. The decylamine and dodecylamine enhance the growth of (220) and (311) facets and result in a decrease of the microhardness of the deposits.

Nakahara (61) studied the growth morphology of hard gold electrodeposits from a proprietary bath (Autronex CI) which is composed of a gold cyanide salt, citric acid as the buffer, and a cobalt salt as the hardening-brightening agent. The growth form described as "rounded mound" structure in hard gold deposits was observed by SEM. It was found by TEM that such rounded mounds are made of extremely fine (~200 Å) grains and their surfaces are preferentially bounded by the cross-packed planes, *i.e.*, (111). It was shown that the formation of the rounded mound structure is promoted by the adsorption and subsequent incorporation of non-metallic molecules which act as growth inhibitors.

The structural aspects of gold deposits produced using high speed selective jet plating from a commercial proprietary bath (Ronovel N bath) was recently studied by Bocking and Dineen using XRD and SEM (62), and a preferential orientation in gold deposits was observed.

1.4.2 Inclusions in gold deposits

For many years, it is well known (51-53,55,63-71) that carbonaceous inclusions exist in gold plates, moreover, impurities containing nitrogen, oxygen, hydrogen and potassium are also frequently involved. The neutral and alkaline cyanide solutions provided the deposits with the highest purity 99.6+ and 99.5+ %, respectively, but no coating from any of the electrolytes evaluated was 100 % pure. The codeposition of an organic film during gold plating has been under study since 1966, when gold plated telephone contact springs were visibly contaminated with an orange-brown organic film after plating from an acid hard gold bath. The historically most important work in this area is perhaps that of Munier published in 1967 (63), who discovered the inclusions of as much as 0.1~0.3 % carbon not only on the surface but within the gold deposit, and isolated the carbon-containing inclusions so called "polymer". Many investigators have since expended efforts to identify the "polymer" and to understand the role played by such inclusions. Various opinions (52,63,64,67,68) on the mechanism, structure and formation of polymer in gold deposition triggered an analysis of coating containing different percent of polymer. Without at least 0.1 % carbon in gold deposits, it has been proved that the coating will not be bright. It was also shown (71) that the carbon in polymer originated from the cyanide ligand, and the amount of "polymer" was increased with codeposited hardener (usually Co or Ni). As more investigative work proceeded the original polymer, initially thought to be a contaminant harmful to the performance of gold deposits, turned out to be somewhat advantageous (64).

The inclusions or "polymer" in gold deposits were identified using various techniques (68) such as elemental analysis, Mössbauer spectroscopy, chemical analysis, Auger spectroscopy and radiation analysis, electron diffraction analysis, *etc.* Carbon and nitrogen was found in the form of cyanide complex in the film (68). It was shown that the dominating cyanide compound in pure gold films and hard gold films is AuCN (65,68,71,72). In addition to AuCN

species, $KCo(Au(CN)_2)_3$ in hard gold films was found by Eisenmann (74). The structure of AuCN is known to be polymeric with infinite linear chains arranged in parallel (75,76):

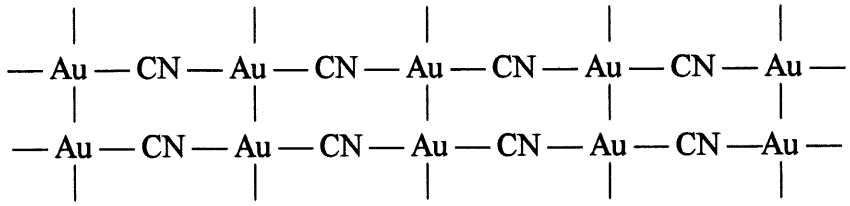

and the size of AuCN crystallites in gold deposits film was found to be 25~30 Å (65). Inclusions in hard gold films as revealed by TEM (55) are homogeneously distributed in the deposit. They act as preferential sites for nucleation leading to a fine grain size and thus high hardness.

Deposit properties which are essential for electrical contact application include sliding wear resistance and electrical contact resistance. Both properties are directly or indirectly affected by inclusions. To obtain good wear resistance, high hardness and low ductility are both necessary. It was found (68) that both high hardness and low ductility of Co hardened gold deposits can be attributed to the inclusions of impurities because they inhibit the growth of gold crystals during the deposition and hence increase nucleation rate which leads to grain refining and, therefore, high hardness and low ductility. It was also shown (77) that hardness of additive free-hard gold is directly related to its carbon content.

CHAPTER 2
THEORY OF NUCLEATION AND CRYSTAL GROWTH

2.1 Introduction

The electrocrystallization of metals, *i.e.*, deposition of metals at solid electrodes has a specific character, which is connected with the kinetics of new phase formation. Its driving force, the electrochemical free energy, is determined by the overpotential applied to the system. An increase of current is initially observed when overpotential is imposed on the substrate undergoing deposition. This rise in current can be interpreted in view of nucleation and crystal growth. Information on the kinetics of electrocrystallization may be obtained by analyzing the current-time transient, whose shape is mainly determined by a particular nucleation and growth mechanism involved. Before describing various nucleation and growth models, first, it is necessary to outline the main theoretical concepts used in the analysis of such a phenomenon.

2.2 Nucleation and crystal growth

2.2.1 Theory of electronucleation

Metal electrocrystallization on a foreign substrate usually starts with the formation of nuclei on certain active sites of the substrate, followed by crystal growth. The nucleus is a cluster of atoms. If nuclei are smaller than the size of the critical nucleus, which is a function of the excess energy, they are unstable and dissolve spontaneously; if their dimensions exceed the critical nuclei, they begin to grow spontaneously. Their formation requires a sufficiently large fluctuation of the variables of state of the system or the presence of sites at the interface at which nuclei can be formed with overall decrease in the surface energy. The nuclei which have

equal rates of formation and dissolution are called critical nucleus. Typically, the process which leads to the formation of a cluster of critical size is called nucleation, while its subsequent expansion beyond this critical size is called growth (78). The nucleation belongs to those processes where the individual events of stochastic nature occurring on the molecular level can be observed because of amplification by subsequent macroscopic processes.

There is a large number of imperfections such as kinks, steps, screw dislocation, *etc.* on polycrystal substrate (79). They are preferred for nucleation and may act as active sites. Several theories were attempted to account for the time dependence of the number of nuclei in the heterogeneous nucleation on active sites (80-86). Fleischmann and Thirsk (80) assumed that all active sites on the electrode surface present the same activity with respect to the nucleation process, *i.e.*, there is a uniform probability (Poissonian distribution) with time of converting active sites into nuclei, then the nucleation rate can be simply expressed as a first-order depletion of active sites. The time dependence of the number of nuclei is given as (80,81):

$$N(t) = N_0[1 - \exp(-A't)] \qquad [2.1]$$

where N is the number of nuclei formed at time t, A' the nucleation rate constant (s^{-1}), and N_0 the number of active sites per unit surface area (cm^{-2}). A' and N_0 are functions of the applied overpotential.

Two limiting cases are of special interest, *i.e.*, instantaneous nucleation and progressive nucleation. If all active sites are immediately converted to nuclei (A' is very large, $A't >> 1$), all nuclei are formed at the very beginning of the measurement, the nucleation process is called instantaneous. In this case, eq. [2.1] becomes:

$$N = N_0 \qquad [2.2]$$

If nucleation is slow (small A', $A't << 1$), nuclei continue to form during the experiment, the process is usually called progressive nucleation, then eq. [2.1] is simplified to:

$$N = A' N_0 t = At \qquad [2.3]$$

In this case, the number of nuclei increases linearly with time or the nucleation rate $dN / dt = A$ is constant. Note that progressive nucleation cannot continue indefinitely (78) because At is no longer much smaller than 1 at very long times. Besides, one seldom needs to wait that long, since the growth of nuclei will cause the ingestion of the active sites.

Nucleation rate depends strongly on the overpotential applied. There are two nucleation theories, *i.e.*, the classical thermodynamic theory (87-91) and the atomistic nucleation theory (92-96) currently used in electrochemical phase formation.

The classical expression for the steady-state rate of heterogeneous nucleation is written as (88):

$$A = K \exp(-\frac{\Delta G}{RT}) \qquad [2.4]$$

where the preexponential factor K is a function of the number of sites on the substrate and ΔG is the free energy of heterogeneous critical nucleus formation. For three-dimensional nucleation, it is given as (88,89):

$$\Delta G = \frac{16\pi V_m \gamma^3}{3Z^2F^2\eta^2} \qquad [2.5]$$

where V_m is the atomic volume of the deposited metal, γ the surface energy and η the overpotential. The rate of three-dimensional nucleation is described in general by the experimentally verified dependence (79):

$$\log A_{3D} = -\frac{K_1}{\eta^2} + K_2 \qquad [2.6]$$

while that of two-dimensional nucleation by (79,90,91):

$$\log A_{2D} = -\frac{K_1'}{\eta} + K_2 \qquad [2.7]$$

At very high overpotentials, the critical nuclei are very small (less than 10 atoms) and macroscopic quantities such as volume, surface, surface energies, *etc.* lose their physical meaning. This circumstance precludes a quantitative treatment of the experimental results on the basis of the classical theory of nucleation (93). In this case, the use of atomic forces becomes more reasonable, and the data can be analysed according to the atomistic theory of nucleation, which does not use macroscopic physical quantities to characterize the critical cluster. According to the atomistic theory, the equation describing the dependence of the nucleation rate with overpotential is (79, 92-96):

$$A = K_1'' \exp(-\frac{\phi(\eta)}{kT}) \exp(\frac{(n+1-\alpha)}{RT} zF\eta) \qquad [2.8]$$

where n is the number of atoms in the critical nuclei, $\phi(n)$ is the measure of the difference between the energy of n atoms when they are part of a bulk crystal and when they form a separate three-dimensional cluster on the substrate, α the transfer coefficient and K_1'' is a constant.

Generally, when a system is subjected to a constant overpotential, a certain period of time is required to reach a steady-state nucleation rate. A time inverval, t_0, is necessary to create a stationary size distribution of embryos of the stable phase, this time t_0 is usually called an induction time.

2.2.2 Kinetics of crystal growth

Crystals grow after nucleation. A current is connected with crystal growth. An important factor which determines the shape of the current-time transient is the geometrical shape of the growth centres formed. Nucleation and growth is considered to be two-dimensional (2D) if the growth of nuclei is confined only to the x-y plane of the electrode surface. However, when crystals grow in all directions, then nucleation and growth is referred to as three-dimensional

(3D). The crystal growth may itself consist of sequence of stages and is characterized by growth rate constant k (mols cm^{-2} s^{-1}).

The overall electrocrystallization reaction may occur *via* two different mechanisms at atomic level (79), *i.e.*:

(a) *Adatom model.* The ion M^{z+} is reduced to an ad-atom which is transported to the step by surface diffusion and then rapidly incorporated in the kinks (half-crystal position). In this case, the rate of deposition depends on the equilibrium concentration of adatoms, their diffusion coefficient, the exchange current density and the overpotential.

(b) *Direct deposition model.* The electrode reaction occurs directly between the metal ion and the kink without intermediate formation of ad-atoms. The rate of deposition is a function of the geometric factors of the surface, the exchange current density and the overpotential.

Provided that either the discharge step is rate-controlling at higher overpotentials, lattice formation being rapid, or else discharge takes place directly at the lattice building sites, the rate of lattice growth may vary with overpotential in the same way as for an electrochemical reaction (80, 97, 98), *i.e.*:

$$k = k_0[\exp(\frac{\alpha nF}{RT}\eta) - \exp(\frac{-(1-\alpha)nF}{RT}\eta)] \qquad [2.9]$$

However, at low overpotential, current is proportional to η^2, rather than η (80). The overall reaction shows a retardation due to surface diffusion additional to that of the primary charge transfer step. At higher η, the charge transfer step becomes rate determining and it is predicted that the current follows a normal Tafel plot. It is found that the kinetics of crystal growth, in fact, follow laws such as the Tafel equation at least at intermediate overpotentials.

2.2.3 Morphology of the growth of electrodeposit

The morphological aspects of deposits are of practical importance in the field of metal deposition. Good reviews on the morphology of the growth of electrodeposits were given by Fleischmann and Thirsk (79), Bockris and Razumny (99) and Despic (100). The epitaxy is often involved in the initial deposits, followed by the subsequent growth. There are various forms of growth of electrodeposits such as whiskers, dendrites, pyramids, hemispheres, layer-by-layer, spirals, *etc.*, depending on many factors, *e.g.*, overpotential, solution composition, substrate and temperature. Whiskers, which are characterized by quite high strength, are sometimes formed in solution with high concentration of surface-active substance. These are long single crystals, growing in only one direction while growth in the remaining directions is retarded by adsorption of surface-active substances. From solution of low concentration, metals are often deposited as dendrites at high current densities. Three-dimensional pyramids and hemispheres are often found in metal deposition.

2.3 Models of nucleation and crystal growth

Immediately after nucleation, crystals grow individually at very initial stages. However, the coalescence of growth centres occurs at later stages. The current induced by growth of crystals differs much from the summation of currents contributed by the discrete growth (80,97). The derivation of current-time equation for electrocrystallization process requires a correct calculation of the actual area of growth centres at any time t prior to and after the overlap of centres. There are basically two approaches treating the problem of the overlap, which can be used for calculating the amount of transformed material at any time t.

The first approach is called the Avrami method (101,102), and it has been widely used. It is assumed that random formation and growth of crystal centres occur in 3D space. According

to Avrami, the actual fractional volume V, transferred *via* three-dimensional nucleation and growth is given by

$$V = 1 - \exp(-V_{ext}) \qquad [2.10]$$

where V_{ext} presents the "extended volume", being the summation of volume of centres at any time provided centres are allowed to grow individually without overlapping. If the distribution of nuclei is not random, Avrami relationship can only be used indirectly.

In the simple case of two-dimensional nucleation and growth such as the random formation of cylindrical centres on a 2D plane and their growth in direction parallel to the plane, eq. [2.10] can be written as:

$$S = 1 - \exp(-S_{ext}) \qquad [2.11]$$

where S is the actual fractional area of the tops of 2D growth centres and S_{ext} the extended fractional area without considering the overlapping of centres. Note that S_{ext} depends on the nature of the nucleation and growth (instantaneous or progressive).

The second method for solving the problem of overlap was contributed by Evans (103), and it was modified recently by Abyaneh (104). In Evans approach, the actual fractional area S in the case of 2D nucleation and growth is now associated with the expection, E, which is the total number of 2D growth centres expected to pass over a representative point in a 2D plane:

$$S = 1 - \exp(-E) \qquad [2.12]$$

It was proved by Bosco and Rangarajan (105) and Abyanech and Fleischmann (106) that the "expectation", E, in the Evans approach has the same meaning as the "extended" area, S_{ext}, in the Avrami postulate. However, Evans method seems to some extent simpler in treating the problem of overlap (106). It should be noted that the statistical treatment of "overlap" problem as outlined by Avrami (102) and Evans (103) cannot be applied directly to cases where nucleation is two-dimensional (random formation of centres in 2D plane) but growth is

three-dimensional (growth of crystals has components in the three perpendicular axes).

In the derivation of current-time equation describing nucleation and growth, one usually assumes that the electrocrystallization process is either under pure diffusion control or under activation control (charge transfer control). In the following subsections, nucleation and growth are assumed under activation control, unless otherwise stated. The nucleation and growth model under diffusion control will be briefly presented in the last subsection.

2.3.1 Two-dimensional nucleation and growth of cylinders

Consider a random distribution of two-dimensional nuclei followed by the growth of cylindrical centres on a uniform substrate (where the substrate is assumed to be of infinite extent so that all edge effects can be neglected). The radius of a growing 2D centre is:

$$r = \frac{Mk_{2D}}{\rho} t \qquad [2.13]$$

where k_{2D} is the growth rate constant of two-dimensional centres, M the atomic weight of metal, ρ its density and t the time.

For instantaneous nucleation ($N = N_0$), the extended area, S_{ext}, is given by:

$$S_{ext} = N_0 \pi r^2 = \frac{\pi M^2 k_{2D}{}^2 N_0}{\rho^2} t^2 \qquad [2.14]$$

According to Avrami (102), the fractional area of a substrate covered by growing centres is

$$S = 1 - \exp(-S_{ext}) = 1 - \exp(-\frac{\pi M^2 k_{2D}{}^2 N_0}{\rho^2} t^2) \qquad [2.15]$$

The current-time transient follows from (79,97)

$$j = \frac{zF\rho}{M}\frac{dV}{dt} = \frac{zF\rho h}{M}\frac{dS}{dt}$$

$$= \frac{2zF\pi M h k_{2D}{}^2 N_0 t}{\rho} \exp(-\frac{\pi M^2 k_{2D}{}^2 N_0 t^2}{\rho^2}) \qquad [2.16]$$

where h is the height of 2D centres.

For progressive nucleation ($N = A_{2D}\, t$), S_{ext} is

$$S_{ext} = \frac{\pi M^2 k_{2D}{}^2 A_{2D}}{3\rho^2} t^3 \qquad [2.17]$$

and one obtains (79,97)

$$j = \frac{zF\pi M h k_{2D}{}^2 A_{2D}\, t^2}{\rho} \exp(-\frac{\pi M^2 k_{2D}{}^2 A_{2D}\, t^3}{3\rho^2}) \qquad [2.18]$$

Eqns. [2.16] and [2.18] predict a maximum on current-time transient followed by a current decrease to zero at longer times as the surface of electrode is completely covered by 2D growing centres. At short times, it is found that:

$$j \sim t \quad \text{for 2D instantaneous nucleation} \qquad [2.19]$$

$$j \sim t^2 \quad \text{for 2D progressive nucleation} \qquad [2.20]$$

Note that eqs. [2.16] and [2.18] are for the formation of a single layer. The problem of layer-by-layer growth can be attempted in a similar manner (107). It was shown (97,107) that the layer-by-layer growth leads to oscillations on current-time transient, followed by a steady-state at longer times after the oscillations have died away.

2.3.2 Three-dimensional nucleation and growth of right-circular cones

Three-dimensional nucleation and growth processes are more commonly encountered in the electrocrystallization of metals than two-dimensional ones. As mentioned above, the overlap of growing centres cannot be directly treated by Avrami or Evens methods because the distribution of 3D centres is certainly not random in 3D space even though the nuclei may be located randomly in the 2D plane of the electrode. However, this problem can be indirectly

solved by considering a slice dx at height x from the surface and applying Avrami theorem to treat the overlap in plane x.

Let us assume that the nuclei are randomly distributed on the surface and growing centres are right circular cones. Consider a cone cut into a series of thin cylinders of height dx at a distance x from the electrode, then the current dj contributed by a slice dx at plane with a distance x can be described by eqs. [2.16] and [2.18] for *2D* growth. By integration over x (from 0 to x), current density induced by three-dimensional instantaneous nucleation and growth of right circular cones is obtained as (97,108):

$$j = zFk'[1 - \exp(-\frac{\pi M^2 k^2 N_0}{\rho^2} t^2)] \qquad [2.21]$$

and for progressive nucleation, current density is (97, 108):

$$j = zFk'[1 - \exp(-\frac{\pi M^2 k^2 A_{3D}}{3\rho^2} t^3)] \qquad [2.22]$$

where k' and k are the growth rate constants (mol cm^{-1} s^{-1}) in the vertical and lateral directions, respectively.

Current densities in eqs. [2.21] and [2.22] increase with time and reache a plateau at later stages. At short time, it is found (97,108) that:

$$j \sim t^2 \qquad \text{for instantaneous nucleation} \qquad [2.23]$$

$$j \sim t^3 \qquad \text{for progressive nucleation} \qquad [2.24]$$

At longer times, current density is given by:

$$j = zFk \qquad \text{for both cases} \qquad [2.25]$$

Eqs. [2.21] and [2.22] are for three-dimensional nucleation and growth of right circular cones when base plane is fixed. These equations can be extended to the case where the base plane grows with the rate of k_0 (97). In this case, current consists of two parts, current j_0 resulted from the outward growth of the base plane which is proportional to the free surface area

uncovered by growing centres, and current, j_1, induced by the growth of right circular cones. For instantaneous nucleation, current density is given as:

$$j = zFk_0 \exp(-\frac{\pi M^2 k^2 N_0}{\rho^2} t^2) + zFk'[1 - \exp(-\frac{\pi M^2 k^2 N_0}{\rho^2} t^2)] \qquad [2.26]$$

and current density for progressive nucleation may be given as:

$$j = zFk_0 \exp(-\frac{\pi M^2 k^2 A_{3D}}{3\rho^2} t^3) + zFk'[1 - \exp(-\frac{\pi M^2 k^2 A_{3D}}{3\rho^2} t^3)] \qquad [2.27]$$

Current densities in eqs. [2.26] and [2.27] increase from the initial value of zFk_0 at time $t = 0$, and reach a plateau ($j_{st} = zFk'$) at later stages.

2.3.3 Three-dimensional nucleation and growth of hemispheroids

Characterization of the behavior of current-time transients induced by three-dimensional nucleation and growth of hemispheres has been attempted by many authors (108-115), notably Armstrong *et al.* (108), Bosco and Rangarajan (109,110), and Abyaneh (113-115). Armstrong *et al.* (108) was the first to derive equations for hemispherical growth, unfortunately, the equation derived for the case of progressive nucleation was incorrect as pointed later by Bosco and Rangarajan (109). Bosco and Rangarajan (109) presented a very general model for hemispherical growth, in which nucleation and growth rates could be time-dependent, they also gave equations for instantaneous and progressive nucleation. A single maximum for instantaneous nucleation and double maximum for progressive nucleation were predicted on the potentiostatic current-time transients. Recently, Aybaneh used the modified Evans method to treat the problem of overlap, and derived a group of equations for the growth of hemispheres (113), and hemispheroids (*i.e.*, ellipsoids) (114) for instantaneous and progressive nucleation. He found that single maximum on potentiostatic current-time transient should be observed for both instantaneous and progressive nucleation. Quite recently, he also developed a more general model of hemispheroidal growth covering a whole range of nucleation rate (eq. [2.1]). The current equation is given as (115):

$$j = 2zF\,k\;\varepsilon P \exp\left[-Pt^2 + \frac{2P}{A_{3D}{}^2}(A_{3D}\,t - 1)\right]$$

$$\times\int_0^t \left\{t - \frac{1}{A_{3D}} - \frac{A_{3D}\,u - 1}{A_{3D}}\exp[-A_{3D}\,(t-u)]\right\}$$

$$\times\exp\left\{Pu^2 - \frac{2P}{A_{3D}{}^2}(A_{3D}\,u - 1)\exp[-A_{3D}\,(t-u)]\right\} du \qquad [2.28]$$

where $\varepsilon = k' / k$ is the eccentricity of the ellipsoids, $P = \frac{\pi M^2 k^2 N_0}{\rho^2}$, A_{3D} the nucleation rate, other symbols were defined previously. This equation can be simplified for limited cases.

If $A_{3D} \rightarrow \infty$, eq. [2.28] is reduced to

$$j = 2zFk\varepsilon Pt\exp(-Pt^2)\int_0^t \exp(Pu^2)du \qquad [2.29]$$

which is the equation derived for instantaneous nucleation and growth of hemispheroids (ellipsoids) (114). The current-time transients described by eq. [2.29] has the following characteristics (114):

- At short times, current density is proportional to t^2, given by

$$j = \frac{2zF\varepsilon\pi M^2 k^2 N_0}{\rho^2} t^2 \qquad [2.30]$$

- Current will go through a maximum, i_{max}, given by

$$j_{\max} \approx 1.285zF\varepsilon k \qquad [2.31]$$

- At longer times current reaches a steady-state value given by

$$j_{st} = zF\varepsilon k \qquad [2.32]$$

When A_{3D} is very small, eq. [2.28] is reduced to

$$j = 3zF\,k\,\varepsilon\,P'\exp(-P't^3)\int_0^t (t^2 - u^2)\exp[-P'(2u^3 - 3tu^2)]du \qquad [2.33]$$

where $P' = \frac{\pi M^2 k^2 A_{3D}}{3\rho^2}$. This equation was derived for the progressive nucleation and growth of hemispheroids (ellipsoids) (114), it also predicts formation of the current maximum on current-time transients followed by a decrease of current to a final steady-state value. The following features can be observed (114):

- At short times, current is proportional to t^3, given by

$$j = \frac{2zF\varepsilon\pi M^2 k^3 A_{3D}}{3\rho^2} t^3 \qquad [2.34]$$

- Current will go through a maximum, j_{max}, given by

$$j_{\max} \approx 1.332 zF\varepsilon k \qquad [2.35]$$

- At longer times, current reaches a steady-state value given by:

$$j_{st} = zF\varepsilon k \qquad [2.36]$$

It should be noted that with $\varepsilon = 1$, eqs. from [2.28] to [2.36] correspond to the specific cases of hemispherical growth (113). As shown above, theoretically, the ratio of the maximum current to the steady-state value is 1.285 or 1.332 for instantaneous and progressive nucleations of hemispheroidal growth, respectively, independent of the eccentricity of the ellipsoids of revolution (113, 114).

2.3.4 Inhibition growth model

Nucleation and growth are very complicated phenomena. As discussed above, the overlap of growth centres results in the maximum followed by a decrease of current (except for the growth of right circular cones, in which a current plateau must be observed at longer times). Besides, it was found that the maximum appearing on current-time transient may also be caused by the deactivation of active sites and the abrupt ceasure of individual nuclei after reaching certain nucleus size (116,117). In practice, nucleation and growth processes are sometimes inhibited, for instance, due to the "poisoning" of the growth of one component by

another (118), the formation of passivation film (119), the adsorption of organic additives (120-123), *etc.* Change in the thermodynamic barrier for nuclei formation as well as kinetic limitations can arise and affect the nucleation and growth processes significantly. The electrode surface may be completely or partially blocked by the formation of passivation film or the adsorption of organic additives, thus reducing the number of active sites for nucleation and decreasing the nucleation rate. The "death and rebirth of growth centres" was assumed by Abyaneh and Fleishmann (124) to describe the electrocrystallization of nickel from the Watts bath.

Armstrong *et al.* (108) proposed a passivation model in which the lateral growth rate is constant, but the vertical growth rate was assumed to be decaying with time. They assumed that the vertical growth rate, V', is proportional to the uncovered surface area by growth centres. For instantaneous nucleation, V' is assumed as:

$$V' = V_0 \exp(-\frac{\pi M^2 k^2 N_0}{\rho^2} t^2) \qquad [2.37]$$

while for progressive nucleation, it is

$$V' = V_0 \exp(-\frac{\pi M^2 k^2 A}{3\rho^2} t^3) \qquad [2.38]$$

Current density for instantaneous nucleation is given as:

$$j = zFk'[1 - \exp(-\frac{\pi M^2 k^2 N_0}{\rho^2} t^2)]\exp(-\frac{\pi M^2 k^2 N_0}{\rho^2} t^2) \qquad [2.39]$$

and for progressive nucleation, it is:

$$j = zFk'[1 - \exp(-\frac{\pi M^2 k^2 A_{3D}}{3\rho^2} t^3)]\exp(-\frac{\pi M^2 k^2 A_{3D}}{3\rho^2} t^3) \qquad [2.40]$$

Current densities in eqs. [2.39] and [2.40] increase with time to a maximum and, subsequently, decrease to zero at longer time. The passivation model (eq. [2.40]) was modified by Barradas *et al.* (125) by introducing a time independent constant x in the last exponential term:

$$j = zFk'[1-\exp(-\frac{\pi M^2 k^2 A_{3D}}{3\rho^2} t^3)]\exp(-\frac{\pi M^2 k^2 A_{3D}}{3\rho^2} t^3)^x \qquad [2.41]$$

Although current in eq. [2.41] still increases to a maximum followed by a decrease to zero at longer times, the shape of current-time transients may be changed by adjusting the parameter x. Such modified passivation model was recently used by Gomez *et al.* (126) to describe the experimental data obtained in the nickel deposition. Unfortunately, Bosco and Rangarajan (127) found that the original passivation models (eqs. [2.39] and [2.40]) are incorrect because the time dependence of growth rate was not considered in their derivation.

Under potentiostatic conditions, growth rate is a constant if no inhibition occurs, as treated in the previous subsections; while the growth is inhibited, its rate is then time-dependent. According to Bosco and Rangarajan (127), a presumable form of growth rate for substrate-aided growth is:

$$\text{growth rate} \sim \exp(-\beta\, t^n) \qquad [2.42]$$

where parameters β and n are positive. Some typical growth geometries other than right circular cones such as exponential profile, error function geometry and incomplete gama function geometry can be observed, respectively, when lateral growth rate is constant but vertical growth rate is described by eq. [2.42] with n = 1, 2 or 3.

Let us assume that nucleation is instantaneous, lateral growth rate is a constant k, but vertical growth is inhibited. Consider an exponential profil of growth geometry (n = 1 in eq. [2.42]). Vertical growth rate constant is described by:

$$k' = k_1 \exp(-\lambda t) \qquad [2.43]$$

then current density is given by (127):

$$j = zFk_1[\exp(-\lambda t) - \exp(-P_2 t^2) + \lambda \exp(-\lambda t)\int_0^t \exp(-P_2 u^2 + \lambda u)du] \qquad [2.44]$$

where $P_2 = \frac{\pi M^2 k^2 N_0}{\rho^2}$, k_1 and λ are constant. If vertical growth rate constant is described as:

$$k' = k_1 \exp(-\lambda t^2) \qquad [2.45]$$

then current density is given by (127):

$$j = 2zFk_1P_2\int_0^t (t-w)\exp(-\lambda w^2)\exp[-P_2(t-w)^2]dw \qquad [2.46]$$

Eqs. [2.44] and [2.46] predict that current increases with time, reaches a maximum and, subsequently, decreases to zero at longer times. Other forms of growth rate may also be treated. In chapter 6, we will modify the Bosco-Rangarajan inhibition model using a new form of growth rate.

2.3.5 Nucleation and growth under diffusion control

For metal with a large exchange current density, the electrocrystallization process is usually under diffusion control, especially at high overpotentials, low concentration of depositing species and long times. The nucleation and crystal growth under diffusion control were studied by various authors (127-135). The theoretical current equations derived by Hill *et al.* (135) are widely used.

It is supposed that a set of hemispherical nuclei are randomly distributed on the electrode surface and are growing under diffusion control. The isolated hemispherical diffusion zones coalesce to columns of diffusion zones, the effect of which becomes equivalent to linear diffusion to a plane surface. The overlap of neighbouring diffusion zones can be treated by the Avrami theorem (102). The corresponding diffusion flux and growth current can be expressed in terms of linear diffusion to that fraction of the electrode surface area contained with the circular perimeters of the growing diffusion zones. For instantaneous nucleation, current is given by (135):

$$j = \frac{zFD^{1/2}C}{\pi^{1/2}t^{1/2}}[1-\exp(-N_0\pi mDt)] \qquad [2.47]$$

where D is diffusion coefficient, C the concentration of the depositing metal (mol cm^{-3}) and constant $m = (\frac{8\pi CM}{\rho})^{1/2}$. For progressive nucleation, current density is given as (135):

$$j = \frac{zFD^{1/2}C}{\pi^{1/2}t^{1/2}}[1-\exp(-\frac{AN_0\pi m' Dt^2}{2})] \qquad [2.48]$$

where constant $m' = \frac{4}{3}(\frac{8\pi CM}{\rho})^{1/2}$.

Eqs. [2.47] and [2.48] both predict a maximum on current-time transients. At very short times, it can be shown (135) that:

$$j \sim t^{1/2} \qquad \text{for instantaneous nucleation} \qquad [2.49]$$

$$j \sim t^{3/2} \qquad \text{for progressive nucleation} \qquad [2.50]$$

At longer times, as a result of the overlap of diffusion zones, current is described by:

$$j = \frac{zFD^{1/2}C}{\pi^{1/2}t^{1/2}} \qquad [2.51]$$

which is the Contrell equation.

CHAPTER 3
EXPERIMENTAL

3.1 Introduction

Electrochemical measurements have been mainly carried out on gold rotating disk electrode (RDE). The advantage of RDE technique lies in controlling mass-transfer. Voltammetric and chronopotentiometric measurements were first performed to establish qualitatively the general behavior of gold deposition in acid solutions. The majority of measurements have been undertaken by chronoamperometry (*i.e.* potentiostatic method), this method has an advantage over voltammetric and chronopotentiometric methods in studying the kinetics of nucleation and growth because the rates of nucleation and growth are controlled at constant overpotential.

In this work, attention has been paid to:

1) Noise in the measurements: A relatively high noise level was found in the initial stage of the work mostly due to a poor electrical contact between a rotating disk electrode and a graphite brush in the external circuit of potentiostats, and the magnetic effect caused by motor of rotator. Noise was obviously reduced to an accepted level after the reconstruction of the RDE where the electrical contact was made through a pool of mercury on the top of the RDE. To further diminish the noise, the motor of rotator was properly shielded with a steel mesh, and electrical equipment was well grounded.

2) The necessity to "activate" the gold plating solution (see chapter 4): The first one or two curves recorded from a freshly prepared gold bath were found to be different from other curves recorded later from the same solution. It was necessary to pass a certain charge through the working electrode to "activate" solution.

3) Reproducibility of the results: The experimental results were found to be highly irreproducible in the beginning of the work. The poor reproducibility was to a great extent due to the instability of

the solution caused by an improper preparation. Other important factors affecting the reproducibility of the results were found to be the age of solution used and its purity, the cleanness of glassware and cell, and the pretreatment of working electrode.

Because of the high cost of gold plating bath, and most importantly due to the need in "activating" solution for good reproducibility of data, each solution had to be used in a series of experiments. For this purpose, a special procedure was run twice a day to check the reproducibility of the results and to determine whether the solution under use should be discarded. This procedure consisted of recording LSV curves at 2700 rpm and 1 mV s^{-1}. If the difference in the peak current on LSVs (see later) was larger than experimental error (5%), then the solution under use was discarded, and new solution was prepared.

3.2 Electrochemical system

All the electrochemical measurements were performed in a conventional three-compartment electrochemical cell made of Pyrex glass. The cathodic and anodic compartments was separated by a Nafion 117 (DuPont) membrane to diminish the effect of anodic products on gold deposition. Cathodic compartment (~250 ml) was thermostated at 60±0.5°C. Anodic part were always filled with the supporting electrolyte. RDEs (made of gold, copper, nickel, glassy carbon or platinum) were used as working electrodes. The rotation rate of the RDE was controlled by the AFASR rotator (Pine). The reference electrode was connected to the cell *via* a bridge equipped with a Luggin capillary probe, positioned near the RDE to minimize the solution resistance, and filled always with the studied solution. Solution in the cathodic compartment was deoxygenated with oxygen-free nitrogen for at least two hours prior to each run, and during the measurement N_2 was passed over the solution.

The reference electrode was a saturated calomel electrode (SCE) and all the potentials reported were referred to this electrode. The routine check for SCE was done by comparing the difference

between the SCE under use and the standard one. If the difference was larger than 2 mV, new reference electrode was prepared.

The counter electrode was either platinum mesh or graphite rod with a large surface area to diminish anodic polarization.

3.3 Solutions

A commercial proprietary acid gold bath based on Renovel N make-up solution (Lea Ronal) has been practically used for hard gold plating for many years. It was shown by Bocking and Cameron (62) that this bath is probably one of the best gold plating baths used in industry. This proprietary bath is selected as model system in the present study.

The solutions used in the experiments consisted of one or more of the following components:
I) The proprietary supporting electrolyte (Renovel N make-up solution, LeaRonal, Freeport, NY), which is a citrate-based buffer solution and contains a current density extender (principally nicotinamide (18));
II) The proprietary nickel containing solution, blue nickel complex (Renovel N nickel concentrate, LeaRonal) containing 25 g l^{-1} Ni^{2+};
III) $KAu(CN)_2$ (SEL-REX, Enthone-OMI).

Four different solutions, as shown in Table 4, were prepared from the above bath components:
A - containing component I only;
B - containing components I and II;
C - containing components I and III (soft gold plating bath);
D - containing all components (hard gold plating bath).
Each of the above listed solutions has been diluted after mixing of its components to the same final volume as the full bath. Solution A was prepared by mixing 75 % (by volume) of the proprietary

supporting electrolyte (component I) with 25 % of deionized water (Barnstead, Nanopure). Solutions B, C and D were prepared by mixing component I with other components. Unless stated elsewhere, the concentration of nickel and gold in solutions, if present, were the same, *i.e.*, Ni (II) 2.73×10^{-2} M and Au (I) 9.12×10^{-2} M. The pH of solutions was adjusted with KOH to 4.4, unless described elsewhere. All other reagents and chemicals used were of analytical grade.

All the glassware and cells used were left overnight in a concentrated sulphuric acid before washing thoroughly with distilled water. It was then kept for several hours in a concentrated nitric acid. After washing with distilled water, it was left in deionized water for a few hours, and, finally, rinsed again with deionized water.

Table 4 Solutions used in the work

Solutions	Components	Ni^{2+} (M)	Au^{+} (M)	pH
A	I	0	0	4.4
B	I+II	2.73×10^{-2}	0	4.4
C	I+III	0	9.12×10^{-2}	4.4
D	I+II+III	2.73×10^{-2}	9.12×10^{-2}	4.4

3.4 Pretreatment of working electrodes

3.4.1 Gold RDE

The majority of electrochemical measurements were carried out with a gold RDE, its geometric surface area was 0.0706 cm^2, which was either commercial electrode AFAD03 Au (Pine Instrument Company) or home-made Au (purity 99.99 %, Johnson Matthey) RDE, embedded in Teflon holder. Prior to use, gold surface was polished on a rotating table (GP-60 Polisher, Leco Corp.) with 1μm and 0.05 μm alumina powder (Gamma Micropolish Alumina, Buehler), washed thoroughly with deionized water, degreased with methanol, kept in a concentrated HNO_3 for 10 s to remove trace of Al_2O_3 on the electrode surface, and again rinsed thoroughly with deionized water. Then, it was immersed in solution for about 2 minutes before experiment.

3.4.2 Copper RDE

Copper RDE (0.0706 cm^2, purity 99.99 %, Aldrich) embedded into Teflon holder was also used as a working electrode in electrochemical measurements. Prior to each use, copper RDE was polished with 1 μm and 0.05 μm Al_2O_3 powder to a mirror-like surface and rinsed thoroughly with deionized water. No chemical pretreatment was used for this RDE. To diminish the formation of surface oxides, copper RDE was kept wet before being transferred to the solution. Besides, the initial potential was kept -0.2 V (rather than 0 V as that for gold RDE) to prevent the dissolution and exchange reactions.

For the preparation of sample for morphology characterization, a copper disk (1.0 cm^2 in area, 1.0 mm in height) was used. It was pretreated in a series of steps starting with polishing with the finest sand-paper to remove mechanic scratches, polishing with 1 μm and 0.05 μm Al_2O_3 powder to a mirror-like surface and rinsed thoroughly with deionized water, installing it into a specially

designed Teflon holder, degreasing with methanol and finally washing again thoroughly with deionized water. The disk surface was kept wet to protect from oxidation before use.

3.4.3 Nickel RDE

Nickel RDE (0.0706 cm^2, purity 99.99 %, Aldrich) embedded into Teflon holder was also used as a working electrode in voltammetric and chronoamperometric measurements. Its pretreatment was similar to that for copper RDE. However, for a few measurements, other chemical pretreatment was also tested to compare the influence of pretreatment on the measurements. After polishing, nickel RDE was subjected to one of the following chemical treatment:

(1) no chemical treatment;

(2) immersion in HNO_3 for 10 s;

(3) immersion in 20 % H_2SO_4 for 10 s;

(4) immersion in concentrated H_2SO_4 for 10 s.

Then, electrode was rinsed thoroughly with deionized water. Similar to copper RDE, the initial potential was kept -0.2 V to prevent the dissolution and exchange reactions.

3.4.4 Glassy carbon RDE

Glassy carbon RDE (0.0706 cm^2, ESS) embedded in Teflon holder was also used in voltammetric and chronoamperometric measurements. Its pretreatment is similar to that for copper RDE. The initial potential was set 0 V in the measurements.

3.4.5 Platinum RDE

Platinum RDE (1.0 cm^2, AFDD 40 Pt, Pine Instrument Company) was used in a few chronoamperometric measurements. It was polished as described for the gold RDE.

3.5 Electrochemical measurement techniques

3.5.1 Voltammetric measurements

Linear sweep voltammetric (LSV) measurements were performed to provide the general behavior of gold deposition in a wide potential range. The initial potential was 0 V for Pt, Au and glassy carbon RDEs, or -0.2 V for Ni and Cu RDEs, and the final value of -1.2 V. LSV measurements were also used to check the reliability of the solution used because LSV curve in our gold plating baths was characterized by an obvious peak at more positive potentials, which was very sensitive to the age of solution used. This test was repeated twice a day with gold RDE at 2700 rpm and 1 $mV\ s^{-1}$.

After establishing the general features of gold deposition, cyclic voltammetric measurements were carried out to give an insight into the phenomenon of nucleation and crystal growth.

3.5.2 Chronopotentiometric measurements

Chronopotentiometric measurements were performed under galvanostatic mode. The potential-time transients were registered at a constant current density (between 0.01 mA cm^{-2} and 150 mA cm^{-2}).

3.5.3 Chronoamperometric measurements

Chronoamperometric measurements were performed to study quantitatively the kinetics of nucleation and crystal growth. These measurements were carried out under potentiostatic mode. Potential was stepped from an initial value at which no deposition reaction occured, to a potential of more negative than -0.5 V, at which deposition reaction took place. Then, current-time

transients were recorded. The kinetic parameters of gold deposition were obtained by analyzing current - time curves in view of nucleation and growth models described in Chapter 2 and presented later in this thesis.

3.5.4 Measurements of solution resistance

To compensate *iR* drop in the measurements, solution resistance was determined by means of ac impedance spectroscopy, and also by the current interruption method with a Clare vacuum mercury relay (HGJM 511 31 NOO). Normally, the value of the solution resistance was kept about 5 Ω by adjusting the distance between the tip of Luggin capillary of the reference electrode and RDE.

3.6 Characterization of deposits

The surface morphology of deposit was characterized *ex-situ* by scanning electron microscopy (SEM) and atomic force microscopy (AFM). For SEM observation, JSM-840 A scanning electron microscopy was used. In AFM study, a Nanoscope III (Digital Instruments, Inc.) was used in a contact-mode. The force exerted by the AFM tip on the sample was larger than 200 nN. All AFM measurements were performed in air atmosphere and ambient temperature. The AFM images were presented in a two-dimensional top view (scan size 15 μm× 15μm) or three-dimensional view.

For the morphology observations of hard gold deposits, a pure gold-plated nickel RDE (diameter 3.0 mm) was used as substrate for hard gold deposition. Nickel RDE was polished with 0.1 μm Al_2O_3, rinsed thoroughly with water, kept in H_2SO_4 (1:2) for 15 s and finally washed with deionized water. Pure (soft) gold layers were plated on the Ni RDE from an alkaline gold solution ($KAu(CN)_2$ 40 g /l, KCN 7.5 g /l and KOH 40 g/l) at 1000 rpm and j = 7.5 mA cm^{-2} for 50 s, its surface was checked by SEM to be very smooth and uniform. Subsequently, SEM

samples were obtained by the deposition of hard gold from solution D on the pure gold-plated Ni RDE.

The deposits obtained on copper disk (1.0 cm^2 in area and 1 mm in height) were characterized with both SEM and AFM techniques.

CHAPTER 4
VOLTAMMETRIC STUDY

4.1 Introduction

First, a linear sweep voltammetric (LSV) technique is used to investigate qualitatively the general kinetic behavior of electrode reactions involved in gold deposition in a wide potential range. To better understand the kinetics of gold deposition, experiments were performed using Au RDE in supporting electrolytes without (solution A) and with (solution B) nickel, in soft gold (solution C) and hard gold (solution D) baths. LSV measurements taken in the solutions, which contained an additional amount of oxalic acid (20 g/l), were reported earlier (136). It was observed that the first (sometime also, to a lesser extent, the second) LSV curve taken either in a fresh solution C or D differed significantly from the others, and repeating the measurement once or twice always removed this discrepancy. This effect is due to some, yet unidentified, reactions in the solution causing an effect of bath "activation". Because the special feature (*i.e.*, peak behavior), which was very sensitive to the impurity and age of the bath, appeared on LSV curves, LSV measurements were also used as a procedure for checking the bath performance throughout the work.

Based on the LSV results, cyclic voltammetric measurements were carried out in solution C and D, respectively, to obtain the information on the heterogeneous nucleation and crystal growth. Potential scanned from an initial potential, E_i, to a reversal cathodic potential, E_f, and, subsequently, returned to its initial potential.

The results obtained from LSV and CV measurements are presented in section 4.2 and 4.3, respectively. The dependence of current density on rotation rate is discussed quantitatively in section 4.4.

4.2 LSV measurements

4.2.1 LSVs in the supporting electrolyte

Fig. 1 shows voltammograms of a supporting electrolyte (solution A) on the Au RDE. A small current is recorded at potentials more positive than -0.725 V. It is probably caused by the reduction of traces of oxygen in the solution (136). Purging O_2 into the solution resulted in a higher background current. Current increases abruptly as potential becomes more negative than -0.725 V due to the hydrogen evolution reaction (HER). H_2 gas bubbles on the surface were observed at *ca.* -1.2 V. Current for the HER decreases with rotation rate, indicating that the HER is not under diffusion control. Theoretically, the equilibrium potential for the HER in this solution is about -0.5 V, however, higher overpotentials are needed for the HER to occur on a gold RDE.

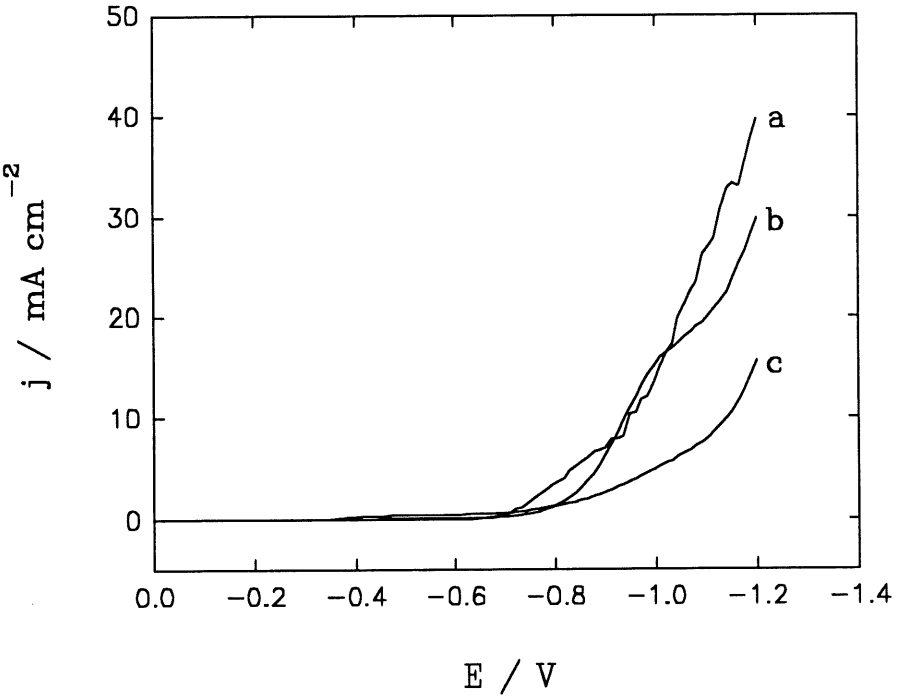

Figure 1. LSV curves on a gold electrode in the supporting electrolyte (solution A); curves: a) stationary electrode; b) 650 rpm; c) 2700 rpm.

LSV curves recorded in solution B (not shown here) are similar to those in solution A. However, the current is about 50% higher than that in solution A. No evidence of nickel reduction was revealed from LSV measurements even doubling the concentration of nickel in solution B up to 0.055 M. It indicates that hydrogen evolution reaction is easier than the nickel reduction in this solution.

In acidic solutions, HER plays an important role in metal electrodeposition. It not only diminishes the cathodic efficiency during deposition, but also influences the kinetics of deposition (*e.g.*, inhibiting its deposition). The overall HER in acidic solution is written as (137):

$$2H^+ + 2e \rightarrow H_2 \qquad [4.1]$$

It proceeds *via* hydrogen adsorption, Volmer reaction [4.2],

$$H^+ + e + M \rightarrow M\text{-}H_{ad} \qquad [4.2]$$

followed by the Tafel-recombination, reaction [4.3],

$$2M\text{-}H_{ad} \rightarrow 2M + H_2 \qquad [4.3]$$

or the ion-atom-recombination, Heyrovsky reaction [4.4],

$$M\text{-}H_{ad} + H^+ + e \rightarrow M + H_2 \qquad [4.4]$$

Depending on the solution composition, substrate and the applied potential, H_2 and/or H_{ad} may affect, to a various extent, the kinetic aspects of gold deposition, especially in the initial stages of nucleation and crystal growth.

Besides the HER, it was found that LSVs in solution A were not reproducible if the electrode was always kept in the solution. A slightly darken solid film was observed on the surface of Au electrode after about 10 cycles. It was not metallic film because no metal existed in the solution. It was insoluble in water but could be removed with a Kimwipe. It is so far unknown which organic compounds were reduced and contributed to the film formation. It is likely that HER is inhibited due to the film formation because of a decrease in the current with rotation rate of electrode.

4.2.2 LSVs in soft gold bath

Unlike the measurements in supporting electrolyte (solution A), LSVs in solution C were reproducible even without pretreatment of the electrode. Fig. 2 illustrates a set of LSVs for soft gold deposition on Au RDE from solution C. Potentials were scanned from 0 to -1.2 V at a sweep rate of 1 mV s^{-1}. A very small current, probably due to the reduction of trace amounts of oxygen in solution (51,136), is observed when potential is more positive than -0.35 V. Current starts to increase at a potential *ca.* -0.35 V, indicating the onset of gold deposition. The reversible equilibrium potential of $Au(CN)_2^-$/Au couple is influenced by a series of dissociation reactions of various compounds (*e.g*, HCN, $HAu(CN)_2$, $Au(CN)_2^-$, *etc.*) in the solution. The

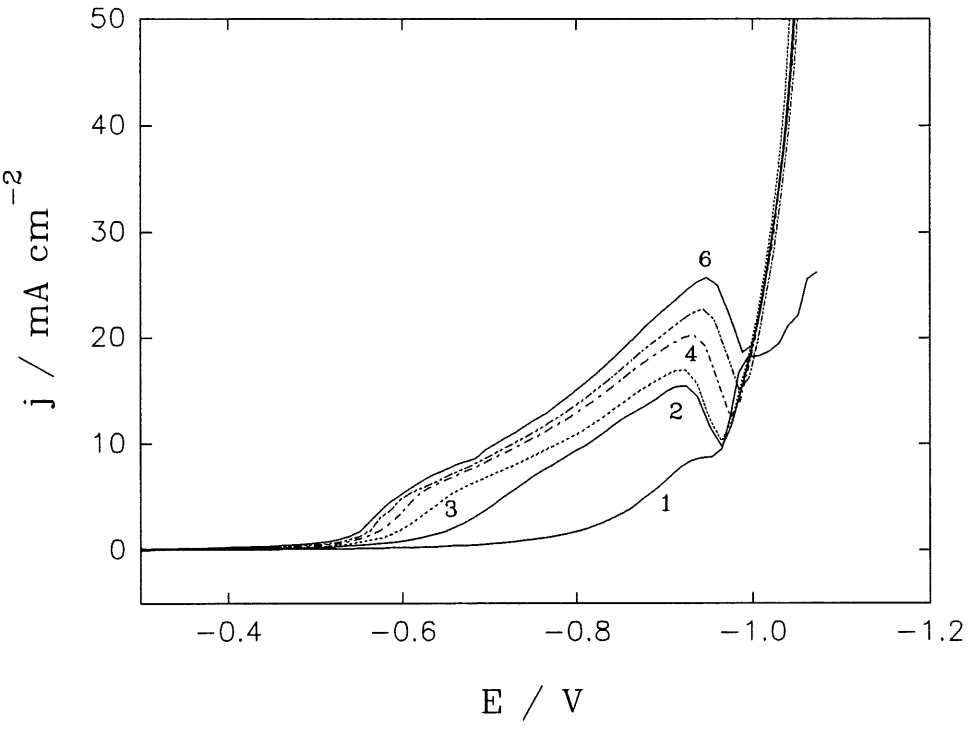

Figure 2. LSV curves of soft gold deposition on a gold RDE under different rotation rates; sweep rate: 1 mV s^{-1}; rotation rates: 1) stationary electrode; 2) 200 rpm; 3) 650 rpm; 4) 1300 rpm; 5) 2700 rpm; 6) 4000 rpm.

reaction for gold deposition in acid solution may be described as

$$Au(CN)_2^- + 2H^+ + e = Au + 2HCN \quad [1.6]$$

Its standard potential is calculated to be about 0.257 V (SCE). The equilibrium potential of $Au(CN)_2^-$ /Au in the bath used (*i.e.*, 0.091 M $Au(CN)_2^-$ and pH 4.4) is

$$E = -0.336-0.118 \log [HCN] \quad [4.5]$$

In practice, HCN continues to be released during gold deposition, and escapes from solution as the saturation of HCN in solution is attained. The concentration of HCN in solution is extremely small before experiment and increases slightly during the measurement, depending on the charge passed. Therefore, the exact concentration of HCN is unknown. If the concentration of HCN in solution is assumed to be 10^{-10}, 10^{-8}, 10^{-6} and 10^{-4} M, then the equilibrium potential can be estimated to be 0.844, 0.608, 0.372 and 0.136 V *vs.* SCE, respectively, although the rest potential of gold electrode is also affected by the adsorption of CN^-, organic additives and AuCN, and other chemical side reactions. The comparison of the onset deposition potential with the estimated equilibrium potential shows that gold deposition needs a higher overpotential, and extra energy is required to overcome the energy barrier of heterogeneous reaction onto the substrate.

The outstanding feature in Fig. 2 is that a current peak appears on LSVs at more positive potentials, *i.e.*, current initially increases with potential, forms a maximum and then decreases to a minimum. At more negative potentials, current increases abruptly with negative potential. No diffusion limited current plateau on LSV is observed even at very negative potentials mostly due to the codeposition of hydrogen evolution reaction (HER). H_2 bubbles were observed at *ca.* -1.2 V. The rotation rate has a large influence on the LSV peak. Its height increases markedly with the rotation rate, while current recorded at more negative potentials is identical at each rotation rate, indicating certain importance of mass-transfer on the process in first potential range. An obvious current peak is still observed even under a relatively high rotation rate of 4000 rpm, and becomes more obvious at higher rotation rate. Appearently, the strong dependence of the LSV peak on rotation rate might imply that the process may be under control of $Au(CN)_2^-$ diffusion.

However, the peak current is much lower than the diffusion limiting one, predicted by Levich equation for $Au(CN)_2^-$ reduction, indicating that this process is under kinetic control (136).

Fig. 3 presents the dependence of sweep rate on LSV at 650 rpm and 4000 rpm. Current peak decreases with an increase in sweep rate. At sweep rates larger than 20 mV s^{-1}, the LSV peak disappears. As also shown in Fig. 4, the peak is largely depressed when a stationary Au electrode is used and sweep rate is not small enough. However, an obvious peak is observed on the stationary electrode at 0.1 mV s^{-1}.

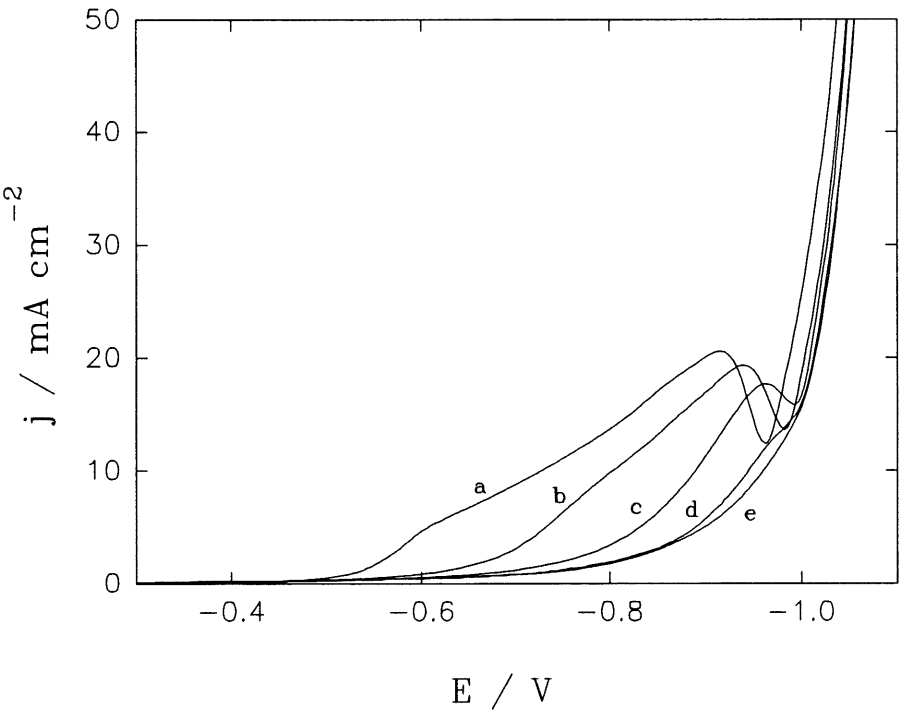

Figure 3. The dependence of LSVs on scan rate for soft gold deposition on a gold RDE; rotation rate: 650 rpm; scan rates (mV s^{-1}): a) 1; b) 2; c) 4; d) 10; e) 20.

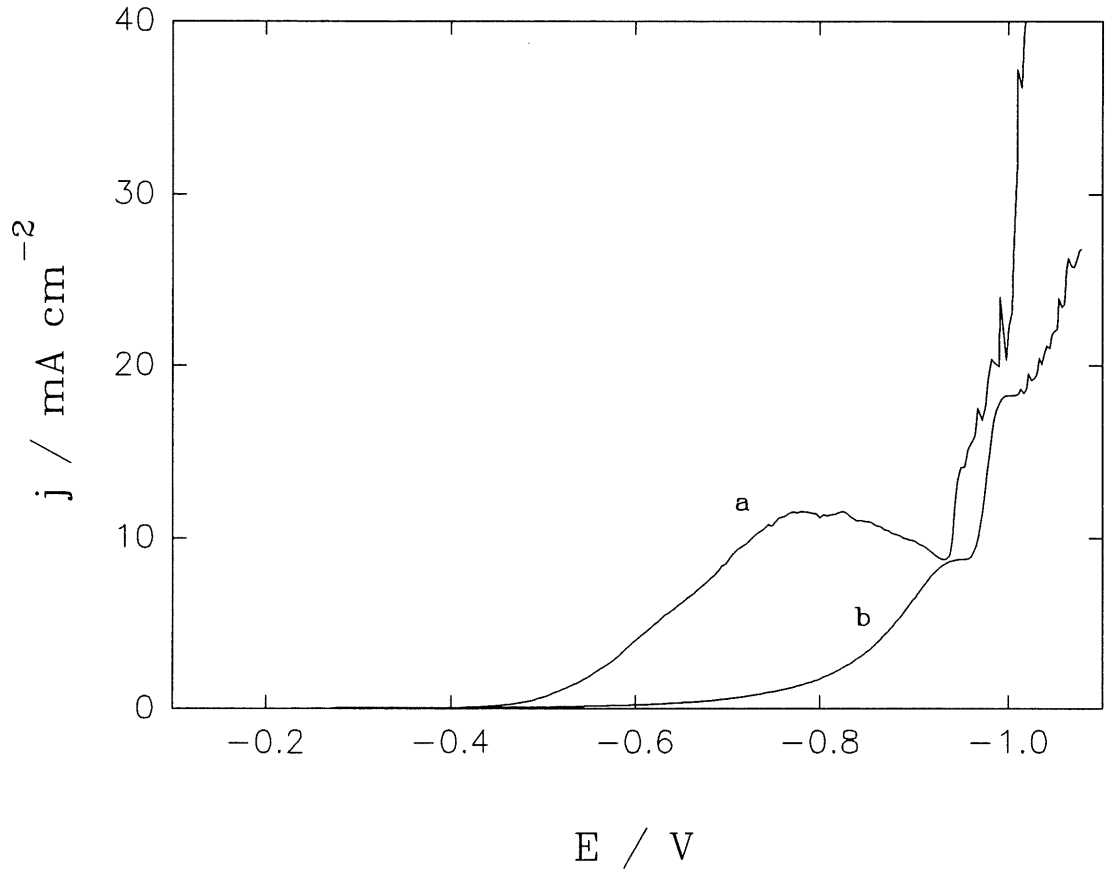

Figure 4. LSV curves of soft gold deposition on a stationary Au electrode; scan rates: a) 0.1 mV s^{-1}; b) 1 mV s^{-1}.

The comparison of Figs. 1 and 2 shows that the HER only contributes a small fraction of the total current at less negative potentials and high rotation rates. As mentioned above, the HER in acid solutions becomes important at very negative potentials. Presumably, the LSV peak might be related to the HER. Roev and Gudin (138) found that in the electrodeposition of Zn-Ni alloy, the HER can result in the formation of a peak on LSVs before the bulk deposition. To determine whether the LSV peak observed during gold deposition is related to the HER, LSV measurements were performed in solutions of different pH. If the HER contributes significantly to this process the peak height should be larger at lower pH (higher concentration of H^+) (138). However, it was found that peak height increased with pH (not shown), *e.g.*, peak current density increased ~10 % as the pH of the bath increased from 4.4 to 5.1, whereas no obvious change in current recorded at more negative potential was observed. Therefore, the HER is not responsible for the peak behavior on LSVs. This conclusion is further confirmed by the measurements performed in hard gold bath.

4.2.3 LSVs in hard gold bath

The general behavior of LSV for hard gold is analogous to that for soft gold. Fig. 5 demonstrates a typical set of LSV curves for hard gold deposition on Au RDE at a sweep rate of 1 mV s^{-1}. Deposition starts at about -0.35 V. All curves are characterized by a pronounced peak at less negative potentials between -0.35 V and -0.725 V. The deposition current, particularly peak current, increases with rotation rate. LSV curves for hard gold also reveal some features different from those for soft gold. The comparison of Figs. 2 and Fig. 5 shows that current for hard gold is much lower than that for soft gold, indicating that the deposition process is depressed due to the addition of nickel in the bath. It is also worth noticing that the peak and minimum on LSV are shifted in more positive direction when moving from soft to hard gold bath. Besides, the peak moves to more positive potentials as rotation rate increases.

The dependence of the sweep rate on LSV curves is similar to that for soft gold deposition, as shown in Fig. 6 at 4000 rpm. The peak current decreases considerably with sweep rate, and

the peak disappears when sweep rate is larger than 10 mV s^{-1}. Fig. 7 illustrates the LSV curves recorded on a stationary Au electrode at sweep rates of 1 and 0.2 mV s^{-1}, respectively. No peak is observed on LSV curve at sweep rate 1 mV s^{-1}, however, at small enough sweep rates, for example 0.2 mV s^{-1}, the LSV peak appears.

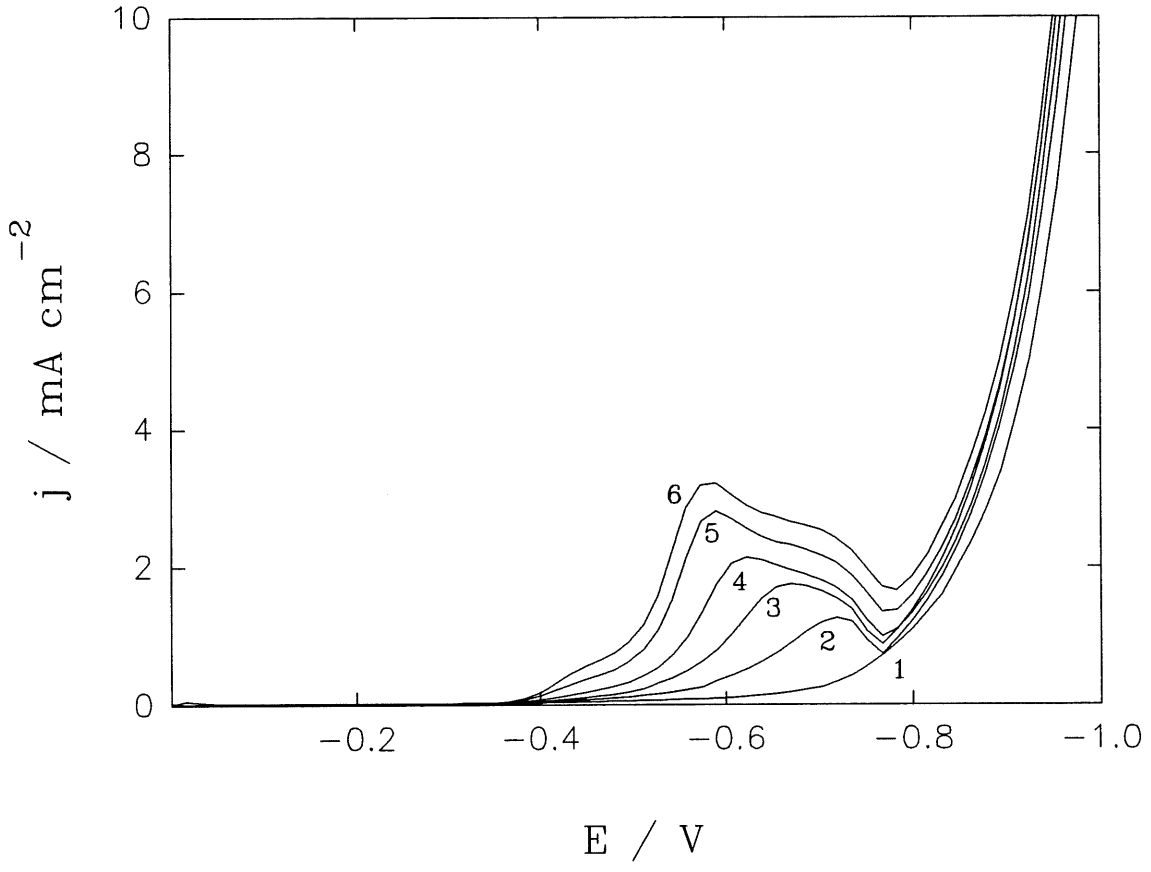

Figure 5. LSV curves of hard gold deposition on a gold RDE at different rotation rates; sweep rate: 1 mV s^{-1}; rotation rate: 1) stationary electrode; 2) 200 rpm; 3) 650 rpm; 4) 1300 rpm; 5) 2700 rpm; 6) 4000 rpm.

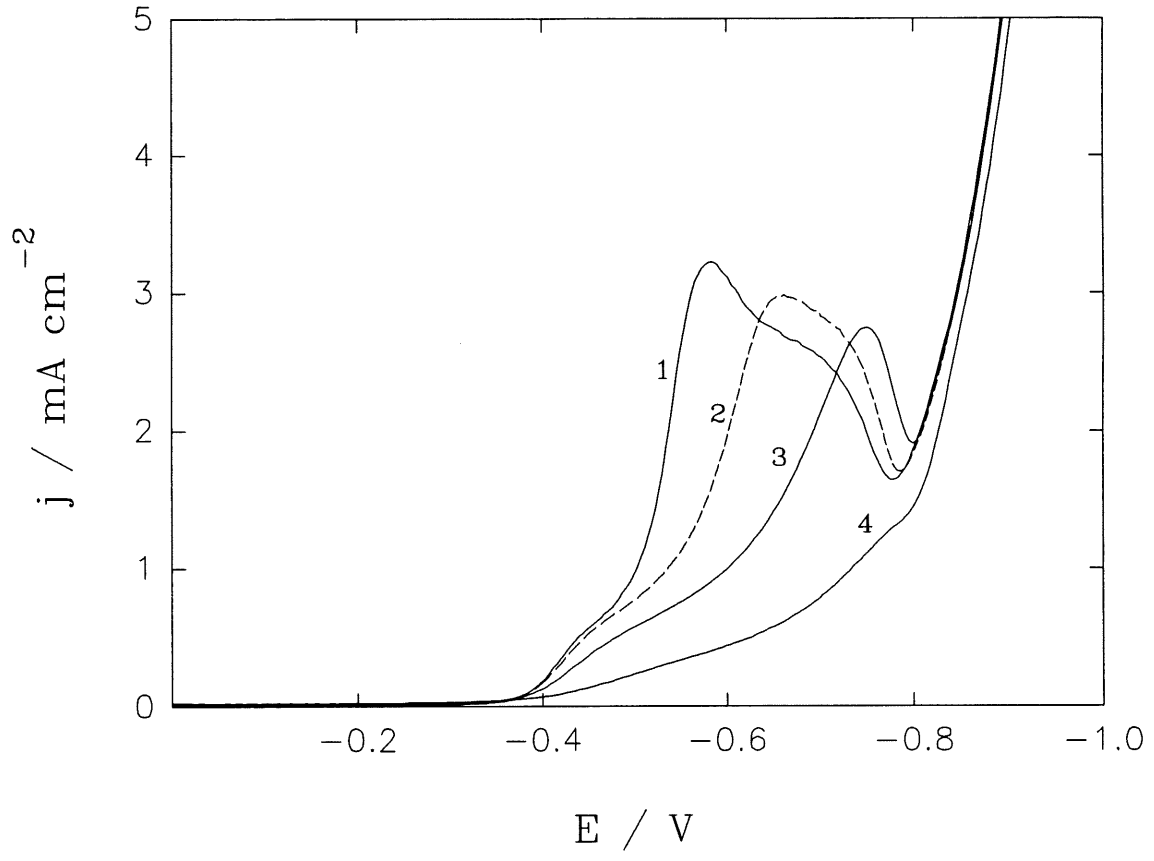

Figure 6. The dependence of LSV curves on scan rate for hard gold deposition on a Au RDE at a rotation rate of 4000 rpm; scan rate (mV s^{-1}): 1) 1; 2) 2; 3) 4; 4) 10.

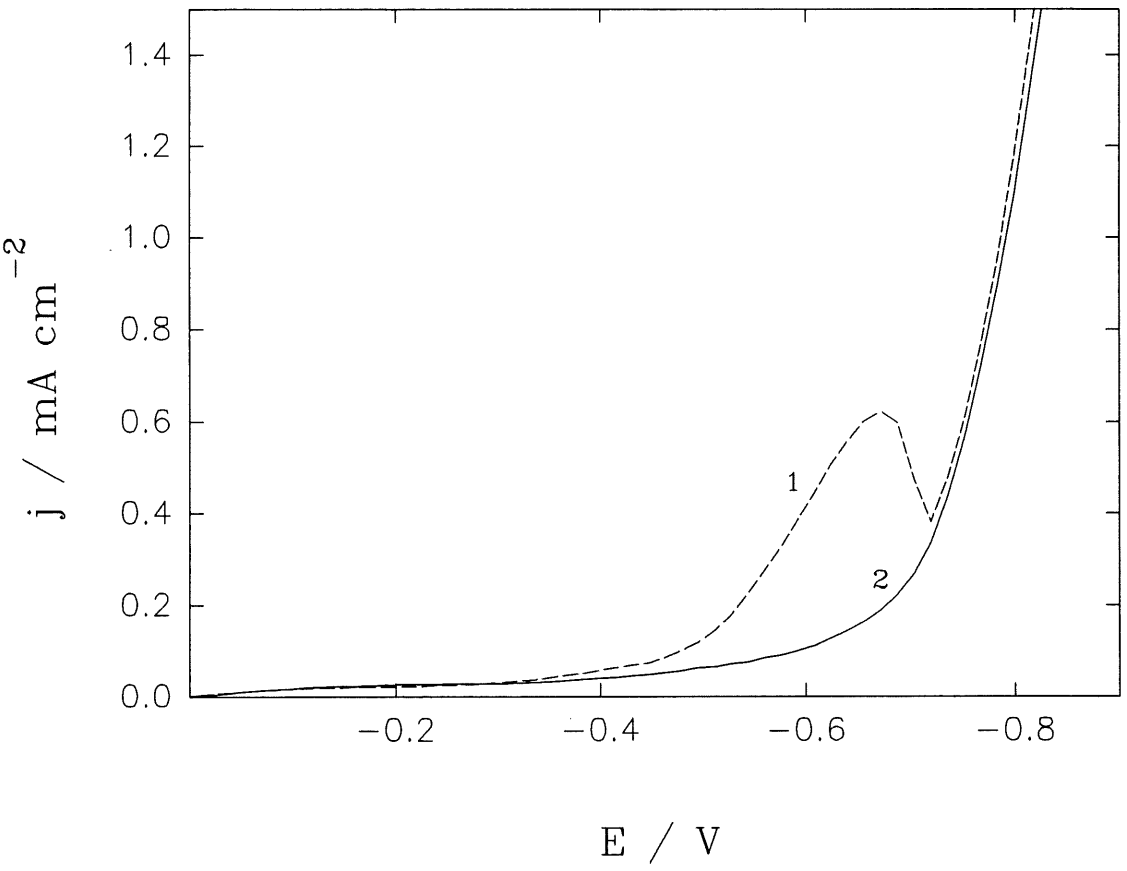

Figure 7. LSV curves of hard gold deposition on a stationary Au electrode; scan rate (mV s^{-1}): 1) 0.2; 2) 1.

To understand the role of the HER, measurements were also performed in the bath with different pH. Fig. 8 presents LSVs of hard gold on Au RDE at pH 4.0 and 4.4, respectively. The peak height increases about 20 % as pH of solution changes from 4.0 to 4.4, and the peak shifts to more negative potentials. No influence is observed at more negative potentials. This suggests that the peak occuring on LSVs in hard gold bath is also not related to the HER, otherwise current would have to increase at lower pH due to the higher H^+ concentration (138).

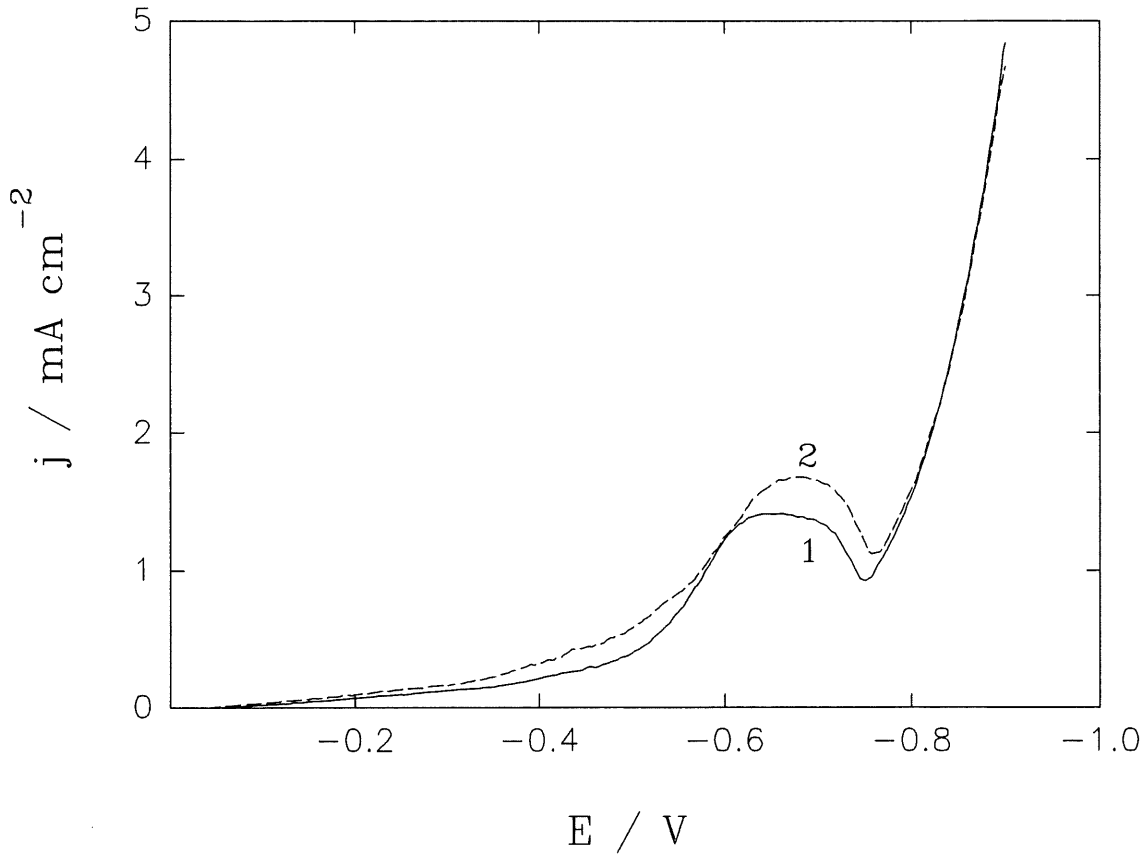

Figure 8. LSV curves for hard gold deposition on a gold RDE at different pH of solution; Ni^{2+}: 0.039 M; rotation rate 650 rpm; pH of solution: 1) 4.0; 2) 4.4.

4. 3 Cyclic voltammetric measurements

4. 3.1 The behavior of soft gold bath

Cyclic voltammetric measurements were performed to detect the nucleation and crystal growth phenomena. A set of cyclic voltammograms (CV) for soft gold deposition on the Au RDE at 650 rpm are illustrated in Fig. 9. All measurements begin at the initial potential of 0 V (vs. SCE) (→) to different cathodic reversal potentials, and returns (←) to 0 V at scan rate 1 mV s^{-1}. The outstanding feature in Fig. 9 is a current loop on CV in the reversal potential scan. The deposition current continues to increase up to a peak after cathodic potential reversal and current is higher than that in cathodic scan. The net deposition current ceases at cross-over potential *ca.* -0.35 V. According to Fletcher (111) and Fletcher and Halliday (139), such a current loop on CV is indicative of the formation of a new phase by nucleation and growth processes. It is due to an increase in the real active surface area of gold crystallites. The increase in the active surface area continues after the reversal of the potential scan and results in the increase of the cathodic current despite a decrease of interfacial charge transfer rate (due to the potential scan in anodic direction) and decrease in the normal growth rate per unit surface area. The peak position of the loop shifts toward more negative potentials, and the peak height increases as the cathodic reversal potential becomes more negative. On changing the cathodic reversal potential, the cross-over potential, at which current in the reversal scan equals approximately to zero, remains the same, *i.e.*, ~ -0.4 V, indicating that the nucleation and growth kinetic is under interfacial control (139). When cathodic reversal potential is more negative than -0.75 V, however, current initially decreases after scan reversal (current is lower than that in cathodic scan similar to the normal case of diffusion control), and, subsquently, current becomes larger than that in cathodic direction and a loop is obtained again (Fig. 9b).

Fig. 10 shows the influenec of sweep rate on CVs. The cross-over potential is appoximately the same (about -0.4 V). The nucleation-growth (N-G) loop decreases as sweep rate increases.

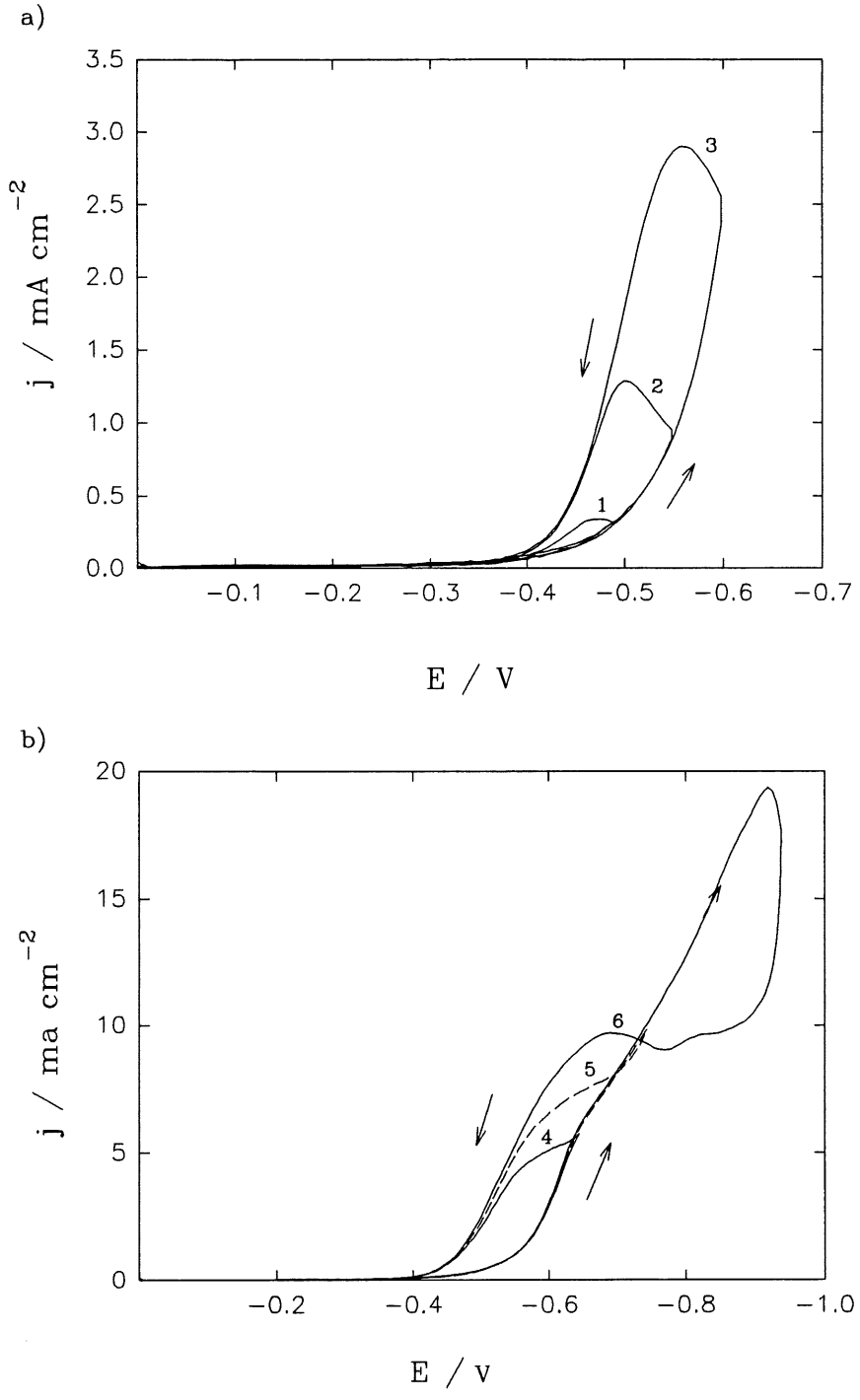

Figure 9. Cyclic voltammograms (CV) for soft gold deposition on a gold RDE at rotation rate 650 rpm; cathodic reversal potential (V): (a): 1) -0.50; 2) -0.55; 3) -0.60; and (b): 4) -0.65; 5) -0.775; 6) -0.925; arrow → cathodic scan; ← reversal scan.

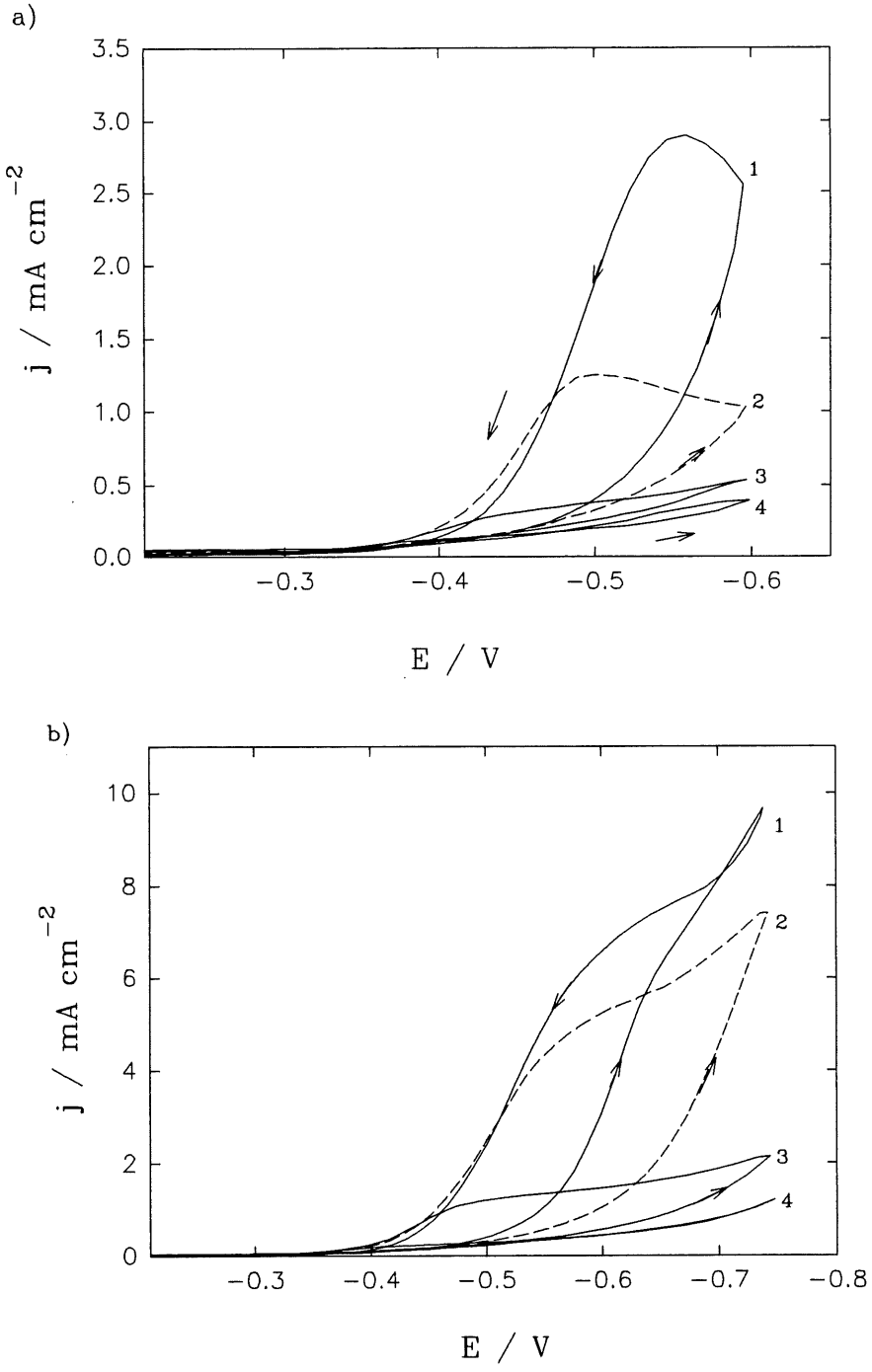

Figure 10. The dependence of CVs on scan rate for soft gold deposition on a gold RDE at 650 rpm; cathodic reveral potential for (a) -0.60 V and (b) -0.75 V; scan rate: 1) 1 mV s^{-1}; 2) 2 mV s^{-1}; 3) 4 mV s^{-1}; 4) 10 mV s^{-1}.

The increase of current with a decrease in scan rate and the appearence of a loop in cathodic current as the direction of the potential scan is reversed, are normal consequences of the features of growth requiring nucleation. There is always a time delay in such a process related to the probability of nucleation. Hence, the faster the scan, the shorter the time, and the smaller the nuclei, *i.e.*, the less are the chance for nuclei to form and grow at a given overpotential. As a result, the current induced by nucleation and growth is smaller than in the same situation at a lower scan rate. As scan rate is larger than 10 mV s^{-1}, no current loop induced by nucleation and growth is observed.

4.3.2 The behavior of hard gold deposition

Fig. 11 shows a typical set of CVs for hard gold deposition on a gold RDE at 650 rpm in the first potential range (0 to -0.70 V). Similar to soft gold, all the CVs are characterized by a N-G current loop on the reversal potential scan, which is evidently associated with the nucleation and growth process in gold deposition. The observed current is smaller than that for soft gold deposition under identical condition. The cross-over potential, at which current recorded at reversal scan direction ceases, is *ca.* -0.4 V, independent of the reveral potential used. The N-G loop position shifts to more negative potentials and its height increases as the cathodic reversal potential becomes more negative.

It is worth noticing that, if cathodic reversal potential is set more negative than peak potential on LSVs, Fig. 5, current initially decreases to a minimum and then increases to a maximum as potential is scaned in the reversed direction (Fig. 12a, line 1). When the reveral potential, E_f, is set in the more negative potential range, Fig. 12a, line 2, initially, no difference in the current recorded in the cathodic and anodic directions is observed at more negative potential. CV taken in the second potential range did not show any obvious "N-G loop" (Fig. 12b), indicating that the reaction mechanism may be quite different as that in first region.

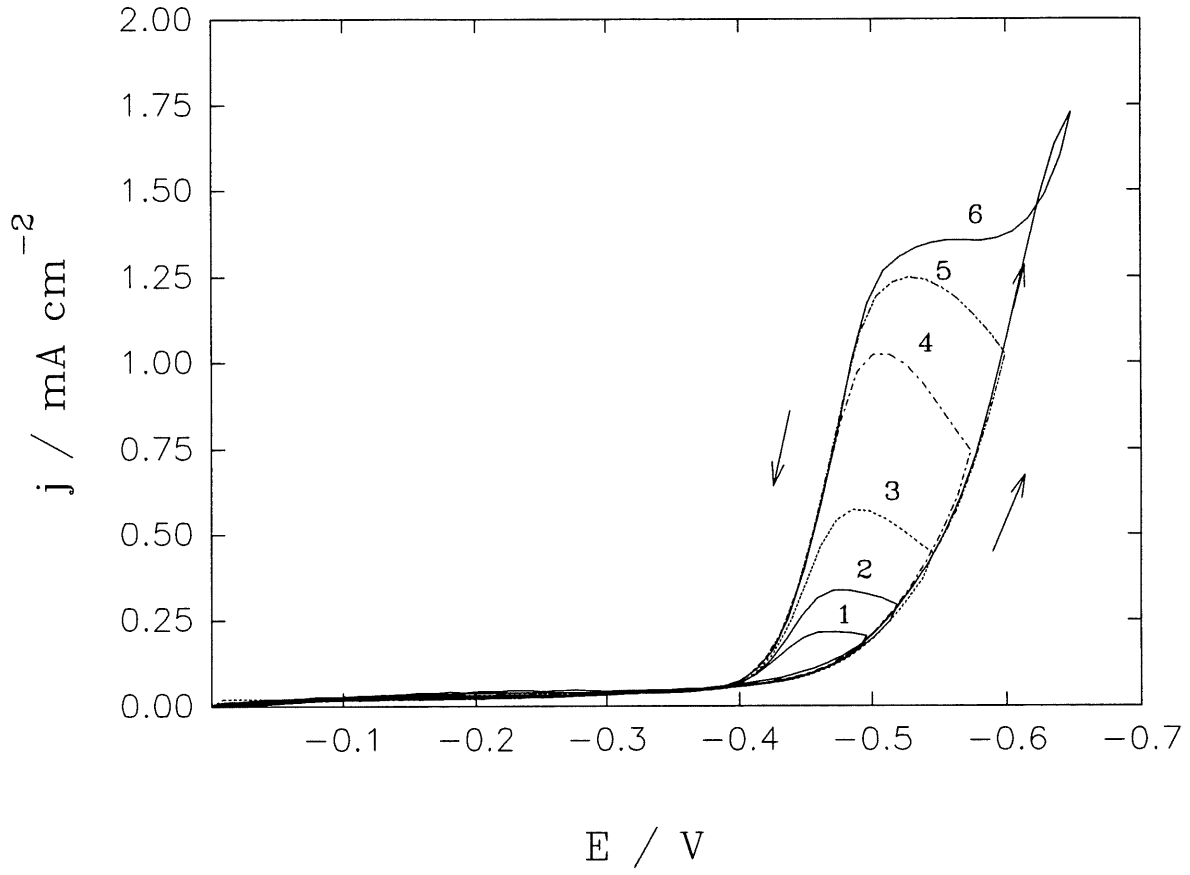

Figure 11. Cyclic voltammograms for hard gold deposition on a gold RDE at 650 rpm; scan rate: 1 mV s^{-1}; reversal potential E_f (V): 1) -0.50; 2) -0.525; 3) -0.55; 4) -0.575; 5) -0.60; 6) -0.65.

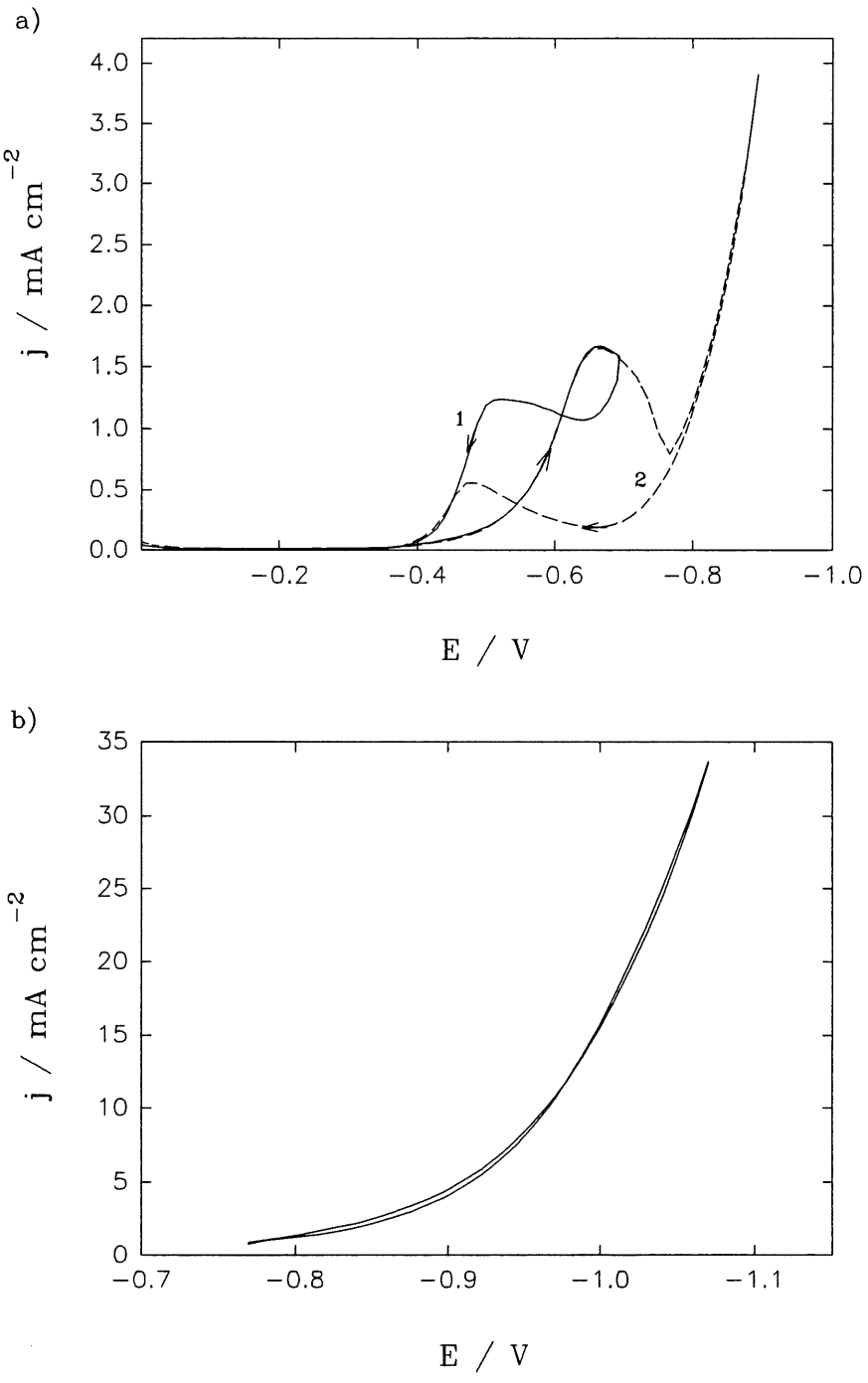

Figure 12. Cyclic voltammograms of hard gold deposition on a gold RDE at 650 rpm; scan rate: 1 mV s^{-1}; in (a) initial potential 0 V, reveral potential (1) -0.7 and (2) -0.9 V; in (b) initial potential -0.75 V; reversal potential -1.1 V.

4. 4 Discussion

It was shown from LSV and CV measurements that two different mechanisms in two potential ranges are involved in gold deposition from Renovel N acidic baths. At more positive potentials, a current peak on LSVs, which depends strongly on the rotation and sweep rates, was observed experimentally. Considering the fact that the peak current is much lower than the diffusion limiting one predicted by Levich equation and it increases with the pH of solution, the above results permit us to conclude that the peak observed on LSVs is neither associated with the diffusion process of gold cyanide species nor with the HER. Gold deposition is under interfacial kinetic control. It is likely that the peak behavior of LSVs may be caused by the reduction of adsorbed AuCN on the electrode surface, and the rotation rate dependence of current is related to the mass-transfer controlled inhibition process.

As reviewed in the first chapter, a prewave or small peak occurring at the foot of polarization curve was also observed by other authors (33, 34, 38, 40-45) in gold deposition from various baths, although the peak height was usually not affected by rotation rate, different from the observation in our experiments. According to the generally accepted view, gold deposition at more positive potentials occurs *via* the adsorption of AuCN,

$$Au(CN)_2^- + H^+ \rightleftharpoons AuCN_{ads} + HCN \qquad [4.6]$$

followed by the charge-transfer step,

$$AuCN_{ads} + H^+ + e \rightarrow Au + HCN \qquad [4.7]$$

It should be noted that different from reactions [1.15] and [1.16], proton is included in reactions [4.6] and [4.7] since in the acidic solution, cyanide species exist mainly as HCN. Current in reaction [4.7] is determined by the coverage of AuCN and the potential applied. It was found (31) that the adsorption of gold cyanide species is potential-dependent, and its coverage decreases with negative potential. That is, the adsorption of AuCN occurs at more positive potentials, while the desorption of AuCN takes place at more negative potentials. As overpotential increases, initially, current must increase due to an increase of rate constant in

reaction [4.7], and, subsquently, current decreases due to the desorption of AuCN at more negative potentials. As a result of these two effects, a peak is observed on LSVs. It is worth noting that the adsorption of AuCN is also affected by the surface concentration of HCN (reaction [4.6]).

A self-inhibition process caused by inhibitor generated on the electrode surface during the deposition may be responsible for the dependence of current on rotation rate. The observed current may be inversely proportional to the local concentration of inhibitor on the surface. There is a conflict existing in the system. On the one hand, current should be exponentially proportional to the applied overpotential; on the other hand, higher generation rate of inhibitor at higher overpotentials leads to a decrease in the deposition rate. With a stagnant electrode, at a certain potential, inhibitor may accumulate on the surface if the diffusion process is slow. The deposition reaction is then highly depressed due to the inhibition. At higher rotation rate, the mass-transfer of the inhibitor becomes faster, and its local surface concentration (or its coverage) is lower. Hence, current increases with rotation speed.

Sweep rate in LSV measurements has a similar effect on the mass-transfer controlled process as the rotation rate. At higher sweep rates (corresponding to shorter times), there is not enough time for the inhibitor generated on the surface to be removed into the bulk of solution. As a result, a higher sweep rate corresponds to a higher local concentration of inhibitor on the surface, and inhibition degree may be expected to be higher, resulting in a lower peak current. Actually, when sweep rate is faster than 20 mV s^{-1} for soft gold (Fig. 3) or 10 mV s^{-1} for hard gold (Fig. 6), current peak on LSV disappears. It implies that if the sweep rate is slow enough, that is, time interval for inhibitor to move into the bulk of solution is long enough, then a higher peak current on LSV would be obtained. It is worth noting that sweep rate has another influence on current induced by nucleation and growth, since an increase in deposition current should also result from an increase in the active area during the nucleation and crystal

growth process. The higher the sweep rate, the shorter the time for crystal growth, and hence the smaller the active area, leading to a lower current.

As discussed above, fast agitation of the solution and a long time (corresponding to a small sweep rate) are needed to obtain a high current. Here, possible inhibitors are CN^- or HCN species released during the deposition process. The self-inhibition caused by the adsorption of cyanide species in gold deposition was also suggested by Davidovic and Adzic (43) without detailed discussion. Although the adsorption of cyanide species on metal electrodes is well known in literature (140-144), its role on gold deposition is not yet quite clear.

In alkaline solutions, the overpotential for H_2 evolution is much higher than that in acidic solutions. Therefore, measurements were allowed to be performed at potentials more negative than -0.8 V without significant H_2 evolution; the phenomenon appearing at potentials more positive than -0.8 V was often ignored by many authors. The main difference between alkaline and acid gold solutions is that the concentration of CN^- is extremely low and nearly all free cyanide species are present as HCN in the latter case.

When the initial concentration of ligand in the bulk solution is high enough, *e.g.*, in the alkaline cyanide gold solution with large excess of free cyanides, it is reasonable to ignore the effect of mass-transfer of CN^-. However, the mass-transfer of HCN from surface to bulk solution in acid gold solution becomes important because the surface concentration of HCN on electrode during deposition is much higher than its bulk concentration and must be taken into account. Qualitatively, as the rotation rate of RDE increases, the thickness of diffusion layer decreases, consequently, the rate of mass-transfer of HCN from surface to the bulk solution increases, and hence the surface concentration of HCN decreases, leading to the higher current density.

The mass-transfer influence of HCN on gold deposition at more positive potentials is now discussed quantitatively as follows. In order to obtain the dependence of current on rotation rate, it is assumed that reactions [4.6] and [4.7] are in quasi steady-state conditions. Besides, other processes (the diffusion of $Au(CN)_2^-$, the adsorption of HCN and organic additives, nucleation and crystal growth, *etc.*) are ignored. The rate of reaction [4.6] is given as:

$$r_1 = k_1'(1-\theta) - k_{-1}[HCN]_0\theta \qquad [4.8]$$

and the rate of reaction [4.7] is:

$$r_2 = k_f'\theta \qquad [4.9]$$

where $k_1' = k_1[H^+][Au(CN)_2^-]$, $k_f' = k_f[H^+]$, k_1 and k_{-1} are the forward and backward rate constants of reaction [4.6], k_f the rate constant of electrochemical reaction [4.7], θ the surface coverage of AuCN on the surface, and $[HCN]_0$ the surface concentration of HCN on the electrode. Since $r_1 = r_2$, one can get:

$$\theta = \frac{k_1'}{k_f' + k_1' + k_{-1}[HCN]_0} \qquad [4.10]$$

Since the total generation rate of HCN, r, is the sum of r_1 and r_2, it follows from eqs. [4.8] to [4.10] that:

$$r = r_1 + r_2 = \frac{2k_1'k_f'}{k_f' + k_1' + k_{-1}[HCN]_0} \qquad [4.11]$$

Now lets consider that the diffusing species is HCN, the current density for the rotation disk electrode under laminal conditions is:

$$j = nFD\frac{[HCN]_0 - [HCN]_\infty}{2\delta} = \frac{nFD}{2}\frac{d[HCN]}{dx}\bigg|_0 \qquad [4.12]$$

where diffusion layer thickness $\delta = 1.62\,D^{1/3}\nu^{1/6}\omega^{-1/2}$, D is the diffusion coefficient of HCN, ν the kinematic viscosity of the solution and ω the angular frequency. The two boundary conditions hold, *i.e.*,

$$x = \infty, \quad [HCN]_\infty \cong 0 \qquad [4.13]$$

and

$$x = 0, \quad -D\frac{d[HCN]}{dx}\bigg|_0 = r_0 \qquad [4.14]$$

From eqs. [4.11], [4.13] and [4.14], one can get:

$$\frac{D[HCN]_0}{\delta} = \frac{2k_1' k_f'}{k_f' + k_1' + k_{-1}[HCN]_0} \qquad [4.15]$$

The solution of eq. [4.15] for $[HCN]_0$ is:

$$[HCN]_0 = \frac{k_1' + k_f'}{2k_{-1}}\left[-1 \pm \sqrt{1 + \frac{8k_{-1}k_1' k_f' \delta}{(k_1' + k_f')^2 D}}\right] \qquad [4.16]$$

Eq. [4.16] has physical meaning only when the second term in the bracket is positive. From eqs.[4.12] and [4.16], current density is obtained as:

$$j = nFD\frac{k_1' + k_f'}{4k_{-1}}\delta^{-1}\left[-1 + \sqrt{1 + \frac{8k_{-1}k_1' k_f' \delta}{(k_1' + k_f')^2 D}}\right] \qquad [4.17]$$

Although current is a complex function of rotation rate, it is clearly seen from eq. [4.17] that current increases with an increase in rotation rate. Now, let's consider two limiting cases. First, it is assumed that

$$\frac{8k_{-1}k_1' k_f' \delta}{(k_1' + k_f')^2 D} << 1 \qquad [4.18]$$

by the expansion of the square root term (*i.e.*, $(1+y)^{1/2} \approx 1 + y/2$), then eq. [4.17] can be simplified to:

$$j = nF\frac{k_1' k_f'}{k_1' + k_f'} \qquad [4.19]$$

and current is independent of the rotation rate. Secondly, if it is supposed that k_{-1} is very large, *i.e.*,

$$\frac{8k_{-1}k_1' k_f' \delta}{(k_1' + k_f')^2 D} >> 1 \qquad [4.20]$$

Then, eq. [4.17], is reduced to

$$j = 0.556nF\left(\frac{k_1' k_f'}{k_{-1}}\right)^{1/2} D^{5/6} \nu^{-1/12} \omega^{1/4} \qquad [4.21]$$

It is shown that current density increases with rotation rate, and under certain circumstances, it is proportional to $\omega^{1/4}$, [4.21]. This is further confirmed by Fig. 13, a good linear dependence of current density against $\omega^{1/4}$ is obtained for soft gold deposition at potentials

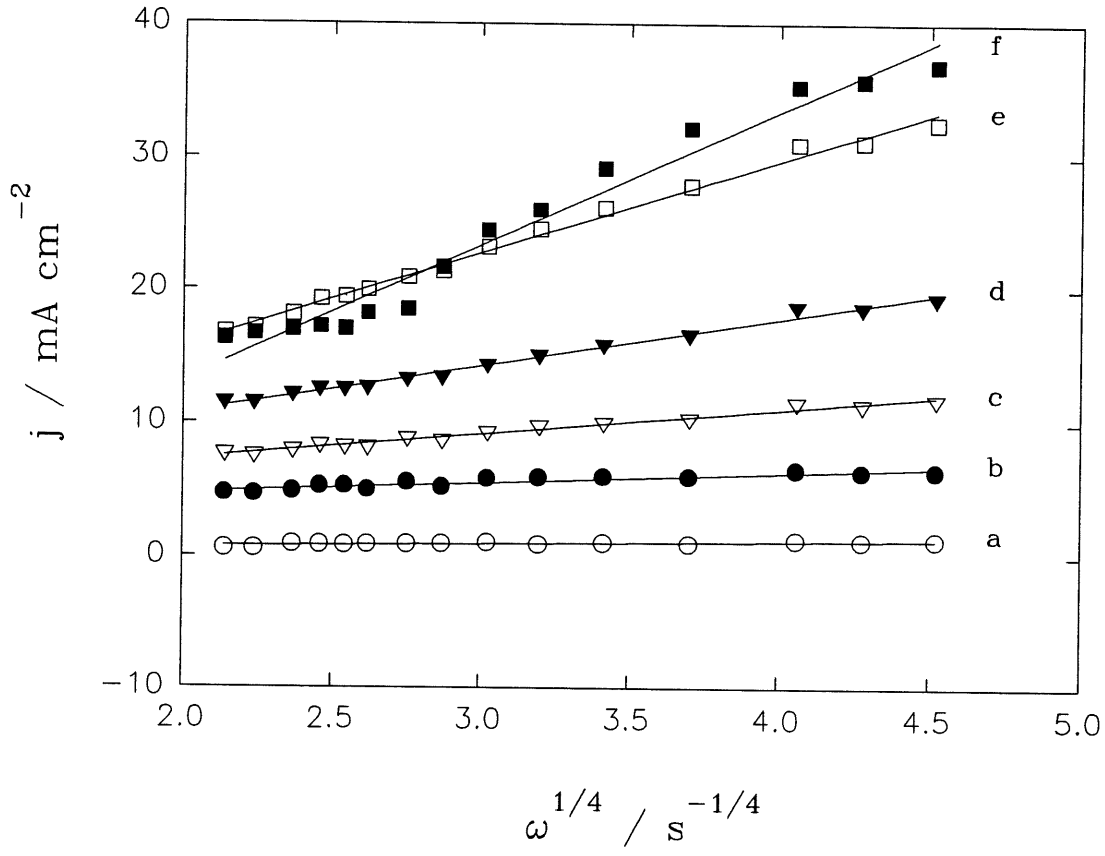

Figure 13. The dependence of current against $\omega^{1/4}$; current is obtained from the LSV curves on a gold RDE in soft gold bath containing an additional amount (20 g/l) of oxalic acid; potential used (V): a) -0.50; b) -0.60; c) -0.70; d) -0.80; e) -0.90; f) -1.0.

between -0.5 and -0.90 V, and for hard gold deposition at potentials more positive than -0.55 V. Such a linear dependence of current density on rotation rate at lower overpotentials was also found by Eisenmann (38), however, it was explained in view of the electroless deposition of gold, rather than from the point of a self-inhibition involved in gold deposition. Interestingly, it is also shown from eq. [4.19] that current density may be independent of the rotation rate under some conditions. Therefore, it is not difficult to understand why the small peak at the foot of polarization curve observed by some authors (33,34,40,42), was not influenced by rotation rate.

The dependence of current density on rotation rate can be explained well by eq. [4.17], however, this equation could not predict a peak behavior on LSV. In the above treatment, other processes (such as the diffusion of $Au(CN)_2^-$, the adsorption of HCN and organic additives, nucleation and crystal growth, *etc.*) are ignored. It should be added that ligand anion CN^- and other additives in the solution may also be adsorbed on the surface, and affect kinetic behavior of gold deposition. The peak behavior on LSV, Figs. 2 and 5, can be influenced by the composition of bath, pH of solution, temperature and the nature of substrate, *etc.* The strong competitive adsorption of CN^- would result in the desorption of AuCN at more negative potentials.

At more negative potentials, $Au(CN)_2^-$ becomes electroactive and gold deposition occurs *via* a direct charge transfer reaction:

$$Au(CN)_2^- + 2H^+ + e \rightarrow Au + 2HCN \qquad [1.6]$$

Current increases with negative potential, and principally, it is not influenced by the rotation rate. It will be seen later that Tafel slope obtained in this range is much lower than that at less negative potentials.

CHAPTER 5
CHRONOPOTENTIOMETRIC STUDY

5.1 Introduction

In chapter 4, LSV and CV techniques were used to establish the general electrochemical behavior in both soft and hard gold baths. As is well known, the practical preparation of thin films is usually performed in a galvanostatic mode. The aim of this chapter is to present the results obtained from galvanostatic measurements. The measurements are carried out in solutions C and D, and solutions containing an additional amount of oxalic acid (20 g/l). Double layer capacity in hard gold bath is determined.

5.2 Chropotentiometric behavior of soft gold baths

A constant current in the range from 0.014 to 141.5 mA cm^{-2} was imposed on Au RDE. Fig. 14 shows a typical set of chronopotentiometric curves for soft gold deposit from solution C at a rotation rate of 4000 rpm. The shape of transients changes in different ranges. At current densities lower than 0.079 mA cm^{-2}, potential attains rapidly an almost constant value after a current is applied. The curves recorded in the current density range from 0.142 to 7.93 mA cm^{-2} are characterized by a pronounced peak, *i.e.*, potential becomes more negative forming a peak and then changes in less negative direction to a steady-state value. According to Fletcher and Smith (145), Kashchiev (146) and Milchev and Montenegro (147), such a peak on galvanostatic transients is attributed to nucleation and crystal growth processes. During electrocrystallization, a large nucleation overpotential is required to overcome an energy barrier and hence ensures the galvanostatic condition. After nucleation, crystals grow, the active surface area available for the crystallization expands, and crystallization overpotential decreases. At later stages, the growth centres coalesce. As a result,

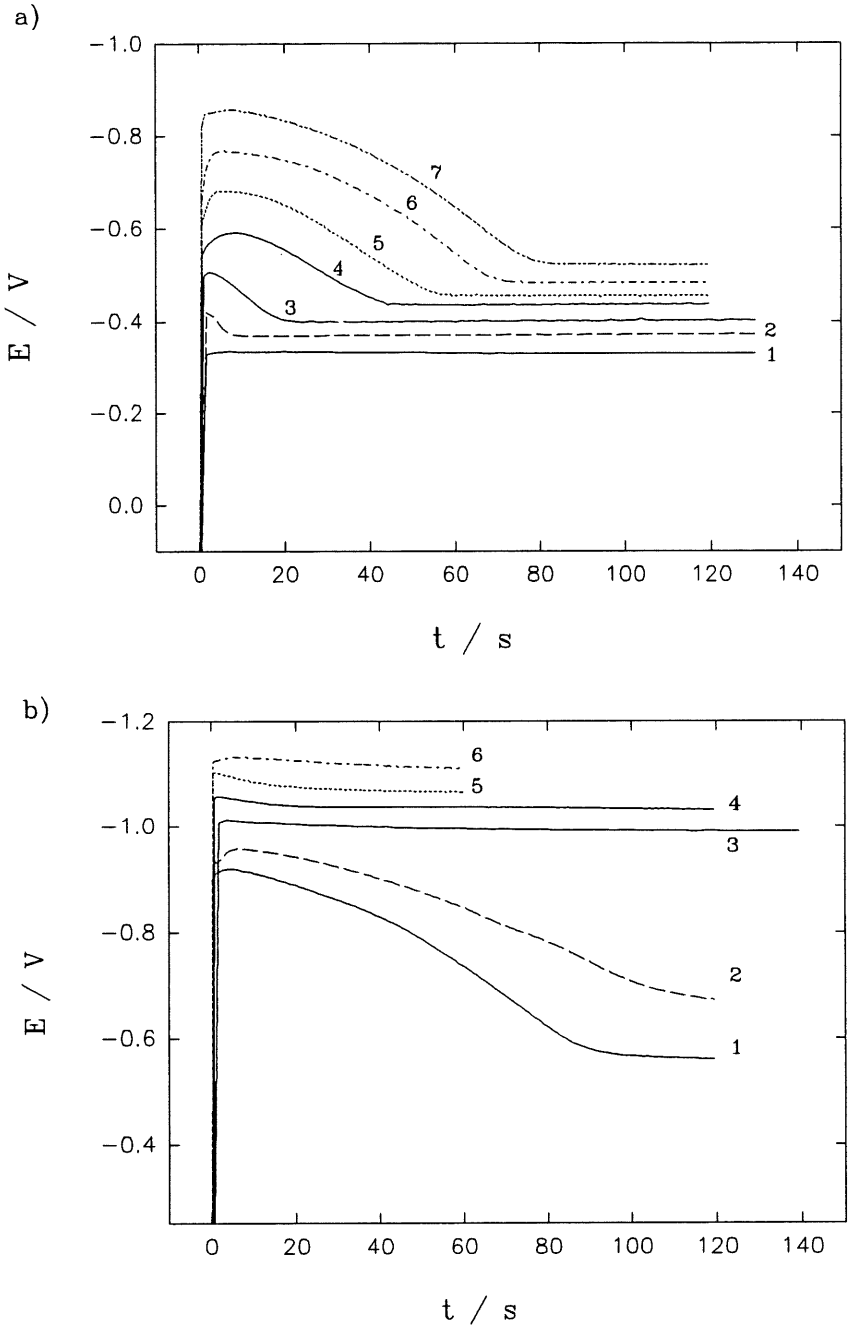

Figure 14. Potential-time transients of soft gold deposition on a gold RDE in solution C; Rotation rate: 4000 rpm; current density (mA cm^{-2}) in (a): 1) 0.079; 2) 0.141; 3) 0.256; 4) 0.453; 5) 0.793; 6) 1.42; 7) 2.55 and in (b): 1) 4.53; 2) 7.93; 3) 14.15; 4) 25.48; 5) 45.29; (6) 79.26.

overpotential reaches its final steady-state value. Similar phenomena were also observed by McIntyre and Peck (42) and Chech and Sard (47) in gold deposition from an alkaline cyanide bath and from a phosphate gold bath, respectively. As shown in Fig. 14, the peak height (corresponding to nucleation overpotential) increases with current density, and the time, required to attain potential peak and steady-state, also becomes longer at higher current densities. When current density is larger than 7.9 mA cm^{-2}, however, the initial potential peak of the transient tends to disappear, and the negative potential reaches quickly an almost constant value. The crystallization overpotential, defined as the potential difference $\Delta\eta$ between the initial peak and the final steady-state, initially increases with an increase in current density up to 4.53 mA cm^{-2}, and, subsequently, it drops abruptly to a very small value close to zero, at higher current densities, Fig. 15. A linear dependence of $\Delta\eta$ against $\log j$ with slope of 0.215 V dec^{-1} is observed at current densities lower than 4.53 mA cm^{-2}. No big difference between the initial peak and the steady-state value is observed in the later range. The drastic changeover in the shape of chronopotentiometric curves may imply a transformation in reaction mechanisms in two current density ranges. It should be noticed that overpotential difference $\Delta\eta$ can attain high values up to ~360 mV. Such high values of $\Delta\eta$ can hardly be explained entirely as overpotential for new phase-formation. Generally speaking, if deposition occurs on same substrate, nucleation overpotential should be lower since large amount of defects on surface may act as active centers. The large values of $\Delta\eta$ cannot be attributed to a phase formation alone (148), so other kinds of processes (*e.g.*, adsorption, inhibition, *etc.*) must be involved in the deposition at lower current densities.

Fig. 16 illustrates the steady-state polarization curve (corresponding to the potential values at long times in Fig. 14) for soft god deposition at 4000 rpm. Two ranges are clearly shown. When potential is more positive than *ca.* -0.95 V, current density increases only slowly with negative potential, whereas current density increases markedly as potential is made more negative than *ca.* -0.95 V. A quasi-plateau appears on the steady-state polarization curve in

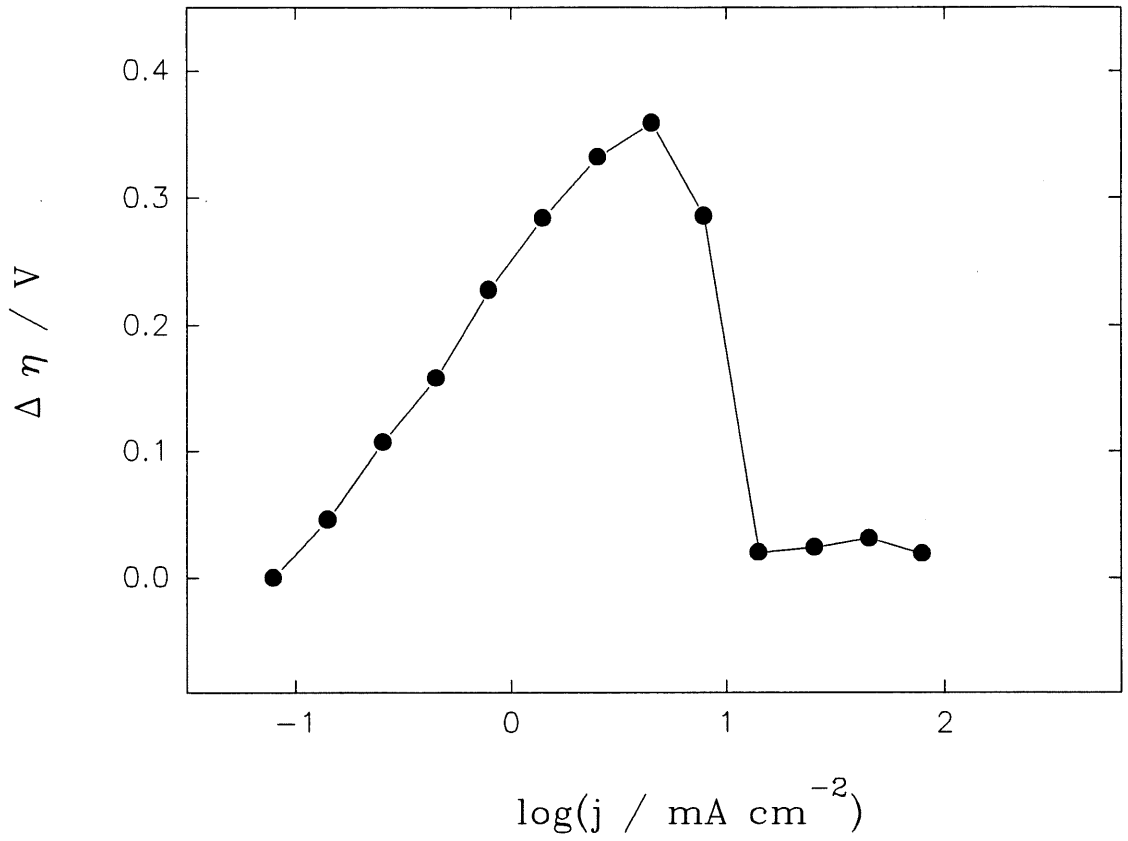

Figure 15. Crystallization overpotential, $\Delta\eta$, determined from the potential difference between the initial peak and final steady-state in Fig. 14 for soft gold deposition on a gold RDE, against logarithm of current density applied for solution C.

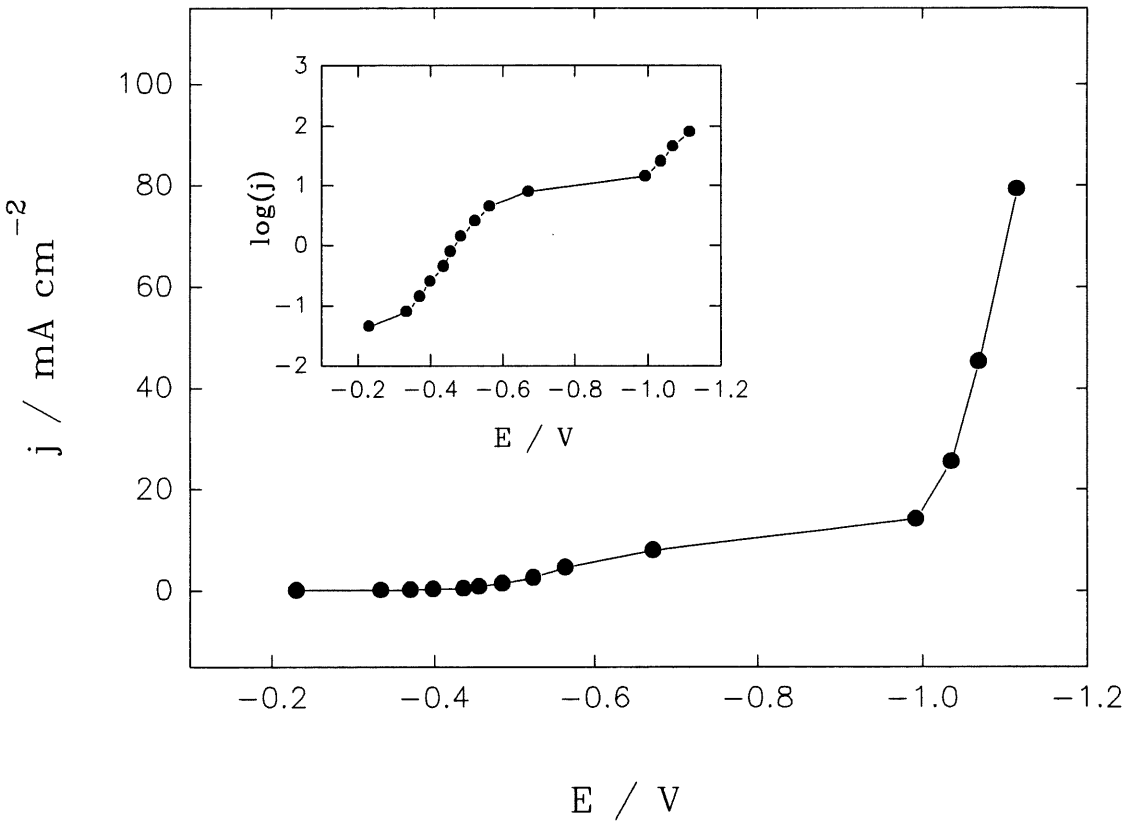

Figure 16. Steady-state polarization curve for soft gold deposition on a gold RDE at 4000 rpm. Data was taken from steady-state value in Fig. 14. The insert of figure shows the dependence of logarithm of current density against potential at steady-state.

the range *ca.* -0.55 V to -0.95 V, as is more clearly shown in the insert of Fig. 16. A big jump of potential exists between two ranges. a linear Tafel dependence of logarithmic current density on the applied potential at the steady-state is obtained in the latter range, while Tafel relationship cannot be attained from steady-state measurements in the first current density range. This also suggests that inhibition has an important influence on crystal growth.

In the galvanostatic mode, total current contains two terms, *i.e*, a double-layer charging current, which predominates at very initial time, and a faradaic current. The time up to the initial peak on chronopotentiometric curves is in the order of 5 ~ 10 seconds, depending on the current density applied. It is reasonable to assume that the contribution of double-layer charging to the total current can be neglected at this moment (149), and only the faradaic component is observed. Hence, Tafel curve may be constructed based on the initial peak potential on the transients (148-150). The linear dependence of logarithmic current density on the initial peak potential is observed in both ranges, as shown in Fig. 17. Tafel plot is characterized by two slopes of 0.34 V dec^{-1} in lower current density range and 0.15 V dec^{-1} at higher current density, respectively. The same method will be used in hard gold deposition. It will be shown later in chapter 6 that these values of Tafel slopes are in a very good agreement with the results obtained by chronoamperometry.

In practice, gold plating bath often contains a suitable reducing agent, *e.g.*, oxalic acid, to diminish the possibility of the oxidation of Au (I) to Au (III) (12). To understand its influence on the bath performance, measurements were also carried out in solution C with addition of 20 g l^{-1} oxalic acid. The general feature, similar to Fig. 14, is maintained, whilst all curves shift in more negative direction. Tafel slopes were also determined under rotation rates of 1000 and 2700 rpm, their values are close to those obtained at 4000 rpm within the experimental error, indicating that rotation rate does not have an important influence on Tafel slopes. However, the shape of curves is greatly influenced by the rotation rate. Fig. 18 represents the effect of rotation rate on transients obtained at 4.53 mA cm^{-2} in soft gold bath,

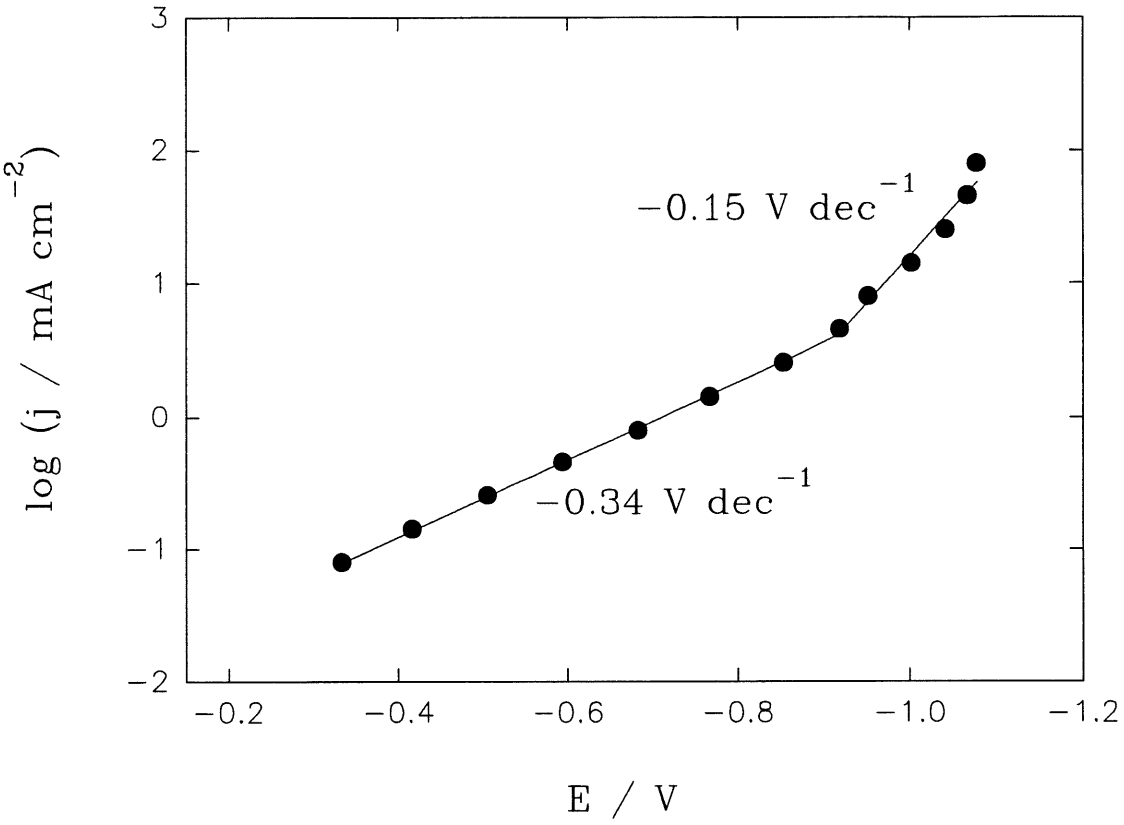

Figure 17. Tafel plot based on the initial peak potential on chronopotentiometricl curve shown in Fig. 14 for soft gold deposition on a gold RDE in solution C.

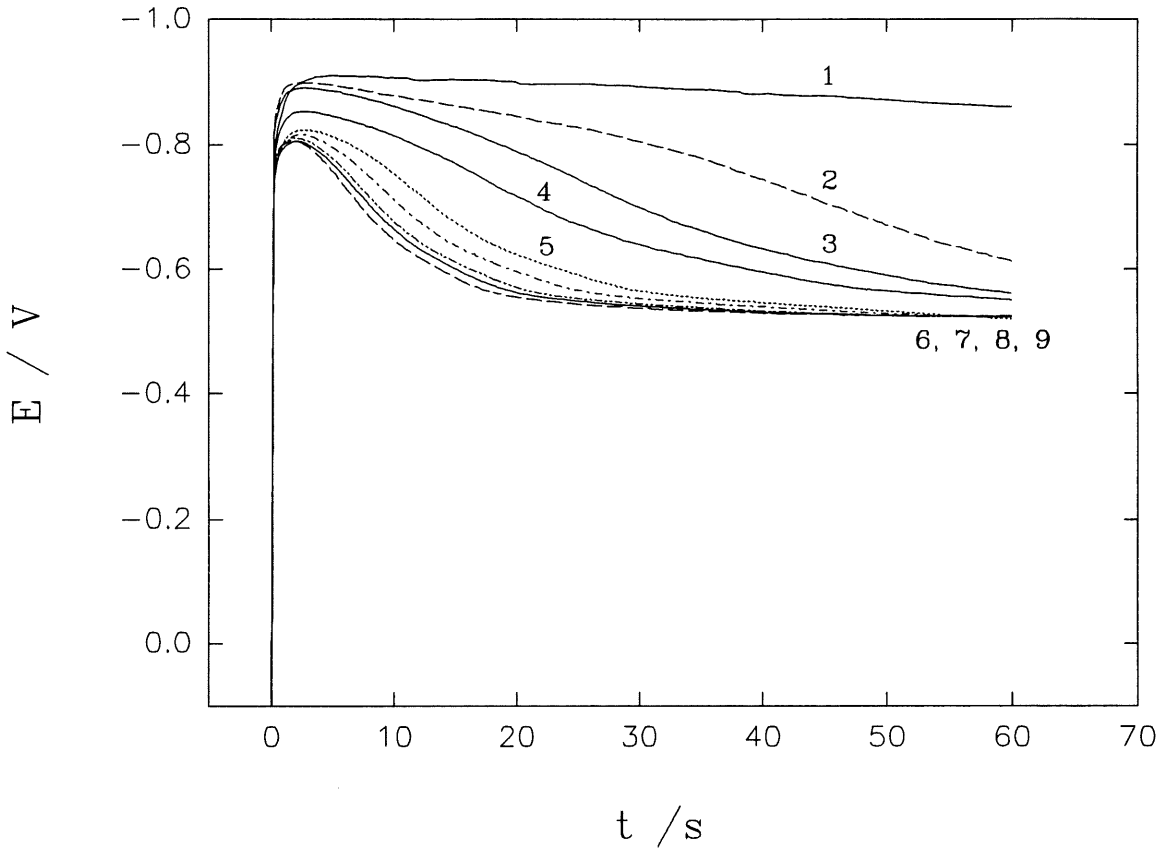

Figure 18. The effects of rotation rate on the shape of potential-time transients for soft gold deposition on a gold RDE from solution C with addtion of 20 g l^{-1} oxalic acid; current density: 4.525 mA cm^{-2}; rotation rate (rpm): 1) 0; 2) 300; 3) 520; 4) 700; 5) 1400; 6) 1800; 7) 2400; 8) 2700; 9) 3200.

in which 20 g l^{-1} of oxalic acid was added into solution C. On a stationary electrode, potential decreases slightly with time after the initial peak. As rotation rate increases, the height of initial potential peak decreases, and the transient curve reaches its final steady-state faster. However, the values of potential at steady-state do not change with rotation rate. This is possibly caused by an inhibitor (HCN or CN^-) produced in the deposition, as discussed in the previous chapter, its mass transfer from the surface to the bulk of solution may be under diffusion control. At higher rotation rates, the mass transfer of inhibitor becomes faster, the fractional surface area available for crystallization increases, hence overpotential for deposition decreases with rotation rate. It is noted that due to the addition of oxalic acid, the curve shifts in more negative direction compared with Fig. 14 at the identical conditions. The influence of pH of solution on chronopotentiometric curves was studied for soft gold bath containing addition of oxalic acid. In spite of change in the peak height and the transition time, characteristic peak-like behavior always appears on transients at lower current densities, as shown in Fig.5. Tafel slopes based on the initial peak potential decrease slightly with a decrease of the pH of solution.

5.3 Chronopotentiometric behavior of hard gold baths

Fig. 19 shows a typical set of chronopotentiometric transients for hard gold deposition from solution D. Similar to soft gold bath, the peak on chronopotentiometric curve is also observed at lower current densities despite of the presence of nickel in solution. However, current density range, in which the characteristic peak occurs, becomes much narrower, and the time required to reach the initial potential peak decreases as current density increases, opposite to that for soft gold deposition (Fig. 14). The potential difference, $\Delta\eta$, between the initial peak potential and the final potential on transients is illustrated in Fig. 20. Its shape is similar to that for soft gold deposition, and the linear dependence of $\Delta\eta$ on $\log j$ is shown in the first range, although the maximum of $\Delta\eta$ corresponds to smaller current as compared with soft gold. Fig. 21 represents the steady-state polarization curve for hard gold deposition.

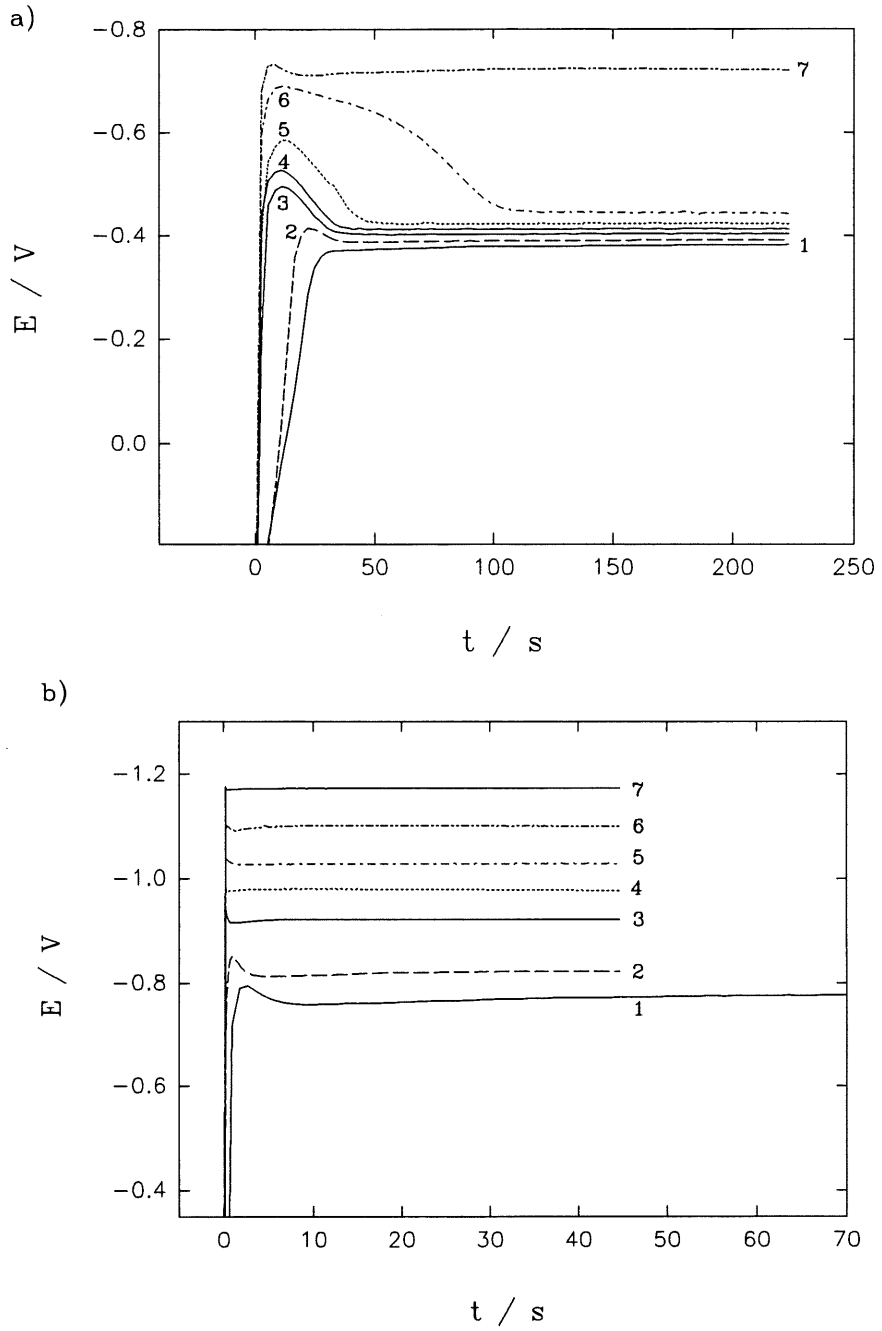

Figure 19. Chronopotentiometric transients for hard gold deposition on a gold RDE in solution D; rotation rate: 4000 rpm; current density (mA cm^{-2}) in (a): 1) 0.110; 2) 0.170; 3) 0.255; 4) 0.354; 5) 0.453; 6) 0.623; 7) 0.793; and in (b): 1)1.42; 2) 2.55; 3) 7.93; 4) 14.15; 5) 25.48; 6) 45.29; 7) 79.26.

It is clearly seen from Fig. 21 and its insertion that, similar to soft gold, a big potential jump from -0.45 V to -0.75 V exists at current densities between 0.62 and 0.79 mA cm^{-2}, reflecting a change in the mechanism of gold deposition. Tafel curve based on the initial peak potential of chronoamperometric curves is given in Fig. 22, it displays two straight lines in two potential ranges. Higher Tafel slope of 0.48 V dec^{-1} is obtained at lower current densities (corresponding to lower overpotentials), which may arise from the reduction of the adsorbed intermediate AuCN on the electrode surface, reaction [4.7], while a lower slope of 0.19 V dec^{-1} in the second range may correspond to a direct reduction of $Au(CN)_2^-$ from solution, reaction [1.6].

Fig. 23 shows influence of the rotation rate on the shape of chronopotentiometric transients at 0.452 mA cm^{-2} for hard gold deposition from solution D with addition of 20 g l^{-1} oxalic acid. Similar to Fig. 18 for soft gold deposition, potential (after the initial peak) changes slightly with time when a constant current density is applied on a stationary Au electrode. As rotation rate increases, the height of initial peak decreases and potential reaches its final steady-state much faster. The potential value in the final steady-state is not affected by the rotation rate. The dependence of initial peak potential on rotation rate is also shown in Fig. 24, rotation rate has less influence on the initial peak potential obtained at higher current densities than that at lower current densities. Though the height and width of initial peak on the curves are markedly affected by rotation rate, Tafel slopes obtained under different rotation rates do not show differences beyond the experiment error. The measurements performed in solution D with an additional amount of oxalic acid showed that the addition of reducing agent does not change the general behavior of potential-time transient, however, the times, after which the initial peak and final steady-state occur, become much shorter and curve shifts in more negative direction as compared with Fig. 19. Furthermore, the addition of oxalic acid gives rise to a decrease in Tafel slopes, their values at pH 4.4 are 0.384 V dec^{-1} and 0.164 V dec^{-1} in two ranges, respectively.

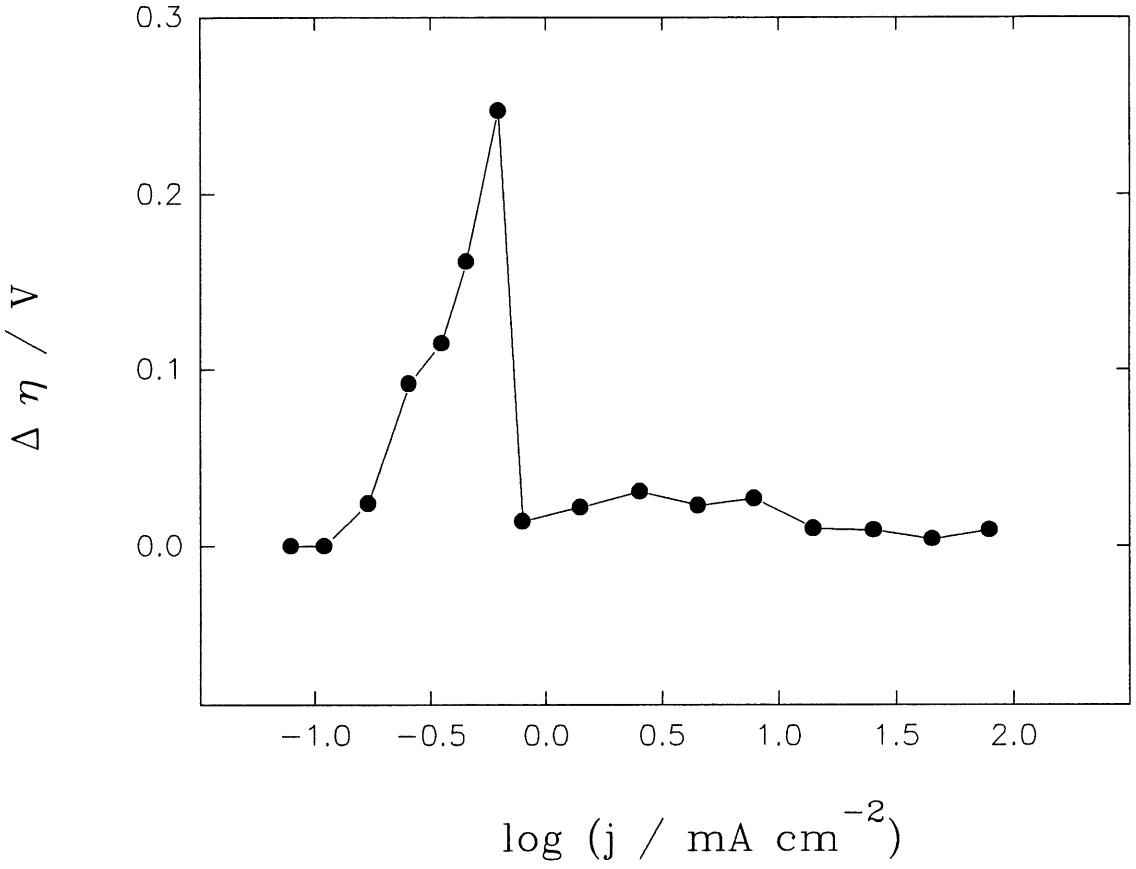

Figure 20. Crystallization overpotential $\Delta\eta$ for hard gold deposition on a gold RDE, determined from the potential difference between the initial peak and final steady-state shown in Fig. 19, against the logarithm of current density applied.

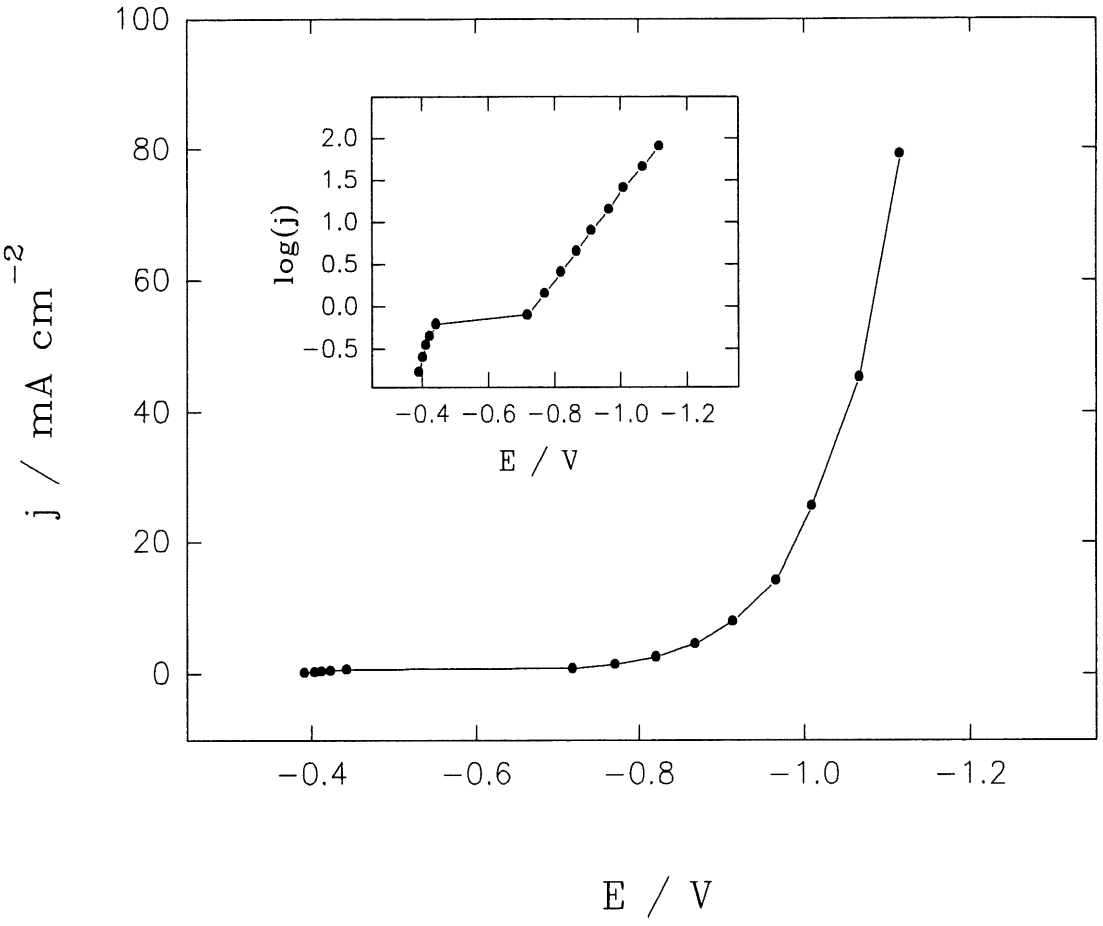

Figure 21. Steady-state polarization curve for hard gold deposition on a gold RDE at 4000 rpm. Data is taken from steady-state value in Fig. 19. The insert of figure shows the dependence of logarithmic current density against potential at steady-state.

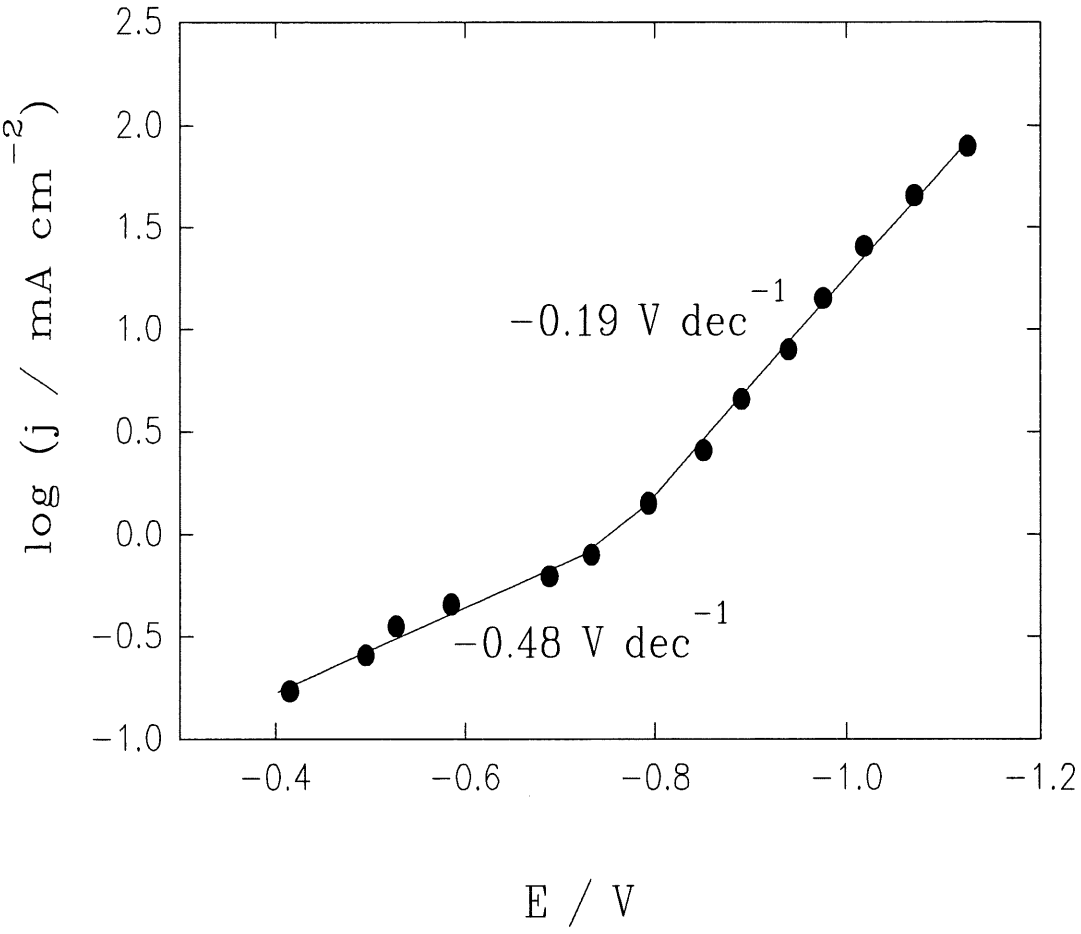

Figure 22. Tafel plot based on the initial peak potential on chronopotentiometric curves shown in Fig. 19 for hard gold deposition on a gold RDE in solution D.

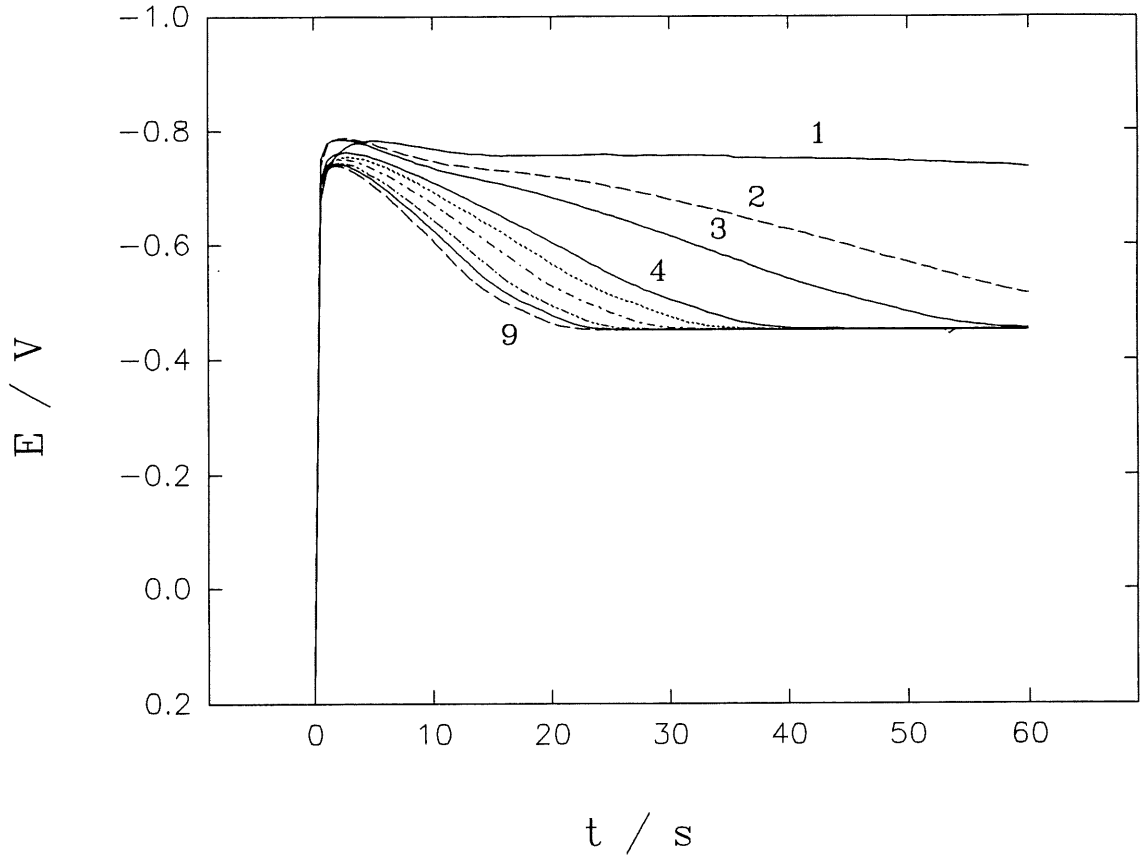

Figure 23. The effects of rotation rate on the shape of chronopotentiometric curves for hard gold deposition on a gold RDE in solution D with the addition of 20 g l^{-1} oxalic acid; current density: 0.452 mA cm^{-2}; rotation rate (from the top to the bottom) (rpm): 1) 0; 2) 300; 3) 520; 4) 700; 5) 1400; 6) 1800; 7) 2400; 8) 2700; 9) 3200.

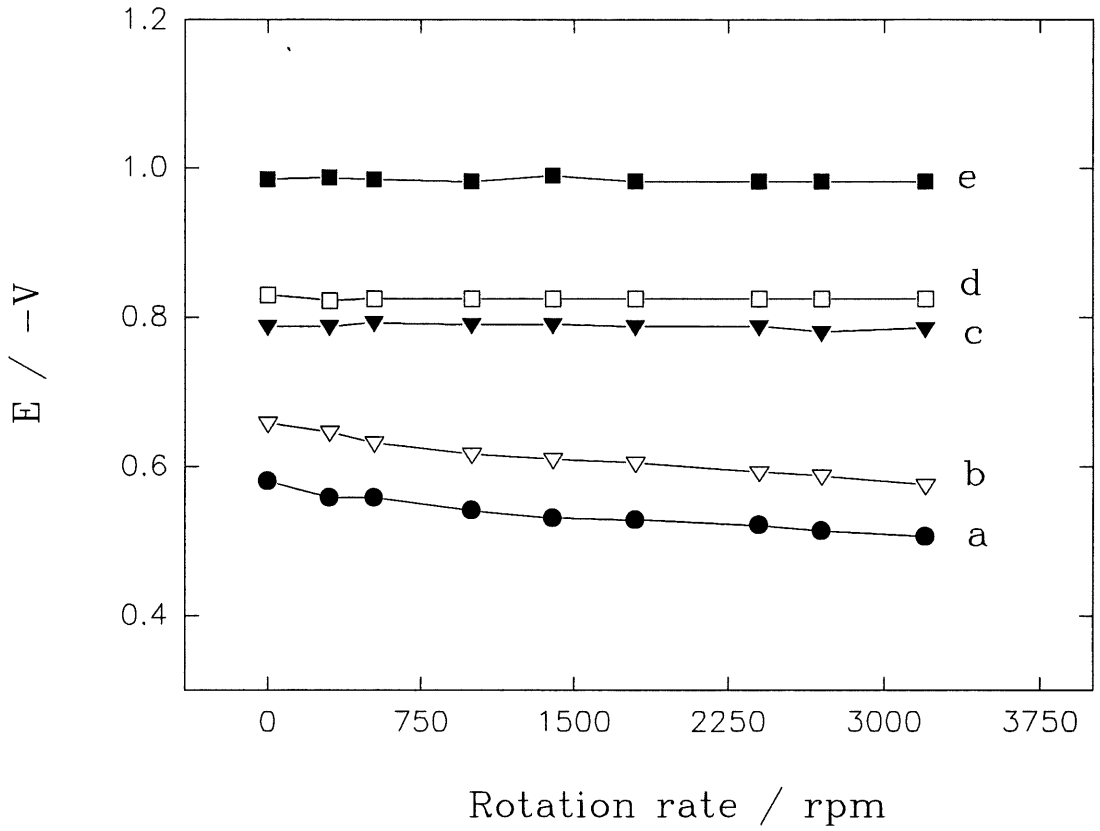

Figure 24. The dependence of initial peak potential on rotation rate for hard gold deposition on a gold RDE; solution D with the addition of 20 g l^{-1} oxalic acid; current densities (mA cm^{-2}): a) 0.142; b) 0.254; c) 0.793; d)1.42; e) 7.93.

It is found that a higher concentration of oxalic acid leads to the chemical instability of bath and the decrease of its life. Besides, gold deposit was observed on the wall of vessel and Teflon holder of electrode, which may be caused by the electroless deposition of gold in the bath due to the high concentration of this reducing agent. This problem is sometimes encountered in industry, leading to a loss of gold and an increase in the production cost.

From galvanostatic potential-time transients, it is possible to measure the double-layer capacity. At a very initial time, the double layer charging current, j_c, dominates the total current, and the contribution of faradaic process can be neglected (149). Current density $j_{t=0}$ is given by:

$$j_{t=0} = C_{dl} \left(\frac{d\eta}{dt}\right)_{t=0} \qquad [5.1]$$

where C_{dl} is a double layer capacity ($\mu F\ cm^{-2}$). By making an extrapolation of potential-time curve to $t = 0$, the capacity C_{dl} may be determined from eq. [5.1]. The determined results are given in Table 5. As seen in Table 5, the capacity C_{dl} are approximately equal to 28 $\mu F\ cm^{-2}$ at current densities from 0.026 to 7.93 $mA\ cm^{-2}$. At higher current densities, it seems that the capacity C_{dl} decreases slightly with current density.

Table 5. Double-layer capacity C_{dl} determined by the galvanostatic method

j ($mA\ cm^{-2}$)	0.026	0.045	0.079	0.142	0.256
C_{dl} ($\mu F\ cm^{-2}$)	29.72	28.29	28.58	29.01	27.53
j ($mA\ cm^{-2}$)	0.432	0.796	1.415	2.548	4.527
C_{dl} ($\mu F\ cm^{-2}$)	27.98	31.86	30.01	26.33	23.64
j ($mA\ cm^{-2}$)	7.926	14.15	25.48	45.29	79.26
C_{dl} ($\mu F\ cm^{-2}$)	23.43	18.03	17.15	16.58	18.27

5.4 Discussion

It is quite evident from chronopotentiometric measurements presented above that the mechanism of gold deposition changes with current densities, resulting in the different shapes of chronopotentiometric curves in two current density ranges. The nucleation and growth related potential peak gives the most pronounced feature for all the curves recorded at lower current densities (corresponding to lower overpotentials). As discussed in the previous chapter, only the intermediate AuCN is electrochemically active species in this potential range. It is likely that the nucleation and growth process occurs on the surface covered by $AuCN_{ad}$. The electrode is similar, to some extent, to a foreign substrate. Additional energy is required for the nucleation and crystal growth together with the adsorption of $AuCN_{ad}$. Therefore, an obvious potential peak (with $\Delta\eta$ = ~300 mV) is observed on chronopotentiometric curves.

For both soft and hard gold deposition, a relatively high Tafel slope is obtained in the first current density range. This may be attributed to the adsorption of reactive species involved in the deposition. In the case of specific adsorption, the actual charge transfer occurs across a fraction of the Helmoholtz layer only, leading to the deviation of the charge transfer coefficient from 0.5 (151). At the higher current density range $Au(CN)_2^-$ becomes active species and the adsorption of $AuCN_{ad}$ is less important. The smaller value of Tafel slope obtained may correspond to a direct electron-transfer reaction mechanism. In this case, a large number of screw dislocation on the surface may act as active sites for the nucleation and growth of crystallites.

In many cases of metal electrodeposition on the same or a foreign inert substrate, galvanostatic potential-time transients are characterized by a peak in the initial stages of the formation of a new phase. Such an initial peak is attributed to slow nucleation. Accordingly, when a current pulse is applied on a foreign substrate, nucleation is required leading to an overpotential peak (superpolarization) occurring on the potential-time transients. However, if

a current pulse is imposed again on the substrate which was deposited, such "nucleation overpotential" peak on the transient should disappear since the electrode surface has been covered by growth centers, a nucleation is not necessary in the subsequent measurements (152). In our case, nevertheless, all potential-time transients have a similar shape when the measurements were repeated a few times after switching off the current, and peak potential for such repeated measurements are close each other, as shown in Fig. 25. There are

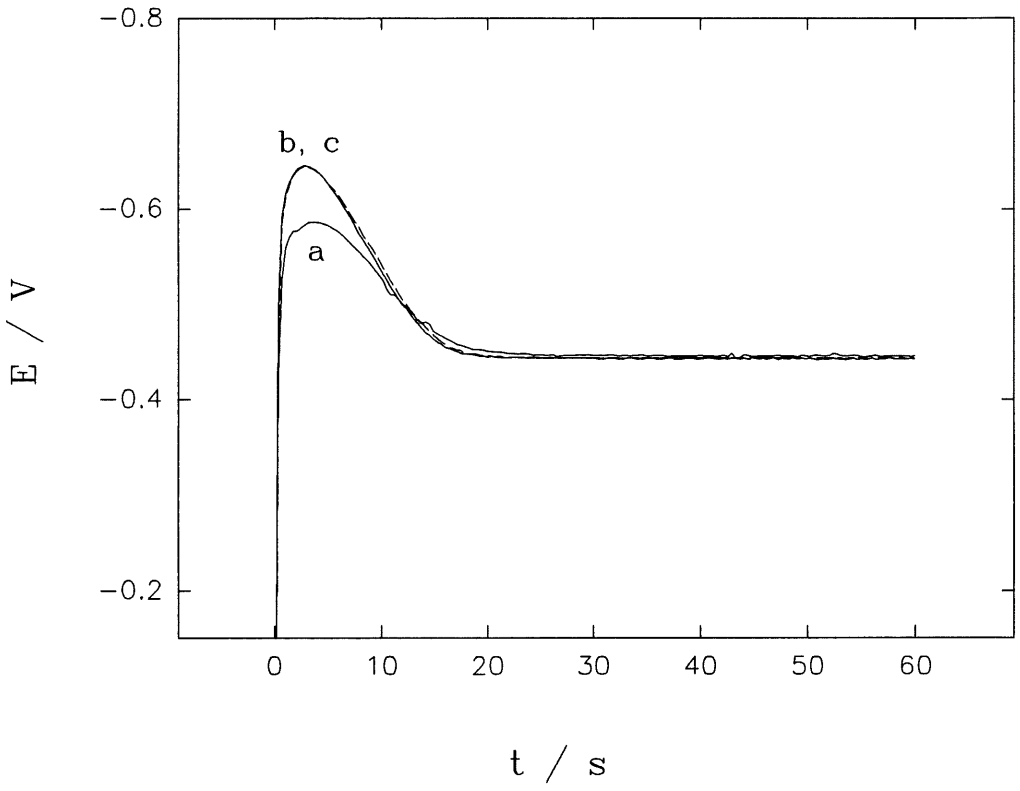

Figure 25. Chronopotentiometric curves obtained on a fresh polished Au electrode (a) and an unpolished Au electrode (b) and (c); solution D with the addition of 20 g l^{-1} oxalic acid; current density 0.254 mA cm^{-2}; rotation rate: 2700 rpm.

other possibilities for the peak formation of the galvanostatic transients, for example, due to the effect of adsorbed impurities as supposed by Bockris (153) in Cu deposition. However, such a peak was still observed in Cu deposition from a highly purified solution (154). In our case, the origin of peak is different because the effect of impurities is obvious only at very initial stages of deposition and it should be diminished in the subsequent experiments (154). It is evident that repeating measurements a few times, leads to a similar behavior, Fig. 25. Except the first curve recorded on the polished electrode, the potential at peak and steady-state are identical for other curves (line b and c in Fig. 25). Obviously the presence of impurities in the present case is not responsible for the peak formation. The obvious peak with $\Delta\eta$ = ~300 mV is mostly due to the slow nucleation of gold deposition on the surface covered by $AuCN_{ad}$. It will be shown in next chapters that the initial potential peak corresponds to the initial minimum on the potentiostatic current-time transients, where the electrocrystallization process can be more conveniently analyzed in terms of nucleation and crystal growth model.

CHAPTER 6
NUCLEATION AND CRYSTAL GROWTH IN SOFT GOLD DEPOSITION

6.1 Introduction

Potentiostatic method is straightforward in studying the nucleation and crystal growth mechansim. In the present chapter, the initial stages of gold electrodeposition onto Au RDE from soft gold bath (without nickel) is studied with this technique. Experimental current-time transients were analysed using nonlinear least-squares fit to various models of nucleation and crystal growth. Kinetic parameters such as Tafel slopes, nucleation rate constants, number of active centres, growth rate constants, *etc.*, were determined. The inhibition of crystal growth is also discussed.

6.2 Results

In order to decrease the influence of mass-transfer on the deposition process, all chronoamperometric measurements were performed at the rotation rate of 4000 rpm. Fig. 26 illustrates a set of current-time transients in a wide potential range obtained in solution C. The initial current decrease could be, in general, caused by four different processes:

- a double layer charging current, which decreases exponentially to zero in milliseconds;
- transient diffusion limited process. For diffusion controlled processes on a rotating disk electrode, current should decrease to a steady-state value after certain time when potential is imposed on a RDE. Time necessary to reach a steady-state depends on the rotation rate. At our conditions, this time was estimated as ~ 0.03 seconds at rotation rate 4000 rpm (155);
- direct deposition of metal onto lattice without nucleation;
- other side reactions like hydrogen evolution, whose influence becomes obvious only at very negative potential.

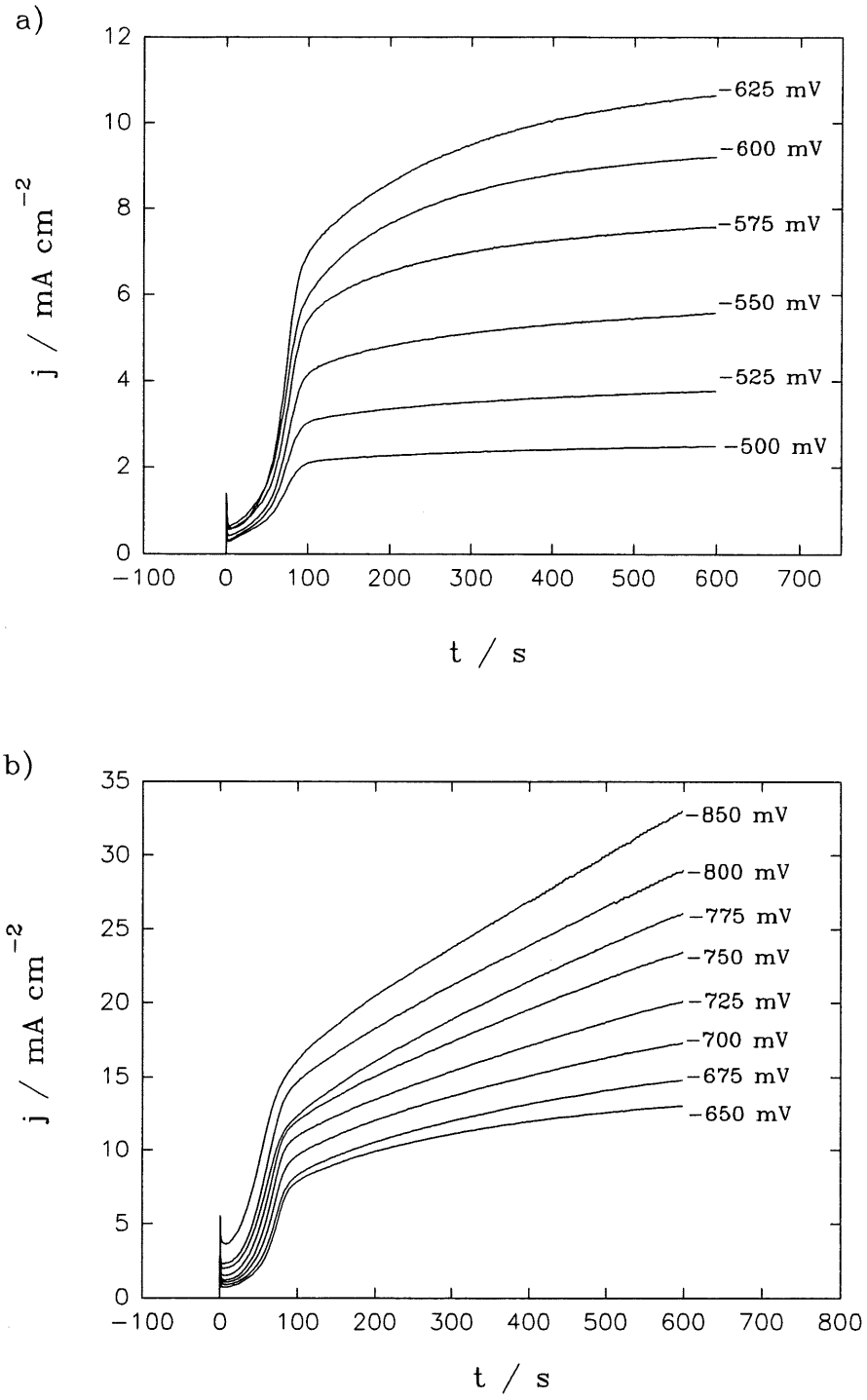

Figure 26(a, b) Current-time transients for soft gold deposition on a gold RDE from solution C; rotation rate: 4000 rpm.

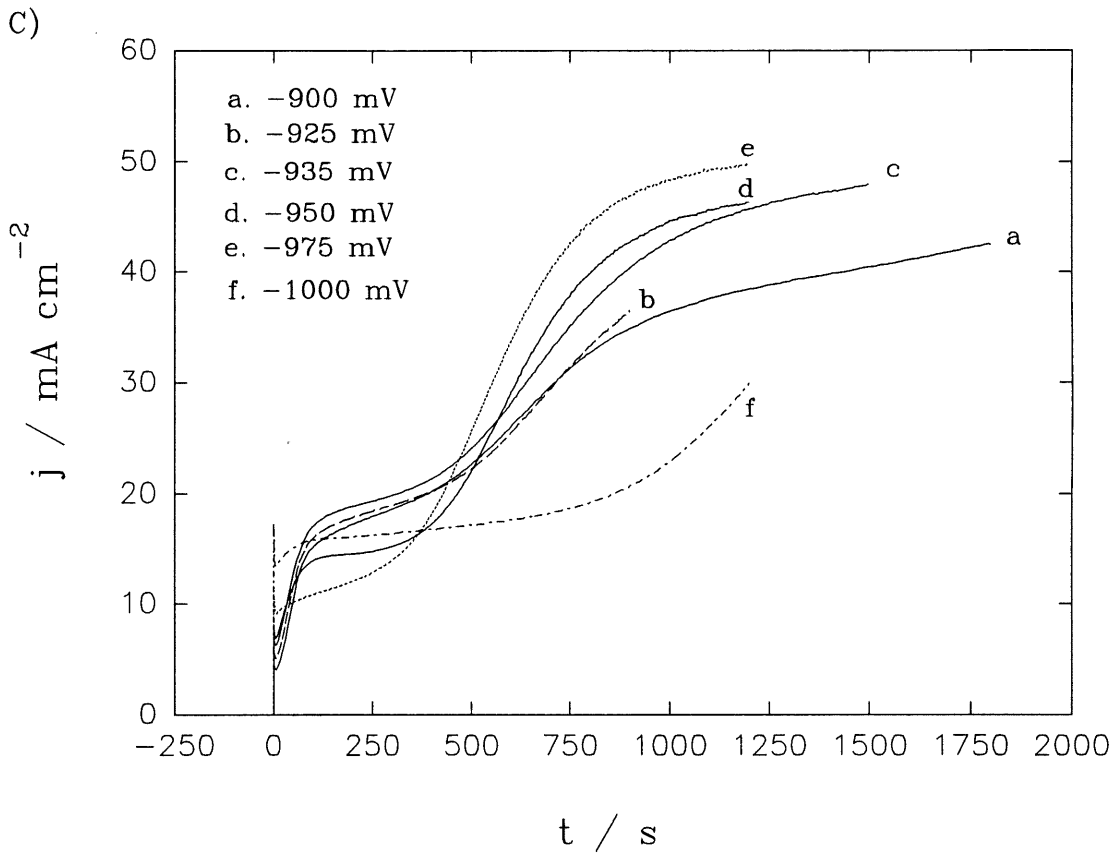

Figure 26c. Current-time transients for soft gold deposition on a gold RDE from solution C; rotation rate: 4000 rpm.

Current minimum, i_{min}, observed at beginning of current-time transients increases with negative potential. The time, t_{min}, necessary to reach a current minimum is up to a few seconds, depending on the potential applied. The charge consumed up to t_{min} corresponds to more than ten compact gold monolayers (~204 C cm^{-2} per monolayer, caculated by assuming a square array of Au atoms) which suggests that gold deposition process starts before t_{min} is reached. The initial current minimum corresponds principally to a direct gold deposition without nucleation (47). After an induction time, nucleation process starts and gold crystals grow. This leads to an increase of current with time as result of the increase of the electroactive surface area. Shape of the current-time transients is determined by the nucleation and crystal growth processes, which depend strongly on the potential applied. At the potentials between -0.500 and -0.850 V, Fig. 26a and b, current first increases quickly and then continues to increase slowly at longer times. In this potential range, no steady-state is reached even after a relatively long time. The slow increase of current at longer times may be related to a second growth process occurring on the top of the initially deposited layers. Furthermore, at low overpotentials, *e.g.*, -0.50 V, the increase of current with time at the foot of transients is quite slow. This may imply that two different nucleation and growth processes occur simultaneously.

When potential is more negative than -0.90 V, Fig. 26c, current increases rapidly with time and then reaches a quasi-plateau. Later, current continues to increase slowly with time and another plateau is observed at longer times. It implies that a second three-dimensional nucleation and growth process occurs on the top of the initial deposit. Current of the second plateau increases with negative potentials in the range -0.90 V to -0.975 V. The first quasi-plateau increases as potential changes from -0.90 V to -0.935 V, and then decreases with negative potential in the range -0.95 V to -0.975 V. This may be caused by an inhibition process, *i.e.*, crystal growth process is inhibited by a certain substance produced on the electrode surface. It is consistent with the conclusions from the LSV measurements, Fig. 2. At potentials more negative than -1.0 V (corresponding to a second potential range on LSVs),

induction time for nucleation becomes very short, current increases and reaches a small plateau faster. At later stages, current continues to increase and no steady-state is observed, *i.e.*, the current increases with negative potential. The HER becomes important at potentials more negative than -1.0 V.

Deposits exhibit different appearance at different potentials. Bright smooth deposits were observed at potentials more positive than the peak potential on LSVs. Surface changed from bright to dull as potentials became more negative than the peak potential. Thereafter, at more negative potentials, deposits were usually bright and smooth. The morphological studies of gold deposits on copper substrate using scanning electron microscopy (SEM) and atomic force microscopy (AFM) will be presented later in chapter 9. It was shown that the growth morphology is strongly potential dependent and grains with various sizes are observed.

Since no steady-state for gold deposition was reached under most experimental conditions, current at longer times could not be used to construct Tafel plots. A Tafel plot based on the initial current minima is shown in Fig. 27. Two linear regions with two different slopes are observed. Tafel slopes are 0.328 ± 0.007 V dec^{-1} in potential range from -0.50 to -0.95 V and 0.157 ± 0.006 V dec^{-1} at potentials between -0.95 and -1.1 V, respectively. These values are in an excellent agreement with the results obtained from the chronopotentiometric measurement, for which Tafel plots were based on the initial potential peak on the potential-time transients (see chapter 5). It indicates that the current minimum in chronoamperometric curve corresponds to the initial potential maximum of the chronopotentiometric curve.

6.3 Approximation of current-time transients: nucleation and crystal growth models

Theory of nucleation and crystal growth phenomena has been reviewed previously in chapter 2. These complex phenomena are affected by many factors and sometimes different processes may occur simultaneously, *e.g.*, combination of two-dimensional (2D) and three-dimensional

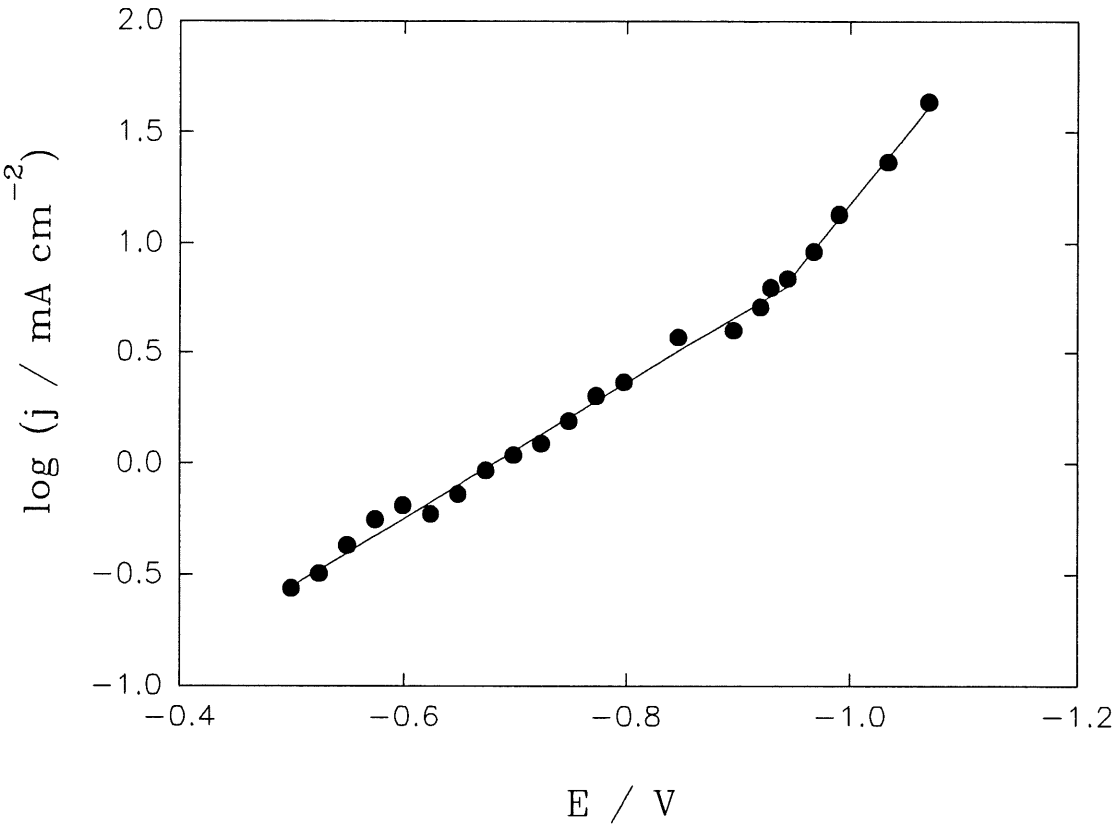

Figure 27. Tafel plot constructed on the basis of the initial current minimum shown in Fig. 26, for soft gold deposition on a gold RDE from solution C.

(3D) growth (156,157), death and rebirth of nuclei (157), secondary 3D growth on the top of the first growth layers (158), *etc.* As shown in Fig. 26, the shapes of current-time transients are different at different potentials. This indicates that the nucleation and growth mechanism depends strongly on the potential applied. In order to approximate initial portions of the experimental current-time transients, various 2D and 3D models were tested.

Assuming that three-dimensional progressive nucleation and growth of right-circular cones occurs onto the same substrate, current consists of two parts, eq. [2.27]. The first term is the current due to the outward growth of substrate base plane at the free surface not covered by growing nuclei, j_f, and it decreases to zero with time, while the second one is due to three-dimensional progressive nucleation and growth, j_{3D}, and it reaches a plateau at later stage. eq. [2.27] may be rewritten as:

$$j = j_0 \exp(-P_2' t^3) + P_1[1 - \exp(-P_2' t^3)] \qquad [6.1]$$

where $j_0 = zFk_0$; $P_2' = \pi M^2 k^2 A_{3D} / 3\rho^2$ and $P_1 = zFk'$, k_0 is the growth rate constant on substrate's base plane; k and k' are the lateral and vertical growth rate constants, respectively (mol cm^{-2} s^{-1}); A_{3D} the nucleation rate (nuclei cm^{-2} s^{-1}); M the atomic weight (g mol^{-1}) and ρ the density (g cm^{-3}) of the deposit; other symbols have been explained earlier. Fig. 28 shows current-time transients fitted to eq. [6.1], in the potential range from -0.725 to -0.85 V. However, transients recorded at more positive potentials could not be described well by this model, especially at the foot of the curves, where current increases rather slowly with time. It is possible that there is also another process whose contribution decreases with negative potentials. In order to describe the current-time transients recorded at potentials between -0.5 V and -0.725 V, it was supposed that a 2D progressive nucleation and crystal growth of cylinders, eq. [2.18], occurs simultaneously with the main process of 3D progressive nucleation and growth of right-circular cones. Therefore, the total current consists of three parts:

$$j = j_f + j_{2D} + j_{3D} \qquad [6.2]$$

where 3D growth process occurs after the induction time t_0. The total current is given by:

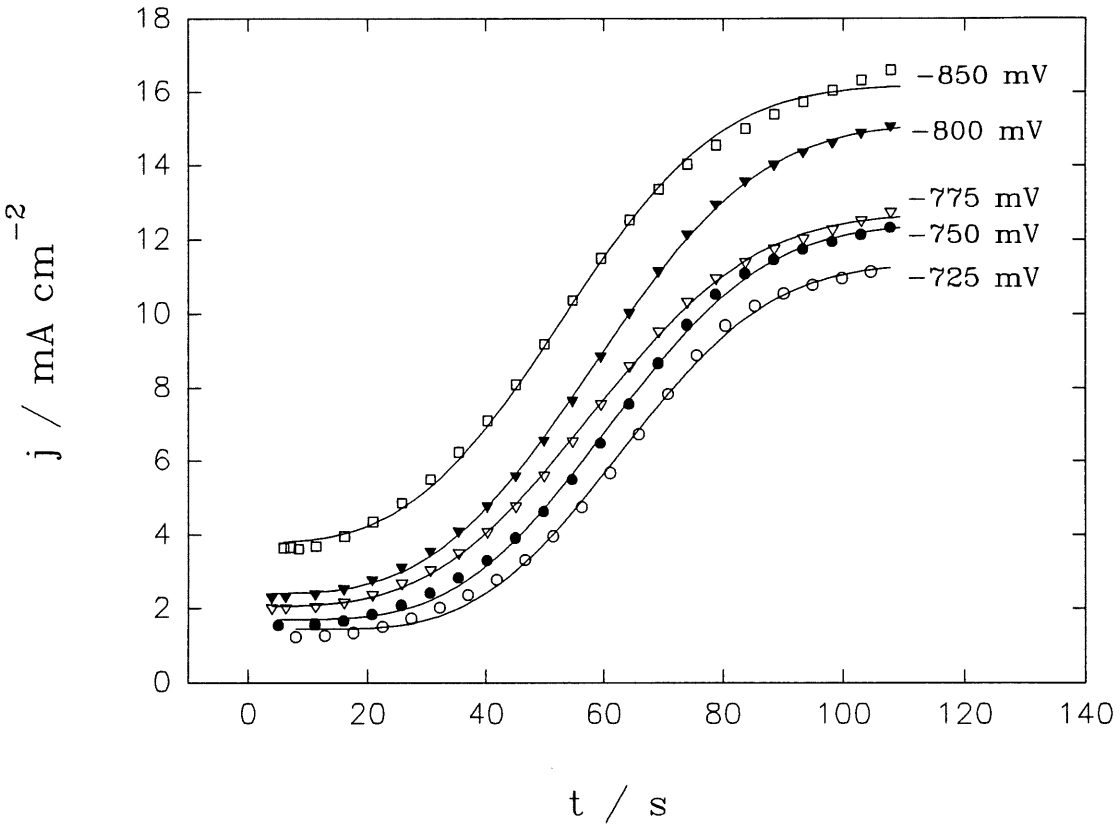

Figure 28. Initial portions of current-time transients shown in Fig. 26 for soft gold deposition on a gold RDE at potentials from -0.725 V to -0.850 V; points - experimental, solid lines - theoretical fit to eq. [6.1].

$$j = j_o \exp(-P_4 t^3) + P_3 t^2 \exp(-P_4 t^3) + P_1[1 - \exp(-P_2'(t - t_0)^3)] \quad [6.3]$$

where $j_0 = zFk_0$, $P_1 = zFk'$, $P_2' = \pi M^2 k^2 A_{3D}/3\rho^2$, $P_3 = zF\pi hMk_{2D}^2 A_{2D}/\rho$ and $P_4 = \pi M^2 k_{2D}^2 A_{2D}/3\rho^2$, k_{2D} the lateral growth rate constants (mol cm^{-2} s^{-1}), h the atomic layer height (cm), N_0 the total number of active centres (cm^{-2}), and A_{2D} the nucleation rate of two-dimensional nucleation (nuclei cm^{-2} s^{-1}).

Fig. 29 shows theoretical fit to the experimental data using eq. [6.3]. The fit is very good. Contributions of two growth processes, at potential -0.500 V and -0.725 V, are illustrated in Fig. 30. The contribution of the 2D process (lines a' and b') decreases as potential becomes more negative and it is negligible at high negative potentials.

When the potential is more negative than -0.90 V, two quasi-plateau appear on the current-time transients, as shown in Fig. 26c. In modeling of the complete transients it was assumed that a secondary 3D progressive nucleation and growth process occurs on the top of first one after a certain induction time. The first growth process becomes 3D instantaneous nucleation and growth of right circular cones. The observed current is described as:

$$j = j_0 \exp(-P_2 t^2) + P_1[1 - \exp(-P_2 t^2)] \quad [6.4]$$

for $t \leq t_s$ and

$$j = j_0 \exp(-P_2 t^2) + P_1[1 - \exp(-P_2 t^2)] + P_s[1 - \exp(-P_{2s}(t - t_s)^3)] \quad [6.5]$$

for $t \geq t_s$, where $P_2 = \pi M^2 k^2 N_0/\rho^2$, $P_s = zFk_s'$, $P_{2s} = \pi M^2 k_s^2 A_s/3\rho^2$, k_s' and k_s are the vertical and lateral growth rate constants for secondary growth process, respectively, A_s the nucleation rate for the secondary nucleation process, and t_s its induction time. Fig. 31 presents experimental data and the fitted curves according to eqs. [6.4] and [6.5] at potentials between -0.9 and -0.975 V. It is obvious that the observed current transients may be well described by the proposed model.

From the analysis presented above, kinetic parameters were estimated. Fig. 32 shows a Tafel plot of the outward growth rate constant, k_0, for the substrate's base plane. Dependence

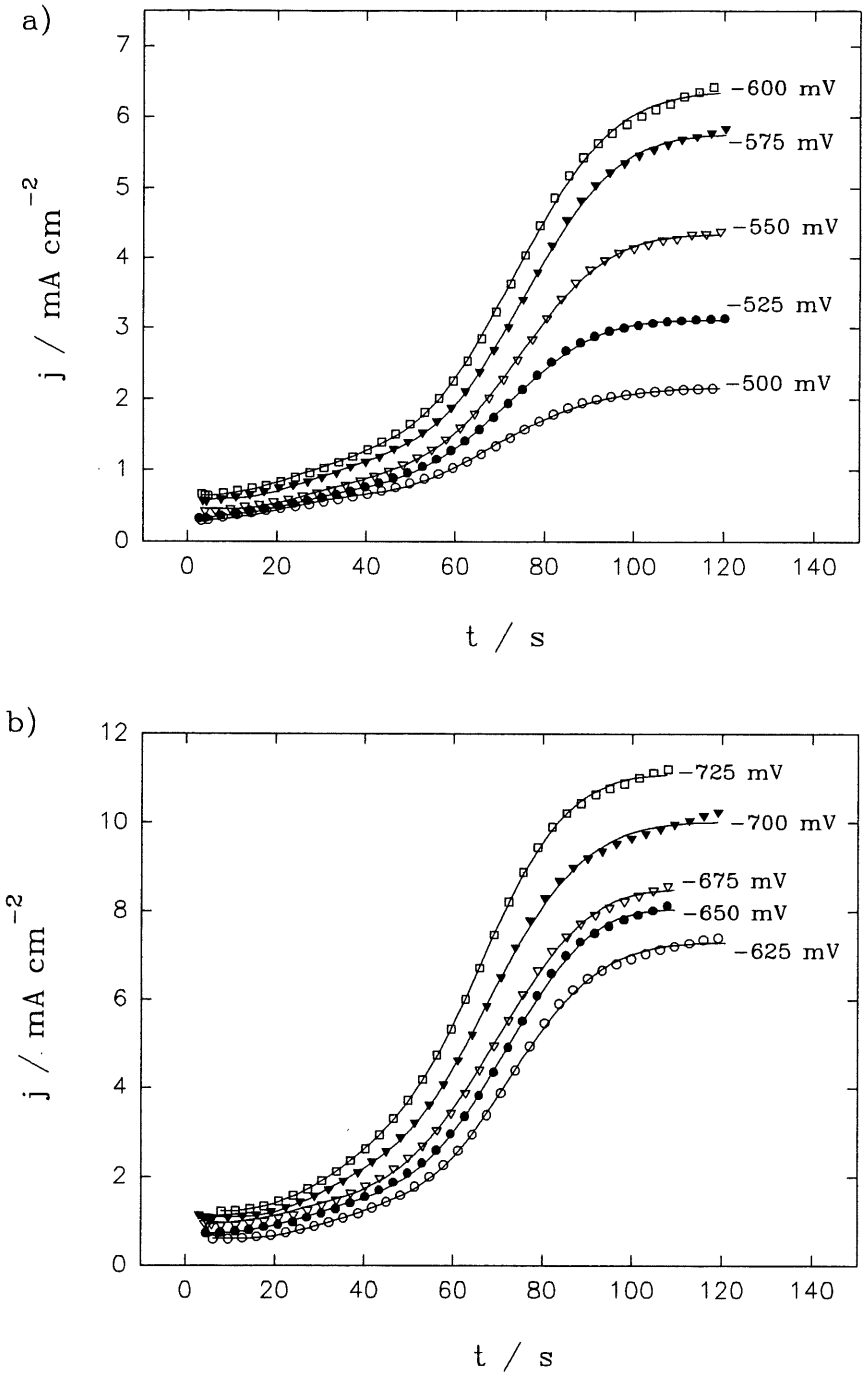

Figure 29. Initial portion of current-time transients shown in Fig. 26 for soft gold deposition on a gold RDE at potentials from -0.500 V to -0.725 V; points - experimental, solid lines - theoretical fit to eq. [6.3].

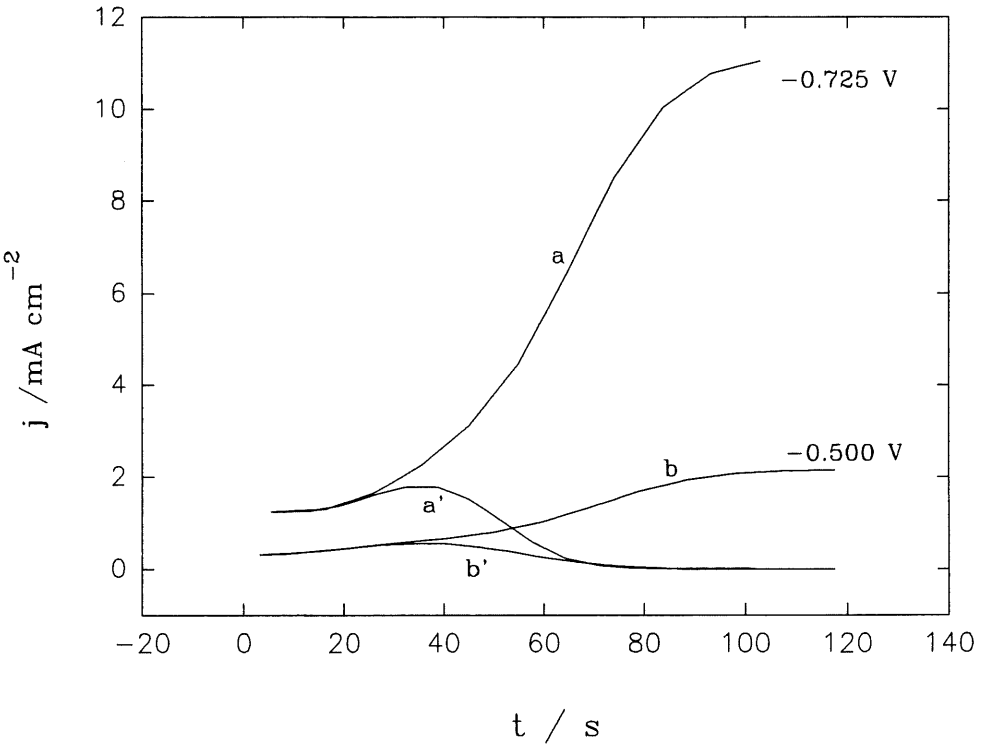

Figure 30. Simulated current-time transients according to eq. [6.3] for soft gold deposition on a gold RDE at -0.500 V (lines b and b') and -0.725 V (lines a and a'), total current (lines a and b), and the contribution of a two-dimensional growth process (lines a' and b'). The parameters used were determined experimentally:

lines b and b': $j_0 = 0.303\pm0.003$ mA cm^{-2}, $P_1 = 2.139\pm0.004$ mA cm^{-2};

$t_s = 20.5\pm2.9$ s, $P_2' = (7.37\pm0.92)\times10^{-6}$ s^{-3}, $P_3 = (4.25\pm0.12)\times10^{-4}$ mA cm^{-2} s^{-2},

$P_4 = (9.16\pm0.01)\times10^{-5}$ s^{-3};

lines a and a': $j_0 = 1.238\pm0.020$ mA cm^{-2}, $P_1 = 11.11\pm0.02$ mA cm^{-2},

$t_s = 18.7\pm1.3$ s, $P_2' = (2.088\pm0.057)\times10^{-6}$ s^{-3}, $P_3 = (2.11\pm0.10)\times10^{-3}$ mA cm^{-2} s^{-2},

$P_4 = (2.19\pm0.23)\times10^{-5}$ s^{-3}.

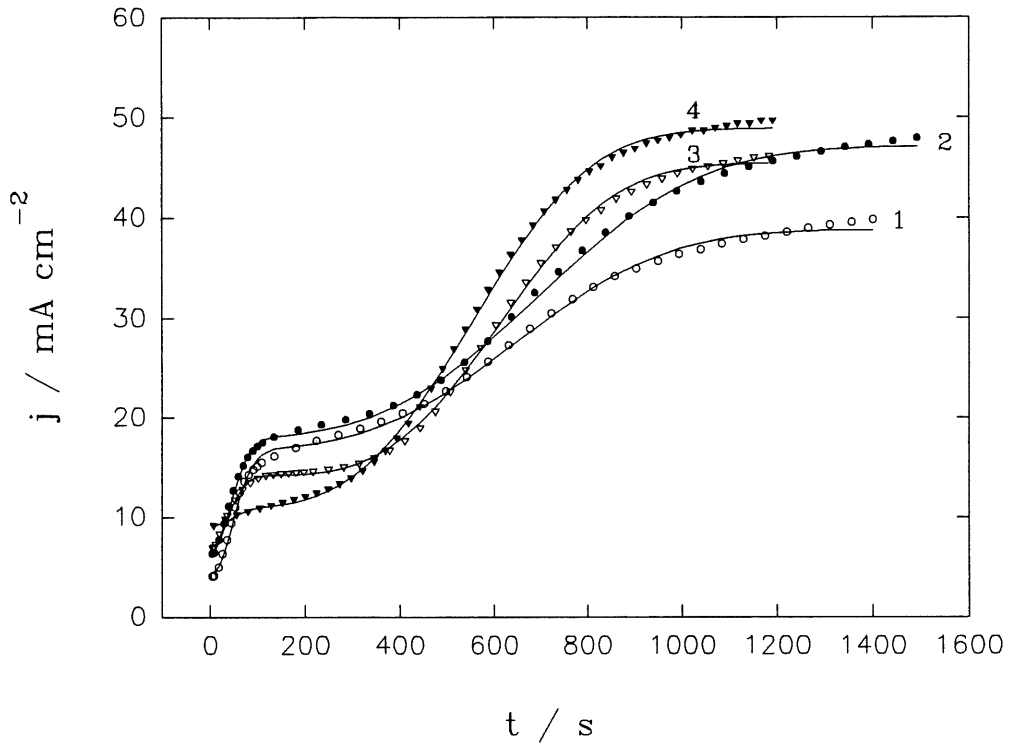

Figure 31. Current-time transients for soft gold deposition on a gold RDE in solution C at potentials between -0.900 V and -0.975 V; potential (V): 1) -0.900; 2) -0.935; 3) -0.950; 4) -0.975; points - experiment, solid line - theoretical fit to eqs. [6.4] and [6.5]. The parameters derived are:

1) E = -0.900 V: j_0 = 4.53±0.16 mA cm^{-2}, P_1 =16.84±0.35 mA cm^{-2}, P_2 = (2.84±0.12)×10^{-4} s^{-2}, P_s = 21.97±0.15 mA cm^{-2}, P_{2s} = (2.58±0.06)×10^{-9} s^{-3} t_s=100.5±6.5 s.

2) E = -0.935 V: j_0 = 6.37±0.20 mA cm^{-2}, P_1 =18.05±0.41 mA cm^{-2}, P_2 = (2.91±0.14)×10^{-5} s^{-2}, P_s = 29.05±0.22 mA cm^{-2}, P_{2s} = (2.10±0.12)×10^{-9} s^{-3}, t_s = 14.1±1.5 s.

3) E = -0.950 V: j_0 = 7.03±0.15 mA cm^{-2}, P_1 =14.24±0.32 mA cm^{-2}, P_2 = (3.83±0.28)×10^{-4} s^{-2}, P_s = 31.23±0.15 mA cm^{-2}, P_{2s} = (5.78±0.22)×10^{-9} s^{-3}, t_s = 125.7±6.3 s.

4) E = -0.975 V: j_0 = 9.16±0.21 mA cm^{-2}, P_1 =10.04±0.14 mA cm^{-2}, P_2 = (3.49±0.12)×10^{-4} s^{-2}, P_s = 37.89±0.18 mA cm^{-2}, P_{2s} = (5.19±0.17)×10^{-9} s^{-3}, t_s = 47.8±6.1 s.

of the vertical growth rate constant, k', on the potential for the first 3D growth process is shown in Fig. 33. A nonlinear dependence of log k' against potential was found. This rate constant increases as potential becomes more negative from -0.500 V to -0.935 V and then it decreases as potential changes from -0.935 to -0.975 V, indicating that crystal growth in the direction perpendicular to the substrate surface is inhibited, probably due to a self-inhibition process caused by the desorption of AuCN and the adsorption of CN^- species. The self-inhibition effect on crystal growth in gold deposition from phosphate electrolyte was also observed by Davidovic and Adzic (43). They suggested the adsorption of cyanide species or other impurities is the reason of such an effect. However, the vertical growth rate, k_s', for the secondary growth process at potentials -0.90 V to -0.975 V increases linearly with negative potential (Fig. 34), similar behavior was also reported in zinc deposition (158). The dependence of the combined rate constant, k^2A_{3D}, for the lateral growth of the first 3D growth process is shown in Fig. 35. Although the obtained points are somewhat scattered, it seems that potential applied does not have a big influence on this parameter. Supposing that the growth rates in two different directions are the same, the nucleation rate, A_{3D}, may be estimated. It decreases as potential becomes more negative, as shown in Fig. 36. This is in contrast to a classical thermodynamic (87-91) and an atomistic nucleation theories (92-96). Although the classical theory applies to large clusters only, and the atomistic theory to small ones, both predict an increase of the nucleation rate with the increase in overpotential. The obtained results imply that nucleation of gold in our experiments is inhibited, probably because active sites for nucleation are partially blocked by adsorbates. At potentials -0.9 to -0.975 V, the total number of nuclei for instantaneous nucleation for the first growth process is estimated to be 2.5×10^7 to 9.6×10^7 nuclei cm^{-2}, only slightly increasing with negative potential.

Generally, during metal deposition without inhibition, the dependence of both the initial minimum and the plateau current (recorded at longer times in chronoamperometric curves) against the applied potential displays a tafelian behavior (50,159,160). In our case,

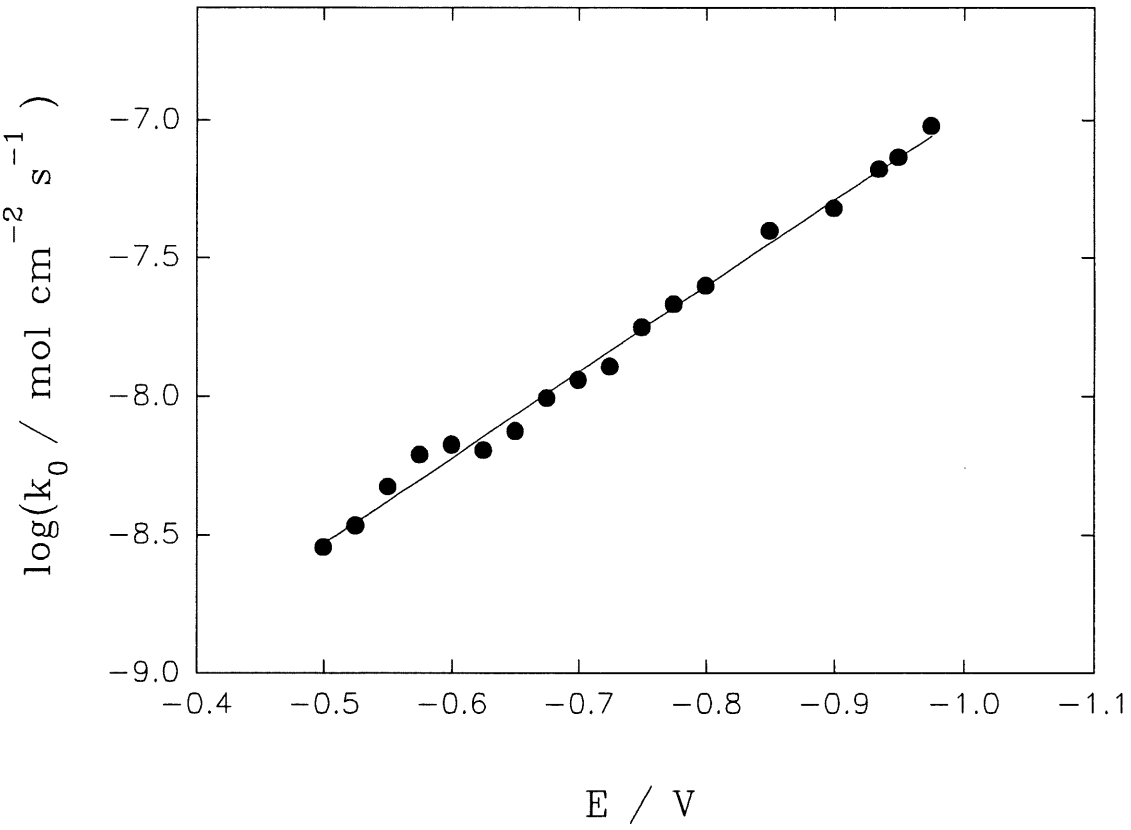

Figure 32. Plot of the logarithm of outward growth rate constant for substrate base plane, log k_0, determined from eqs. [6.1] and [6.3], against potential for soft gold deposition on a gold RDE from solution C.

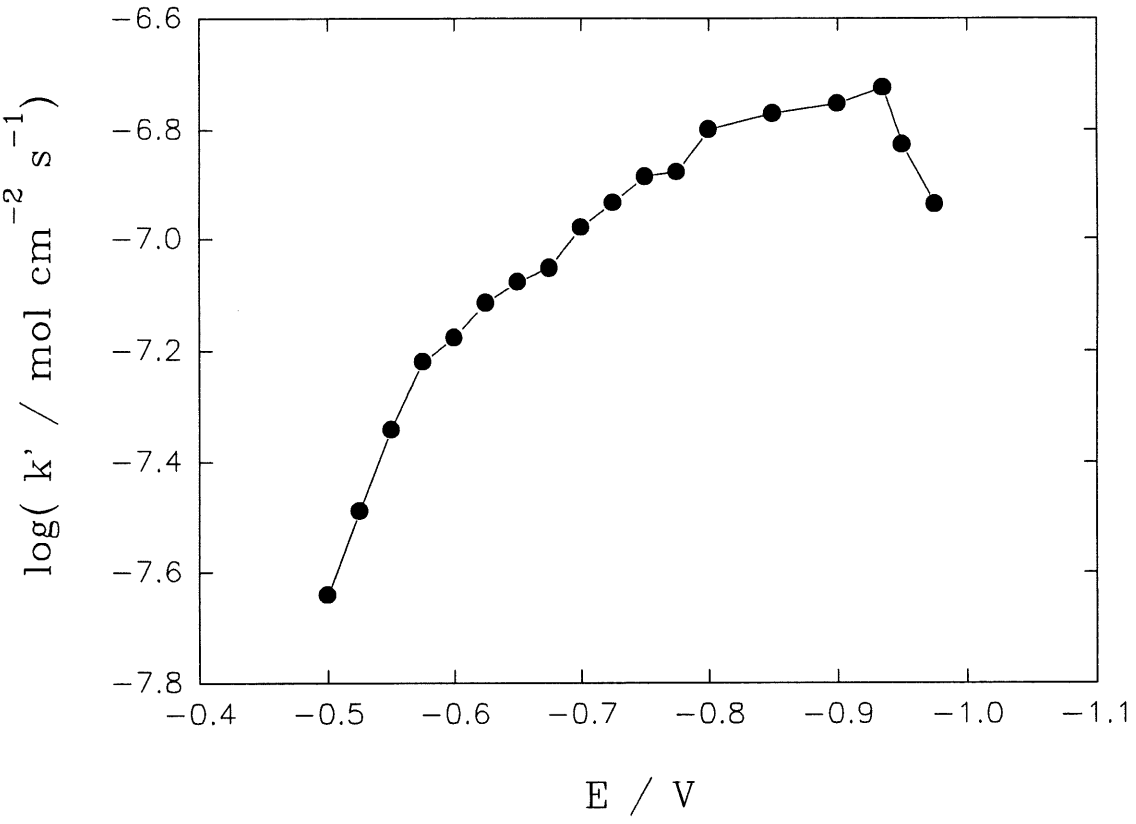

Figure 33. Plot of the logarithm of vertical growth rate constant, log *k'*, determined from eqs. [6.1] and [6.3], against potential for soft gold deposition on a gold RDE from solution C.

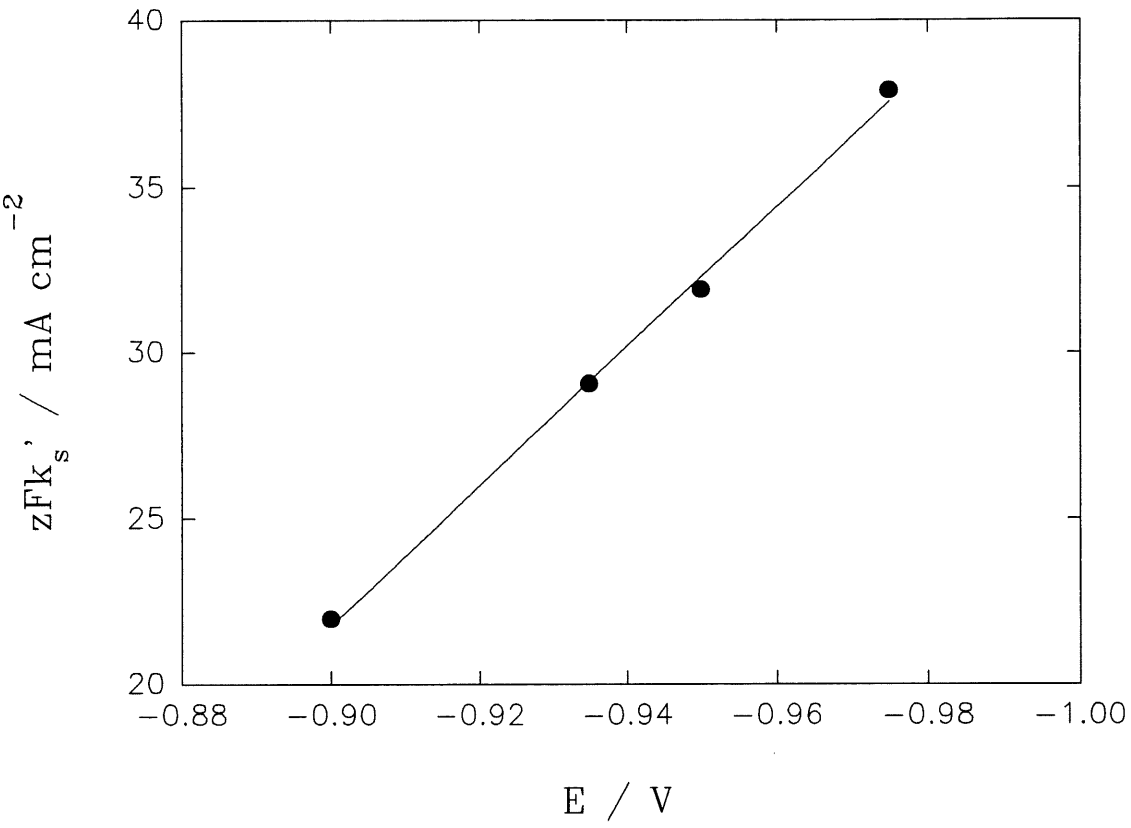

Figure 34. Plot of current for a secondary growth process, zFk_s, determined from eq. [6.5], against potential for soft gold deposition on Au RDE at potentials from -0.900 V to -0.975 V.

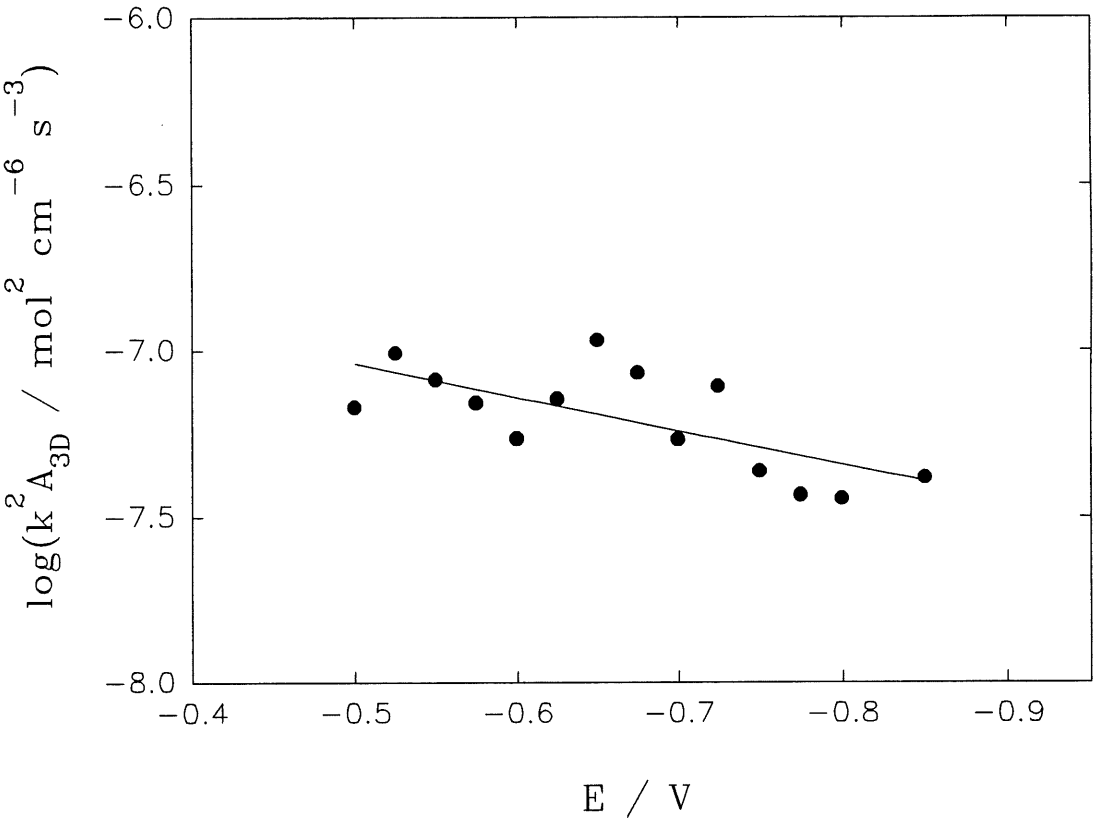

Figure 35. Plot of log k^2A_{3D}, determined from eqs. [6.1] and [6.3], against potential for soft gold deposition on a gold RDE from solution C.

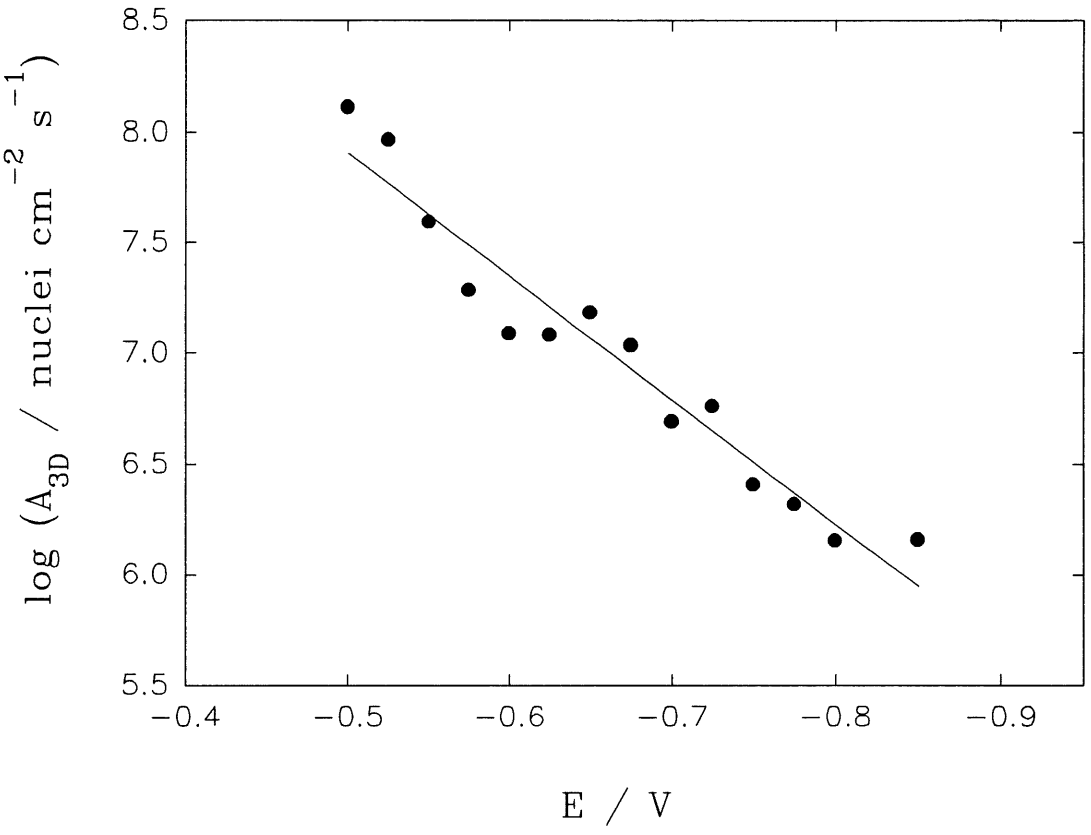

Figure 36. Plot of nucleation rate of soft gold on a gold RDE in solution C, A_{3D}, eqs. [6.1] and [6.3], *versus* potential assuming that the growth rate constants in vertical and lateral directions are equal.

only the dependence of the initial minimum current density shows such behavior, indicating that the growth of substrate's base plane is not inhibited, probably because at this time the concentration of cyanides generated on electrode surface is very low and their inhibition effect may be neglected. However, dependence of the plateau current density against potential does not show a simple tafelian behavior. The surface concentration of cyanides is higher at longer times and the vertical growth of 3D centres is thus retarded.

In above analysis nucleation and crystal growth mechanism varied with the applied potential. Similar procedures were used by Creus *et al.* (156) and Abyaneh *et al.* (157,158) in the analysis of various nucleation and crystal growth processes occurring simultaneously. It should be added that other 2D and 3D processes were also tried but the models presented above gave the best and statistically distinguished results. The current-time transients recorded at potentials more negative than -1.0 V could not be analyzed and they were largely influenced by the HER.

6. 4 Summary

The results presented above show that soft gold deposition from Renovel N bath proceeds *via* two different mechanisms. At the more positive potentials in the range from -0.50 V to -0.95 V, a higher Tafel slope of 0.328 V dec^{-1} was obtained, indicating that deposition reaction occurs *via* adsorption of AuCN followed by the charge-transfer step. At more negative potentials, a lower Tafel slope of 0.157 V dec^{-1} was obtained, corresponding to the mechanism of a direct charge-transfer together with the HER. These results are in excellent agreement with those obtained by chronopotentiometric measurements.

The finding of the inhibition phenomena, occurring in gold deposition at more positive potentials, shown in the previous chapter using LSV technique, was further confirmed by the analysis of experimental current-time transients.

The mechanisms of nucleation and crystal growth in the initial stages of gold electrocrystallization depends strongly on potentials applied. The 2D progressive nucleation and crystal growth of cylinders, and the 3D progressive nucleation and growth of right circular cones occur simultaneously at lower overpotentials. The contribution of 2D process decreases with negative potential and then becomes negligible. At potentials between -0.725 and -0.85 V, a simple model of 3D progressive nucleation and crystal growth of right-circular cones well describes the initial portion of experimental curves. Nucleation changes from progressive at potentials between -0.725 and -0.85 V to instantaneous at more negative potentials between -0.90 V and -0.975 V. A secondary 3D progressive nucleation and growth process was found to occur on the top of the first layers at potentials from -0.90 to -0.975 V. Kinetic parameters k_0, k', k, N_0 and A_{3D} were estimated. It was shown that vertical growth of crystals is inhibited. The dependence of the vertical growth rate constant on the applied potential showed a nonlinear dependence due to the inhibition process. Nucleation rate of soft gold deposition decreases with negative potential, in contrast to the nucleation theories, implying that nucleation process is also inhibited.

The dependence of growth rate for substrate's base plane on potential applied shows a linear tafelian dependence. The initial minima on the current-time transients correspond to the outward growth of substrate's base plane and may be used to construct Tafel plots in the case of metal electrocrystallization onto the same substrate.

CHAPTER 7
NUCLEATION AND CRYSTAL GROWTH IN HARD GOLD DEPOSITION

7.1 Introduction

The initial stages of soft gold deposition were studied using chronoamperometric technique in chapter 6. Kinetic parameters were obtained by analysis of current-time transients. In this chapter, the same technique as in the previous chapter is used to investigate the mechanism and kinetics of nucleation and crystal growth in hard gold deposition.

First, a partial inhibition model is derivated in section 7.2. The experimental results are given in section 7.3, the inhibition of crystal growth in gold deposition is further discussed, and a comparison between soft gold and hard gold is presented. The mechanism and kinetics of nucleation and crystal growth are analysed in section 7.4.

7.2 Development of the partial inhibition model

As reviewed in Chapter 2, several models concerning nucleation and crystal growth phenomena have been developed for different cases. For instance, hemispherical growth model (110,113,-115) may be used to explain the formation of a peak and a plateau on current-time transients, which are usually observed during electrocrystallization of nickel (161). The ratio of the peak to the plateau currents is expected to be 1.285 for instantaneous nucleation or 1.333 for progressive nucleation (110,113-115). It is worth to note that in some experiments, *e.g.*, copper deposition on Pd (162), silver deposition on vitreous carbon substrate (163), and gold deposition on Au (43), *etc.*, although a similar shape of current-time transients was observed the ratio of the peak to the plateau current was much higher than the values predicted by model. Hence, this model could not well explain such experimental

phenomena. It is well known that the crystal growth at later stages may be determined by overlapping of crystals and also other unknown nuclei death process. The latter factor results in the time-dependence of growth rate in particular direction, *e.g.*, due to an inhibition process. Although models dealing with inhibition in nucleation and growth process were attempted by various authors (108,118,124,125,127), they are far to be completed. Rangarajan and Bosco (127) considered various cases of vertical growth with inhibition, in which the vertical growth rate constant, k', was assumed to be time dependent, eq. [2.42], rewritten as:

$$k' = k_1 \exp(-\lambda t^n) \qquad [2.42]$$

Models considering time-dependence of growth rate constant, eq. [2.42], described in ref. 127 for $n = 1$, 2 and 3 predict that current increases with time to a maximum and then decreases to zero at longer times.

If the product adsorbed on the surface acts as an insulator, current should decrease to zero at longer times, when the surface of electrode becomes completely covered. This phenomenon was observed for anodic oxidation of Hg (108). However, for the case of partial surface coverage by an inhibitor, current would be expected to decrease and then reach a plateau. Therefore, in such a case, we propose a more general form of time-dependence of vertical growth rate constant as:

$$k' = k_1 \exp(-\lambda t^n) + k_2 \qquad [7.1]$$

where k_2 is a constant. The rate constant of vertical growth changes from $k_1 + k_2$ at $t = 0$ to k_2 at $t \rightarrow \infty$. Modified inhibition models may be derived using the method presented in ref. 127.

Assuming that $p(t)$ and $q(t)$ are growth rates in the lateral and vertical directions, respectively, and the number of nuclei is N (cm^{-2}), Bosco and Rangarajan (127) showed that the Avrami extended area without overlap at a height h and after time t is given as:

$$S_{X,h} = \pi \int_0^s d\tau \left(\frac{dN}{dt}\right)_\tau \left(\int_w^t p(u)du\right)^2 \qquad [7.2]$$

where τ is the time at which the centre nucleated, w the time at which the vertical growth attains the height h; variables s is a function of height h and time t, given as:

$$h = \int_s^t q(u)du = \int_\tau^w q(u)du \qquad [7.3]$$

The total volume of the deposit is:

$$V = \int_0^t q(s)[1 - \exp(-S_{X,h})]ds \qquad [7.4]$$

Differentiation of eq. [7.4] leads to calculation of the current:

$$j = \frac{zF\rho}{M}\frac{dV}{dt} \qquad [7.5]$$

In the derivation of the modified Bosco-Rangarajan inhibition model, an instantaneous nucleation is considered, *i.e.*, $\frac{dN}{dt} = N_0\,\delta(t)$, where $\delta(t)$ is the Dirac δ function. It is assumed that lateral growth velocity k (mol cm^{-2} s^{-1}) is constant and vertical growth velocity k' (mol cm^{-2} s^{-1}) is given by eq. [7.6]:

$$k' = k_1 \exp(-\lambda t) + k_2 \qquad [7.6]$$

The extended surface area $S_{X,h}$ becomes:

$$S_{X,h} = \pi\int_0^s d\tau N_0\delta(\tau)(\int_w^t \frac{Mk}{\rho}du)^2$$

$$= P_2(t-w)^2 \qquad [7.7]$$

where $P_2 = \frac{\pi M^2 k^2 N_0}{\rho^2}$. From eq. [7.4], the volume, V, equals:

$$V = \int_0^t \frac{M}{\rho}[k_1 \exp(-\lambda s) + k_2][1 - \exp(-P_2(t-w)^2)]ds \qquad [7.8]$$

Differentiation of eq. [7.3], taking t and τ as constants, leads to:

$$q(s)ds = q(w)dw \qquad [7.9]$$

and

$$ds = \frac{q(w)}{q(s)}dw = -\frac{k_1 \exp(-\lambda w) + k_2}{k_1 \exp(-\lambda s) + k_2}dw \qquad [7.10]$$

Therefore, eq. [7.8] becomes:

$$V = \int_0^t \frac{M}{\rho}[k_1 \exp(-\lambda w) + k_2][1 - \exp(-P_2(t-w)^2)]dw$$

$$= \frac{Mk_1}{\rho}\int_0^t \exp(-\lambda w)[1 - \exp(-P_2(t-w)^2)]dw$$

$$+ \frac{Mk_2}{\rho}\int_0^t [1 - \exp(-P_2(t-w)^2]dw \qquad [7.11]$$

The current density, eq. [7.5], equals:

$$j = zFk_1[\exp(-\lambda t) - \exp(-P_2 t^2) + \lambda \exp(-\lambda t)\int_0^t \exp(-P_2 u^2 + \lambda u)du]$$

$$+ zFk_2[1 - \exp(-P_2 t^2)] \qquad [7.12]$$

It should be noticed that current in eq. [7.12] consists of two terms, the first one is identical to eq. [2.42] derived by Rangarajan and Bossco (127), in which vertical growth rate was assumed to decrease with time to zero, and the second term actually is the current equation, eq. [2.21], derived by Armstrong *et al.* (108) for 3D instantaneous nucleation and growth of right-circular cones with vertical growth rate constant k_2 and lateral growth rate constant k. It should be mentioned that equations developed in ref. 108 for both instantaneous or progressive nucleation and growth of right-circular cones with constant growth rate in two directions can also be derived using the general model of Bosco and Rangarajan (127). The modified inhibition model, eq. [7.12], predicts that after nucleation current increases with time to a maximum and then decreases to a steady-state value ($j_{ss} = zFk_2$) at longer times. The ratio of the peak to the steady-state currents depends on various parameters of the process, as illustrated in Fig. 37. It is obvious that if k_1 or λ equals zero this model simplifies to 3D instantaneous nucleation and growth of right-circular cones (108), whereas when k_2 equals zero, it corresponds to the case of complete inhibition of vertical growth, eq. [2.44].

The model for the partial inhibition of vertical growth with $n = 2$ in eq. [7.1] may be similarly derived. It is assumed that vertical growth velocity is:

$$k' = k_1 \exp(-\lambda t^2) + k_2 \qquad [7.13]$$

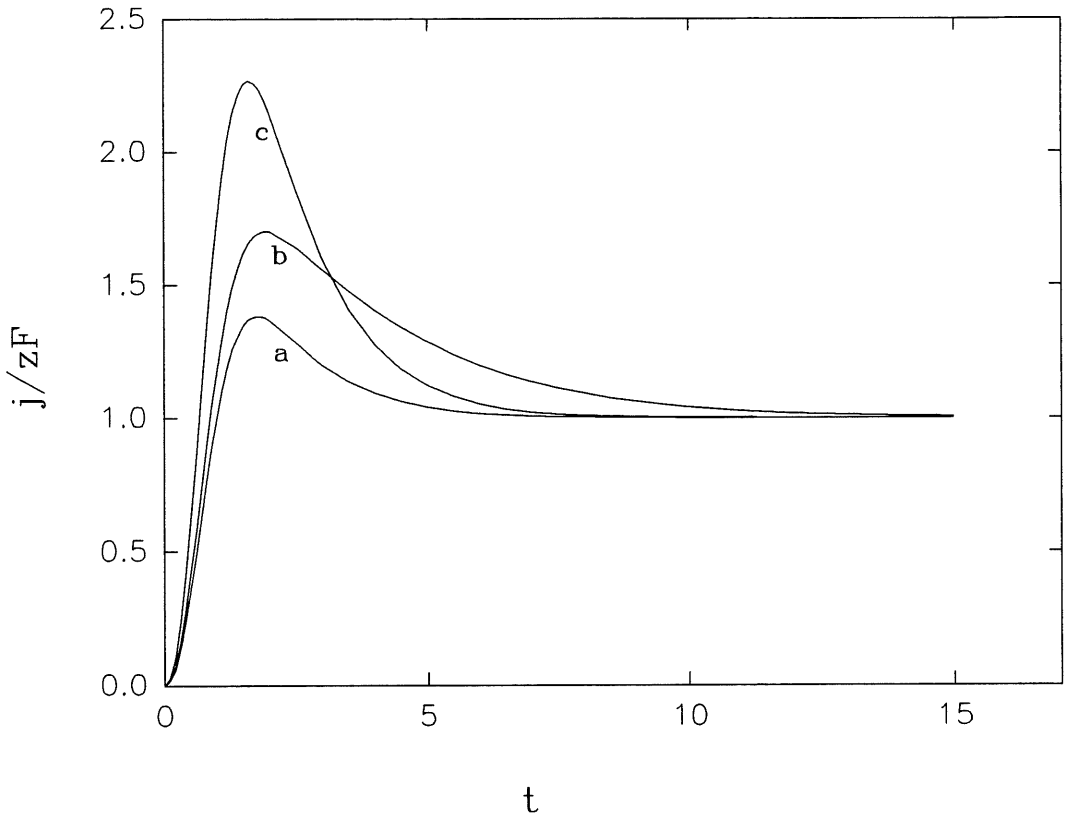

Figure 37. Simulated current-time transients according to eq. [7.12]; (a) $k_1 = k_2 = P_2 = \lambda = 1$; (b) $k_1 = k_2 = P_2 = 1$, $\lambda = 0.5$; (c) $k_2 = P_2 = \lambda = 1$, $k_1 = 3$.

For instantaneous nucleation, the extended area is:

$$S_{X,h} = \pi \int_0^s d\tau N_0 \delta(\tau) \left(\int_w^t \frac{Mk}{\rho} du \right)^2 = P_2 (t - w)^2 \qquad [7.14]$$

and volume is:

$$V = \frac{Mk_1}{\rho} \int_0^t \exp(-\lambda w^2)[1 - \exp(-P_2 (t - w)^2)] dw$$

$$+ \frac{Mk_2}{\rho} \int_0^t [1 - \exp(-P_2 (t - w)^2)] dw \qquad [7.15]$$

By differentiation of eq. [7.15], the current becomes:

$$j = 2zFk_1 P_2 \int (t - w) \exp(-\lambda w^2) \exp(-P_2 (t - w)^2) dw$$

$$+ zFk_2 [1 - \exp(-P_2 t^2)] \qquad [7.16]$$

Eq. [7.16] also consists of two terms. First term corresponds to the case in which vertical growth rate is defined by eq. [2.42] with $n = 2$. Notice that some parameters were missing in the equation given in ref. 127. Second term in eq. [7.16] corresponds to 3D instantaneous nucleation and growth of right-circular cones, as discussed above.

Other models for partial vertical growth inhibition based on eq. [7.1] may also be similarly derived. It may be shown that in all the cases of a partial inhibition of vertical growth, current would be expected to go through a maximum and then reach a steady-state value at longer times. However, the shape of the transients depends on the parameters in eq. [7.1].

7. 3 Results and discussion

Measurements under stationary conditions were not carried out because they led to relatively long transients, up to a few hours, recorded in first potential range. This observation indicates that the nucleation and growth processes were strongly inhibited. In order to decrease the influence of mass-transfer on the deposition, all chronoamperometric measurements were performed under the rotation rate of 4000 rpm.

Fig. 38 displays a typical set of current-time transients for hard gold deposition from solution D in a wide potential range. The shape of transients was different from that for soft gold deposition, especially at more negative potentials. It is clear that different shape of current transients indicates different nucleation and growth mechanisms. At more positive potentials (from -0.5 to -0.725 V), the behavior of current-time transient is somewhat similar to that of soft gold, *i.e.*, after the initial fast decrease, current increases with time due to nucleation and crystal growth, and then reaches a quasi-plateau. The quasi-plateau current increases with an increase in negative potential, reaches a maximum at -0.55 V and then decreases until potential of -0.70 V, which is probably caused by an inhibition process.

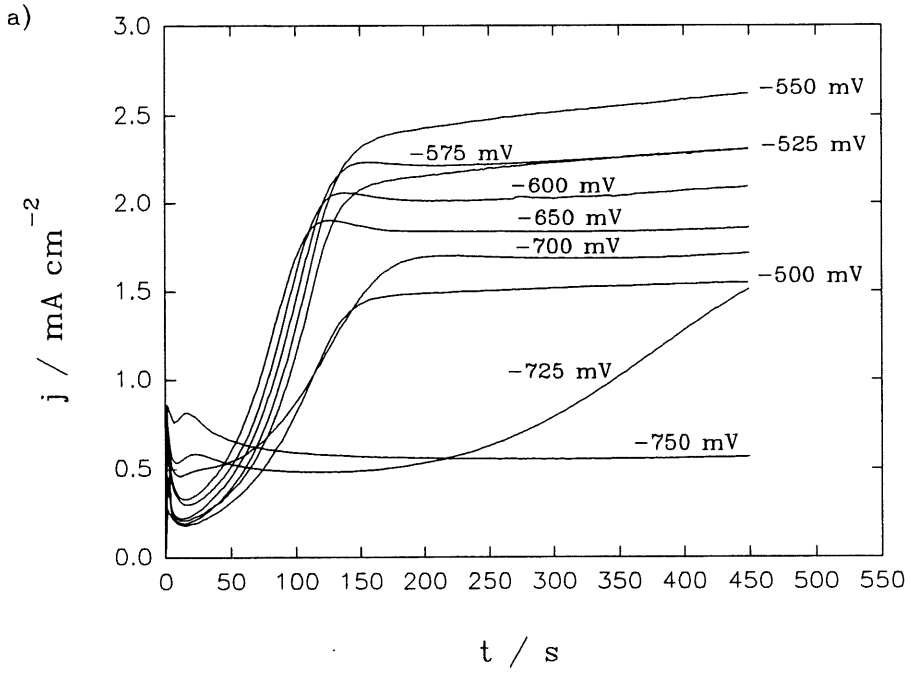

Figure 38a. Experimental current-time transients for hard gold deposition on a gold RDE at various potentials; rotation rate: 4000 rpm.

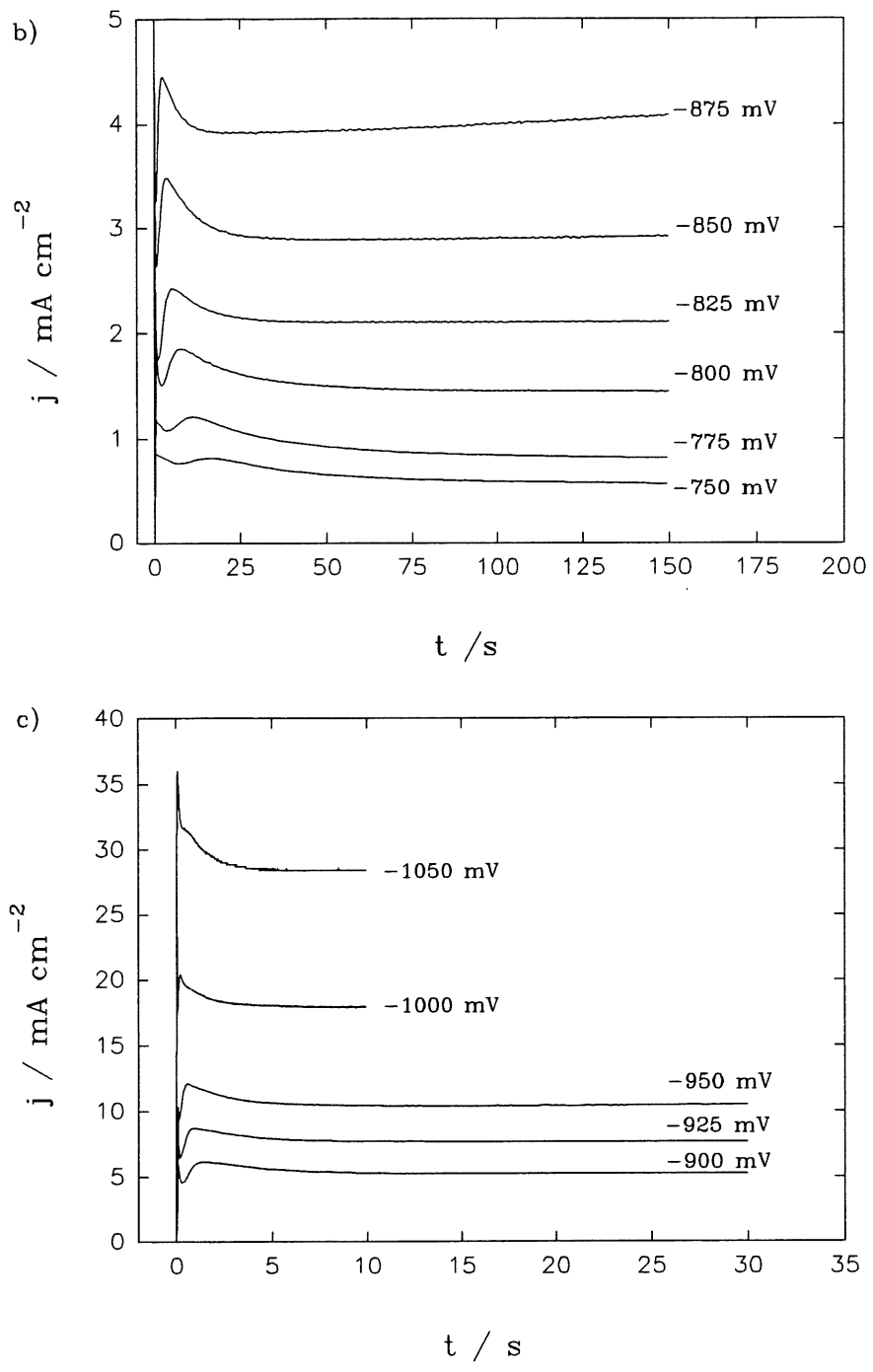

Figure 38(b, c). Experimental current-time transients for hard gold deposition on a gold RDE at various potentials; rotation rate: 4000 rpm.

Similar to soft gold deposition, the initial current minimum increases as potential becomes more negative. The fact that the current for hard gold deposition is much lower than that for soft gold indicates that crystal growth is inhibited by the presence of nickel. At more negative potentials between -0.725 V and -1.0 V, after the initial fall, current increases to a maximum and then decreases with time to a steady-state. Current values at minima, maxima and steady-state conditions in this potential range increase with negative potential, and Tafel plots based on these current values show similar slopes, Fig. 39. These current values also increase with the rotation rate (not shown here). It is most likely that such a shape of current transients is not determined by a mass transfer of gold cyanide because the observed current is much lower than the diffusion limited one predicted by the Levich equation.

As discussed in chapter 6, current recorded at longer times under potentiostatic conditions, in the case of electrocrystallization with an inhibition, could not be used to construct Tafel plots. However, the initial minimum current was suitable to be used for such a purpose. This was further confirmed for hard gold deposition. A Tafel plot based on the initial current minima is displayed in Fig. 39. It shows two linear regions with two different slopes of 0.47 V dec^{-1} in the range from -0.50 V to -0.75 V and 0.18 V dec^{-1} at potentials between -0.75 V and -1.1 V. These values are in good agreement with the results obtained by chronopotentiometric measurements, for which Tafel plots were based on the initial peak occurring on the potential-time transients, Fig. 19. It should be noticed that the Tafel slope for hard gold deposition is higher than that for soft gold. Such relatively high Tafel slope may correspond to the adsorption of an intermediate, especially at lower overpotentials.

Higher Tafel slopes for hard gold deposition may be related to the presence of nickel. Although nickel contents in deposits is only ~ 0.3 %, the nucleation and growth mechanism is modified by its presence. The growth of gold crystals may be inhibited because a part of active sites is occupied by nickel adatoms. This results in a decrease of gold crystal growth rate. Current efficiency of hard gold deposition on Pt RDE at longer times is about 50 - 75 %

(136). The HER may be preferred on growing crystals containing nickel. It is possible that both nickel adsorbate and H adatom influence the mechanism of nucleation and crystal growth, especially at more negative potentials.

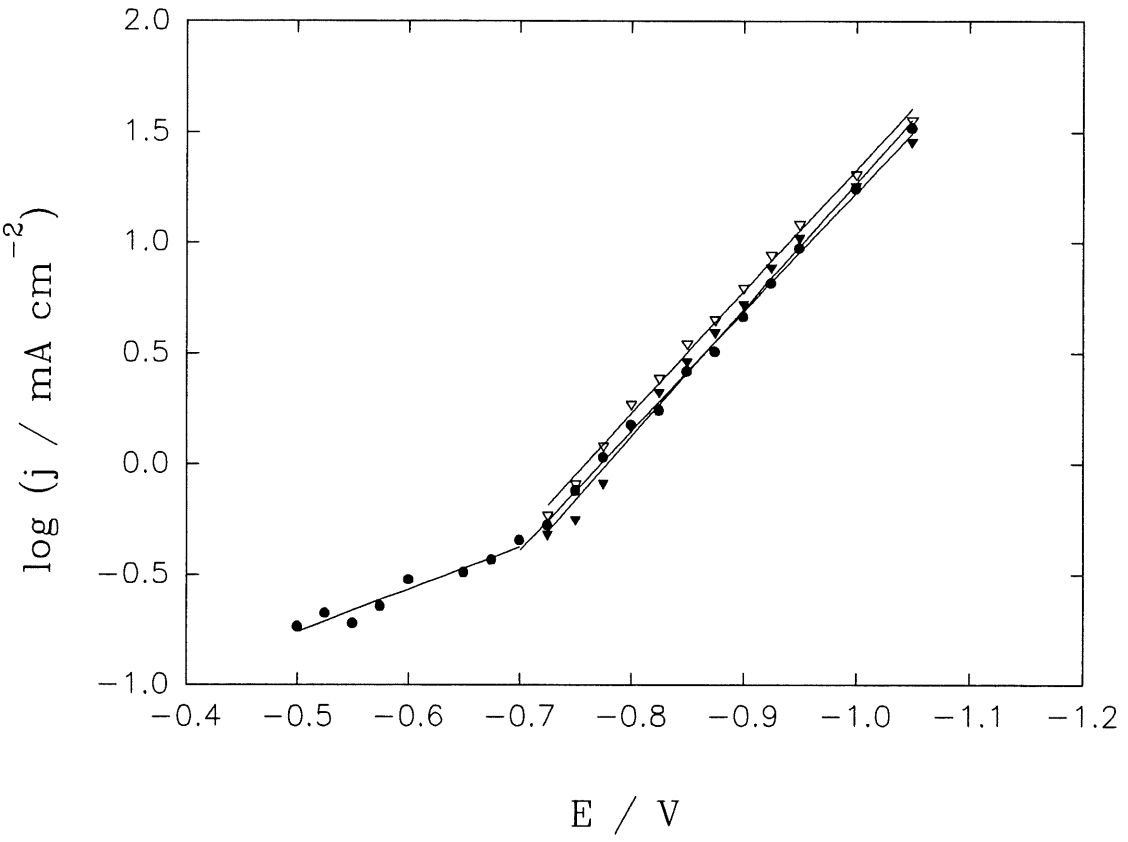

Figure 39. Tafel plots constructed on the basis of the initial minumum (•), maximum (∇) and steady-state current (▼), shown in Fig. 38, for hard gold deposition on a gold RDE.

7.4 Approximations of current-time transients: nucleation and crystal growth models

As illustrated in Fig. 38, two different shapes of current-time transients are observed for hard gold deposition, which corresponds to two distinct nucleation and crystal growth mechanisms. At potentials between -0.5 and -0.70 V, the plateau-like behaviour may result from the 3D nucleation and crystal growth of right-circular cones. To fit these transients, it was assumed that three dimensional nucleation is progressive, similarly as for soft gold deposition. Then, growth current consists of two parts, eq. [2.27] written as:

$$j = zFk_0 \exp(-\frac{\pi M^3 k^3 A_{3D}}{3\rho^3} t^3) + zFk'[1 - \exp(-\frac{\pi M^3 k^3 A_{3D}}{3\rho^3} t^3)] \qquad [2.27]$$

The first term in eq. [2.27] corresponds to the current for the growth of the substrate's base plane on a free surface area not covered by growing crystals, and the second one due to the growth of right-circular cones. Fig. 40 shows approximations of the experimental data by eq. [2.27], the fit is very good.

Kinetic information on crystal growth process may be estimated from the parameters derived. As discussed in chapter 6, zFk_0 in eq. [2.27] is interpreted as the initial current minimum on a current-time transient. Fig. 41 gives a linear Tafel dependence of log k_0 on potential. Hence, it is reasonable to construct a Tafel plot based on the initial minimum. The dependence of the vertical growth rate constant, k', on potential is shown in Fig. 42. It increases as potential changes from -0.50 V to -0.550 V, whereas it decreases with negative potential in the range of potentials from -0.550 to -0.70 V. This suggests that vertical growth of crystals is inhibited, in an agreement with the finding obtained for soft gold, where it was supposed that an inhibitor is produced on the electrode surface. Furthermore, the value of k' for hard gold is much smaller than that for soft gold. The combined rate constant, $k^2 A_{3D}$, initially increases and then decreases with negative potential, as shown in Fig. 43. Contrary to the dependence found for soft gold, the nucleation rate A_{3D} for hard gold deposition at more positive potentials,

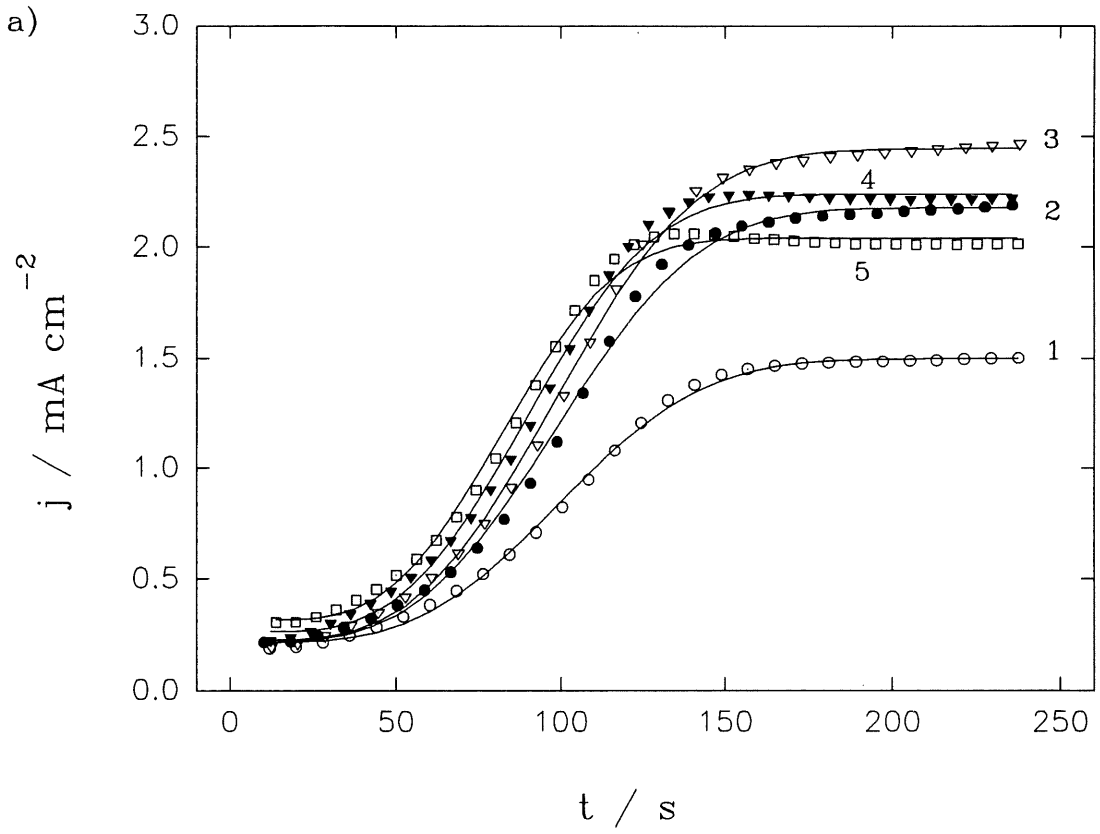

Figure 40a. Initial portion of current-time transients shown in Fig. 38 for hard gold deposition on a gold RDE at potentials between -0.50 V and -0.70V; points - experimental data; solid line - theoretical fit to eq. [2.27]; potentials (V): 1) -0.500; 2) -0.525; 3) -0.550; 4) -0.575; 5) -0.600.

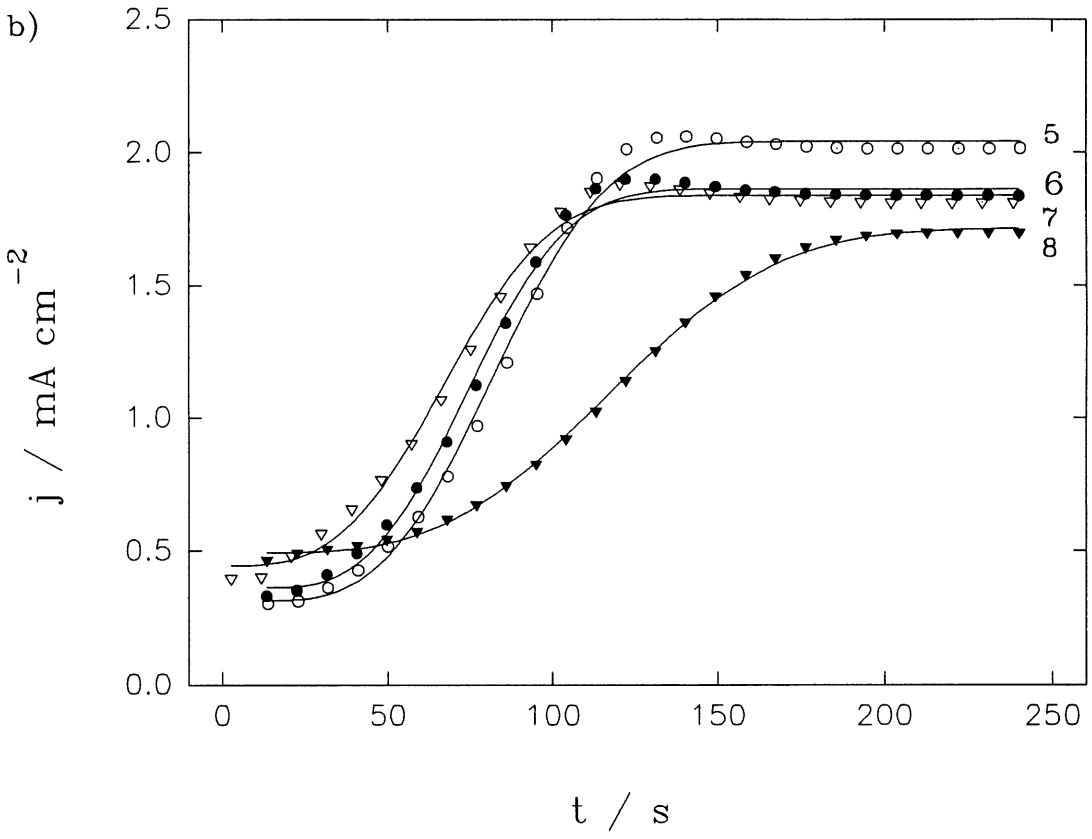

Figure 40b. Initial portion of current-time transients shown in Fig. 38 for hard gold deposition on a gold RDE at potentials between -0.50 V and -0.70V; points - experimental data; solid line - theoretical fit to eq. [2.27]; potentials (V): 5) -0.600; 6) -0.650; 7) -0.675; 8) -0.700.

between -0.525 and -0.675 V, seems to increase with negative potential applied, Fig. 44, provided that lateral and vertical growth rate constants are equal to each other. The plot of log A_{3D} against potential is a straight line, Fig. 44, in a good agreement with the prediction of the atomistic nucleation theory (92-96).

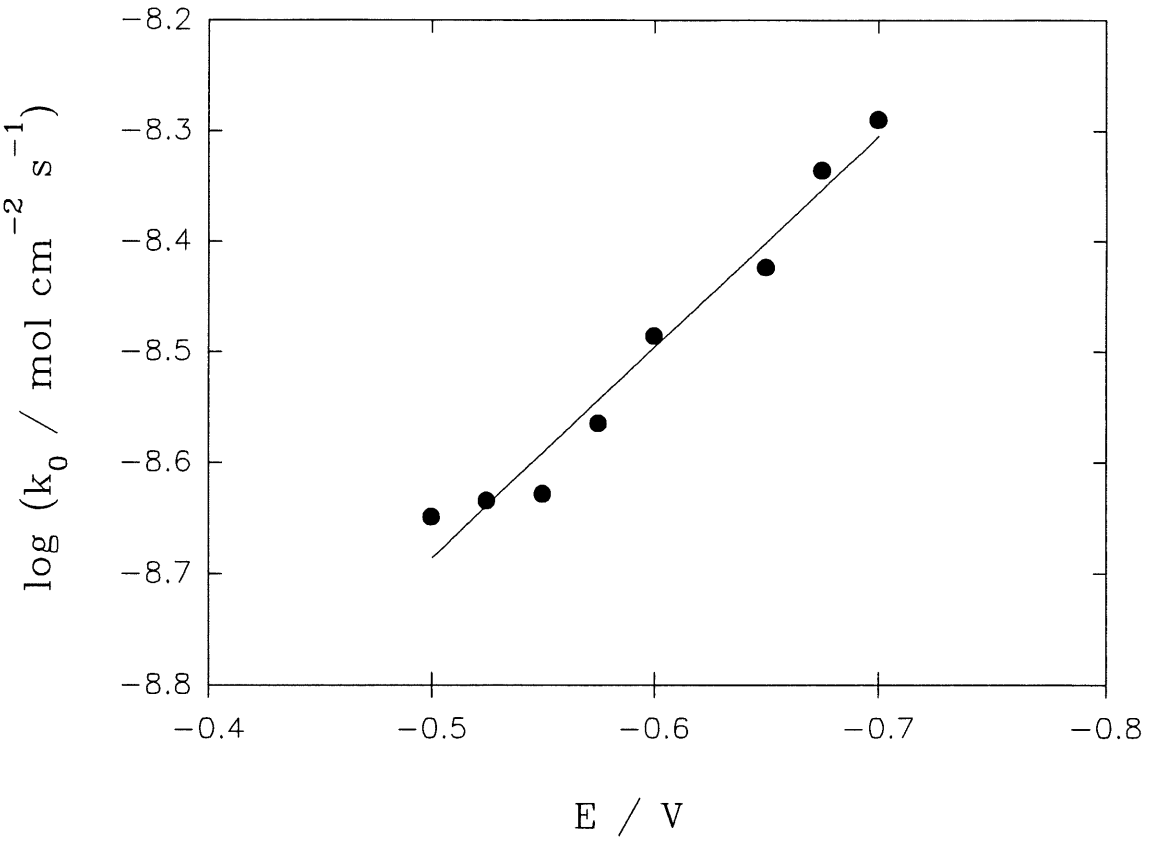

Figure 41. Plot of log k_0, determined from eq. [2.27], against potential applied for hard gold deposition on a gold RDE at potentials between -0.5 and -0.7 V.

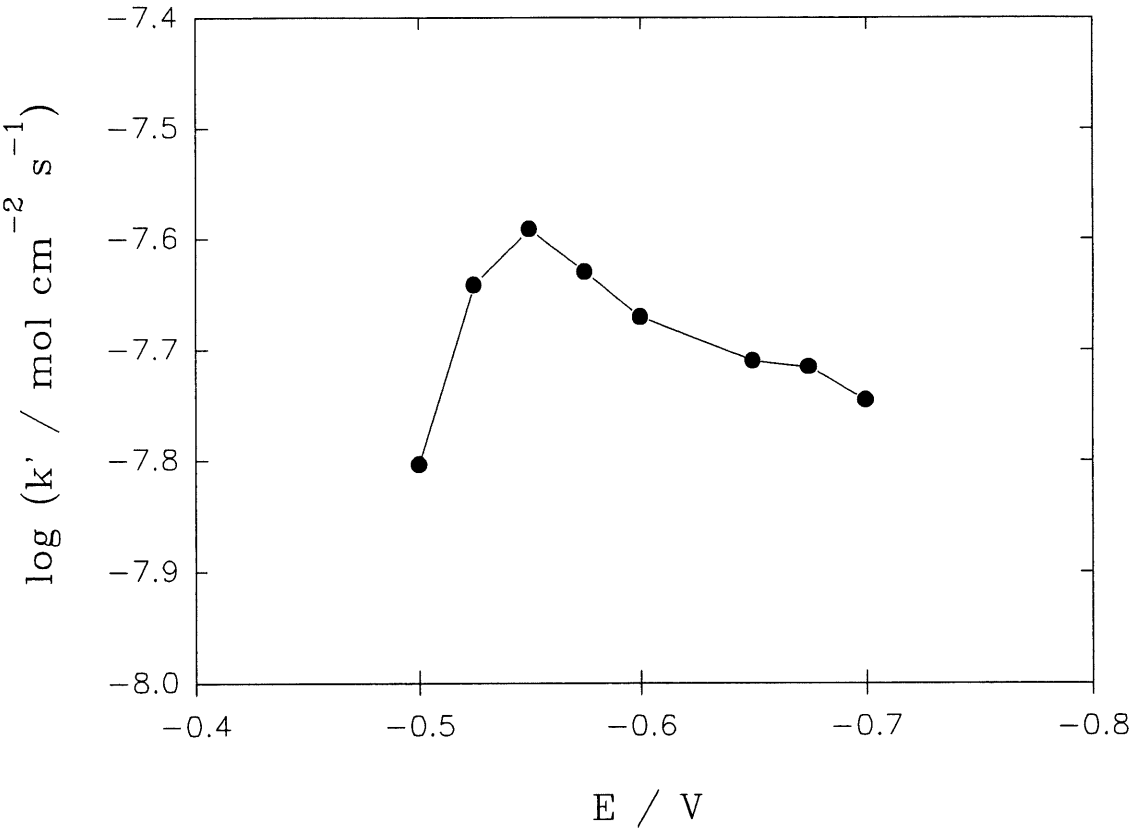

Figure 42. Plot of log k', eq. [2.27], against potential applied for hard gold deposition on a gold RDE at potentials between -0.5 and -0.7 V.

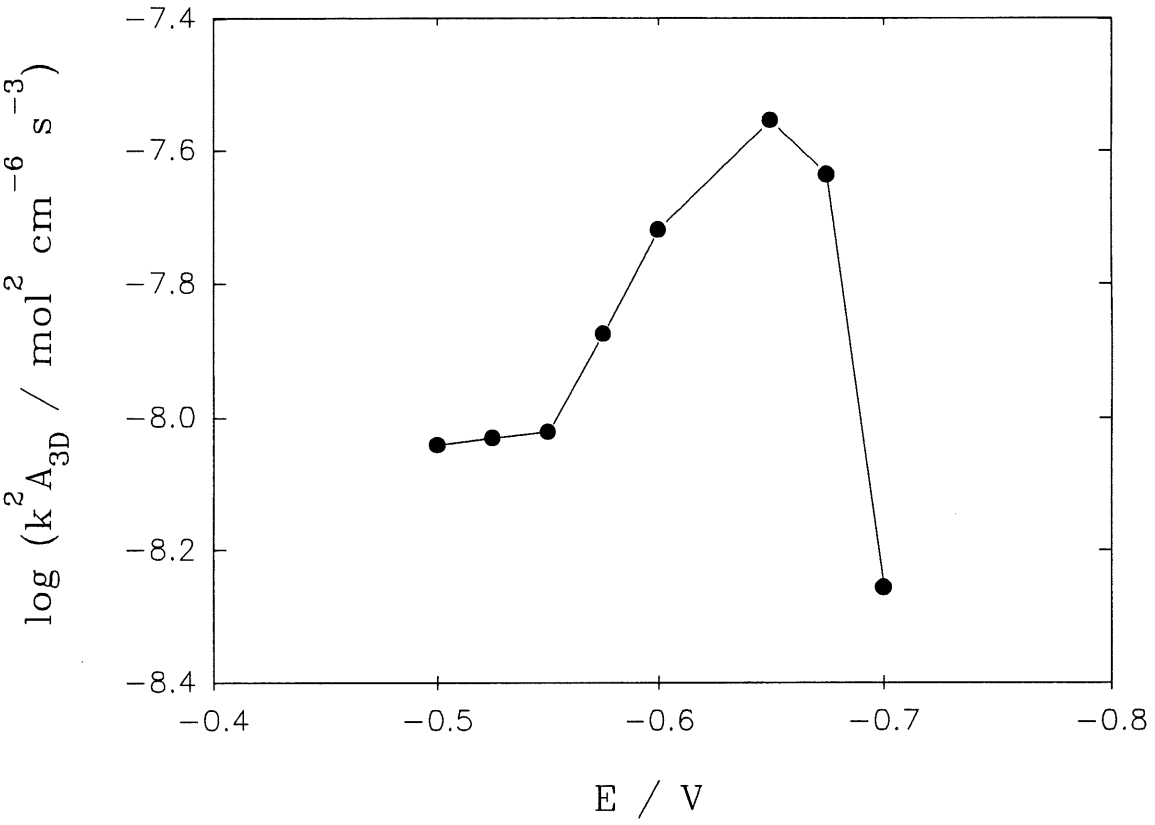

Figure 43. Plot of log $k^2 A_{3D}$,, eq. [2.27], against potential applied for hard gold deposition on a gold RDE at potentials between -0.5 and -0.7 V.

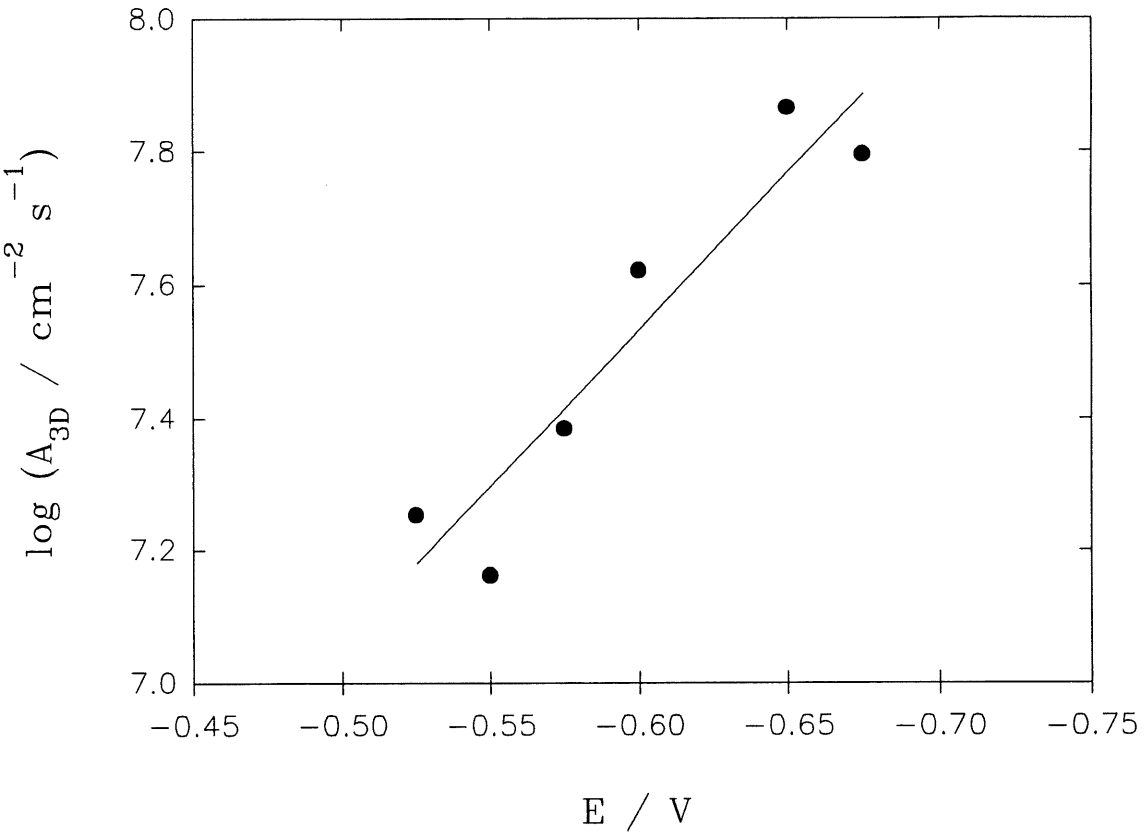

Figure 44. Plot of log A_{3D}, eqn. [2.27], assuming that growth rate constants in vertical and lateral directions are equal, against potential applied for hard gold deposition on a gold RDE at potentials between -0.5 and -0.7 V.

The nucleation and crystal growth process for hard gold deposition at potentials between -0.750 and -1.0 V is more complex. No simple model published in literature could describe the complete current-time transients recorded in this potential range. A few more complex models, *e.g.*, combined 2D and 3D nucleation/growth of right-circular cones, hemispherical or ellipsoidal growth (110,113-115), 3D nucleation and growth of right-circular cones with passivation (108), could not reproduce the correct shape of current-time transient. It should be noticed that after maxima, current decreases exponentially with time, and reaches a steady-state value at longer times, which is still potential dependent (see Fig. 38). An exponential decay of current with time following maxima was also assumed by Fleischmann *et al.* (116) to describe the death of crystal growth. Besides the effect of overlap of adjacent growing centres, the growth of centres at later stages of electrocrystallization could be largely determined by certain not yet known death processes (116,117). The adsorption of an inhibitor on the electrode surface would block the active sites available for nucleation and growth, and result in an abrupt cease of growth of nuclei (or death of nuclei). In order to describe the current-time transients recorded in potential range of -0.75 to -1.0 V, it was assumed that (a) 3D nucleation is instantaneous; (b) vertical growth velocity, k', decreases exponentially with time and reaches a constant at longer times, according to eq. [7.6]; (c) lateral growth rate constant, k, is time-independent; (d) to describe the initial minima recorded on current transients, outward growth of substrate's base plane was also taken into account. Therefore, the observed current consists of two parts, the first one due to outward growth of substrate's base plane and the second one due to instantaneous nucleation and 3D growth with a partial inhibition, eq. [7.12]. The obtained equation may be represented as:

$$j = P_0 \exp(-P_2 t^2)$$
$$+ P_1[\exp(-\lambda t) - \exp(-P_2 t^2) + \lambda \exp(-\lambda t)\int_0^t \exp(-P_2 u^2 + \lambda u)du]$$
$$+ P_3[1 - \exp(-P_2 t^2)] \qquad [7.17]$$

where $P_0 = zFk_0$, $P_1 = zFk_1$ and $P_3 = zFk_2$, other symbols have been defined previously. It is clear from eq. [7.17] that at $t = 0$, $j = zFk_0$ and as $t \rightarrow \infty$, $j = zFk_2$. Eq. [7.17] predicts that

current initially increases from a minimum to a maximum and, subsequently, decreases to a steady-state value at longer times. The minimum current may be smaller or larger than the steady-state one, depending on the magnitude of k_0 and k_2. This model can be used to explain both initial minima and final steady-state on current-time transients shown in Fig. 38.

Fig. 45 presents approximations of the experimental transients by eq. [7.17]. It is evident that experimental data are very well approximated by the proposed model. The parameters derived are displayed in Table 6. The dependence of the rate constants k_0 and k_2 on potential are illustrated in Fig. 46. Linear Tafel relationship were obtained for both constants with similar slopes. The results indicate that Tafel plots at potentials between -0.75 and -1.0 V

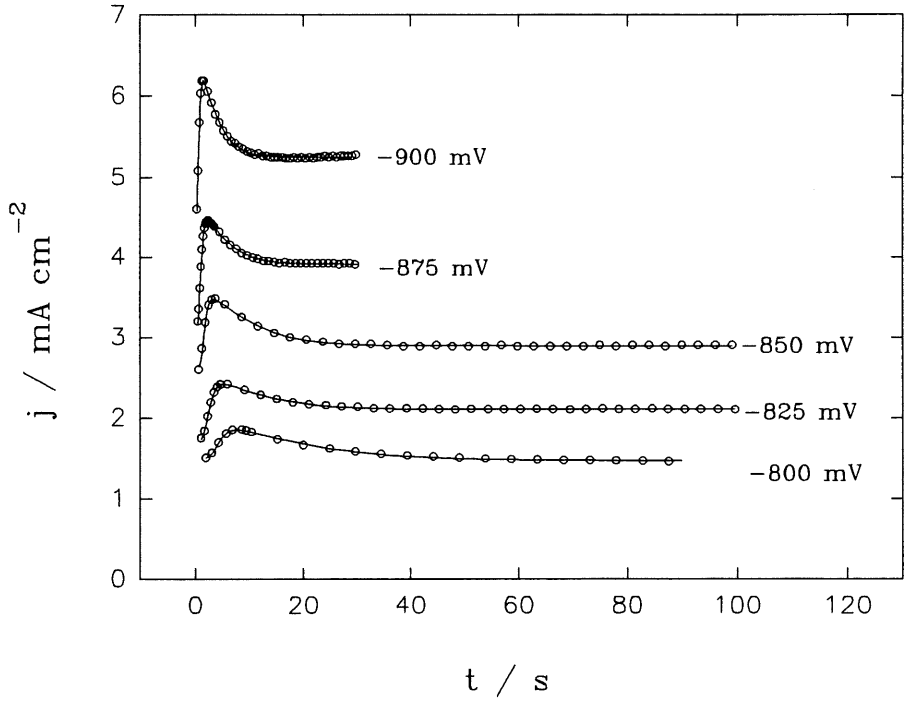

Figure 45. Theoretical fit of experimental transients to eq. [7.17] for hard gold deposition on a gold RDE from solution D at potentials more negative than -0.75V; points - experimental data; solid line - fitted. The parameters derived are shown in Table 6.

Table 6. Kinetic parameters of hard gold deposition on a gold RDE derived from the nonlinear least-squares fit of experimental j - t curves to eq. [7.17].

Potential (V)	P_0 (mA cm^{-2})	P_1 (mA cm^{-2})	P_2 (s^{-2})	λ (s^{-1})	P_3 (mA cm^{-2})
-0.750	0.685±0.016	0.303±0.006	0.011±0.001	0.048±0.001	0.571±0.001
-0.775	1.147±0.008	0.368±0.006	0.128±0.026	0.069±0.002	0.900±0.002
-0.800	1.506±0.002	0.438±0.003	0.123±0.003	0.097±0.001	1.467±0.002
-0.825	1.723±0.003	0.391±0.004	0.222±0.003	0.159±0.002	2.104±0.001
-0.850	2.635±0.007	0.652±0.006	0.683±0.012	0.190±0.003	2.893±0.002
-0.875	3.083±0.021	0.676±0.006	1.053±0.039	0.347±0.004	3.913±0.002
-0.900	4.506±0.027	1.098±0.019	2.811±0.137	0.486±0.004	5.253±0.002
-0.925	6.303±0.013	1.157±0.007	9.269±0.260	0.575±0.007	7.654±0.003
-0.950	9.377±0.029	1.710±0.012	23.47±1.18	0.806±0.008	10.44±0.004

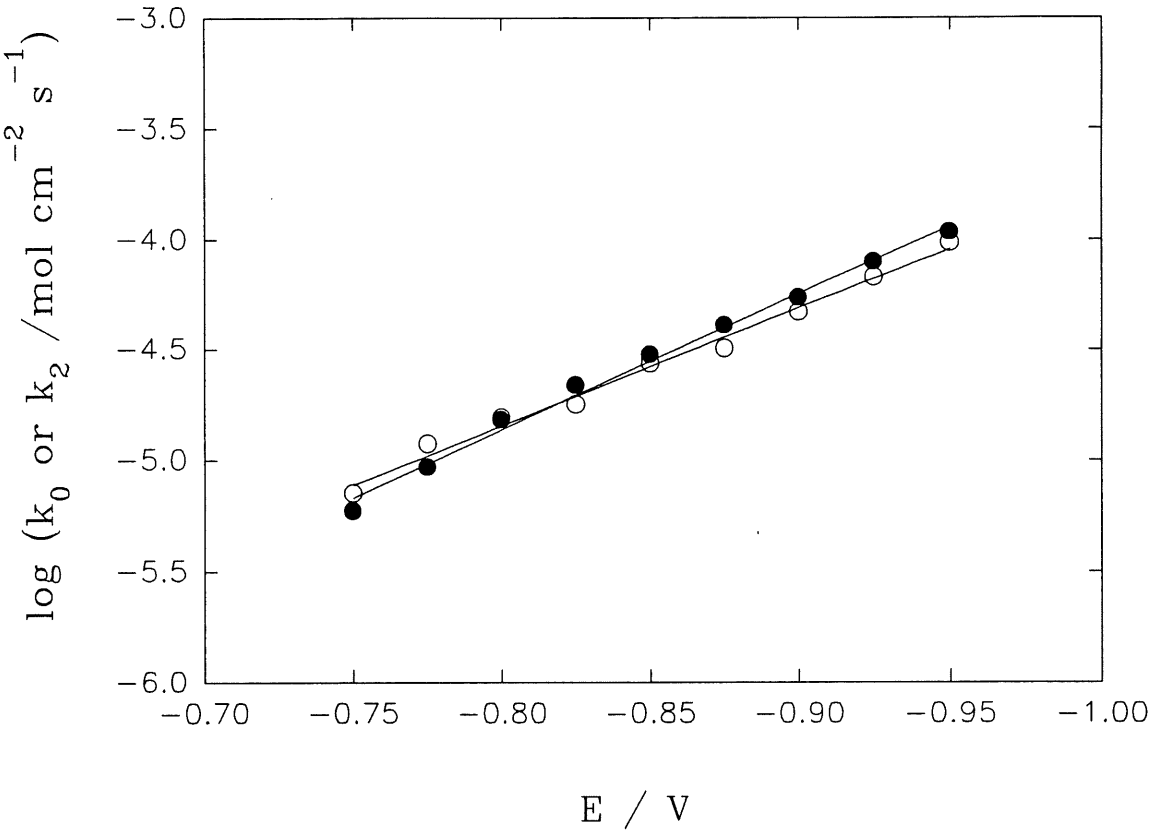

Figure 46. Dependence of k_0 (circle) and k_2 (full circle), determined from eq. [7.17], on potential applied for hard gold deposition on a gold RDE at potentials more negative than -0.750 V.

may be constructed using the initial minimum or steady-state current. Though the dependence of log k_1 on potential is also linear (Fig. 47), the slope of 0.26 V dec^{-1} is higher than that based on the initial current minimum. From Fig. 39, however, it can be seen that the Tafel slope based on the current maximum is the same as that based on the initial current minimum. This result indicates that the maximum is not only determined by the rate constant k_1 but also by other parameters. The dependence of the combined rate constant k^2N_0 on potential is given in Fig. 48. This parameter increases with negative potential. Since lateral growth rate constant, k, is unknown, N_0 cannot be estimated. The inhibition parameter λ increases with negative potential but its values are always smaller than 1 in our measurements, as shown in Fig. 49.

It should also be added that other effects like HER are ignored in eq. [7.17]. However, the HER is important at very negative potentials only. Its effect can be taken into account using an approach similar to that presented by Abyaneh and Fleischmann (157). In this case parameters P_0, P_1 and P_3 would be increased by a constant term including the rate constant of hydrogen evolution.

Although the experimental data are well described by eq. [7.17], the physical meaning of this model is still not clear. It is unknown what causes the exponential decrease of growth rate to a constant value. Apparently, this may be attributed to a partial surface coverage by an inhibitor. As the surface coverage by an inhibitor increases and reaches saturation, growth rate decreases with time to a constant value. There are some possibilities for the time dependent inhibition of vertical growth, *e.g.*, the adsorption of nickel and hydrogen. In the electrocrystallization of nickel, H_{ads} causes inhibition of nickel crystal growth (164,165) Intermediate $NiOH_{ads}$ is also claimed to inhibit the nickel deposition (165).

Another plausible explanation for such time-dependence of vertical growth is a simultaneous growth of two phases during the deposition. It is possible that the vertical growth rate for one growing phase decreases with time to zero and another is constant. During nickel

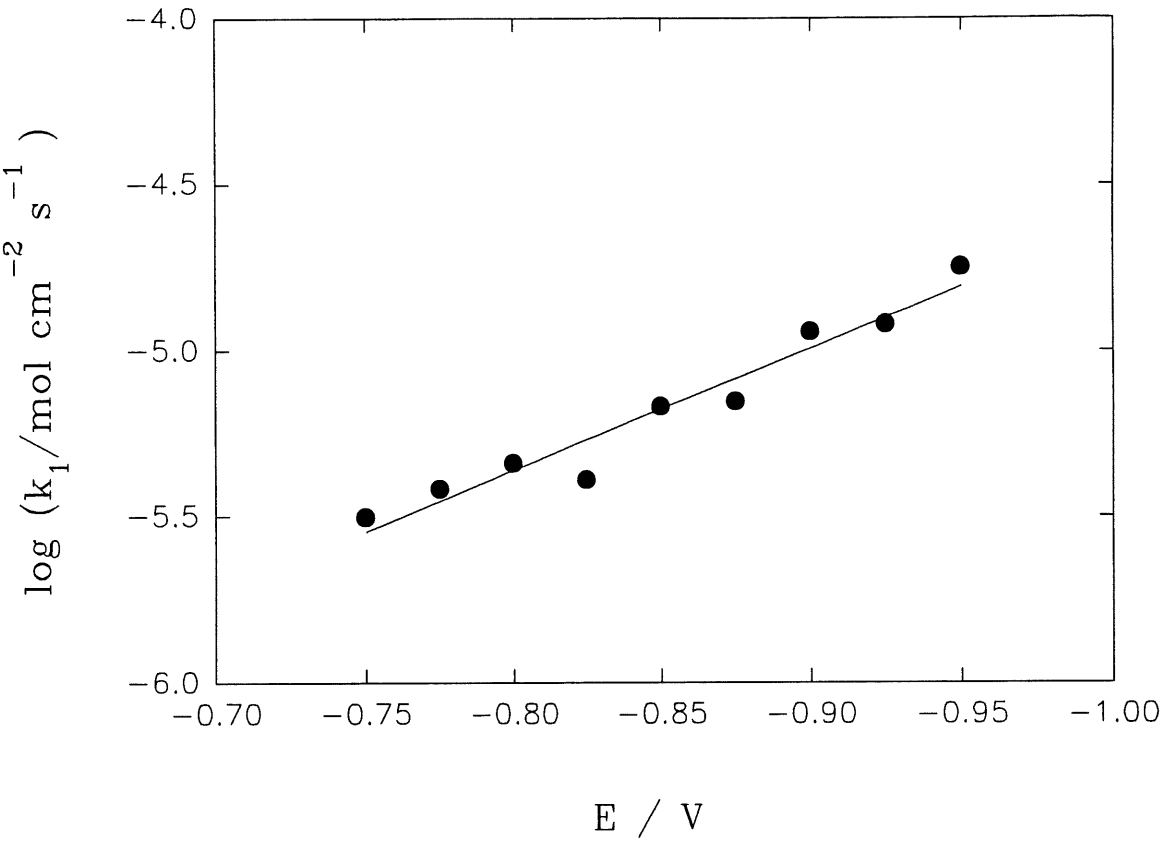

Figure 47. Dependence of k_1, eq. [7.17], on the applied potential for hard gold deposition on a gold RDE at potentials more negative than -0.75 V.

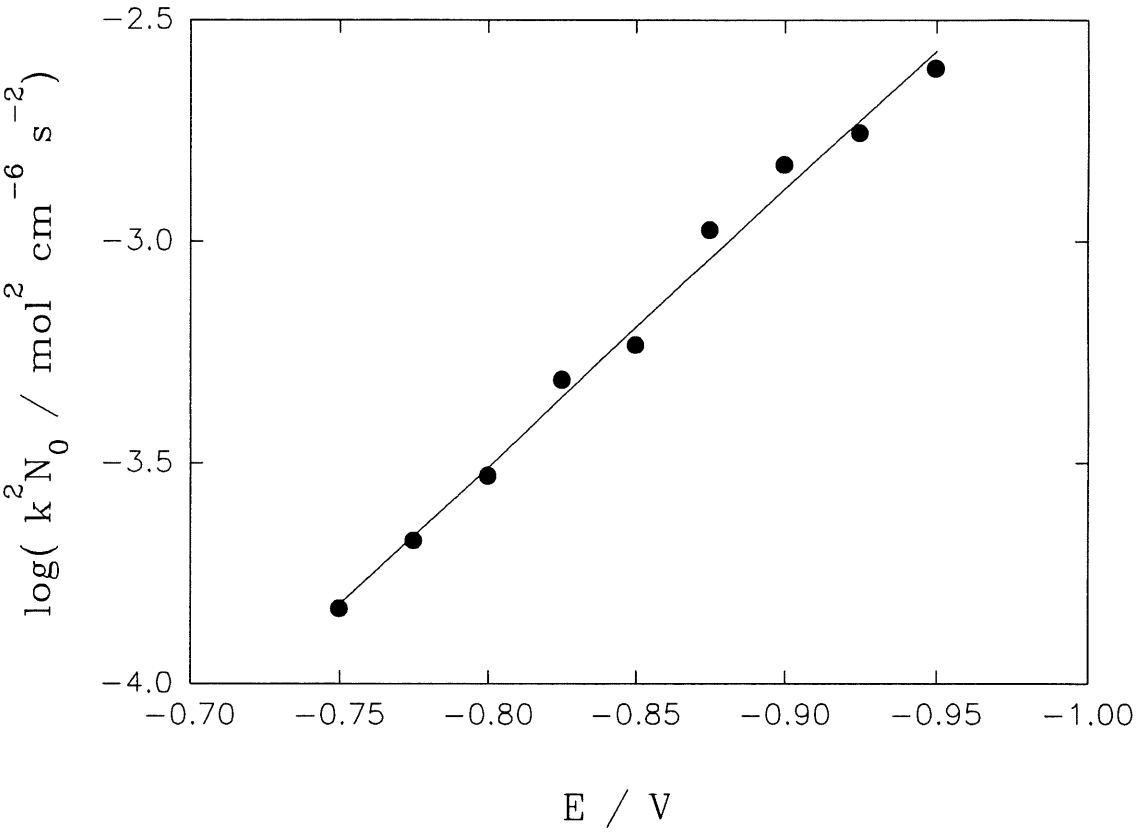

Figure 48. Dependence of log (k^2N_0), eq. [7.17], on the applied potential for hard gold deposition on a gold RDE at potentials more negative than -0.75 V.

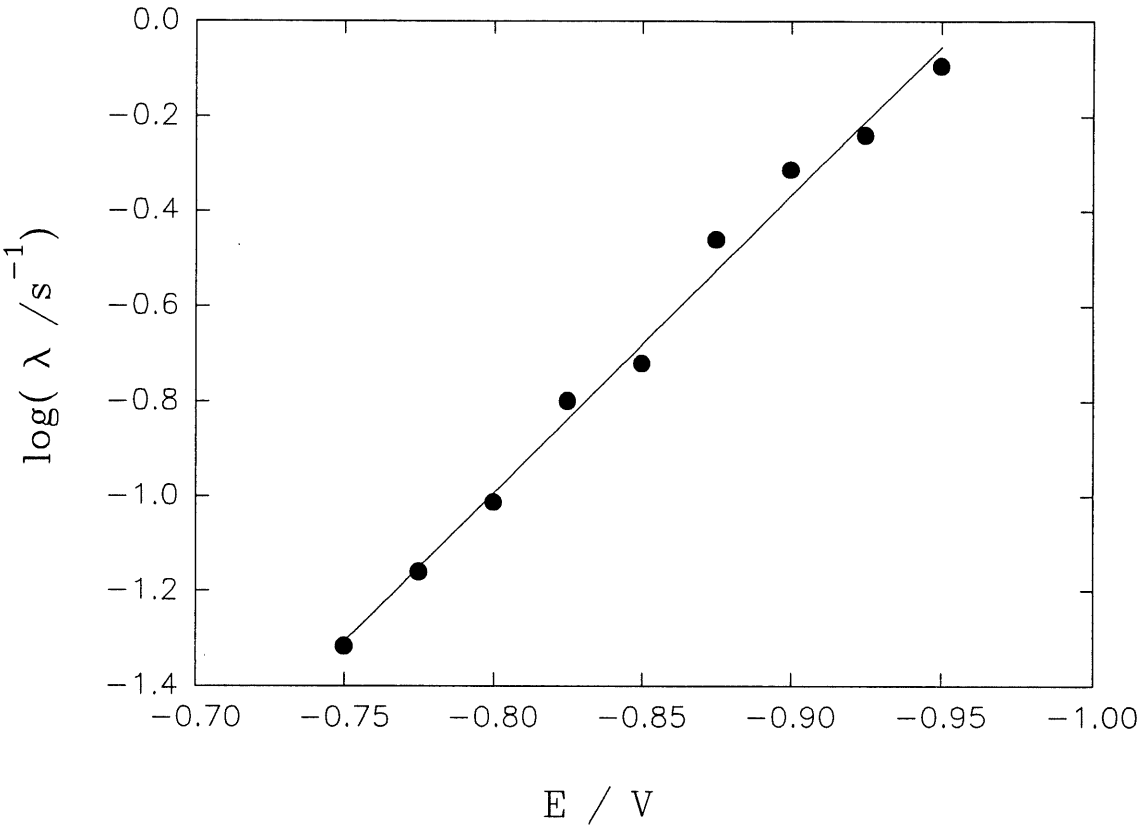

Figure 49. Dependence of log λ, eq. [7.17], on the applied potential for hard gold deposition on a gold RDE at potentials more negative than -0.750 V.

electrocrystallization, indeed, Fleischmann and Saraby-Reintjes (166) found that α-Ni, which is defined as a solid solution of hydrogen in nickel, was codeposited simultaneously with β-Ni phase, which is an interstitial hydrogen alloy of nickel with an atomic ratio H/Ni exceeding 0.6. In this case, the maximum on current-time transients was caused by the codeposition of β-Ni, whose growth rate was time-dependent. It is possible that two growing phases may be involved in the hard gold deposition. The maximum might be attributed to the one phase whose vertical growth rate is time-dependent, and the steady-state may be caused by another phase whose vertical growth rate is constant.

The results obtained lead us to conclude that two mechanisms are involved in both hard gold and soft gold deposition from Renovel N acid solutions. At more positive potentials, similar to the soft gold deposition, a self-inhibition process occurs in hard gold deposition. It is worth to notice that so-called self-inhibition phenomenon is a potential rather than time-dependent process, *i.e.*, in this potential range, the growth rate of 3D crystals is constant at each potential, however, the inhibition of vertical growth is observed with an increase in negative potential. Such inhibition phenomenon is probably connected with the potential-dependent desorption of AuCN which is obviously influenced by the production of CN^- or HCN species on the electrode surface, reactions [4.6] and [4.7], as well the adsorption of other unknown inhibitors. The largest difference between soft and hard gold deposition processes results from the deposition at more negative potentials. Due to the presence of nickel, current for hard gold is much lower than that for soft gold, indicating that crystal growth is retarded. A maximum-like behavior of current-time transient may be related to a nucleation and growth process with partial inhibition which might be caused by a time dependent partial coverage by an inhibitor or two different growing phases.

7. 5 Summary

The mechanism of hard gold deposition from Renovel N bath is similar to that for soft gold,

i.e., adsorption of AuCN followed by a charge-transfer step in a more positive potential range and a direct charge-transfer reaction mechanism at more negative potentials. Tafel slopes in these two regions are higher than those for soft gold.

A self-inhibition phenomenon, which was observed during soft gold deposition at more positive potentials, was further confirmed for hard gold by chronoamperometric experiments. A simple model of three-dimensional progressive nucleation and growth of right-circular cones was used to interpret the experimental current-time transients recorded in potential range of -0.50 V to -0.70 V. The parameters of k_0, k', k^2A_{3D} and A_{3D} were obtained. The growth rate constant for hard gold is much smaller than that for soft gold deposition, indicating that gold deposition process is slowed down by the presence of nickel. Nucleation rate A_{3D} increases with negative potential, contrary to that for soft gold deposition.

A modified Bosco-Rangarajan inhibition model was derived to explain the experimental current-time transients recorded at more negative potentials from -0.75 to -1.0 V. The nucleation and crystal growth mechanism of hard gold deposition in this potential range is well described by a model of three-dimensional instantaneous nucleation and crystal growth with time-dependent inhibition in vertical direction. Vertical growth rate was assumed to decrease exponentially with time to a constant value. The kinetic parameters of k_0, k_1, k_2, λ and k^2N_0 were determined.

CHAPTER 8
EFFECTS OF SUBSTRATES ON THE KINETICS OF GOLD DEPOSITION

8.1 Introduction

The nucleation and growth mechanisms in the initial stages of metal deposition are obviously influenced by the substrate's nature, relative to the interfacial energy between substrate and depositing film (167). In previous chapters, gold electrodeposition on Au substrate was studied with voltammetric, chronopotentiometric and chronoamperometric methods. The results obtained using Cu, Pt, Ni and glassy carbon RDEs are presented and discussed in the present chapter. The measurements were mainly carried out in hard gold bath. A comparison is made between Au and other substrates. A simple new model, *i.e.*, three-dimensional cylindrical growth, is developed in section 8.3, which may be used to describe the chronoamperometric curves recorded on glassy carbon substrate. In section 8.4, various nucleation and growth models are attempted to analyze the current-time transients obtained on different substrates.

8.2 Voltammetric studies

Fig. 50 illustrates a sets of linear sweep voltammograms (LSV) for hard gold deposition on various substrates at 650 rpm and sweep rate 1 mV s^{-1}. LSV curve for Au as a substrate is also shown in Fig. 50 for the purpose of comparison. It is found that the LSVs recorded on different substrates reveal some common features. All LSVs are characterized by a peak followed by a minimum at more positive potentials (between -0.4 and -0.8 V), and, subsequently, current increases quickly as potential is made more negative. The peak height and its position are different, depending on the nature of substrates used. It is evident that the peak observed on metallic substrates is more obvious than that on glassy carbon RDE, only a

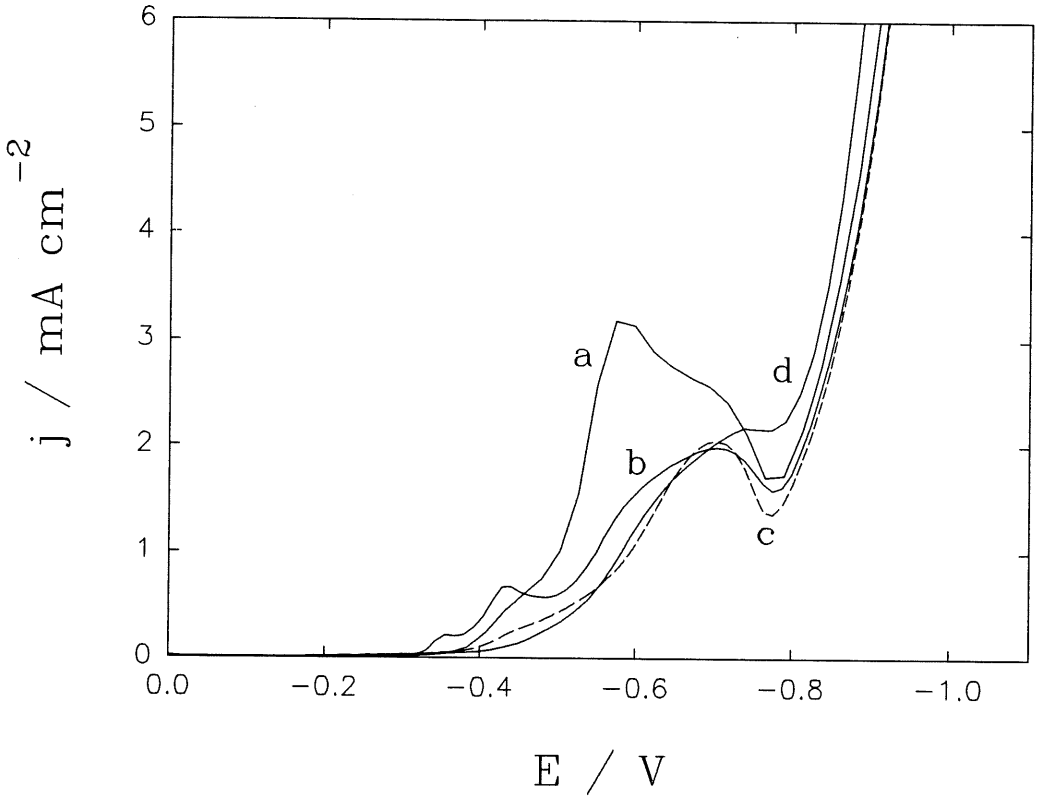

Figure 50. LSV curves of hard gold deposition on various substrates at 4000 rpm and 1 mV s^{-1}; substrates: a) Au; b) Cu; c) Ni; d) Glassy carbon.

a shoulder exists on LSV in the latter case. Figs. 51, 52 and 53 display typical sets of LSVs obtained on copper, nickel and glassy carbon RDEs at different rotation rate, respectively. Another important feature for all LSVs is that peak current increases with rotation rate. Similar finding was obtained with Au RDE. The peak height and its position are affected by the surface treatment of electrode, as observed using Ni RDE with various prechemical treatment (not shown). It is worth to note that the peak current of LSV curves on different substrates is much lower than the diffusion limiting one for $Au(CN)_2^-$ species, estimated by from the Levich equation. As discussed in chapter 4, such peak behavior of LSVs is neither relative to the diffusion control of $Au(CN)_2^-$ species nor to the HER. It was suggested that the reduction of adsorbed AuCN and the diffusion controlled mass transfer of HCN are responsible for the peak and its dependence of rotation rate.

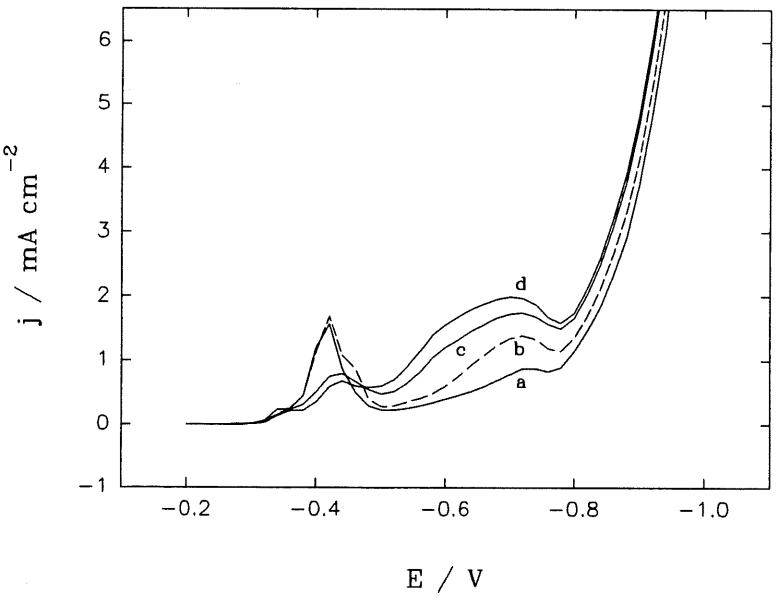

Figure 51 LSV curves of hard gold deposition on a Cu RDE at different rotation rates; sweep rate: 1 mV s^{-1}; rotation rates (rpm): a) 650; b) 1300; c) 2700; d) 4000.

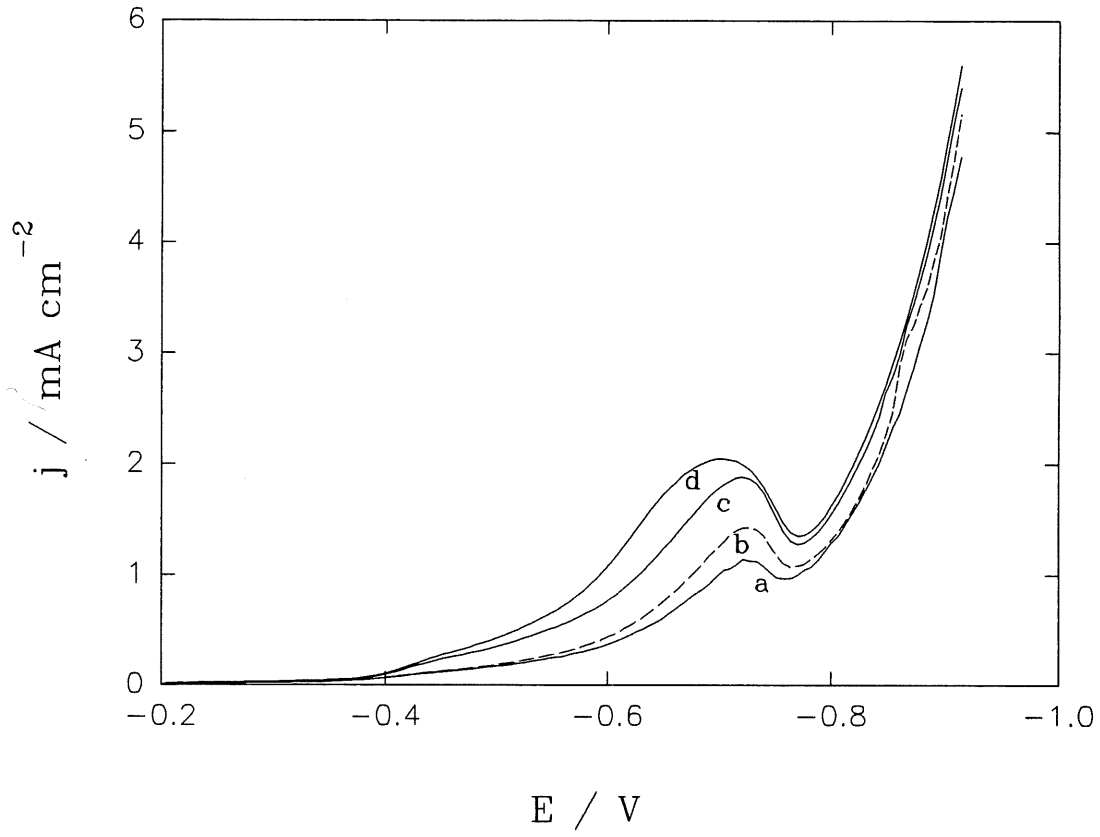

Figure 52. LSVs of hard gold deposition on a Ni RDE at different rotation rates; sweep rate: 1 mV s^{-1}; rotation rate (rpm): a) 650; b) 1300; c) 2700; d) 4000.

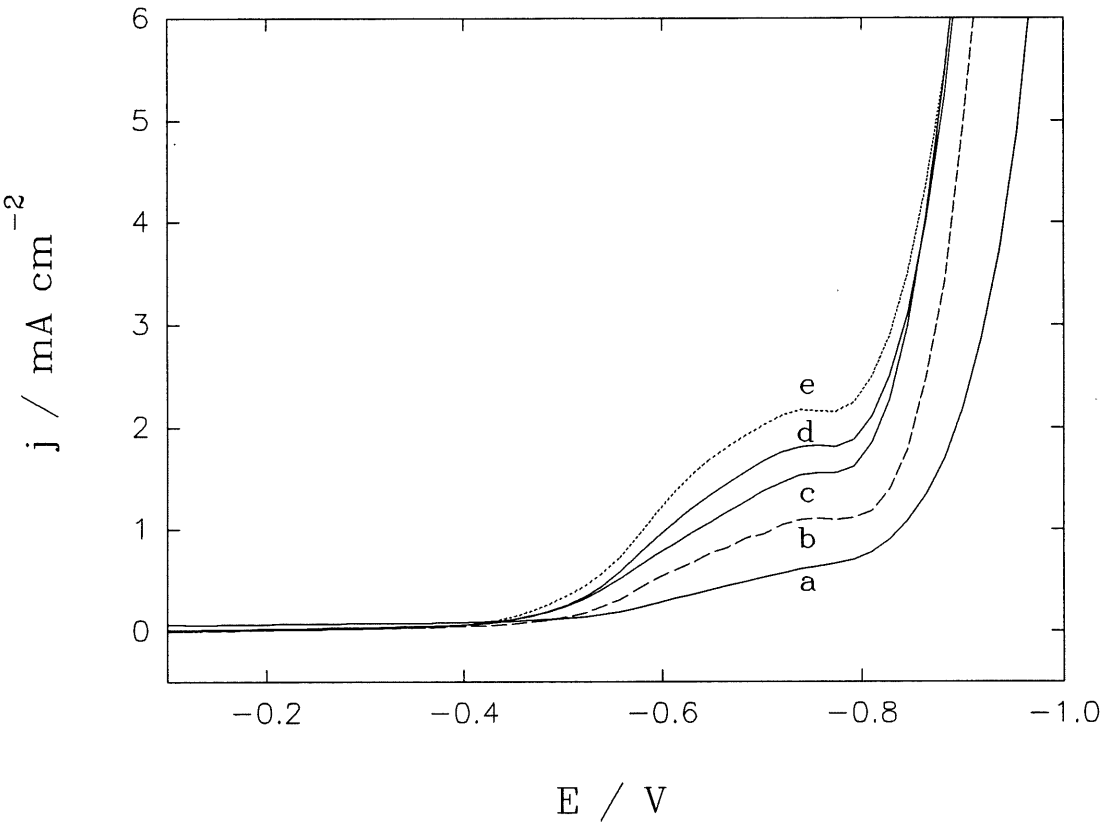

Figure 53. LSV curves of hard gold deposition on a glassy carbon RDE at different rotation rates; sweep rate: 1 mV s^{-1}; rotation rate (rpm): a) 200 b) 650; c) 1300; d) 2700; 5) 4000.

For all substrates, current recorded in the second potential range increases monotonously as the potential is made more negative. No diffusion limiting current plateau due to the HER is observed even at very negative potentials. The current of HER depends on the substrates used, and decreases in the order: Pt > Ni > Au > Cu > glassy carbon, as seen from the LSV curves recorded in the supporting electrolyte, Fig. 1, Fig. 54 and 55.

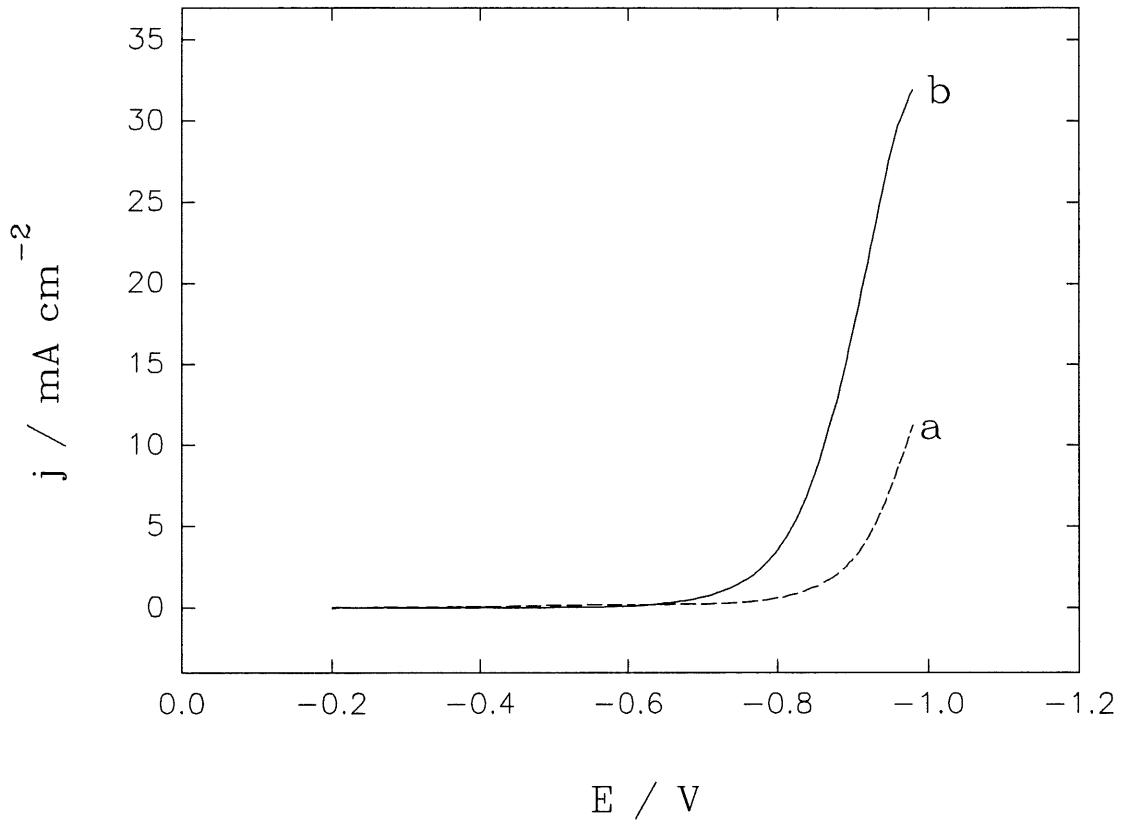

Figure 54 LSV curves recorded on copper (a) and nickel (b) in the supporting electrolyte (solution A); rotation rate: 650 rpm; sweep rate: 1 mV s^{-1}.

It is not clear yet what caused a peak (together with some small shoulders) appearing at potentials around -0.4 V for copper substrate, Fig. 51. Such a peak was not observed in the case of deposition on Au, Pt, Ni and glassy carbon substrates. Its peak height seems to decrease with an increase in rotation rate. Presumably, it may be caused by the reduction of trace oxide on Cu substrate, the adsorption of organic additive, gold cyanide, CN^- and/or HCN. In order to understand possible reasons, LSV measurements were undertaken in the supporting electrolyte with (solution A) and without (solution B) addition of nickel complex, and also in soft gold plating solution (without nickel complex). LSV curves taken in the supporting electrolytes in the absence and presence of nickel complex show a similar feature, *i.e.*, current increases as potential is made more negative than ~ -0.7 V due to the HER and no peak is observed, Fig. 55. These results suggest that the peak occurring at ~ -0.35 V on LSV

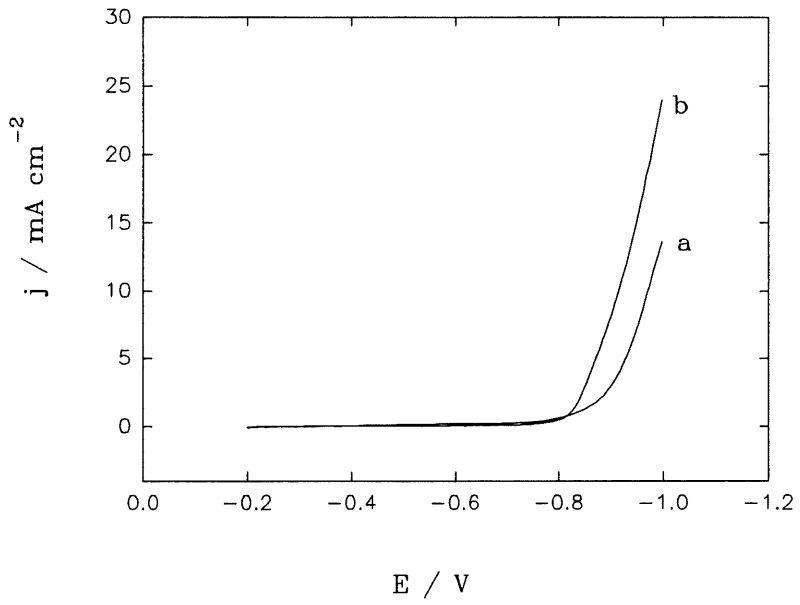

Figure 55. LSV curves on a Cu RDE in the supporting electrolyte (curve a) and the supporting electrolyte containing 0.0273 M Ni^{2+} (curve b); sweep rate: 1 mV s^{-1}; rotation rate: 650 rpm.

in hard gold solution (Fig. 51) is contributed neither by the reduction of trace oxide on Cu substrate, nor by the adsorption of organic additives in the supporting electrolyte or in the nickel complex. Fig. 56 illustrates LSVs on Cu RDE in soft gold solution, a small peak is also observed at about -0.25 V, and it is shifted in more positive direction in comparison with hard gold solution (Fig. 51). It is possible that such a small peak observed in soft and hard gold solutions is connected with the adsorption of gold cyanide or other cyanide species. The possibility of adsorption of CN^- species or CuCN as an origin of peak can be discarded because the LSV measurements performed in supporting electrolyte containing 0.01 M KCN do not show such a feature. Therefore, it is reasonable to assume that the adsorption of gold cyanide is an origin of the small peak appearing at ~ -0.25 to -0.4 V.

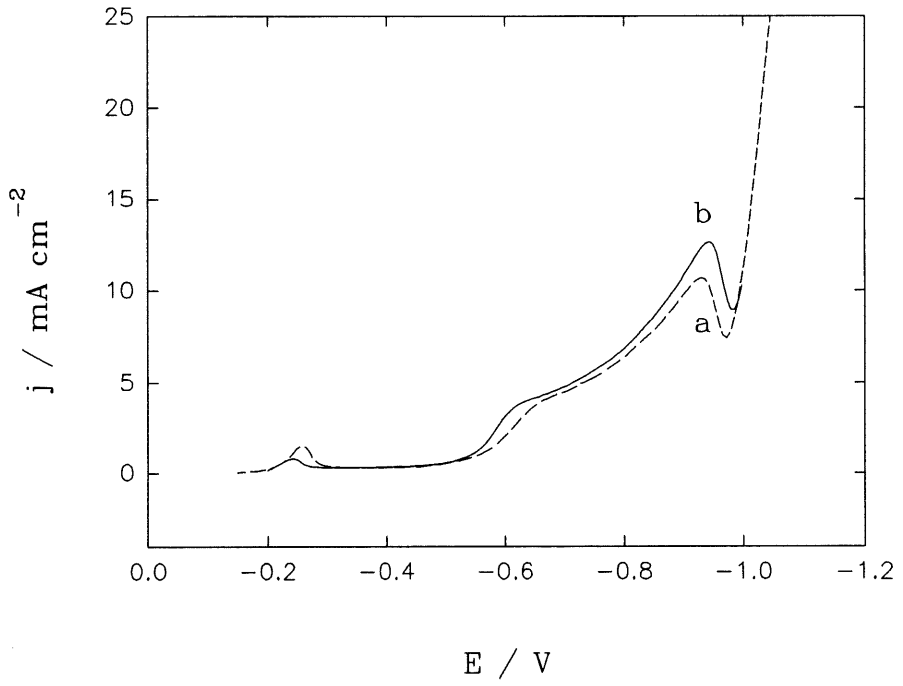

Figure 56. LSV curves of soft gold deposition on a Cu RDE; sweep rate: 1 mV s^{-1}; rotation rate (rpm): (a) 1000; (b) 2700.

The cyclic voltammograms recorded on Ni and glassy carbon substrates are displayed in Figs. 57 and 58. Similar to that on Au substrate, Fig. 11, the characteristic "nucleation/growth loops" (111, 139) are observed on CV in the first potential range, showing that nucleation process is important in such time interval (corresponding to the scan rate).

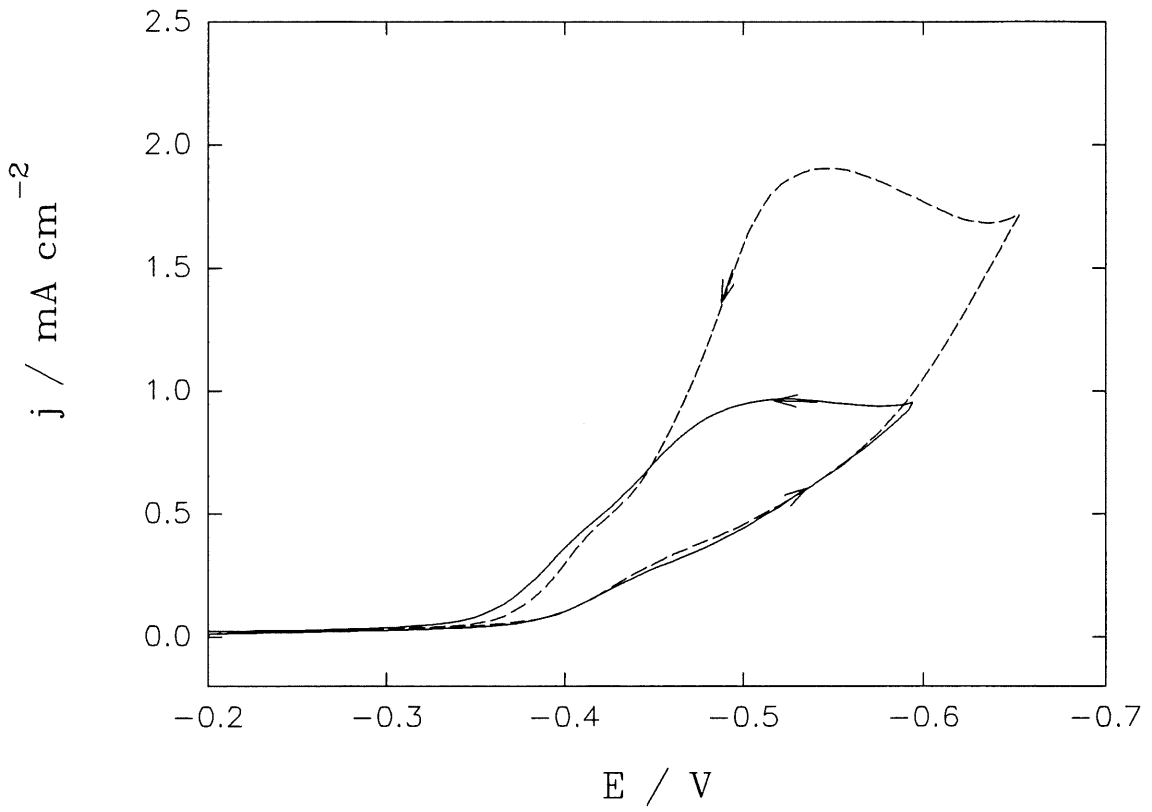

Figure 57. Cyclic voltammograms of hard gold deposition on a Ni RDE; rotation rate: 4000 rpm; sweep rate: 1 mV s^{-1}; reversal potential (V): -0.6 (solid line) and -0.65 (dashed line).

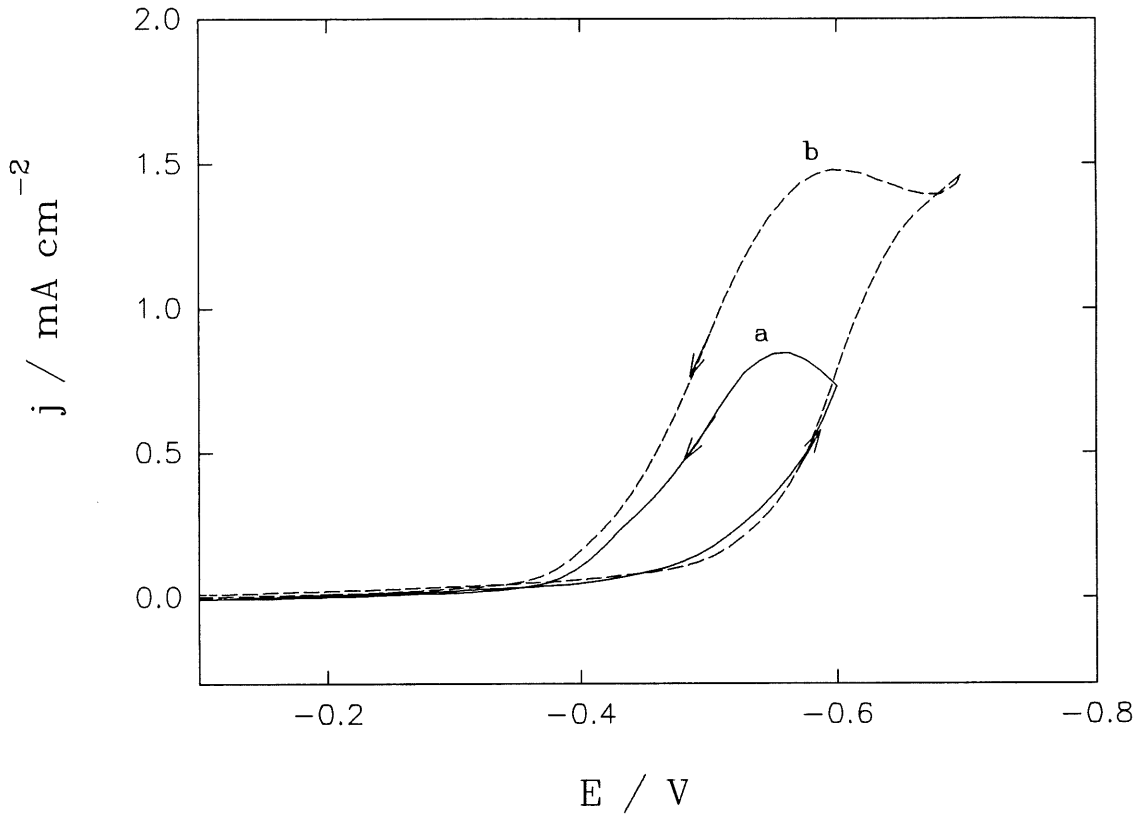

Figure 58. Cyclic voltammograms of hard gold deposition on a glassy carbon RDE; rotation rate: 4000 rpm; sweep rate: 1 mV s^{-1}; reversal potential (V): a) -0.6; b) -0.7.

8.3 Chronoamperometric studies

8.3.1 Copper substrate

Fig. 59 illustrates a typical set of chronoamperometric curves for hard gold deposition on Cu RDE at 2700 rpm. Two distinct features were observed in two potential ranges, indicating different nucleation and growth mechanisms. At potentials between -0.55 V and -0.70 V, current initially falls to a minimum and, subsequently, increases to a quasi-plateau as a result of nucleation and crystal growth. The curves are similar to those obtained on Au substrate. Current at the initial minimum increases with overpotential. The time, t_{min}, at which the minimum appears, is of the order of 40 seconds, much longer than that for Au substrate. It was suggested previously that gold deposition may start prior to the minimum, after which a three-dimensional nucleation and crystal growth process starts. The use of the Cu substrate enables us to verify this hypothesis. When the measurements were performed at times prior to the minimum, gold deposit was clearly seen on Cu substrate, indicating that deposition process actually occurs before t_{min}. The charge consumed up to a minimum corresponds to about 80 compact gold monolayers, depending on the potential applied. Thus, gold deposition may occur before three-dimensional nucleation and crystals growth start. Possibly, substrate-aided epitaxial growth progress occurs before the bulk deposition, as found by Chech and Sard (47). At later stages, current increases and reaches a quasi-plateau. Such a behavior on current-time transients may result from a three-dimensional nucleation and growth of right-circular cones (97,108). It was found that the height of quasi-plateau decreases as potential changes from -0.55 to -0.70 V, as shown in Fig. 59a.

At potentials more negative than -0.75 V, plateau-like behavior of current-time transients disappears. Current falls down to a steady-state at longer times, Fig. 59b. The shape of the curves recorded in this potential range is quite different from that for hard gold deposition on Au substrate, where a maximum followed by a quasi steady-state forms on

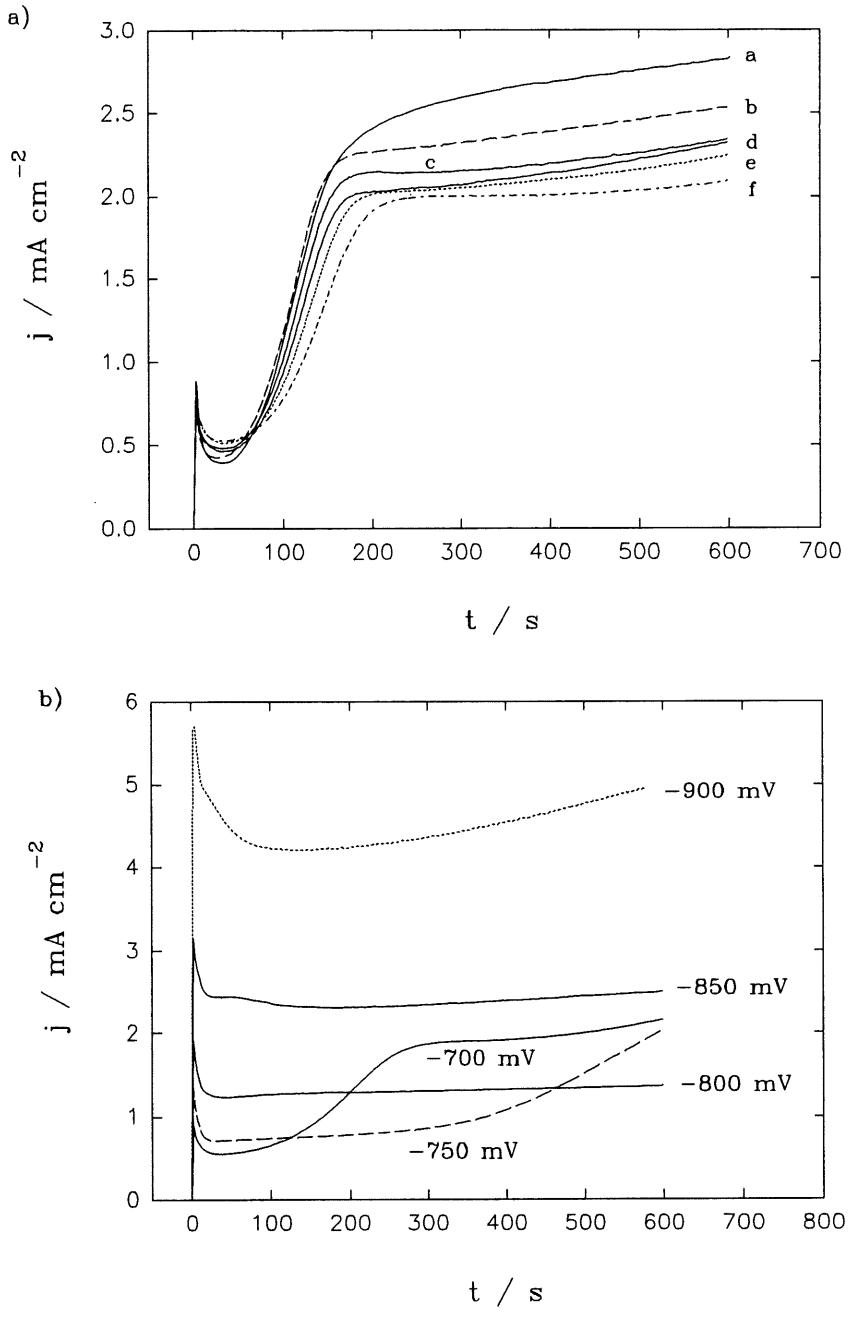

Figure 59. Chronoamperometric curves of hard gold deposition on a Cu RDE; rotation rate: 2700 rpm; potentials in Fig. 59a (mV): a) -550; b) -575; c) -600; d) -625; e) -650; f) -675. Potentials used in Fig. 59b are given in figure.

the transients, Fig. 37. However, at very negative potentials, initial current fall is accompanied by a shoulder, which was also observed in the case of Au substrate.

8.3.2 Platinum substrate

Fig. 60 shows examples of chronoamperometric curves recorded on Pt substrate. The shape of curves is also similar to that on gold electrode. However, the curves on Pt are distorted presumably due to the HER because Pt substrate facilitates the HER. The current efficiency of gold deposition on Pt RDE is about 50 ~ 70 % (136).

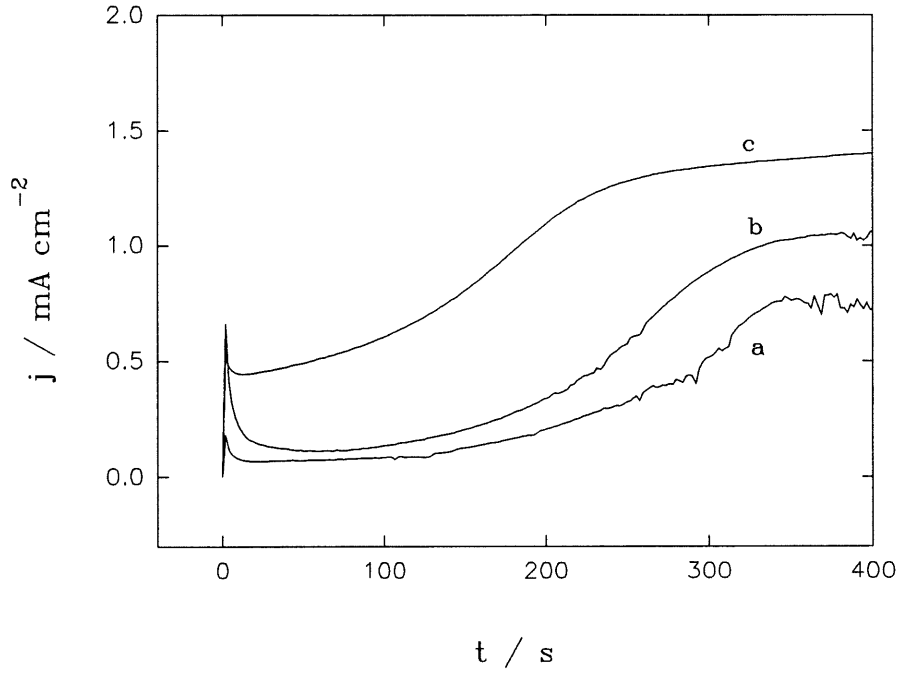

Figure 60. Chronoamperometric curves of hard gold deposition on a Pt RDE; rotation rate 4000 rpm; potentials (mV): a) -550; b) -600; c) -650.

8.3.3 Nickel substrate

Chronoamperometric curves recorded on nickel substrate, Fig. 61, are of entirely different character than those on Au, Pt and Cu RDEs, especially in first potential range. It is surprising that, contrary to all other metallic substrates, the curves obtained on Ni RDE do not show any initial fall or minimum at the beginning of transient for nickel substrate. At more positive potentials, immediately after a constant potential is applied, current increases from zero, and continues to increase slowly at the later stages.

Although an initial minimum is still not observed on the curves at potentials more negative than -0.75 V, its shape becomes completely different from that recorded in the first potential range. The transient is now characterized by a pronounced wide peak, after which current decreases greatly to a low steady-state value, Fig. 61b. The time, t_{max}, required to attain the maximum decreases as potential is made more negative. The values of current at maximum and final steady-state all increase with cathodic potential. It is worth to note that the ratio of the maximum to the steady-state current increases from 2.9 to 4.5 as potential becomes more negative than -0.75 V.

8.3.4 Glassy carbon substrate

Fig. 62 displays the chronoamperometric curves on a glassy carbon RDE. For the glassy carbon substrate, except the initial minimum current which was observed in the cases of Au, Cu and Pt substrates, the chronoamperometric curves exhibit similar features as those on nickel substrate, *i.e*, an obvious maximum is also observed at potentials more negative than -0.875 V. The time necessary to reach the maximum is much longer than that for nickel substrate. Besides, the ratio of the maximum to the steady-state current is about 1.45 at potentials between -0.90 and -1.0 V, smaller than that obtained on the nickel electrode.

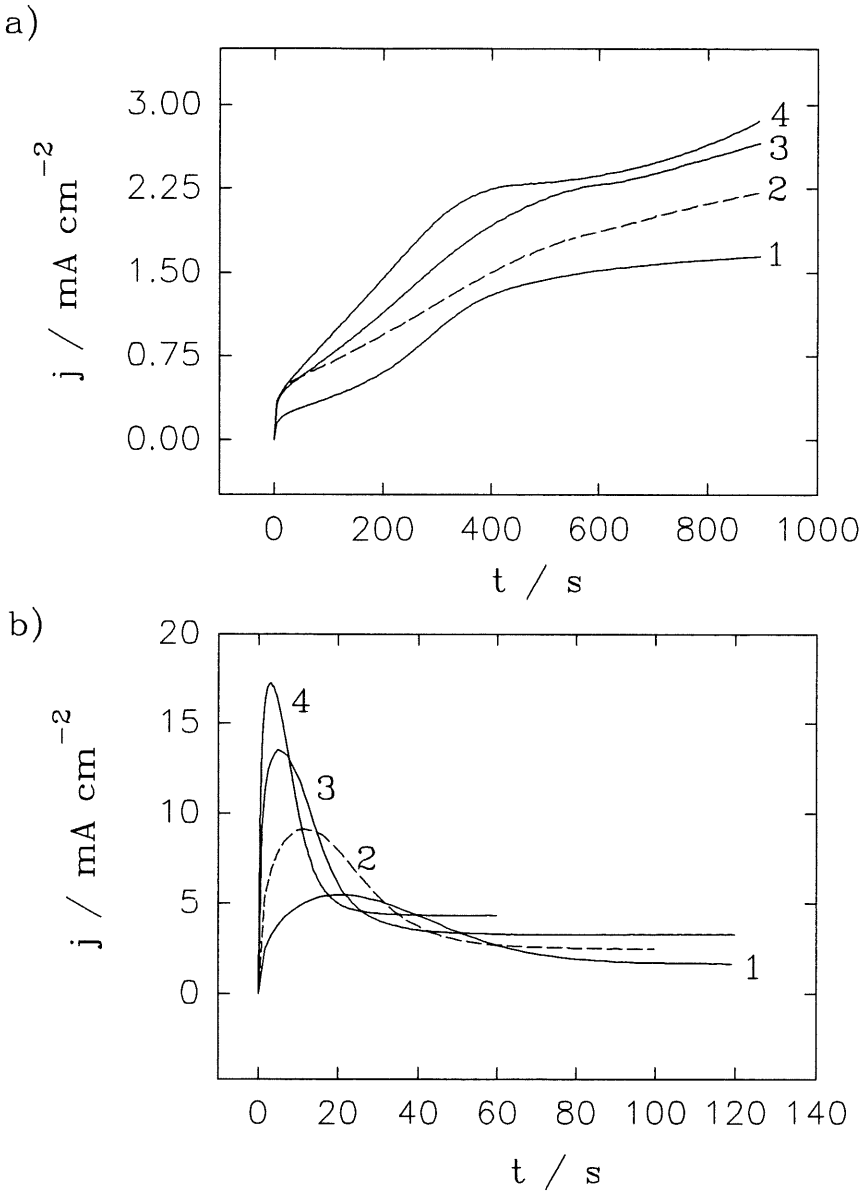

Figure 61. Chronoamperometric curves for hard gold deposition on a Ni RDE; rotation rate: 4000 rpm; potentials (mV) in (a): 1) -500; 2) -525; 3) -600; 4) -650 and in (b): 1) -825; 2) -850; 3) -875; 4) -900.

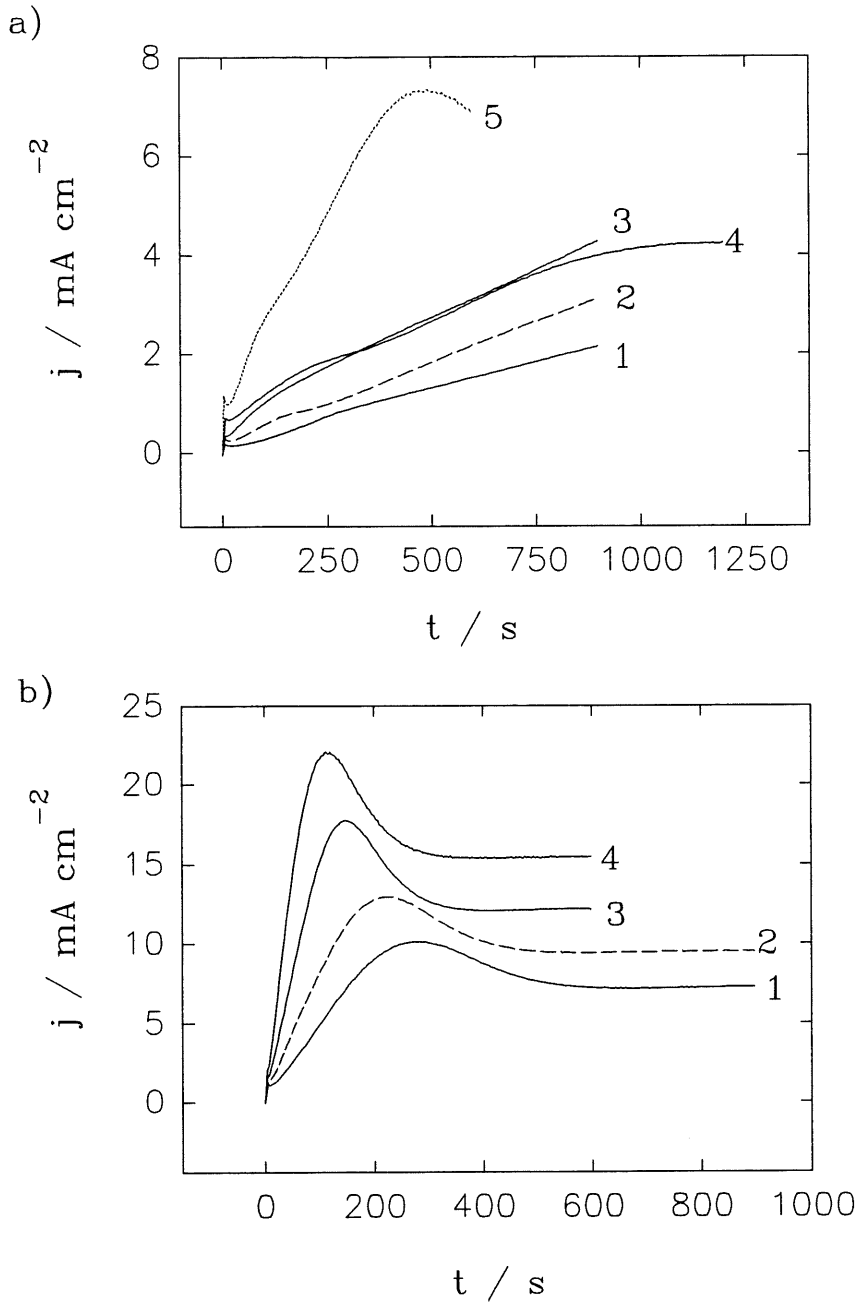

Figure 62. Chronoamperometric curves of hard gold deposition on a glassy carbon RDE; rotation rate: 4000 rpm; potentials (mV) in (a): 1) -550; 2) -600; 3) -650; 4) -850; 5) -900 and in (b): 1) -925; 2) -950; 3) -975; 4) -1000.

The deposit obtained on glassy carbon is different from those on metallic substrates, it is usually dull, and cohesion between deposit and glassy carbon substrate is not very good. The deposit could be easily removed with a cloth.

8.4 Derivation of current-time equation for three-dimensional cylindrical growth

The development of two-dimensional growth model (*i.e.*, cylindrical growth) has been demonstrated an important basis for the derivation of various three-dimensional growth models (97,110), *e.g.*, the growth of the right-circular cones. For two-dimensional cylindrical growth, crystal centres grow only in lateral direction (in x-y plane), while its height h is constant (corresponding to atomic layers). Such growth model was observed in the UPD (168) as well in overpotential deposition of metals (before bulk deposition) (124).

In this section, the concept of cylindrical growth is expanded to three-dimensional growth. It is assumed here that cylinders grow both in lateral and vertical directions, as shown in Fig. 63, their growth rate constant are k and k', respectively. Experimentally, such growth

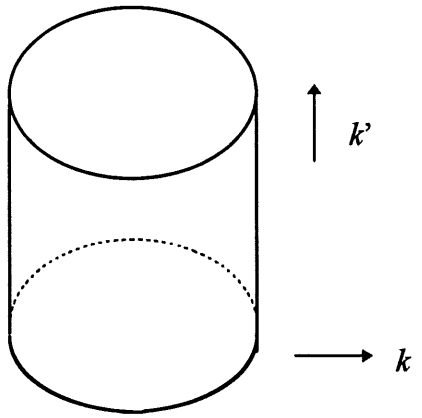

Figure 63. Three-dimensional cylindrical growth with growth rate constants k and k' in lateral and vertical directions, respectively.

mode could be an approximation of polyangular structure. The current-time equations describing 3D cylindrical growth are derived as following.

Consider a slice *dh* cut from growth center at the height of *h*. The fractional area, S_h, covered by growing centres in this slice can be calculated from extended area S_{ext}, according to the Avrami theory. It is worth to note that for such a growth, the fractional area S_h is identical at any height, being independent of *h*. The volume formed in time *t* is given by:

$$V = \int_0^{h_m} S_h \, dh = S_h \, h_m \qquad [8.1]$$

where h_m is the maximum height of cylinders at time *t*, given as:

$$h_m = \frac{Mk'}{\rho} t \qquad [8.2]$$

For instantaneous nucleation ($N = N_0$), the fractional area, S_h, is:

$$S_h = 1 - \exp(-S_{ext}) = 1 - \exp(-\frac{\pi M^2 N_0 k^2}{\rho^2} t^2) \qquad [8.3]$$

Therefore, the volume transferred, *V*, becomes:

$$V = \frac{Mk'}{\rho} t[1 - \exp(-\frac{\pi M^2 N_0 k^2}{\rho^2} t^2)] \qquad [8.4]$$

By differential of eq. [8.4], current is obtained as:

$$j = \frac{zF\rho}{M}\frac{dV}{dt} = 2P_2 P_3 t^2 \exp(-P_2 t^2) + P_3[1 - \exp(-P_2 t^2)] \qquad [8.5]$$

where $P_2 = \frac{\pi M^2 N_0 k^2}{\rho^2}$ and $P_3 = zFk$.

For progressive nucleation ($N = A\,t$), S_h is:

$$S_h = 1 - \exp(-S_{ext}) = 1 - \exp(-\frac{\pi M^2 A_{3D} k^2}{3\rho^2} t^3) \qquad [8.6]$$

Then, the volume formed at time *t* is:

$$V = \frac{Mk'}{\rho} t[1 - \exp(-\frac{\pi M^2 A_{3D} k^2}{3\rho^2} t^3)] \qquad [8.7]$$

Therefore, current density is given as:

$$j = \frac{zF\rho}{M}\frac{dV}{dt} = 3P_2' P_3 t^3 \exp(-P_2' t^3) + P_3[1 - \exp(-P_2' t^3)] \qquad [8.8]$$

where $P_2' = \dfrac{\pi M^2 A_{3D}\ k'}{3\rho^2}$.

Note that current densities in eqs. [8.5] and [8.8], consist of two terms, the first term corresponds to the contribution of current in the side area of cylinders, similar to current in eqs. [2.16] and [2.18] (with height of $Mk't/\rho$); the second is the current in the top area of the centres, same as eqs. [2.21] and [2.22] for the growth of right-circular cones. In fact, eqs. [8.5] and [8.8] can also be derived in an alternative way, *i.e.*, total current is the sum of the current induced in the side area of cylinders which is calculated from the current equations for two-dimensional growth (eqs. [2.16] and [2.18]), and the current observed on the top area S_h of growing centres, where S_h is given by eq. [8.3]. It is found that current induced by 3D cylindrical growth passes through a maximum and reaches a steady-state ($j = zFk'$) at longer times. The maximum current, j_m, and time, t_m, required to reach maximum is obtained by setting

$$\frac{dj}{dt} = 0 \qquad [8.9]$$

For instantaneous nucleation, t_m and i_m are given by:

$$t_m = \left(\frac{3\rho^2}{2\pi M^2 N_0 k^2}\right)^{1/2} \qquad [8.10]$$

$$j_m = 1.446zFk \qquad [8.11]$$

For progressive nucleation, they are:

$$t_m = \left(\frac{4\rho^2}{\pi M^2 A_{3D}\ k^2}\right)^{1/3} \qquad [8.12]$$

$$j_m = 1.791zFk \qquad [8.13]$$

It is interesting that for the two cases, the time t_m is determined by N_0 or A_{3D}, and the lateral growth rate constant k, independent of vertical growth rate constant; while maximum current, j_m, is determined only by vertical growth rate constant k'. The ratio of the peak height to the steady-state current is 1.446 and 1.791 for instantaneous and progressive nucleation, respectively.

8.5 Discussion and approximation of current-time transients

The above results obtained on various substrates show that the mechanisms of gold deposition are different in two potential regions since the shape of LSV and chronoamperometric curves change systematically, the same conclusion was found for gold substrate in the previous chapters.

The growth mode depends mainly on the deposit-substrate interaction, relative to the deposits cohesion (167). If the deposit atomic adsorption, E_a, is smaller than the deposit atomic cohesion energy, E_c, an island growth mode (Volmer-Weber) is induced. This situation may be obtained on a glassy carbon substrate because of the probably week bonding energy between glassy carbon and electrodeposited gold (deposit on glassy carbon could be easily removed). While a layer-by-layer growth process (Frank-van der Merwe) is induced when $E_a > E_c$. For metallic substrates, in contrast to glassy carbon, the bond between the substrate material and the deposited gold is metallic and E_a should be in the same range as E_c, therefore, the second situation may be obtained.

It was shown that higher cluster surface density on metallic substrates than on glassy carbon is usually observed, and is probably due to the higher adhesion energy between gold and metallic substrates than that between gold and glassy carbon because when the adhesion energy increases for a given overpotential, the nucleation rate increases (167).

As reviewed in chapter 2, the shape of chronoamperometric curves reflects the mechanism and kinetics of nucleation and crystal growth involved in deposition. Theoretically, two-dimensional cylindrical growth induces a current increasing to a maximum followed by a decrease to zero as surface is completely covered by growing crystals (80,97); three-dimensional growth of right-circular cones gives arise to a plateau-like shape of *j-t* curves, *i.e.*, current increases and reaches a plateau at later stages (80,97); ellipsoidal growth leads to an increase of current to a peak followed by a decrease in current to a steady-state value, the ratio of the peak current to steady-state being 1.27 and 1.32 for instantaneous and progressive nucleation, respectively (110,113), independent of the eccentricity ε. In practice, however, the situation is usually more complicated than that expected by a simple model, as seen in gold deposition on Au RED. This was further confirmed by the following observation. The selection of model depends on the substrates used.

8.5.1 Nucleation and growth of gold deposition on Cu substrate

For Cu substrate, the current-time transients recorded at less negative potentials, Fig. 60a, are quite similar to those observed in the case of deposition on Au substrate, indicating a similar mechanism of nucleation and crystal growth in both cases. It was found earlier that in such conditions a three-dimensional progressive nucleation and growth of right-circular cones is involved in hard gold deposition on Au substrate. Accordingly, current for the progressive nucleation is given by:

$$j = zFk_0 \exp(-\frac{\pi M^2 k^2 A_{3D}}{3\rho^2} t^3) + zFk'[1 - \exp(-\frac{\pi M^2 k^2 A_{3D}}{3\rho^2} t^3)] \qquad [2.27]$$

as described in chapter 2.

The experimental data obtained at potentials from -0.55 to -0.70 V, Fig. 59, are fitted well to eq. [2.27] and the results are illustrated in Fig. 64 The fit to a three-dimensional instantaneous nucleation and growth model was rejected on the basis of the statistical comparison.

From these approximations, kinetic parameters of nucleation and growth may be estimated. The dependence of k_0 and k' on potential applied are together given in Fig. 65. It is obvious that growth rate constant, k_0, increases as potential is made more negative. However, vertical growth rate constant, k', for three-dimensional growth of right-circular cones decreases with negative potentials, opposite to a typical case where growth rate increases

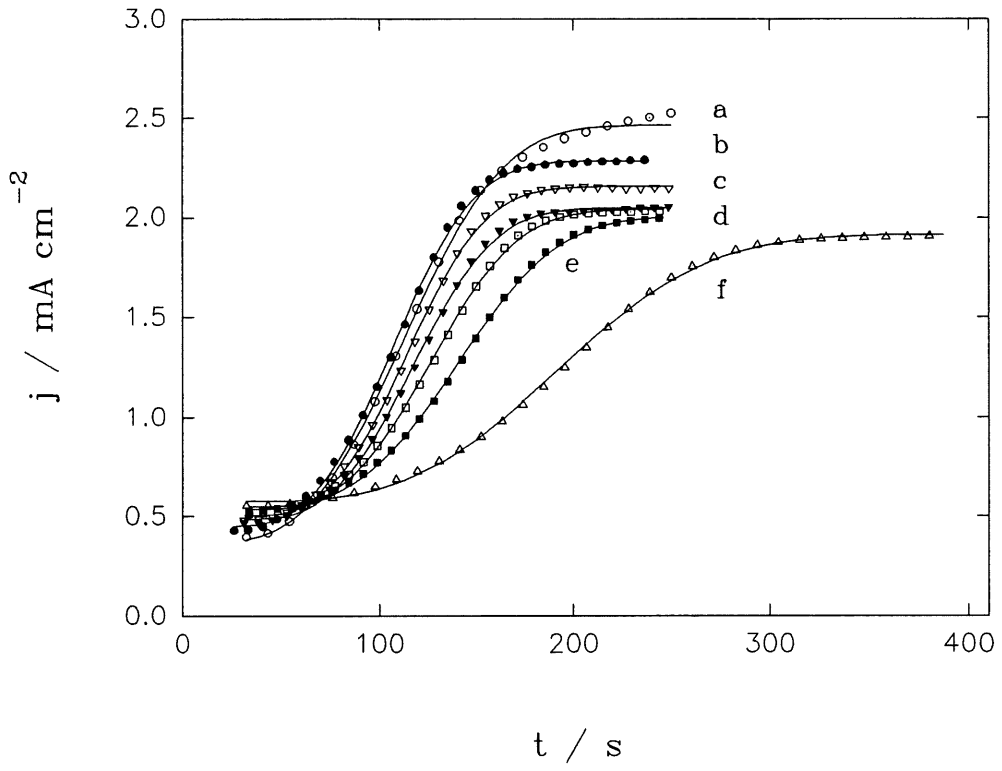

Figure 64. Initial portion of current-time transients shown in Fig. 59a for hard gold deposition on a Cu RDE at potentials between -0.55 and -0.70 V; points - experimental data; solid line - theoretical fit to eq. [2.27].

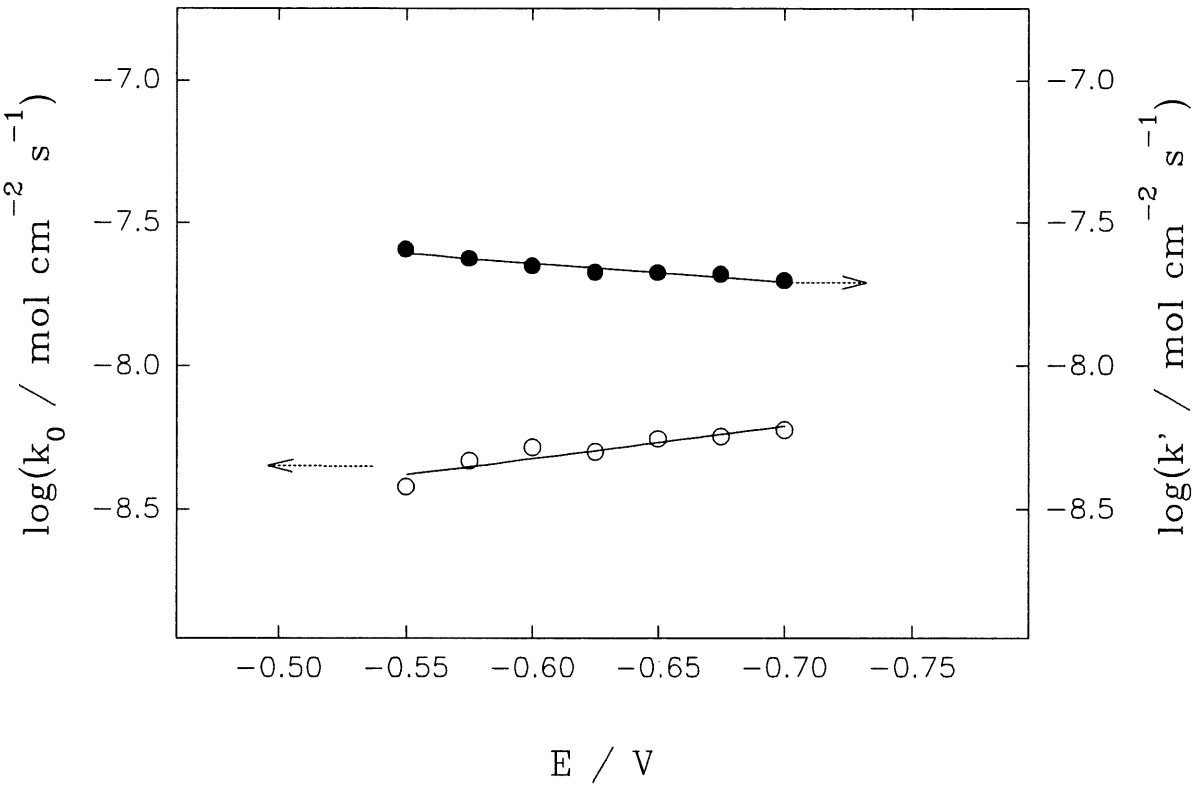

Figure 65. Plot of log k_0 (O) and log k' (●) for hard gold deposition on a Cu RDE, determined from eq. [2.27], against potential applied between -0.55 and -0.70 V.

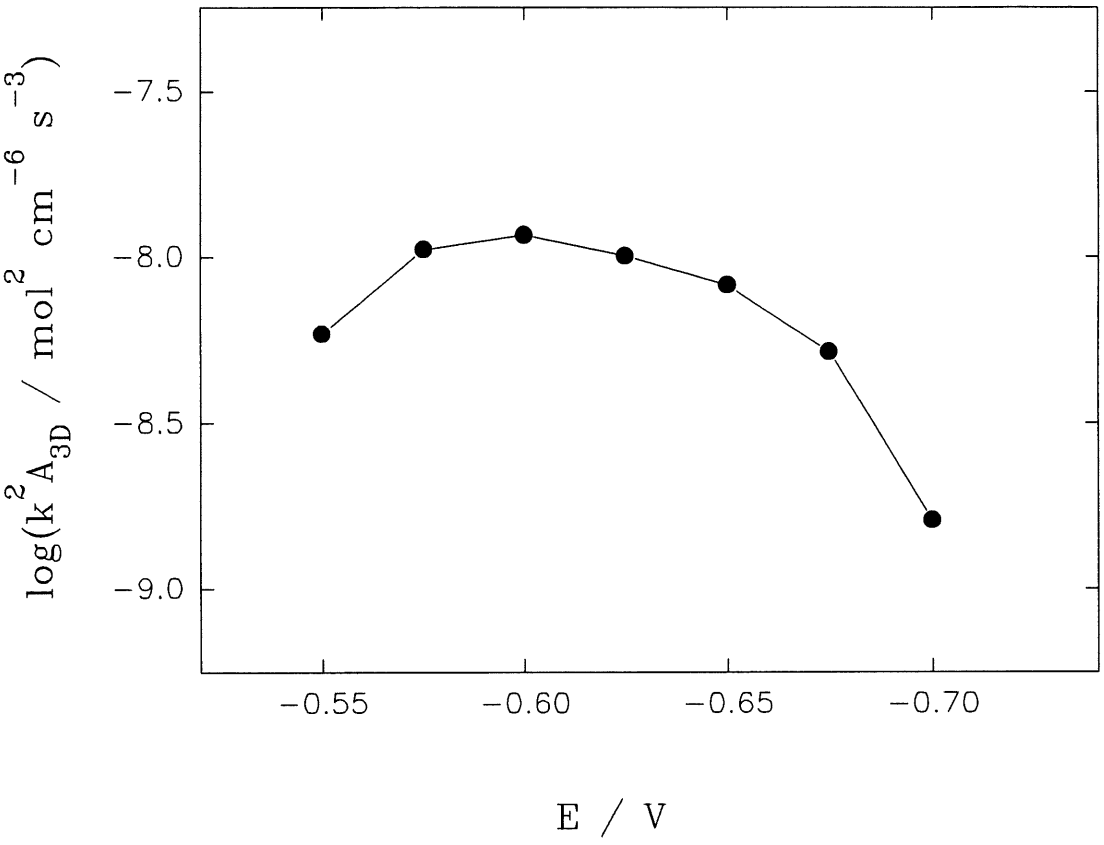

Figure 66. Plot of log k^2A_{3D} for hard gold deposition on a Cu RDE, determined from eq. [2.27], against potential applied between -0.55 and -0.70 V.

with overpotential (80,97,98), indicating an inhibition of crystal growth. Such an abnormal growth process was first found in gold deposition on Au substrate. It is probably related to the self-inhibition of gold deposition caused by the desorption of AuCN and the adsorption of CN^- or other CN^- containing species, as discussed in previous chapters. Fig. 66 shows a potential dependence of the combination of the lateral growth rate constant and the nucleation rate, k^2A_{3D}. This combined constant initially increases, and then decreases with negative potential. The results obtained above indicate that an inhibition of growth occurs in gold deposition. The conclusion will be confirmed by morphology characterization using microscopic techniques in the next chapter.

The behavior of current-time transients recorded at more negative potentials is different to some extent from those obtained on the Au substrate. For gold substrate, current goes through a maximum followed by a slow decrease to a steady-state at longer times, although the maximum is replaced by a shoulder at very negative potential. For copper substrate, however, a shoulder rather than a maximum forms on the transient, a monotonous decay of current to a steady-state is observed at later stages, while this behavior is more similar to that observed on gold substrate at relatively negative potentials. We were unable to analyze the current-time transients recorded on Cu substrate at potentials more negative than -0.75 V in view of nucleation and growth models because no well defined features were observed on these transients

8.5.2 Nucleation and growth of gold deposition on Ni substrate

The current-time transients recorded on nickel substrate have special features, different from those observed on other metallic substrates, especially at more negative potentials. No initial current minimum is observed on all transients, Fig. 62, suggesting the nucleation occurs immediately after a constant potential is imposed on the substrate (*i.e*, its induction time is very short).

Various models were tested to describe the well-defined peak and steady-state behavior of current-time transients recorded at more negative potentials. First, one of the possible models would be the hemispherical growth model derived by Bosco and Rangarajin (110), and Abyanech (113). Although this model does predict peak and steady-state behavior on j - t curves, unfortunately, however, our experimental j - t transients could not be explained by this model since the ratios of peak current to steady-state obtained on nickel electrode in our experiments are 2.9 to 4, quite different from that predicted theoretically by hemispherical growth model. Hence, this model can not be used in the present work. The modification of hemispherical growth model by considering the HER occurring on the surface of growing crystals still cannot describe the experimental data, although the HER alters the ratio of peak height to steady-state current, as shown by Abyaneh (114). Other possible models, for example, combined 2D and 3D growths, and 3D cylindrical growth model proposed in previous section, also couldn't reproduce the correct shape of experimental curves. Finally, the partial inhibition model, eq. [7.17], was attempted to approximate the current-time transients. Eq.[7.17] may be rewritten as:

$$j = P_0 \exp(-P_2 t^2)$$
$$+ P_1[\exp(-\lambda t) - \exp(-P_2 t^2) + \lambda \exp(-\lambda t)\int_0^t \exp(-P_2 u^2 + \lambda u)du]$$
$$+ P_3[1 - \exp(-P_2 t^2)] \qquad [7.17]$$

where $P_0 = zFk_0$, $P_1 = zFk_1$ and $P_3 = zFk_2$, other symbols have been defined previously. Fig. 67 shows an example of fit of the experimental transients obtained on nickel electrode. Although this model gives the best result, unfortunately, the fit is still not very satisfied, especially for the experimental curves recorded at more negative potentials.

8.5.3 Nucleation and growth of gold on glassy carbon

Since j - t curves recorded at more positive potentials do not show well-defined features, analysis was attempted only for the experimental data obtained at more negative potentials

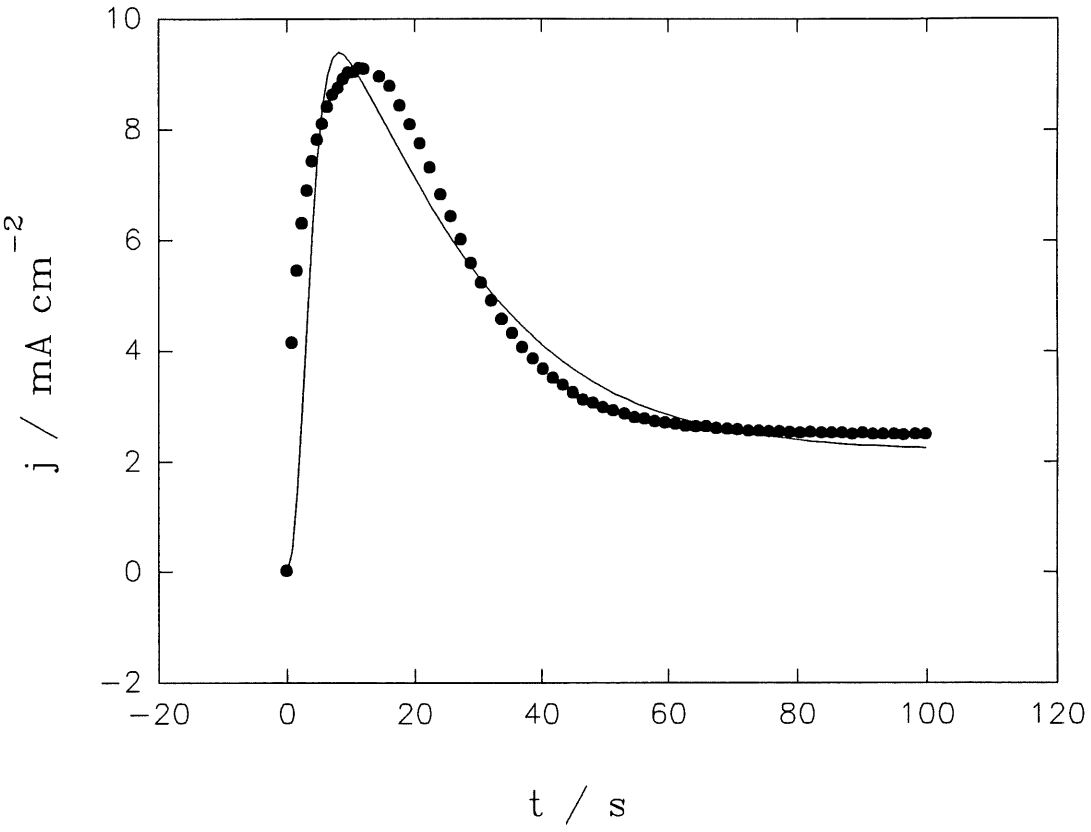

Figure 67. Theoretical fitting curves of experimental chronoamperometric curves for hard gold deposition on a Ni RDE; potential -850 mV; points - experimental data; solid line - theoretical fit curves to eq. [7.17]; parameters derived from eq. [7.17] are:

$P_0 = 0$; $P_1 = (5.99 \pm 1.01) \times 10^{-2}$ mA cm^{-2}; $P_2 = 8.34 \pm 0.49$ s^{-2};

$\lambda = (7.0 \pm 0.7) \times 10^{-2}$ s^{-1}; $P_3 = 2.2 \pm 0.3$ mA cm^{-2}

to explain the well-defined peak and a steady-state behavior, Fig. 62b. Various models were tested. Again like the case of nickel substrate, the combined 2D and 3D growth model, the ellipsoidal growth model and its modification by taking into account the HER on the top surface of growing centres (113), cannot reproduce the whole experimental curves. However, the experimental data can be well described by the partial inhibition model, eq. [7.17]. Fig. 68 displays the theoretical fit of eq. [7.17] to experimental curves. The kinetic parameters were estimated from the least-squares fit, as shown in Table 7. The parameters k^2N_0 and k_2 increase as potential becomes more negative. It is noted that parameter λ obtained for glassy carbon substrate is much smaller than that for Au as a substrate (Table 6) because the time necessary to reach maximum on chronoamperometric curves is much longer than that in the latter case.

Besides the partial inhibition model, it is found that three-dimensional cylindrical growth presented in previous section, alternatively, may also give good description for the experimental data. It is worth to note that the ratio of the peak current to the steady-state value is about 1.45, very close to that predicted by instantaneous nucleation and three-dimensional cylindrical growth model, eq. [8.5]. To fit the experimental data, it was thus assumed that nucleation is instantaneous ($N = N_0$), and three-dimensional cylinders grow in lateral and vertical directions. Besides, the initial current, $j_0 = zFk_0$, is also taken into account. Therefore, total current density is given as:

$$j = j_0 + 2P_2 P_3 t^2 \exp(-P_2 t^2) + P_3[1 - \exp(-P_2 t^2)] \qquad [8.14]$$

where parameters have been defined before.

Fig. 69 shows the theoretical fit of eq. [8.14] to experimental j - t curves recorded a glassy carbon electrode at more negative potentials. The kinetic parameters derived from this model are given in Table 8. The vertical growth rate constant k' and the combined constant k^2N_0 increase as potential is made more negative. If supposed that growth rate constants in lateral and vertical directions are equal to each other, then the total number of active centers, N_0

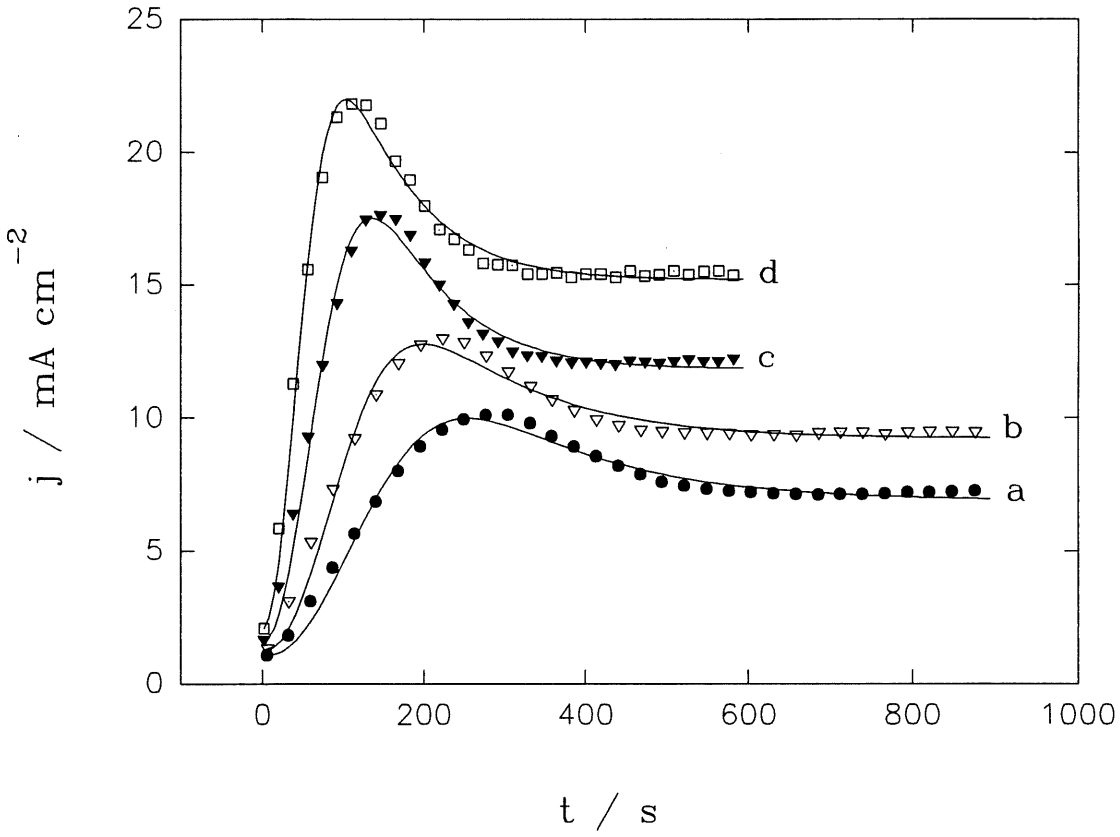

Figure 68. The theoretical fitting curves of experimental data for hard gold deposition on glassy carbon RDE (Fig. 62) to a partial inhibition model (eq. [7.17]); points - experimental data; solid line - theoretical fit to eq. [7.17]. Potential (mV): a). -925; b). -950; c). -975; d) -1000.The parameters derived from the least-square fit are given in Table 7.

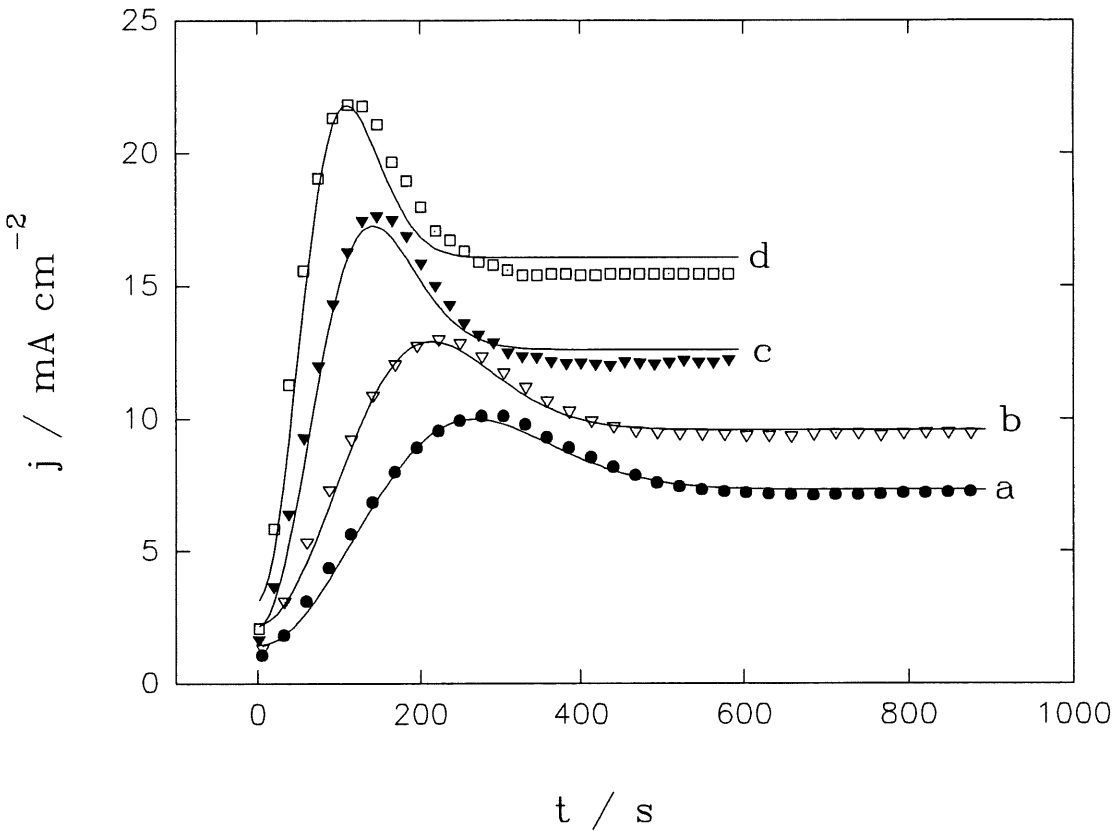

Figure 69. Theoretical fitting curves of experimental data (Fig. 62) to eq. [8.14] for hard gold deposition on a glassy carbon RDE; points-experimental data; solid line - theoretical fit to 3D cylindrical growth (eq. [8.14]). Potential (mV): a). -925; b). -950; c). -975; d) -1000. The parameter derived from least-squares fit are given in Table 8.

Table 7. Kinetic parameters of hard gold deposition on glassy carbon electrode derived from least-squares fit of experimental j-t curves to eq. [7.17].

Potential (V)	j_0 mA cm^{-2}	k^2N_0 (mol^2 cm^{-6} s^{-2})	k_1 (mol cm^{-2} s^{-1})	λ (s$^{-1}\times10^3$)	k_2 (mol cm^{-2} s^{-1})
-0.925	1.06	$(1.39\pm0.04)\times10^{-7}$	$(9.8\pm1.1)\times10^{-8}$	7.8±0.8	$(7.17\pm0.08)\times10^{-8}$
-0.950	1.31	$(2.50\pm0.10)\times10^{-7}$	$(9.61\pm1.2)\times10^{-8}$	9.3±0.7	$(9.59\pm0.09)\times10^{-8}$
-0.975	1.65	$(4.70\pm0.12)\times10^{-7}$	$(1.84\pm0.18)\times10^{-7}$	14.5±0.08	$(1.23\pm0.01)\times10^{-7}$
-1.0	2.05	$(8.74\pm0.28)\times10^{-7}$	$(1.66\pm0.12)\times10^{-7}$	15.8±0.8	$(1.57\pm0.01)\times10^{-7}$

Table 8. Kinetic parameters of hard gold deposition on glassy carbon electrode derived from least-squares fit of experimental *j-t* curves to eq. [8.14].

potential (V)	j_0 mA cm^{-2}	k^2N_0 mol^2 cm^{-6} s^{-2}	k' mol cm^{-2} s^{-1}	N_0 nuclei cm^{-2}
-0.925	1.41±0.07	$(6.41\pm0.08)\times10^{-8}$	$(6.16\pm0.06)\times10^{-8}$	1.69×10^7
-0.950	2.20±0.10	$(9.96\pm0.02)\times10^{-8}$	$(7.78\pm0.10)\times10^{-8}$	1.69×10^7
-0.975	2.15±0.20	$(2.27\pm0.05)\times10^{-7}$	$(1.08\pm0.02)\times10^{-7}$	1.94×10^7
-1.0	3.13±0.30	$(3.80\pm0.12)\times10^{-7}$	$(1.34\pm0.03)\times10^{-7}$	2.11×10^7

can be estimated. It is found that N_0 increases as potential becomes more negative.

The comparison of Fig. 68 and 69 shows that both models give a good fit to the experimental data, but a better quality of fitting curves could be obtained by the partial inhibition model, eq. [7.17], especially at more negative potentials. However, more parameters are used in this model. At this moment, we are not able to determine which model explains better the experimental data.

8.6 Summary

The effect of substrate on the deposition of hard gold was studied using voltammetric and chronoamperometric methods. The results obtained are summarized as follows:

All LSVs obtained on different substrates are characterized by an obvious peak followed by a minimum. This common feature may result from the self-inhibition phenomena in gold deposition, *i.e.*, the reduction of AuCN adsorbed on substrate at less negative potentials. However, the peak height and its position are affected by the nature of substrates studied. The increase in the mass transfer of HCN generated during the deposition leads to an increase of current with increasing rotation speed.

The shape of chronoamperometric curves depends strongly on the nature of substrates. The substrates studied may be classified into two groups. The first group consists of metallic substrates except nickel electrode, the cohesion between deposit and substrate is good, and current-time transients show a quasi-plateau at less negative potential. The second group consists of nickel and glassy carbon, where deposits are loose and easily removed, and a wide maximum followed by a steady-state is observed on current-time transients. Various models were attempted to describe the experimental data. For copper electrode, three-dimensional progressive nucleation and growth of right-circular cones is found and the potential-dependent

inhibition of growth was observed at more positive potentials. For nickel electrode, partial inhibition growth model gives a better description of the peak and steady-state observed at more negative potentials. For glassy carbon electrode, the partial inhibition model describes well the experimental data, however, alternatively, a simple model of three-dimensional instantaneous nucleation and cylindrical growth also gives a good fit to the experimental curves.

CHAPTER 9
CHARACTERIZATION OF GOLD DEPOSITS

9.1 Introduction

In the previous chapters, gold deposition on various substrates was studied by electrochemical techniques. The mechanisms of nucleation and crystal growth during initial stages were analyzed. The inhibition of crystal growth during the deposition was established at some potentials. In the present chapter, gold deposits are characterized with microscopic techniques to better understand the nucleation and crystal growth processes.

Scanning electron microscopy (SEM) and atomic force microscopy (AFM) were applied as *ex-situ* techniques to characterize the morphology of deposits. SEM, transmission electron microscopy (TEM) and X-ray diffraction techniques have been widely used in the morphology studies of gold deposits (16-21,38,40,43,47,51-62). It appears that there are no publications dealing with the application of AFM in gold deposition. Several studies on the use of AFM in investigation of metal bulk electrodeposits have been published (169-179). This technique was mainly used as an *in-situ* method to monitor the growth morphology during deposition. In recent years, deposits of copper (169-174), lead (175), silver (176), *etc.*, were successfully studied *in-situ* by AFM. However, artifacts introduced by AFM due to the interaction between the tip and substrate during electrochemical processes were also reported (171,176,180). For example, AFM was used to modify the nucleation and crystal growth in Cu deposition (171) and to enhance the dissolution of aluminum (180). Besides its advantage as an *in-situ* method for electrochemical studies, AFM was also widely used as an *ex-situ* method for morphological observation of the surface structure from nanometer to micrometer scales. For instance, Zn-Co deposit on highly oriented pyrolytic graphite (177), Zn deposit on a low carbon steel substrate (174) and Sn deposit on NiP substrate (179) were studied *ex-situ*

by AFM. In the present chapter, SEM and/or AFM techniques were used *ex-situ* to evaluate the growth morphology of gold deposits under different conditions. The influence of deposition time and potential on growth morphology, surface roughness and grain size are described.

In section 9.2, hard gold deposits on soft gold-plated nickel electrode was characterized using SEM. Since gold deposition on Cu substrate is the most similar to that on Au substrate, copper substrate was mainly used in surface studies. The surface morphology of both soft and hard gold deposits on copper substrate are characterized by SEM and AFM. The result will be presented in section 9.3.

9.2 SEM observations of hard gold deposits on gold plated-nickel electrode

For the purpose of morphology observation, a pure gold-plated nickel RDE (diameter 3.0 mm) was used as a substrate. It's surface was verified using SEM and found to be uniform. Besides, the electrochemical response of such a gold-plated Ni RDE was similar to the Au RDE used in the electrochemical measurements. Subsequently, hard gold samples were obtained after gold deposition on the gold-plated Ni RDE in solution D.

Fig. 70 shows SEM pictures of hard gold deposited at -0.65 V for 250 s. This represents a typical measurement in a more positive potential range. A large number of nearly hemispherical granular crystals with different polygonal surfaces are distributed randomly on the surface of a thin deposit. Since during the deposition time of 250 s current reached a quasi-plateau (Fig. 38a), therefore, the overlaps of adjacent growing crystals are observed in Fig. 70. The grain size of crystals varies, as clearly seen in Fig. 70c. This indicates that nucleation is progressive, in a good agreement with the assumption presented previously in the nucleation and crystal growth model (eq. [7.18]).

a)

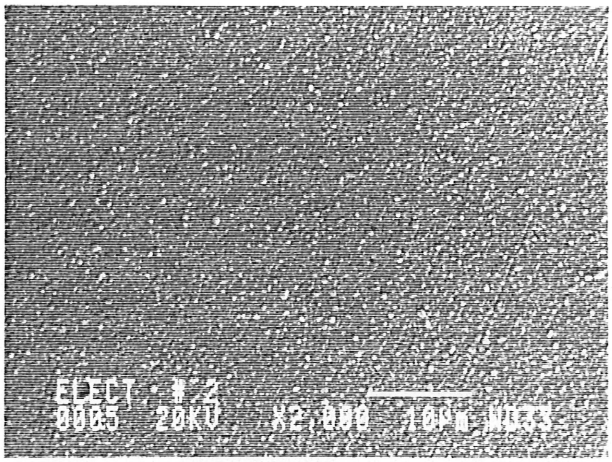

b)

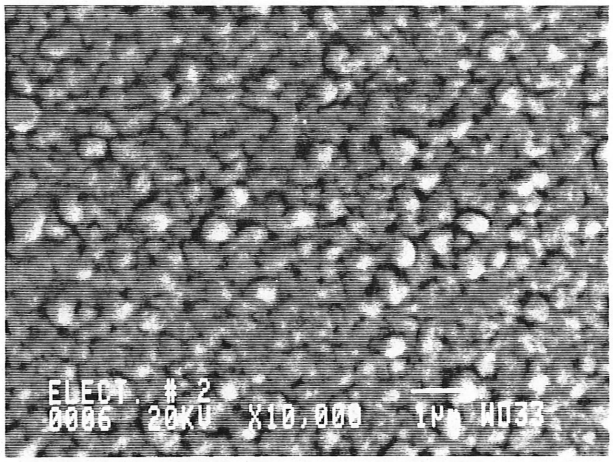

c)

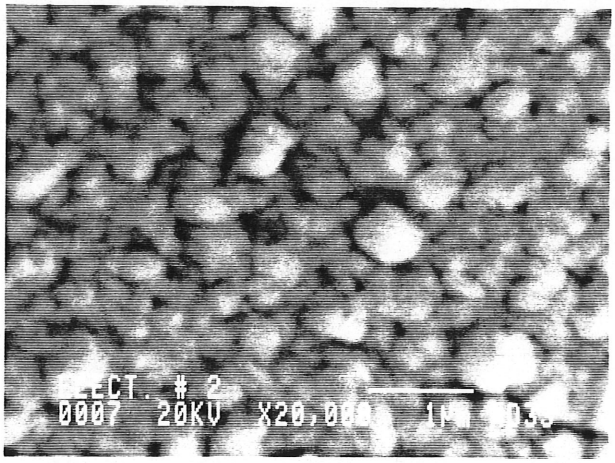

Figure 70. SEM of hard gold deposits on the gold-plated Ni electrode at -0.65 V after 250 s; magnification: a) 2,000×, b) 10,000×, c) 20,000×.

Fig. 71 shows the surface morphology of hard gold deposited at -0.90 V for 150 s. This measurement is an example of deposition at more negative potentials. Two growing phases are revealed from the SEM micrographs, Fig. 71b, *i.e.*, the distribution of grain size is almost bimodal; one phase consists of large number of uniform and small crystals, the other contains bigger grains. Such a bimodal distribution of grain sizes was also observed by Pindra *et al.* (40) during nickel hardened gold deposition as a result of partial inhibition of crystal growth. Hence, the partial inhibition model proposed in this work seems reasonable.

The influence of nickel and/or non-metallic inclusions may also play a role in the nucleation and crystal growth. Nakahara (61) studied morphology of the cobalt hardened gold deposits in acid solution by means of SEM and TEM, and found similar hemispherical structure, or "rounded mound" growth. Accordingly, the "rounded mound" growth consists of extremely fine gold grains, the nucleation of which was accompanied by the incorporation of numerous nonmetallic molecules, which may act as growth inhibitors. Although nonmetallic inclusions in nickel hardened gold deposits were not yet identified, similar effect as that for cobalt hardened gold might be expected, *i.e.* inhibition of growth in certain direction may result from the nonmetallic inclusion in the deposits.

The primary study using XRD technique shows that nickel content in hard gold deposits is about 0.3 to 0.6 %, nonmetallic elements such as carbon, nitrogen, etc. also were detectable, but no qualitative results were obtained.

9.3 Characterization of deposits obtained on Cu substrate

The surface morphology of deposit depends strongly on the applied potential, deposition time, solution composition, and also preparation of the substrate. The visual inspection showed that the surface of deposit is smooth and bright when potential applied is more positive than the peak potential on LSV. It becomes dull, especially at longer deposition times,

a)

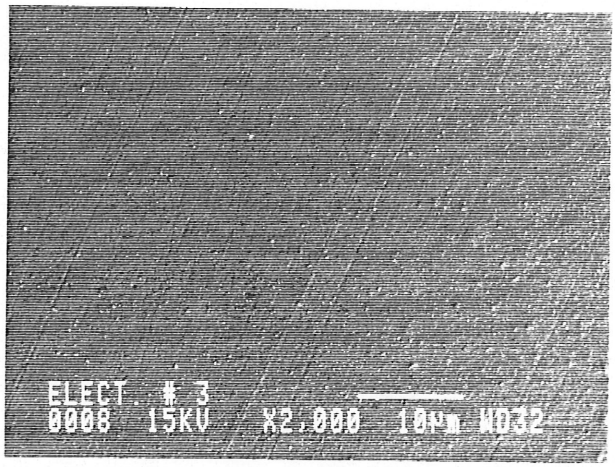

b)

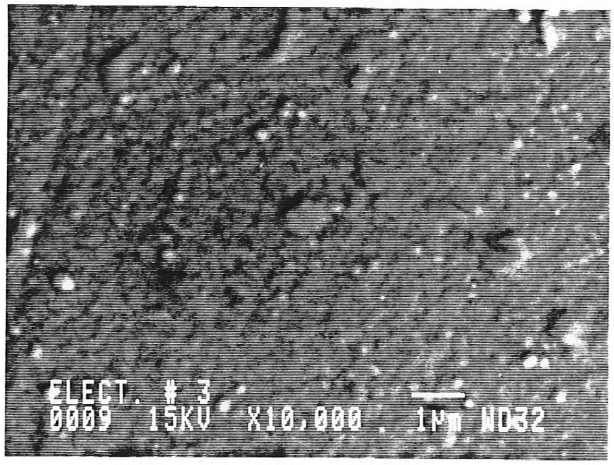

Figure 71. SEM of hard gold deposits on the gold-plated Ni electrode at -0.9 V after 120 s; magnification: a) 2,000×, b) 10,000×.

times, as potential is made more negative than the peak potential. Similar appearance of deposits was observed in the cases of other substrates. However, in the second potential range (characterized by current increase), surface becomes smooth and bright again. For the purpose of comparison, gold deposits were obtained from solutions in the absence and presence of nickel to understand its influence on gold deposition.

The voltammetric and chronoamperometric behavior of gold deposition on copper substrate has been established in chapter 8. Three-dimensional progressive nucleation and growth of right circular cones was found at potentials between -0.5 V and -0.75 V under potentiostatic mode. Potential-dependent inhibition of crystal growth was observed similar to the case of gold deposition. This conclusion is further confirmed by the morphological observation performed below.

9.3.1 Observation of morphology by SEM

First, SEM was used to observe the growth morphology of soft gold. SEM micrographs of soft gold deposits on Cu substrate obtained at potential -0.60 V at different times are presented in Fig. 72, together with the SEM for copper substrate before deposition. Surface of Cu substrate is smooth, Fig. 72a, although mechanical scratches may be seen. Immediately after deposition, a large number of small crystals with different sizes are shown randomly distributed on the surface, Fig. 72b. Crystals are polyangular with somewhat rounded features and their grain size increases with time. No well defined surface topography is visible at later stages, presumably due to the overlap of crystals. Fig. 73 shows SEM of soft gold deposits at different potentials. Grain size increases as potential changes from -0.60 V to -0.80 V. At -0.80 V, truncated pyramidal features are clearly shown with grain size up to ~ 4 μm (Fig. 73b). At -1.00 V, it is apparent that surface consists of two growing phases, one with smaller grain size is uniformly distributed on the surface and it forms earlier; the other

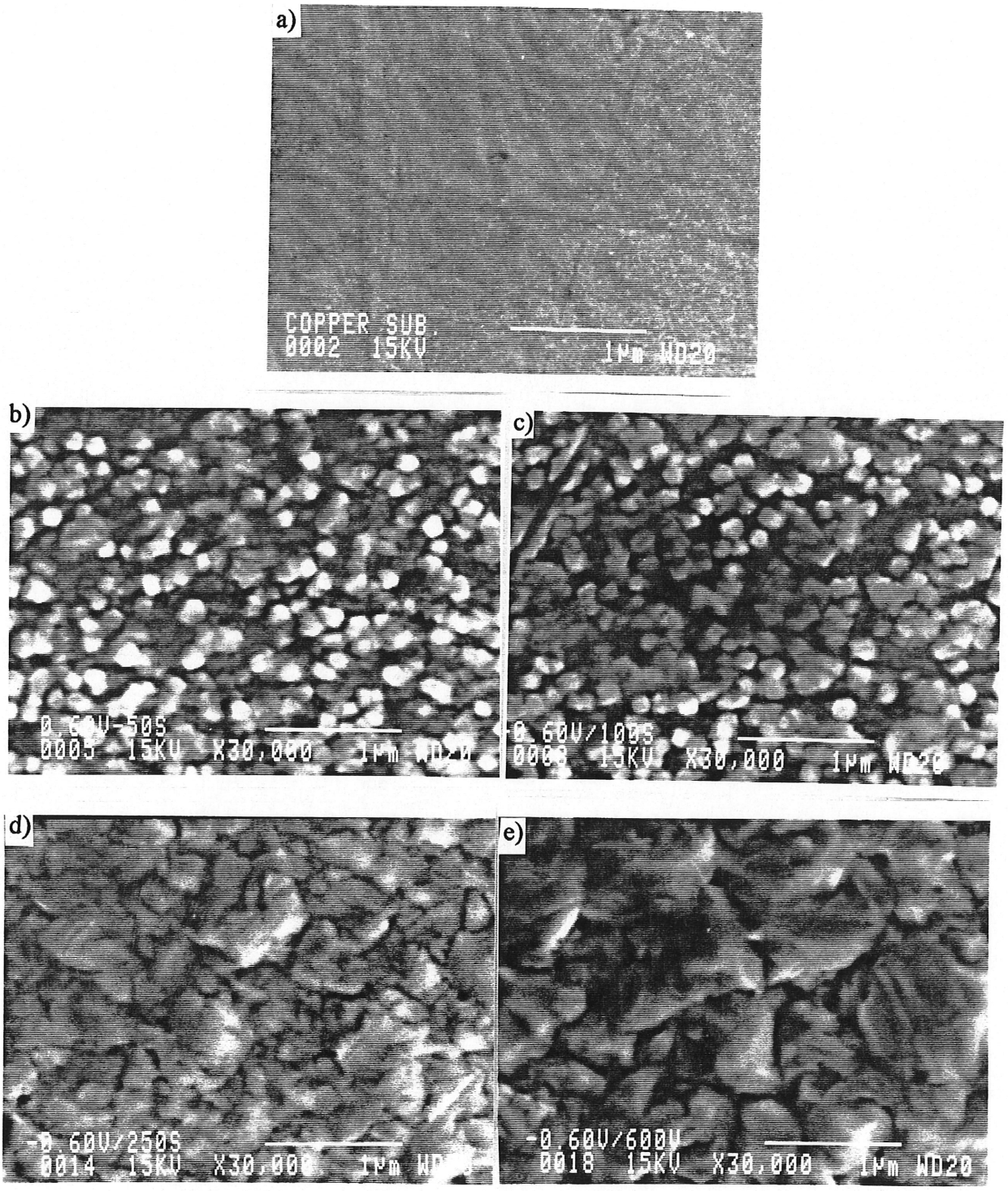

Figure 72. SEM of soft gold deposits on Cu at -0.60 V; deposition time (s): (a) before deposition; (b) 50; (c) 100; (d) 250; (e) 600.

a)

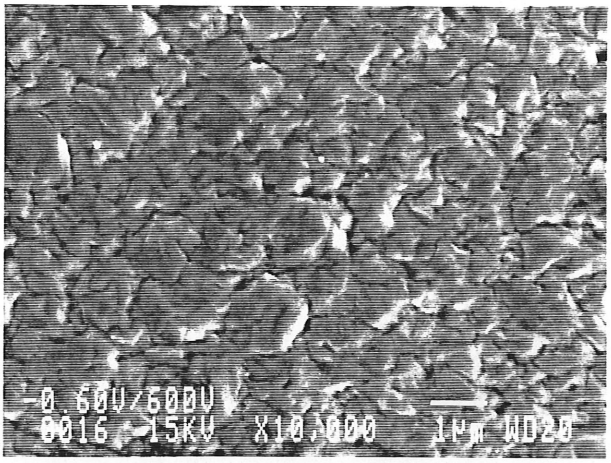

b)

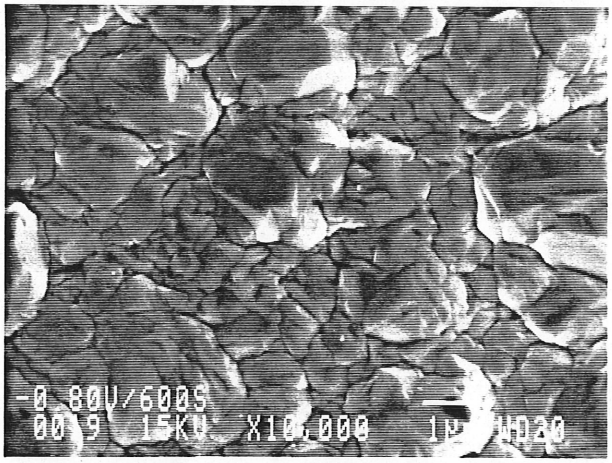

c)

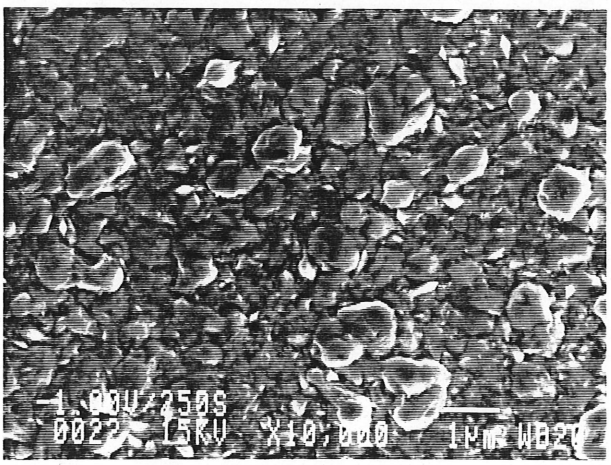

Figure 73. SEM of soft gold deposits on Cu at different potentials; (a) -0.60 V, 600 s; (b) -0.80 V, 600 s; (c) -1.00 V, 250 s.

with bigger grain sizes up to about 1 μm is formed upon the underlaying layers of the first phase, Fig. 73c.

Fig. 74 presents SEM of hard gold deposits at -0.60 V and different deposition times. The deposit consists of a large number of crystals with various grain sizes. Grain size increases with an increase in the deposition time (*i.e.*, corresponding to a thicker film). It is evident from Fig. 74d that the growth morphology is hemispherical or pyramidal, showing some polyangular features. The overlap of crystals is clearly seen from Fig. 74d. At -0.75 V, the grain size decreases as compared with that obtained at -0.60 V after 450 s (Fig. 75b), indicating that the inhibition of growth occurs. The SEM of hard gold deposit at -1.0 V after 450 s is illustrated in Fig. 75c. It shows that the grains are more rounded than those observed at -0.60 V.

9.3.2 Characterization of surface morphology by AFM

To study nucleation and growth, it is important to obtain the grain size, the topography of growth, the roughness, the height of clusters, the distribution of crystals, *etc.* Such quantitative information may be obtained from the AFM measurements. The grain size in lateral direction may be assessed from the white area in the top view image, while the height of the surface feature is encoded according to the gray scale shown in the right side of Fig. 76. Although it is possible, in principle, to estimate the grain height on the surface from the gray scale, a better estimation of height may be obtained from the section analysis of the AFM images.

Fig. 76 shows the top-view AFM images in the scan size of 15 μm × 15 μm for soft gold deposits on copper RDE obtained at -0.60 V and different times. After 50s of deposition, there are no important changes in the surface morphology. At 250 s, a large number of small clusters randomly distributed on the surface, Fig. 76b, is visible as white spots. As the crystals

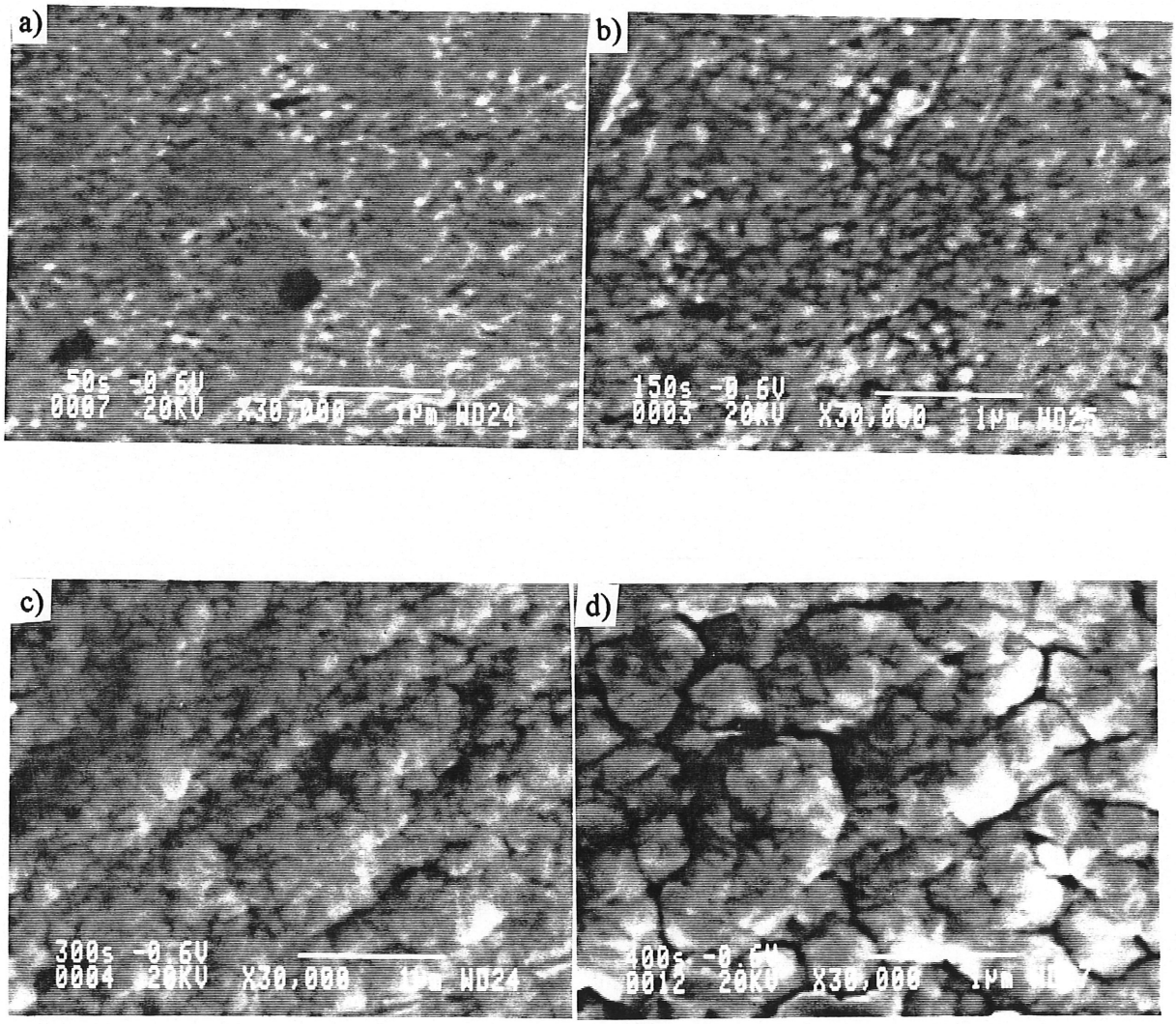

Figure 74. SEM of hard gold deposits on Cu at -0.60 V; deposition time (s): (a) 50; (b) 150; c) 300; (d) 400.

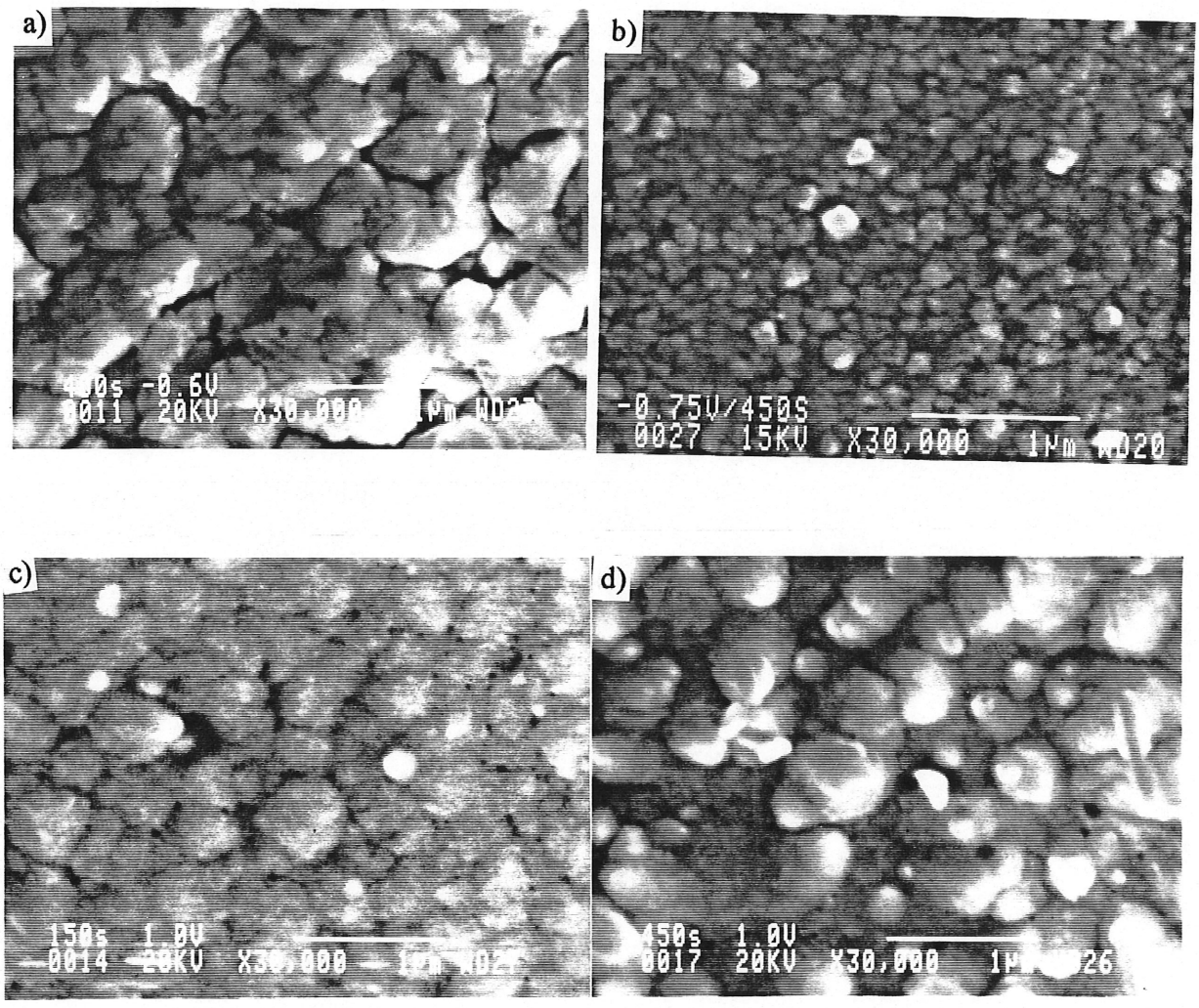

Figure 75. SEM of hard gold deposits on Cu at different potentials; (a) 450 s, -0.60 V; (b) 450s, -0.75 V; (c) 150 s, -1.00 V; (d) 450 s, -1.00 V.

grow, the grain size of clusters increases. The white area in the image becomes larger at longer times, the grain size of crystals at 600 s increases up to about 2 μm in lateral direction, and about 50~500 nm in height.

AFM images of soft gold deposits obtained at different potentials are given in Fig. 77. It seems that as potential changes from -0.60 V to -0.80 V, the number of clusters decreases, while the grain size increases, Fig. 77a and b, the biggest grains obtained at -0.80 V after 600 s of deposition are ~ 4 μm in lateral direction. Fig. 77c and d show the AFM images at potentials -0.95 V and -1.0 V after 250 s of deposition, respectively. The observed clusters show more rounded structures. Clusters at -1.0 V have various grain sizes up to 2.4 μm, bigger than those at -0.95 V. It is not convenient to compare the grain size at -0.80 V and -0.95 V from the above results since the deposition time and charge are different.

Fig. 78 depicts the AFM images of hard gold deposits on Cu substrate obtained after 450 s at different potentials. When potential changes from -0.50 V to -0.70 V, grains are more rounded, and their grain size increases up to about 1.2 μm in lateral direction at -0.70 V. However, grain size seems to decrease at more negative potential. For example, the clusters at -0.80 V, Fig. 78e, are much smaller than those observed at -0.70 V, Fig. 78d, their size in lateral direction is only about 500 nm, much smaller than that obtained at -0.65 V or -0.70 V, presumably indicating the inhibition of growth. However, at -1.0 V (corresponding to the second potential range on LSV in Fig. 70), grain size increases again in comparison with that at -0.80 V.

In order to reach a better insight into the growth morphology, AFM images for hard gold deposit are replotted in three-dimensions. The surface topography of gold deposits is more explicit in these images. AFM images in 3D views are 5 μm div^{-1} for the x-y plane but 500 nm div^{-1} in the z-direction, the vertical features of growth are significantly enhanced.

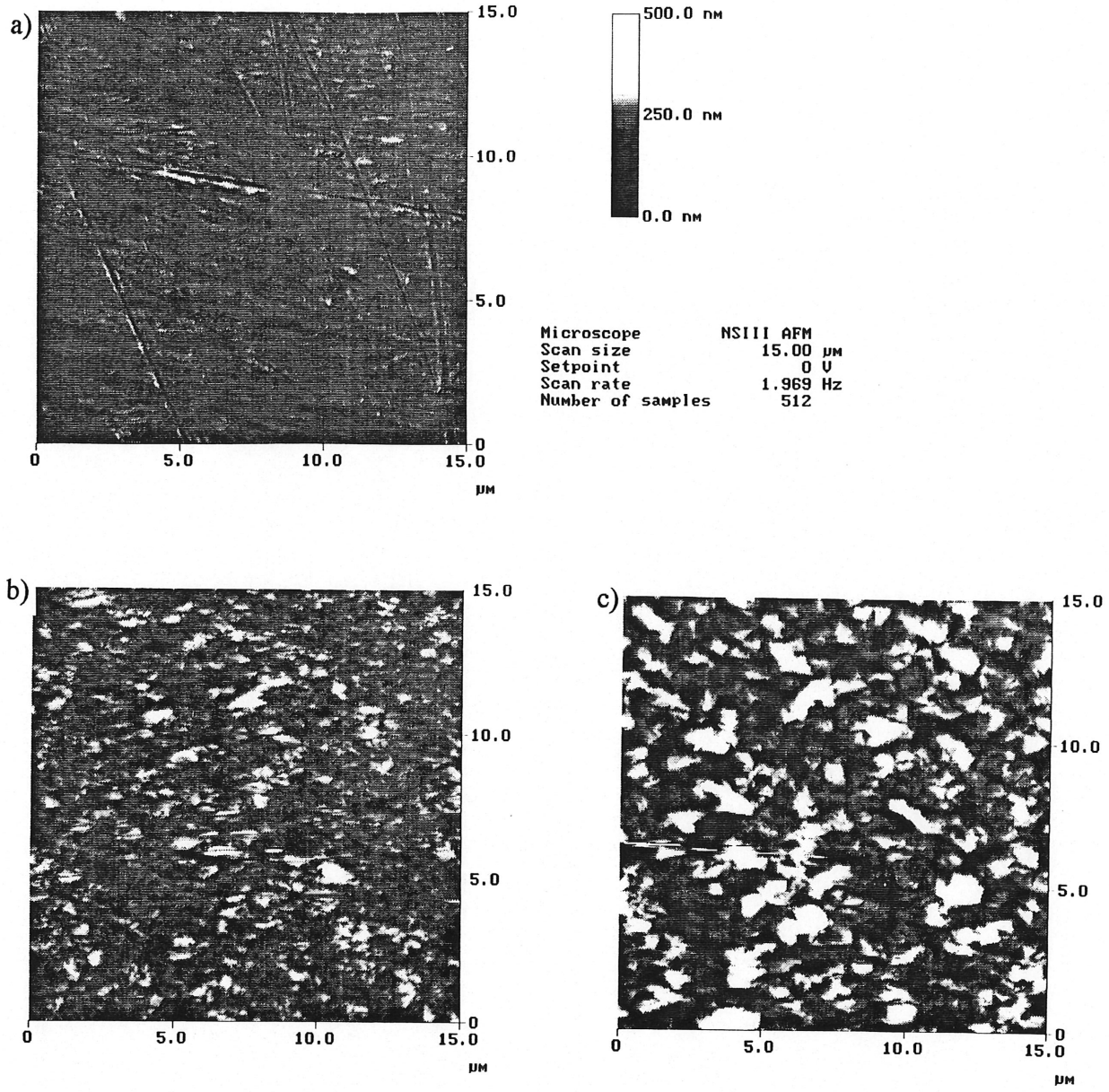

Figure 76. Top-view AFM images of soft gold deposits on Cu at -0.60 V at different times; deposition time (s): (a) 50; (b) 250; (c) 600.

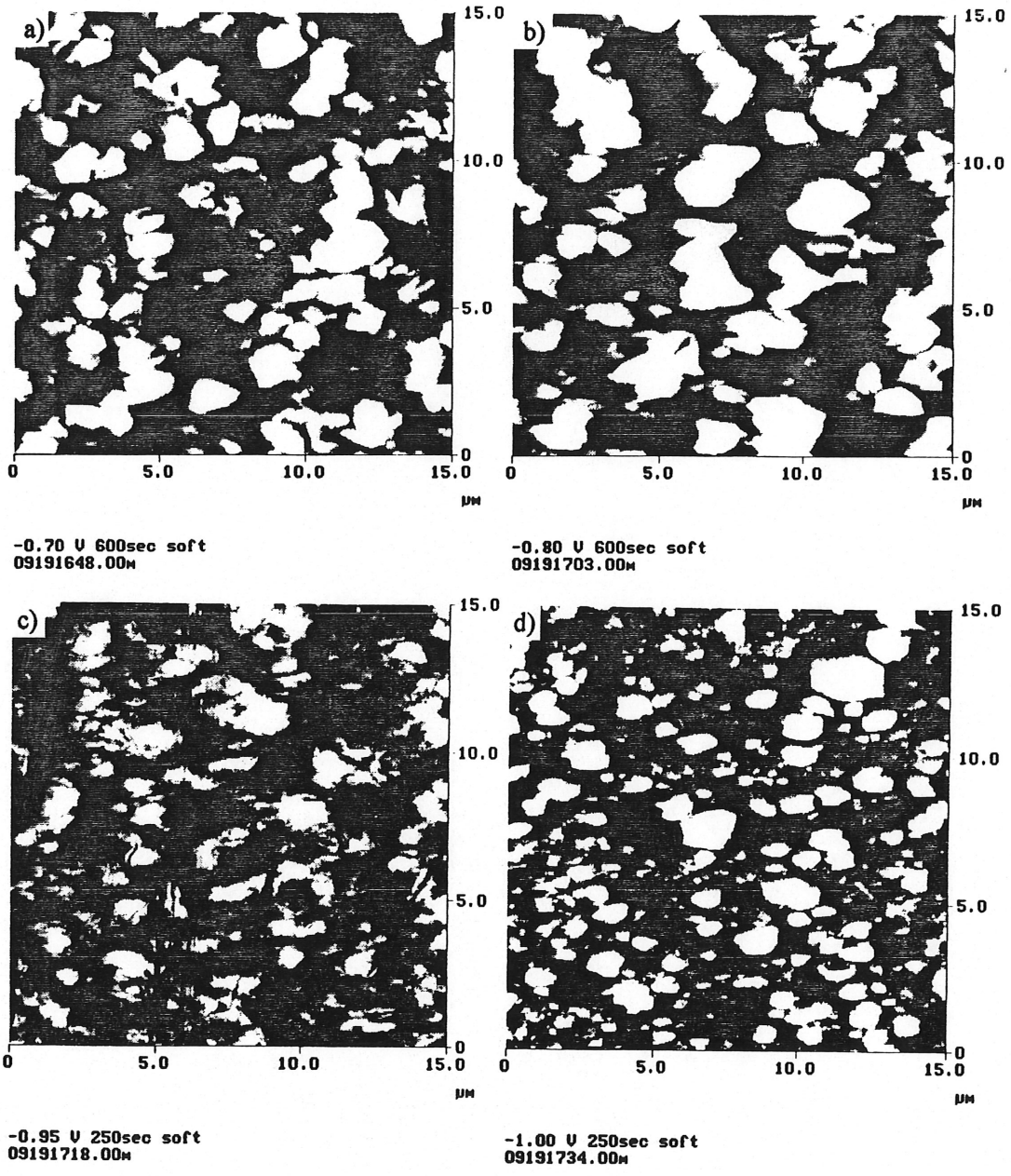

Figure 77. Top-view AFM images of soft gold deposits on Cu at different potentials: (a) -0.70 V, 600 s; (b) -0.80 V, 600 s; (c) -0.95 V, 250 s; (d) -1.00 V, 250 s.

Fig. 79 provides AFM images of hard gold grown at -0.60 V and at different times. At very initial stages, immediately after minimum on current-time transients (Fig. 73), after 50 s, growth of cluster is observed, however, their shape is not well defined at this early stage, Fig. 79a. After 150 s, three-dimensional growth of crystals is observed, they are randomly distributed on the surface, and become better defined at this stage. However, the separation of crystals is not good, the overlap of crystals is observed even at the beginning of deposition. As deposition time increases, grain size also increases. A quantification of the "roughening" of the surface may be described by the mean roughness of the surface, R_a (nm), which is calculated as (176):

$$R_a = (L_x L_z)^{-1} \int_0^{L_x} dx \int_0^{L_z} dz\, f(x,z) \qquad [9.1]$$

where $f(x,z)$ is the surface relative to the central plane, and L_x, L_z, the horizontal and vertical dimensions of the image, relatively. Table 9 displays the mean roughness of deposits and the maximum height of grains at -0.60 V and different times. The mean roughness of the deposit and the maximum height of grains increase with time. There seems to be no preferential growth on the defects, and the deposition proceeds randomly on the surface. The growth

Table 9. The mean surface roughness, R_a, and the maximum grain height, R_{max}, for hard gold deposits on Cu at -0. 60 V.

Deposition time (s)	50	150	400
R_a (nm)	13.1	17.4	39.3
R_{max} (nm)	165.6	190.5	466.4

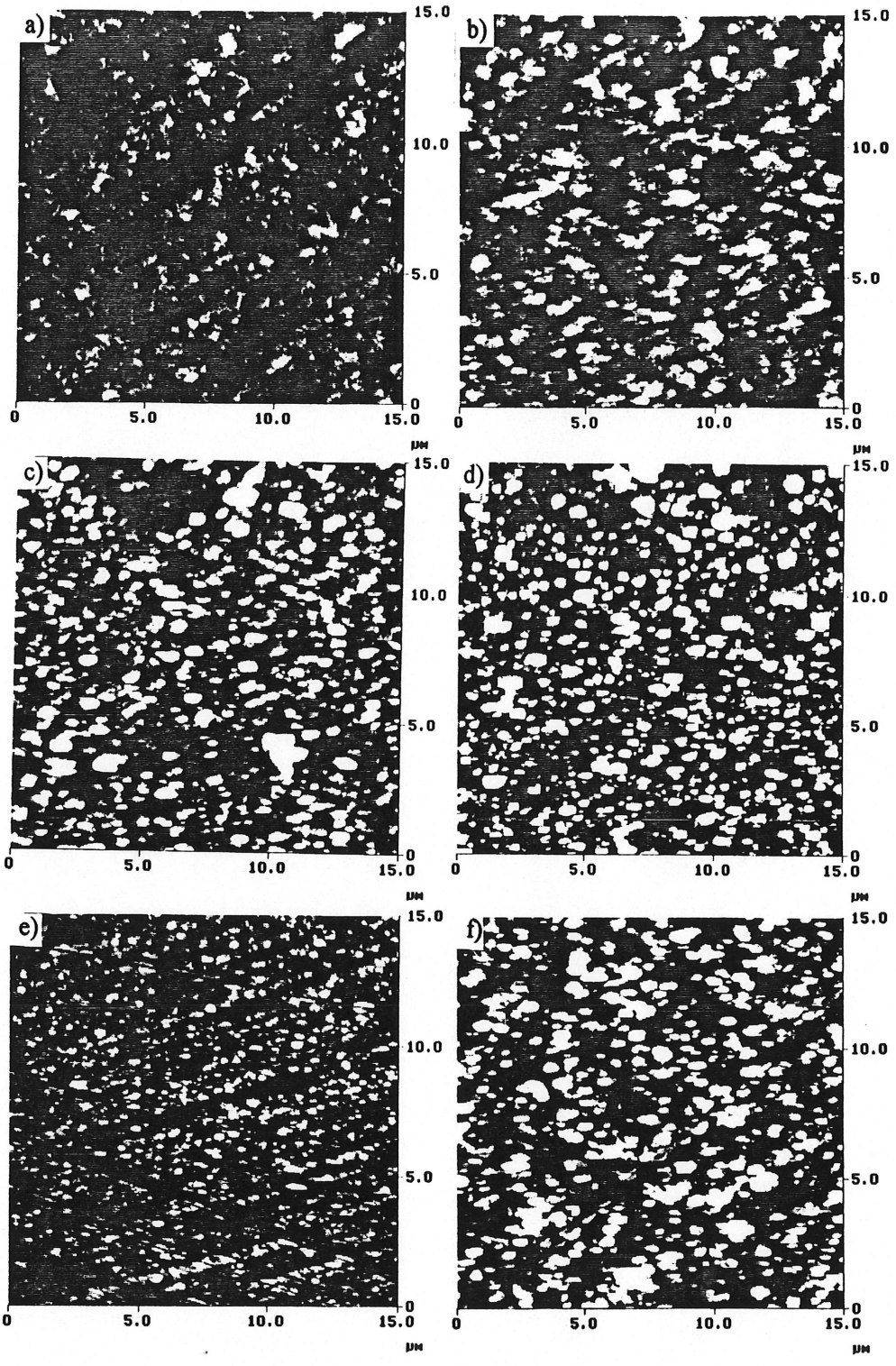

Figure 78. Top-view AFM images of hard gold depositon Cu; deposition time 450 s; potentials (V): (a) -0.55; (b) -0.60; (c) -0.65; (d) -0.70; (e) -0.80; (f) -1.00.

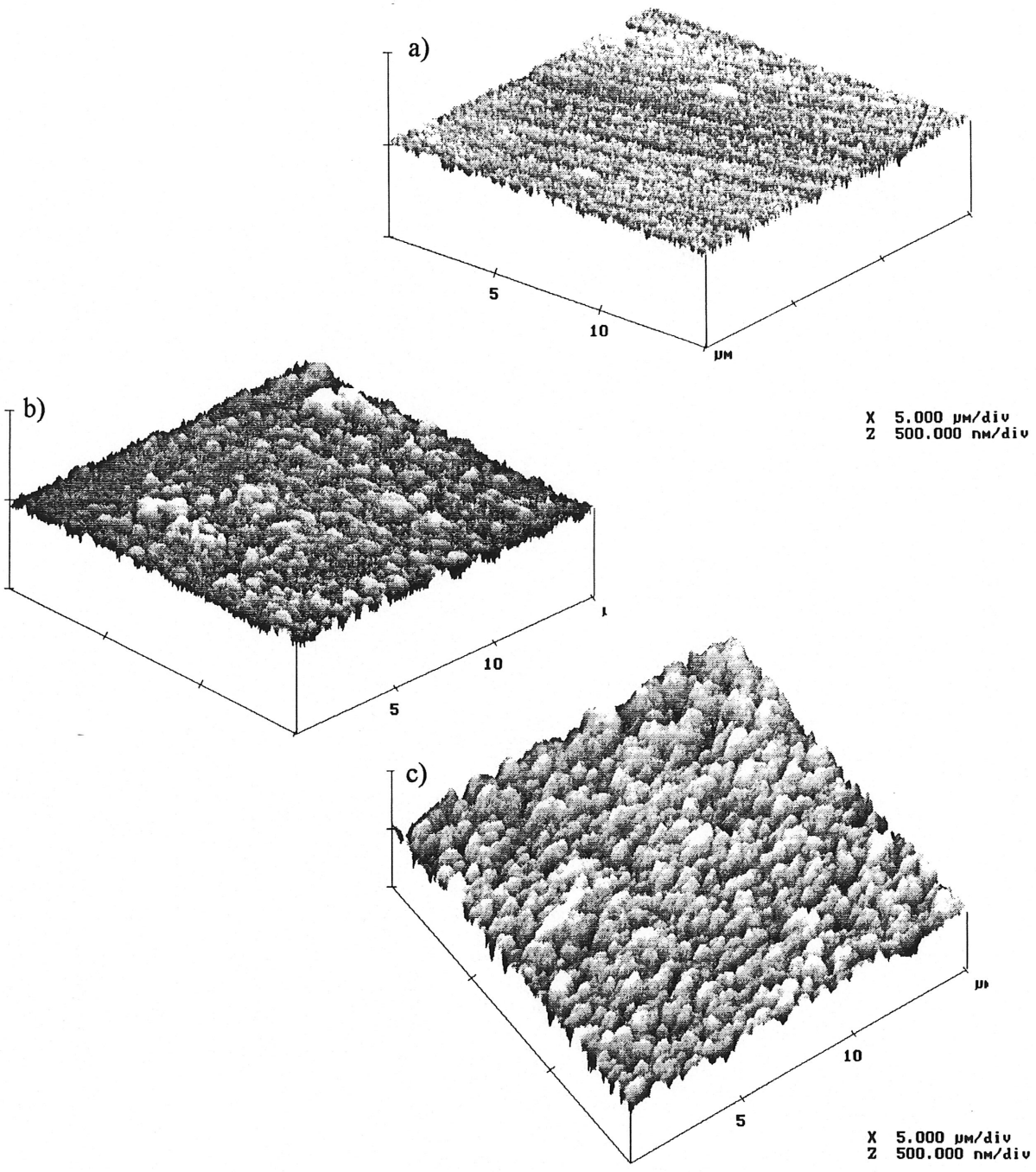

Figure 79. 3D view AFM images of hard gold deposits on Cu at -0.60 V; deposition time (s): (a) 50; (b) 150; (c) 450.

topography is clearly seen at a later stage at 450 s to be pyramidal with different grain sizes, Fig. 79c. Similar growth pattern, *i.e.*, three-dimensional pyramids, are observed at all potentials applied. AFM images obtained at different potentials are illustrated in Fig. 80. The pyramids have various sizes, indicating that such a nucleation is time-dependent, *i.e.*, the progressive one. Obviously, it is evident from Fig. 80 that the grain heights and their lateral sizes increase as potential becomes more negative from -0.50 to -0.70 V. The 3D AFM images obtained at other potentials also revealed similar surface morphology. Fig. 81 shows the mean roughness and the maximum grain height of hard gold deposits obtained at potentials between -0.50 and -0.80 V. The mean roughness increases and surface becomes rougher with negative potential, however, at -0.80 V, the roughness drops again to a very low value. Meanwhile, the maximum grain height increases from 226 nm at -0.50 V to 728 nm at -0.70 V, and drops to 285 nm at -0.80 V. The results suggest that growth in vertical direction is inhibited.

Fig. 82 illustrates the cross-sectional analysis of AFM images of hard gold deposits at -0.60 and -0.70 V along the black line shown on each image. Pyramidal growth may also be clearly viewed from this figure. Note that the scale in z-direction is greatly expanded with respect to that in x-y plane, and the shape evolution of AFM images illustrates that growth rate in lateral direction is nearly four times that in the vertical direction.

Since all the clusters are not well separated, the values of both cluster density and the mean cluster size were not measured. The AFM lateral resolution does not provide the separation of the very close clusters, the result being an overestimation of the cluster size together with an underestimation of the density of clusters.

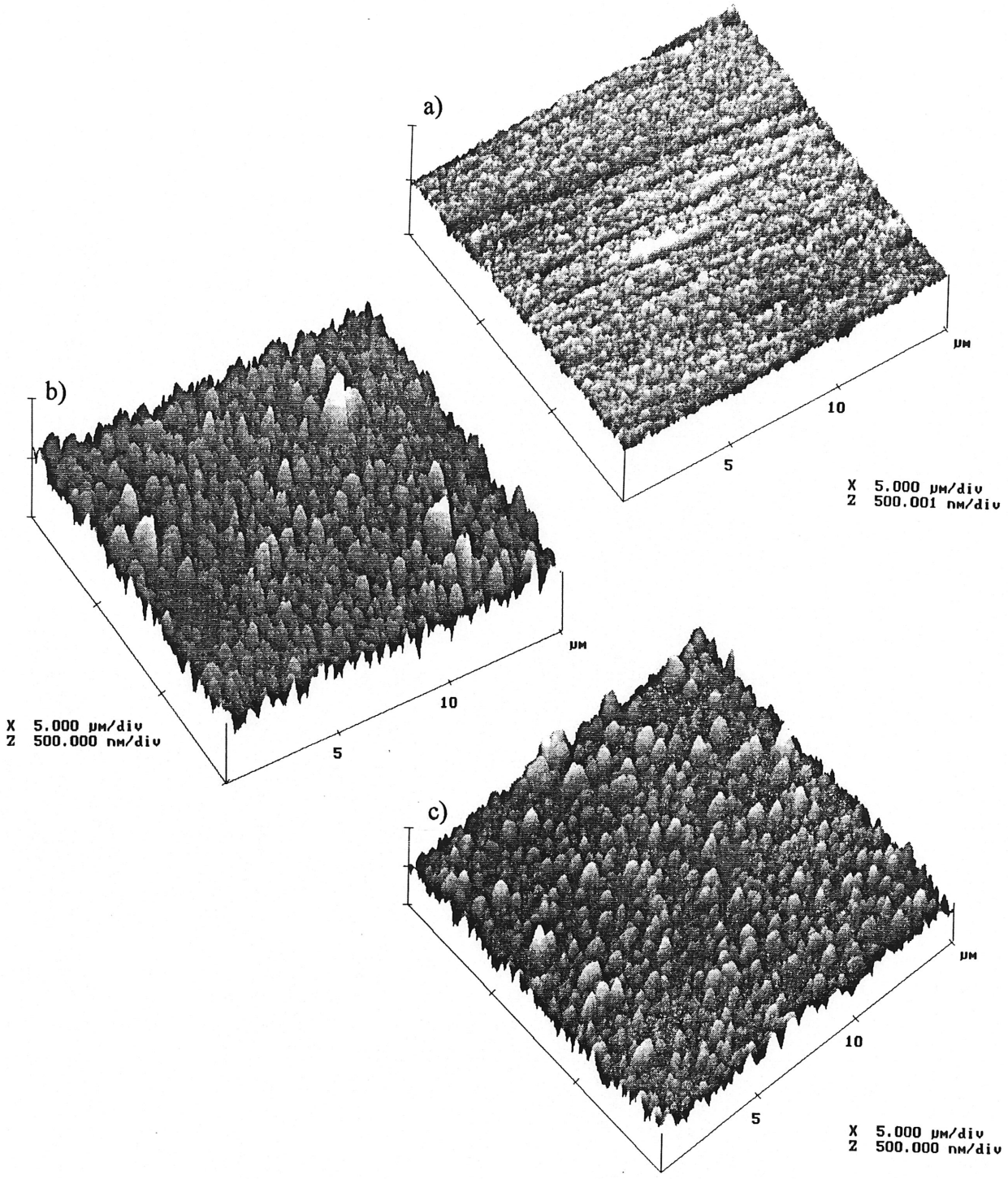

Figure 80. 3D view AFM images of hard gold deposits on Cu at different potentials; deposition time: 450 s; potential (V): (a) -0.50; (b) -0.65; (c) -0.75.

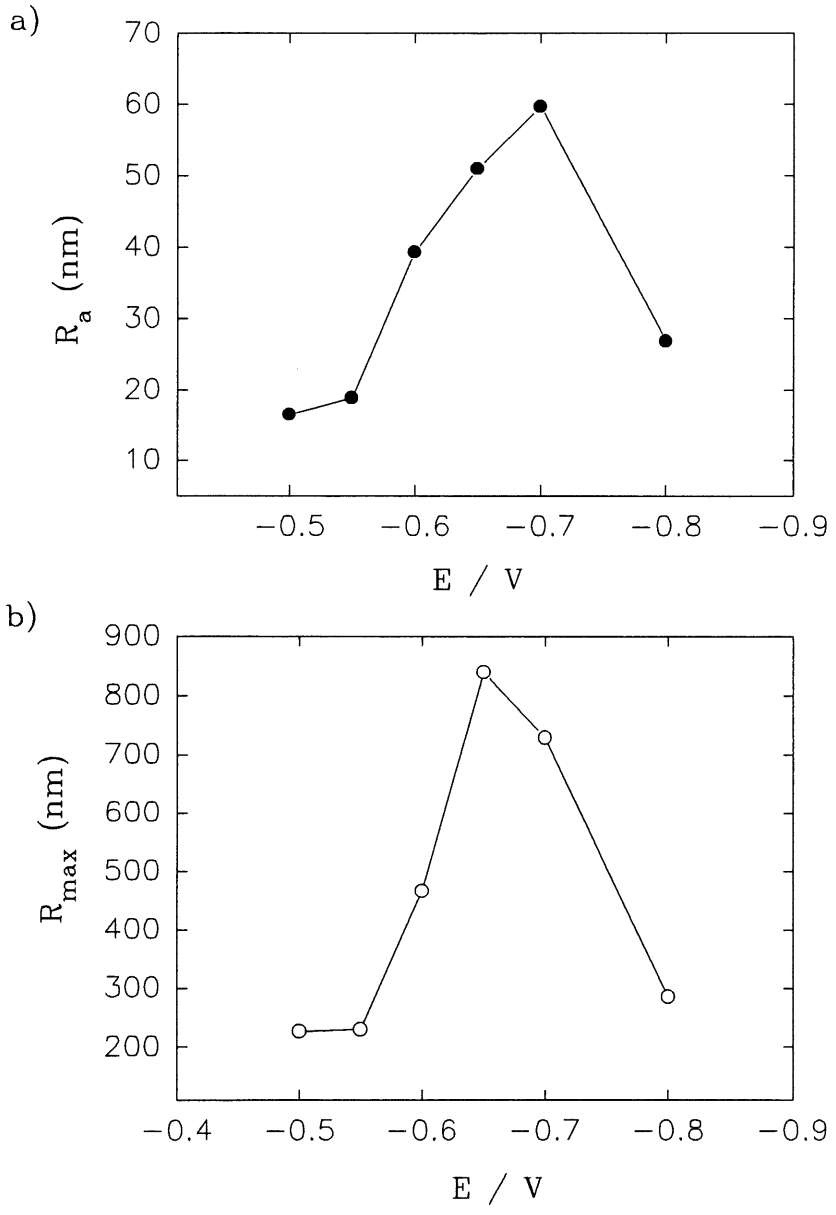

Figure 81. The dependence of the mean surface roughness, R_a, and the maximum grain height, R_{max}, for gold deposits on Cu obtained from hard gold bath, against the applied potential between -0.50 V and -0.80 V.

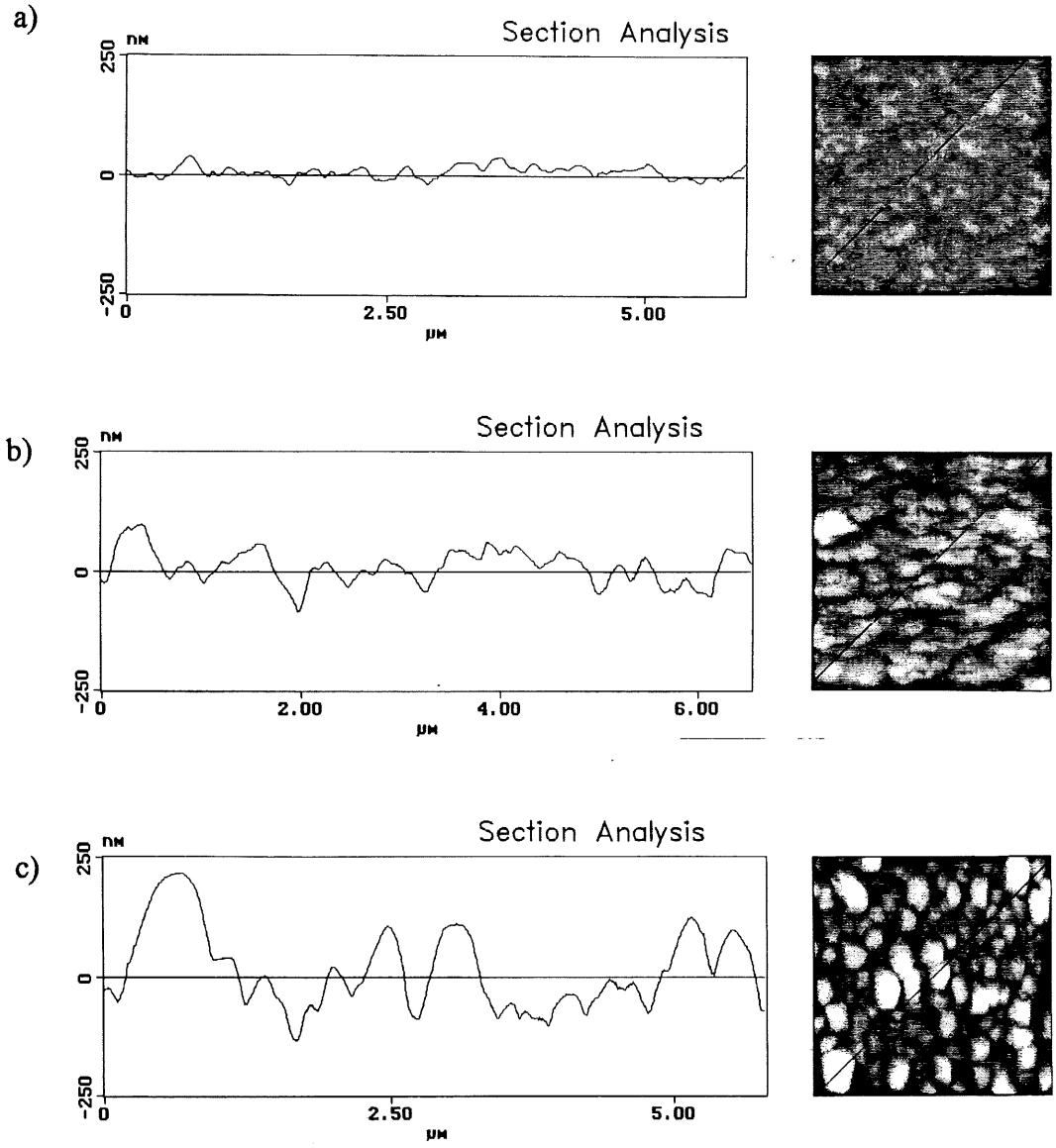

Figure 82. Section analysis of AFM images (left) and top-views (right) of hard gold deposits on Cu at different potentials. Cross-sections through the top view shown at the right side are marked as a black line; deposition time: 450 s; potential (V): (a) -0.55; (b) -0.65; (c) -0.70.

9. 3 Discussion

From the results presented above it was shown that three-dimensional nucleation and crystal growth are involved in gold deposition. The surface morphology of deposits was characterized using SEM and AFM. SEM shows that the topography of gold deposits is hemispherical or pyramidal with various grain sizes. The structural aspects of gold deposits from the same proprietary bath under galvanostatic mode and high speed jet plating condition was also studied by Bocking and Cameron using SEM (18,62), a rounded mound structure (hemispherical one) of crystal was shown to some extent to be similar to our finding. The so-called "rounded mound structure" was also reported by Nakahara (61) in his SEM study of cobalt hardened gold deposition. However, it is impossible to distinguish pyramidal and hemispherical growth patterns by SEM techniques. It is quite evident from AFM results that the surface topography of hard gold deposits is better described by three-dimensional pyramidal growth, rather than the hemispherical one. The growth rate in lateral direction is about four times that in vertical direction. Clusters of various sizes are randomly distributed on the surface.

The results obtained by SEM and AFM in our work show that the number of crystals and their grain size vary with time, indicating the progressive nucleation with three-dimensional pyramidal growth. Therefore, the model of three-dimensional progressive nucleation and crystal growth of right-circular cones found in the previous section is further confirmed by surface studies. Both techniques show that inhibition of growth is involved in gold deposition, in good agreement with the theoretical model. In comparison with soft gold deposits, the crystals of hard gold are more rounded and more uniformly distributed. Furthermore, the grain sizes of hard gold deposits are much smaller due to the addition of nickel in the bath, resulting in fine-graine deposits. Nickel appears to act as a grain refiner as well as a hardener.

9.4 Summary

The surface morphology of gold deposits on Au and Cu substrates were characterized using SEM and AFM techniques. SEM may only provide general information on the growth morphology. The height, growth morphology, grain size, roughness were determined using AFM. The results obtained from SEM and AFM showed that progressive nucleation is involved in gold deposition at more positive potentials. The growth of hard gold was shown by AFM to be three-dimensional pyramidal. The mean surface roughness and the maximum grain height increase with time, and these values also increase with negative potential from -0.50 to -0.75 V, and, subsequently, they decrease steeply after -0.80 V. Therefore, inhibition of growth observed at some potentials was further confirmed by AFM. Besides, it was shown from SEM of hard gold deposited on the gold-plated Ni RDE that the bimodal distribution of growing crystals is observed in hard gold deposits at more negative potentials due to the partial inhibition of growth. Hence, the conclusions obtained from chronoamperometric measurements are in a good agreement with microscopic observation.

CONCLUSIONS

The mechanism and kinetics of gold electrodeposition from a typical commercial gold plating bath (Renovel N) were investigated using voltammetric, chronopotentiometric and chronoamperometric techniques, mainly focused on the study of nucleation and crystal growth phenomena. The mechanism and kinetics of nucleation and crystal growth in both soft and hard gold deposition were determined. The influence of substrate on the deposition was also studied. The surface morphology of deposits was characterized using SEM and AFM techniques. Two new models of nucleation and crystal growth were developed. The inhibition in gold deposition was found. It was shown from the results that in order to obtain a good quality of deposits in practice, gold plating should be performed at a more negative potential (although more HER occurs) and at high mass-transfer conditions such as jet-plating. This work has also led to a better understanding of the nucleation and crystal growth phenomena during metal deposition. The overall results are concluded as follows:

A partial inhibition model was developed. Potential dependent minimum, maximum and steady-state occurring on the current-time curves are predicted by this model. It can well explain the varying ratios of the peak current to the steady-state value which are not predicted by the hemispherical growth model in literature. The right-circular cones growth model developed by Amonstrong *et al.* (108) and the inhibition growth model given by Bossco and Rangaranjan (110) are combined in one partial inhibition model. It was used to explain the experimental current-time transients of hard gold deposition at more negative potentials.

The concept of 2D cylindrical growth was expanded to 3D growth. Current equations for 3D cylindrical growth were derived. The model predicts the ratios of the peak current to the steady-state value being 1.46 and 1.79 for instantaneous and progressive nucleation, respectively. An attempt was made to describe the current-time curves on glassy carbon.

It was found that a self-inhibition phenomenon occurs in gold deposition at more positive potentials due to the reduction of adsorbed AuCN and the influence of the mass transfer of HCN produced in the deposition. A general equation describing the dependence of current on the rotation rate of RDE at more positive potentials was derived. A linear dependence of current with $\omega^{1/4}$ is obtained at certain conditions, in excellent agreement with experimental finding. Some experimental observations obtained in various solutions by other authors are also well explained.

It was found that Tafel curves can be constructed based on both the initial peak potential of the chronopotentiometric curves and the initial minimum current of the chronoamperometric curves. For both soft and hard gold deposition, relatively high Tafel slopes were obtained at more positive potentials because of the adsorption of AuCN. Tafel slopes for hard gold are much higher than those for soft gold.

The mechanism and kinetics of nucleation and growth of soft and hard gold deposition on various substrates were determined.

For soft gold deposition, various nucleation and crystal growth mechanisms are involved in the initial stages of deposition at different potentials. The 2D progressive nucleation and crystal growth of cylinders and the 3D progressive nucleation and growth of right circular cones occur simultaneously at lower overpotentials, in which the contribution of 2D process decreases with negative potential and then becomes negligible. At potentials between -0.725 and -0.85 V, 3D progressive nucleation and crystal growth of right-circular cones were found. Nucleation changes from progressive at potentials between -0.725 and -0.85 V to instantaneous at more negative potentials from -0.90 V to -0.975 V. A secondary 3D progressive nucleation and growth process was found to occur on the top of the first layers at potentials between -0.90 and -0.975 V. The inhibition of vertical crystal growth was observed.

Nucleation rate of soft gold deposition was found to decrease with negative potentials due to inhibition, in contrast to the nucleation theories.

The nucleation and crystal growth in hard gold deposition at potential between -0.5 to -0.7 V occurs *via* 3D progressive nucleation and growth of right circular cones. The growth rate constant is much smaller than that for soft gold deposition, showing that the crystal growth is depressed by nickel. The vertical growth rate also shows a nonlinear tafelian dependence with potential due to inhibition, similar to soft gold. However, nucleation rate of hard gold deposition increases with an increase in negative potential, in agreement with the atomistic nucleation theory. At more negative potentials, vertical crystal growth in hard gold deposition is partially inhibited. The inhibition parameter is always less than one.

The mechanism and kinetics of nucleation and crystal growth in gold deposition depends strongly on the substrate's nature. Copper substrate shows most similar electrochemical behavior to the Au RDE. The three-dimensional progressive nucleation and growth of right circular cones occurs at more positive potentials and the inhibition of vertical growth was also observed. The nucleation and crystal growth of hard gold deposition on nickel RDE may be described by the partial inhibition model. For glassy carbon electrode, the partial inhibition model also gives the best description for the experimental data. Alternatively, the three-dimensional cylindrical growth also can explain the current-time transient curves.

The inhibition of crystal growth observed electrochemically was further confirmed by SEM and AFM techniques. Progressive nucleation was found. AFM confirmed that the growth feature of gold deposits on Cu RDE is better described as right-circular cones (pyramidal growth), in a good agreement with the assumption in the use of nucleation/crystal growth model. The bimodal distribution of crystal sizes was observed in hard gold deposition using SEM, giving an evidence for the partial inhibition model.

Bibliography

1. I. R. CHRISTIE and B. P. CAMERON, Gold Bull. **27**, 12 (1994).
2. F. H. REID and W. GOLDIE (Eds.), Gold Plating Technology, Electrochemical Publications Ltd, Ayr, 1974.
3. G. R. ELKINGTON, British Patent 8447 (1840).
4. A. M. WEISBERG, Prod. Finish. (Cincinnati), **58** (2-A), 166 (1993).
5. F. R. SCHLODDER, H. H. BEYER and W. G. ZILSKE, GOLD 100, Vol. 3: Proceedings of the International Conference on Gold, Johannesburg, SAIMM, 1986, p.21.
6. R. T. PAGE, Metal Finishing Journal, **20**, 4 (1974).
7. J. HENDRIKS, *in* Connectors 91, One day Symp. Exhib. *Edited by* G. D. Wilox and D. H. Ross, Inst. Met. Finish. Birmington, UK, 1991, p20.
8. S. J. HEMSLEY and R. V. GREEN, Trans. Inst. Metal Finish. **69**, 149 (1991).
9. J. A. LOCHET, Proc. AESF Annu. Tech. Conf. Vol. **2**, 1990, 77th, p.983.
10. J. A. LOCHET, U. S. Pat. 4670107 (1986); 4744871 (1988); 4755264 (1988).
11. A. FLETHER and W. L. MORIARY, U. S. Pat. 4197172 (1980).
12. Y. OKINAKA and C. WOLOWODIUK, J. Electrochem. Soc. **128**, 288 (1981).
13. P. BIBERBACH, W. DIETSCHMANN and H. J. LUEBKE, Ger. Offen. 2355581 (1975).
14. W. T. MATSON, U. S. Pat. 4436595 (1984).
15. P. WINGENFELD, *in* Connectors 91, One day Symp. Exhib. *Edited by* G. D. Wilox and D. H. Ross, Inst. Met. Finish. Birmington, UK, 1991, p.143.
16. C. BOCKING, Trans. I M F. **66**, 50 (1988).
17. C. BOCKING, Proc. 59th International Conf. on Surf. Finish., IMF. **2**, 51(1991).
18. C. BOCKING and B. CAMERON, Trans. I M F. **72**, 33 (1994).
19. J. K. DOREY, R. HAYNES, R. E. SINITSKI and R. E. WOODS, Plat. and Surf. Finish. **67**, 81(1987).
20. D. W. ENDICOTT and G. J. GASEY, Plat. and Surf. Finish. **67**, 58(1980).
21. H. Y. CHEH, J. Electrochrem. Soc. **118**, 551 (1971).

22. B. VINENT, P. BERCOT, G. F. CREUSAT, G. MESSIN and J. PAGETTI, Plat. and Surf. Finish. **77,** 71 (1990).

23. L. SJÖGREN, B. STHNER, L. G. LILJESTRAND and L. B. RÉVAY, Plat. and Surf. Finish., **73**, 70 (1986).

24. V. A. ZABLUDOVSKII, A. V. KRAPIVNOI, V.I KAPTANOVSKII, N. A. KOSTIN, I. Z. GUBAIDULLIN and A. M. AVIDON, Zashch. Met. **23**, 1038 (1986).

25. C. J. RAUB, H. R. KHAN and M. BAUMYÄRTNER, Gold Bull. **19**, 70 (1986).

26. M. MAJA, Atti. Accad. Sci. Torino Cl. Sci. Fis. Mat. Nat. **99**, 1111(1965)

27. "Handbook of Chemistry and Physics" 53rd ed., Chemical Rubler Publishing Company, Cleveland, 1972.

28. L. G. SILLEN, Stability Constants of Metal-Ion Complexs, Section 1, Special publication No 17, The Chemical Society, London, 1964.

29. V. I. MIROSHNICHENKO, K. I. LITOVCHENKO, V. S. KUBLANOVSKY, Dokl. Akad. Nauk. Ukr. SSR, **5**, 130 (1991).

30. D. POSKUS and G. AGAFONOVAS, J. Electroanal. Chem. **393**, 105 (1995).

31. D. POSKUS and G. AGAFONOVAS, J. Electroanal. Chem. **395**, 279 (1995).

32. H. G. SILVER, J. Electrochem. Soc. **116**, 26C (1969).

33. D. M. MAC ARTHUR, J. Electrochem. Soc. **119**, 672 (1969).

34. I. R. BURROWS, J. A. HARRISON and J. THOMPSON. J. Electroanal. Chem. **53**, 283 (1974).

35. J. A. HARRISON and J. THOMPSON. J. Electroanal. Chem. **40**, 114 (1972).

36. M. BETTOWSKA-BRZEZINSKA and E. DUTKIEWICZ, J. Electroanal. Chem. **99**, 341 (1979).

37. G. A. KURNPSKIN, V. N. FLEROV, A. N. MOSKVICHEV and A. O. ROZHDESTVENSKII, Elektrochimiya, **22**, 1124 (1986).

38. E. T. EISENMANN, J. Electrochem. Soc. **125**, 717 (1978).

39. A. SURVILA, V. MOCKEVICIUS and R. VISOMIRSKIS, Elektrochimiya, **23**, 816 (1987).

40. P. BINDRA, D. LIGHT, P. FREUDENTHAL and D. SMITH, J. Electrochem. Soc. **136**, 3616 (1987).

41. A. N. MOSKVICHEV, G. A. KURNOSKIN, V. N. FLEROV, and Y. M. TYURIN, Izv. Vyssh. Uchebn. Zaved. Khim. Khim. Tekhnol. **26**, 1458 (1983).

42. J. D. E. MCINTYRE and W. F. PECK . Jr., J. Electrochem. Soc. **123**, 800 (1976).

43. D. J. DAVIDOVIC and R. R. ADZIC, Electrochim. Acta, **33**, 103 (1988).

44. J. HOFMANN and D. W. WABNER, Metalloberfläche, **27**, 1(1973).

45. V. N. FEDOROVA and B. S.KRASIKOV, Zh. Prikl. Khim. **50**, 792 (1977).

46. V. S. KUBLANOVSKY, K. I LITOVCHENGKO, V. I. MIROSHICHENKO, Dokl. Akad. Nauk. Ukr. **11**, 115(1991).

47. H. Y. CHEH and R. SARD, J. Electrochem. Soc. **118**, 1737 (1971).

48. L. A. TARAN, S. I. BEREZINA, and G. S. VOZDVIZHENSKII, Tr. Kazan. Khim. Tekh. Inst. **36**, 591 (1967).

49. J. W. M. JACOBS and J. M. G. ROKKEN, J. Electrochem. Soc. **136**, 3633 (1989).

50. J. A. HARRISON and J. THOMPSON, J. Electroanal.Chem. **59**, 273 (1975).

51. H. ANGERER and N. IBL, J. Appl. Electrochem. **9**, 219 (1979).

52. M. ANTLER, Plating, **60**, 468 (1973).

53. H. A. REINHEIMER, J. Electrochem. Soc. **121**, 490 (1974).

54. S. E. CRAIG, R. E. HARR, J. HENRY and P. TURNER, J. Electrochem. Soc. **117**, 1450 (1970).

55. Y. OKINAKA and S. NAKAHARA, J. Electrochem. Soc. **123**, 1284 (1976).

57. G. HOLMBOM and B. E. JACOBSON, J. Electrochem. Soc. **135**, 2720 (1988).

58. S. T. RAO and R. WEIL, Trans. Inst. Met. Finish. **57**, 97 (1979).

59. K. L. LIN, W. C. LIU, M. H. M. LIN and Y. W. HU, J. Electrochem. Soc. **138**, 3276 (1991).

60. E. MATULIONIS and A. DZIUVE, Chemija, **178**, 44 (1990).

61. S. NAKAHARA, J. Cryst. Growth, **75**, 221 (1986).

62. C. BOCKING and C. DINEEN, Trans. IMF. **72**, 101 (1994).

63. G. B. MUNIER, Plating, **56**, 1151 (1967).

64. D. MASON, Plat. and Surf. Finish. **73**, 56 (1986).

65. S. NAKAHARA and Y. OKINAKA, J. Electrochem. Soc. **128**, 284 (1981).

66. R. L. COHEN, F. B. KOCH, L. N. SCHOENBERG and K. W. WEST, J. Electrochem. Soc. **126**, 1608 (1979).

67. Y. OKINAKA, F. B. KOCH, C. WOLOWODIUK and D. R. BLESSINGTOM, J. Electrochem. Soc. **125**, 1745 (1978).

68. Y. OKINAKA, Proc. - Electrochem. Soc. (Proc. Symp. Electrodeposition Technol., Theory, Pract.), 1987, p. 147.

69. C. J. RAUB, A. KNODLER and J. LENDVAY, Plat. Surf. Finish. **63**, 35 (1976).

70. L. HOLT, R. J. ELLIS and J. STANYER, Plating, **60**, 910 (1973).

71. L. HOLT and J. STANYER, Trans. Inst. Met. Finish. **50**, 24 (1972).

72. R. L. COHEN, K. W. WEST and M. ANTLER, J. Electrochem. Soc. **123**, 1284 (1976).

73. G. HOLMBOM and B. E. JACOBSON, J. Electrochem. Soc. **135**, 787 (1988).

74. E. T. EISENMANN, J. Electrochem. Soc. **124**, 1957 (1977).

75. C. S. GIBSON, Proc. R. Soc. Ser. A, **173**, 160 (1939).

76. H. ZHDANOV and E. SHUGAM, Acta Physicochim. URSS, **20**, 253 (1945).

77. C. VANDECASTEELE, J.DEWAELE, J. HOSTE, R. DE DONKER, F. VANGAEVER and J. VANHUMBEECK, J. Radioanal. Nucl. Chem. Letters, **95**, 167 (1987).

78. R. DE LEVIE, *in* Advances in Electrochemistry and Electrochemical Engineering. *Edited by* H. Gerischer and C. W. Tobias, John Wiley & Sons, New York, 1984, Vol.13, p.1.

79. E. B. BUDEVSKI, *in* Comprehensive Treatise of Electrochemistry, *Edited by* B. E. Conway, J. O'M. Bockris, E. Yeager, S. U. M. Khan and R. E. White, Plenum Press, New York, Vol. 7, p. 399.

80. M. FLEISCHMANN and H. R. THIRSK, *in* Advances in Electrochemistry and Electrochemical Engineering, *Edited by* P. Delahay. Wiley-Interscience, New York, 1963, Vol. 3, p.123.

81. M. FLEISCHMANN and H. R. THIRSK, Electrochim. Acta, **2**, 22 (1960).

82. R. KAISCHEV and B. MUTAFTSHIEV, Electrochim. Acta, **10**, 643 (1965).

83. I. MARKOV and D. KASCHIEV, J. Crystal Growth, **16**, 170 (1972).

84. I. MARKOV, Thin Solid Films, **35**, 11 (1976).

85. S. FLETCHER and T. TWIN, Electrochim. Acta, **28**, 237 (1983).

86. I. MARKOV and D. KASCHIEV, J. Crystal Growth, **13/14**, 131 (1972).

87. I. MARKOV and E. STOYCHEVA, Thin Solid Films, **35**, 21(1976).

88. R. KAISCHEV, Bull. Acad. Bulg. Sci. (Phys.) **1**, 100 (1950).

89. R. KAISCHEV, Bull. Acad. Bulg. Sci. (Phys.) **2**, 191 (1951).

90. R. KAISCHEV and G. BLIZNAKOV, C. R. Acad. Bulg. Sci. **1**, 23 (1949).

91. I. MARKOV and R. KAISCHEV, Kristall und Technik, **11**, 685 (1976).

92. D. WALTON, J. Chem. Phys. **37**, 2182 (1962).

93. A. MILCHEV, S. STOYANOV and R. KAISCHEV, Thin Solid Films, **22**, 255 (1976).

94. A. MILCHEV, S. STOYANOV and R. KAISCHEV, Thin Solid Films, **22**, 267 (1976).

95. A. MILCHEV and S. STOYANOV, J. Electroanal. Chem. **72**, 33 (1976).

96. A. MILCHEV and E. VASSILEVA, J. Electroanal. Chem. **107**, 337 (1980).

97. J. A. HARRISON and H. R. THIRK, *in* Electroanalytical Chemistry. *Edited by* A. J. Bard, Marcel Dekker, New York, 1971, Vol. **5**, p. 67.

98. S. FLETCHER, J. Electroanal. Chem. **118**, 419 (1981).

99. J. O'M. BOCKRIS and G. A. RAZUMNEY, *in* Fundamental Aspects of Electrocrystallization, Plenum Press, New York, 1967.

100. A. R. DESPIC, *in* Comprehensive Treatise of Electrochemistry, *Edited by* B. E. Conway, J. O'M. Bockris, E. Yeager, S. U. M. Khan and R. E. White, Plenum Press, New York and London, Vol. **7**, p 451.

101. KOLMOGOROV, A. N., Izv. Akad. Nauk SSSR, Ser. Mat. **3**, 355 (1937).

102. M. AVRAMI, J. Chem. Phys. **7**, 1103 (1939); **8**, 212 (1940); **9**, 177 (1941).

103. U. R. EVANS, Trans. Faraday. Soc. **41**, 365 (1945).

104. M. Y. ABYANEH and M. FLEISCHMANN, Electrochim. Acta, **27**, 1513 (1982).

105. E. BOSCO and S. K. RANGARAJAN, J. Chem. Soc., Faraday Trans. I, **77**, 483 (1981).

106. M. Y. ABYANEH and M. FLEISCHMANN, J. Electrochem. Soc. **138**, 2485 (1991).

107. R. D. ARMSTRONG and J. A. HARRISON, J. Electrochem. Soc. **116**, 328 (1969).

108. R. D. ARMSTRONG, M. FLEISCHMANN and H. R. THIRK, J. Electroanal. Chem. **11**, 208 (1966).

109. S. K. RANGARAJAN, Faraday Symp. **12**, 101 (1977).

110. E. BOSCO and S. K. RANGARAJAN, J. Electroanal. Chem. **134**, 213 (1982).

111. S. FLETCHER, Electrochim. Acta, **28**, 917 (1983).

112. V. A. ISAEV and A. N. BARABOSHKIN, Elektrokhimiya, **30**, 225 (1994).

113. M. Y. ABYANEH, Electrochim. Acta, **27**, 1329 (1982).

114. M. Y. ABYANEH, Electrochim. Acta, **36**, 727 (1991).

115. M. Y. ABYANEH, J. Electroanal. Chem. **387**, 29 (1995).

116. M. FLEISCHMANN, M. LABRAM and C. GABRIELLI, Surface Science, **101**, 583 (1980).

117. E. BOSCO and S. K. RANGARAJAN, J. Chem. Soc., Faraday Trans. I, **77**, 1673 (1981).

118. B. BHATTACHARJEE and S. K. RANGARAJAN, J. Electroanal. Chem. **366**, 271 (1994).

119. W. H. MULDER, J. Electroanal. Chem. **366**, 287 (1994).

120. V. TROFIMENKO, V. ZHITNIK, T. ALEKSANDROV and Y. LOSHKARYEV, Elektrokhimiya, **16**, 1139 (1980).

121. V. TROFIMENKO, V. ZHITNIK, T. ALEKSANDROV and Y. LOSHKARYEV, Elektrokhimiya, **17**, 1644 (1981).

122. V.TSAKOVA, A. DANILOV, E. MICHAILOVA, I. VITANOVA, D. STOYCHEV and A. MILCHEV, Elektrokhimiya, **20**, 1498 (1984).

123. V. TSAKOVA and A. MILCHEV, J. Electroanal. Chem. **235**, 249 (1987).

124. M. Y. ABYANEH and M. FLEISCHMANN, J. Electroanal. Chem. **119**, 187, 197 (1981).

125. R. G. BARRADAS, F. C. BENSON and S. FLETCHER, J. Electroanal. Chem. **80**, 305 (1977).

126. E. GÓMEZ, C. MÜLLER, R. POLLINA, M. SARRET and E. VALLÉS, J. Electroanal. Chem. **333**, 47 (1992).

127. E. BOSCO and S. K. RANGARAJAN, J. Electroanal. Chem. **134**, 225 (1982).

128. T. VARGAS and R. VARMA, in Techniques for Characterization of Electrodes and Electrochemical Processes, *Edited by* R. Varma and J. R. Selman, John Wiley & Sons, Inc., 1991, Chapter 15, p. 717.

129. M. F. BELL and J. A. HARRISON, J. Electroanal. Chem. **41**, 15 (1973).

130. J. A. HARRISON, J. Electroanal. Chem. **36**, 71 (1972).

131. W. DAVISON and J. A. HARRISON, J. Electroanal. Chem. **44**, 213 (1973).

132. B. R. SCHARIFKER and J. MOSTANY, J. Electroanal. Chem. **177**, 13 (1984).

133. S. FLETCHER, J. Chem. Soc., Faraday Trans. I, **79**, 467 (1983).

134. G. GUNAWARDENA, G. HILLS and I. MONTENEGRO, Electrochim. Acta, **23**, 693 (1983).

135. G. GUNAWARDENA, G. HILLS, I. MONTENEGRO and B. SCHARIFKER, J. Electroanal. Chem. **138**, 225 (1982).

136. W. CHRZANOWSKI, Y. G. LI and A. LASIA, J. Appl. Electrochem., in press (1996).

137. R. GREEF, R. PEAT, L. M. PETER, D. PLETCHER and J. ROBINSON, Instrumental Methods in Electrochemistry, Ellis Horwood Limited, 1985. p. 235.

138. V. G. ROEV and N. V. GUDIN, Elektrokhimiya, **31**, 532 (1980).

139. S. FLETCHER and C. S. HALLIDAY, J. Electroanal. Chem. **159**, 267 (1983).

140. H. BALTRUSCHAT and J. HEITBAUM, J. Electroanal. Chem. **157**, 319 (1983).

141. M. R. MAHONEY and R. P. COONEY, J. Chem. Soc., Faraday Trans. I, **81**, 2115 (1985).

142. P. GAO and M. J. WEAVER, J. Phys. Chem., **93**, 6205 (1989).

143. N. ROGOZHNIKOV, Elektrokhimiya, **27**, 683 (1980).

144. H. S. DONG and K. KWAN, Bull. Korean Chem. Soc. **15**, 357 (1994).

145. S. FLETCHER and A. SMITH, Can. J. Chem. **56**, 908 (1978).

146. D. KASHCHIEV, Thin Solid Films, **29**, 193 (1975).

147. A. MILCHEV and M. I. MONTENEGRO, J. Electroanal. Chem. **333**, 93 (1992).

148. N. A. SALTYKOVA, O. V. PORTNYAGION, L. T. KOSIKHIN, A. N. BARABOSHKIN, N. O. ESINA and A. P. KOROVENKOV, Elektrokhimiya **27**, 1496 (1991).

149. G. A. GUMAWARDENA, G. J. HILLS and I. MONTENEGRO, Faraday. Symp. Chem. Soc. **12**, 90 (1977).

150. L. T. KOSIKHIN, N. A. SALTYKOVA, and A. N. BARABOSHKIN, Elektrokhimiya **27**, 1219 (1991).

151. D. S. GNANAMUTHU and J. V. PETROCELLI, J. Electrochem. Soc. 114, 1036 (1967).

152. F. LANTELME AND J. CHEVALET, J. Electroanal. Chem. **121**, 311 (1981).

153. G. RAZUMNEY and J. O'M. BOCKRIS, J. Electroanal. Chem. **46**, 185 (1973).

154. D. A. VERMIYEA, J. Chem. Phys. **25**, 1254 (1956).

155. A. J. BARD and A. R. FAULKNER, Electrochemical Methods (Fundamentals and Applications), John Wiley & Sons, New York, 1980, p. 304.

156. A. H. CREUS, P. CARRO, S. GONZALEZ, R. C. SALVAREZZA and A. J. ARVIA, Electrochim. Acta **37**, 2215 (1992).

157. M. Y. ABYANEH and M. FLEISCHMANN, Trans. IMF. **58**, 91 (1980)

158. M. Y. ABYANEH, J. HENDRIKX, W. VISSCHER and E. BARENDRECHT, J. Electrochem. Soc. **129**, 2654 (1982)

159. I. R. BURROWS, J. A. HARRISON and J. THOMPSON, J. Electroanal. Chem. **58**, 241 (1975).

160 J. A. HARRISON, H. B. S. ALCAZAR and J. THOMPSON, J. Electroanal. Chem. **53**, 145 (1974).

161. J. AMBLARD, M. FROMENT, G. MAURION, N. SPRELLIS and E. TREVISAN-SOUTEYRAND, Electrochim. Acta **28**, 909 (1983).

162. P. M. RIGANO, C. MAYER and T. CHIERCHIE, Electrochim. Acta **35**, 1189 (1990).

163. M. FLEISCHMANN, G. SUNDHOLM and Z. Q. TIAN, Electrochim. Acta **31**, 907 (1986).

164. E. CHASSAING, M. JOUSSELLIN and WIART, J. Electroanal. Chem. **157**, 75 (1983).

165. E. VALLÉ, R. POLLINA and E. GÓMEZ, J. Appl. Electrochem. **23**, 508 (1993).

166. M. FLEISCHMANN and A. SARABY-REINTJES, Electrochim. Acta **29**, 69 (1984)

167. W. J. LORENZ and G. STAIKOV, Surf. Sci. **335**, 32 (1995).

168. V. D. JOVIC, J. N. VICEVIC, Electrochim. Acta **30**, 1455 (1985).

169. S. MANNE, P. K. HANSMA, J. MASSIE, V. B. ELINGS and A. A. GEWIRTH, Science **251**, 183 (1991).

170. R. M. RYNDERS and R. C. ALKIRE, J. Electrochem. Soc. **141**, 1166 (1994).

171. J. R. LAGRAFF and A. A. GEWIRTH, J. Phys. Chem. **98**, 11246 (1994).

172. M. KOINUMA and K. UOSAKI, Electrochim. Acta **40**, 1345 (1995).

173. R. J. NICHOLS, D. SCHRÖER and H. MEYER, Electrochim. Acta **40**, 1479 (1995).

174. N. IKEMIYA, S. MIYAOKA and S. HARA, Surface Science **327**, 261 (1995).

175. S. A. HENDRICKS, Y. T. KIM and A. J. BARD, J. Electrochem. Soc. **139**, 2818 (1992).

176. K. KOWAL, L. XIE, R. HUQ and G. C. FARRINGTON, J. Electrochem. Soc. **141**, 1166 (1994).

177. E. GÖMEZ, E. Valles, P. Gorostiza, J. Servat and F. Sanz, J. Electrochem. Soc. **142**, 4091 (1995).

178. N. M. MARTYAK and R. J. NICHOLS, Proc. AESF Annu. Tech. Conf. 1994, 81st, p. 561.

179. G. WOUTERS, M. BRATOEVA, J.-P. CELIS, J. R. ROOS, Electrochim. Acta **40**, 1434 (1995).

180. L. CHEN and D. GUAY, J. Electrochem. Soc. **141**, L43 (1994).